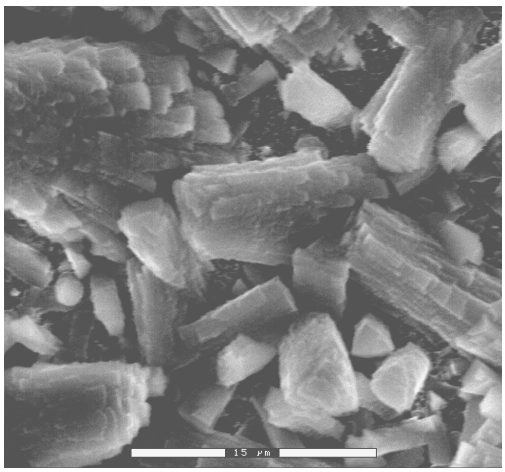

Carbon Dioxide: The Unknown Factor in the Atmospheric Corrosion of Light Metals

A Laboratory Study

Daniel Bengtsson Blücher

Department of Chemical and Biological Engineering
Chalmers University of Technology
Göteborg, Sweden 2005

THESIS FOR THE DEGREE OF DOCTOR OF PHILOSOPHY

Carbon Dioxide: The Unknown Factor in the Atmospheric Corrosion of Light Metals

A Laboratory Study

DANIEL BENGTSSON BLÜCHER

Department of Chemical and Biological Engineering
CHALMERS UNIVERSITY OF TECHNOLOGY
Göteborg, Sweden, 2005

DANIEL BENGTSSON BLÜCHER
ISBN 91-7291-623-0

Doktorsavhandlingar vid Chalmers Tekniska Högskola
Ny serie nr 2305
ISSN 0346-718X

Department of Chemical and Biological Engineering
Chalmers University of Technology
SE-41296 Göteborg
Sweden
Telephone +46 31 7721000

Cover: Bayerite crystals, α-$Al(OH)_3$, formed on commercially pure Al (AA1070) exposed for 4 weeks at 38°C in the absence of CO_2. The relative humidity was 95%. The sample was coated with 70µg NaCl/cm^2 prior to exposure.

Majornas CopyPrint
Göteborg, Sweden 2005

Carbon Dioxide: The Unknown Factor in the Atmospheric Corrosion of Light Metals

A Laboratory Study

DANIEL BENGTSSON BLÜCHER

Department of Chemical and Biological Engineering

Chalmers University of Technology

Abstract

The atmospheric corrosion of Al and Mg-Al alloys was investigated using controlled air in the laboratory. The effects of CO_2, temperature, NaCl, relative humidity, SO_2, NO_2 and O_3 on corrosion rate and corrosion product composition were examined. Initial stages of corrosion were studied *in situ* using Scanning Kelvin Probe Force Microscopy (SKPFM), which monitors the Volta potential and the topography at sub-micrometer resolution. The corrosion products were analyzed by techniques including IC, GI-XRD, ESEM/EDX, SKP, FIB/SEM and AES.

The main finding is that ambient concentrations of CO_2 (350ppm) inhibit the NaCl-induced atmospheric corrosion of Al and Mg-Al alloys. In the absence of CO_2, high pH regions form in the surface electrolyte due to the cathodic reduction of oxygen. The high pH electrolyte dissolves the alumina-containing passive film, resulting in rapid corrosion. When CO_2 is present, it forms carbonic acid that neutralizes the hydroxide formed in the cathodic vicinity, which slows the corrosion. On aluminum-based alloys NaCl produces general corrosion in humid air without CO_2, while pitting is observed at ambient CO_2 levels. The temperature-dependence of the NaCl induced atmospheric corrosion of aluminum alloys is strongly non-linear. With increasing temperature, the inhibitive effect of CO_2 declines due to the decreasing solubility of CO_2 in water. On Mg-Al alloys, corrosion attack is localized in the absence of CO_2, while general corrosion prevails in its presence. The inhibitive effect of CO_2 is relevant to occluded areas, where the supply of CO_2 is limited, for example in crevice corrosion and corrosion beneath organic coatings.

In humid air, SO_2 accelerates the atmospheric corrosion of Al and Mg-Al alloy. The surface electrolyte is acidified by sulfuric acid formation, destabilizing the passive film. However, for aluminum alloys, SO_2 inhibits the NaCl-induced pitting corrosion. The precipitation of aluminum hydroxy sulfates was believed to retard pit propagation. The deposition rate of SO_2 on Al is slow and almost independent of the SO_2 concentration. In contrast, SO_2 deposition on Mg-Al alloys is transport limited at high humidity. In the presence of SO_2, Mg-Al alloys suffer pitting corrosion that preferentially attacks the α phase.

Keywords: Atmospheric corrosion, aluminum alloys, magnesium, Mg-Al alloys, CO_2, temperature, NaCl, SO_2, NO_2, O_3.

List of Acronyms

AES	Auger electron spectroscopy
AFM	atomic force microscopy
BSE	backscattered electrons
EBSD	electron backscattered diffraction
EDX	energy dispersive X-ray
ESEM	environmental scanning electron microscopy
FCC	face centered cubic
FEG	field emission gun
FIB	focused ion beam
GI-XRD	grazing incidence X-ray diffraction
HCP	hexagonal close packing
IC	ion chromatography
PLA	pressure limiting aperture
PVD	physical vapor deposition
RE	rare earth
SE	secondary electrons
SEM	scanning electron microscopy
SKP	scanning Kelvin probe
SKPFM	scanning Kelvin probe force microscopy
ss	solid solution
TEM	transmission electron microscopy
TRAD	time resolved analysis of the deposition
XRD	X-ray diffraction
RH	relative humidity

Preface

The research for this thesis was carried out at the Department of Chemical and Biological Engineering, Chalmers University of Technology, Göteborg, Sweden. This work is a part of the EC project "Mg-Chassis", contract number *G3RD-CT-2000-00287*. The "Mg-Chassis" project aims to reduce the weight of cars and is a joint venture between Volkswagen AG, Adam Opel AG, the Fraunhofer Institute, Centro Ricerche Fiat (CRF), Dead Sea Magnesium Ltd., DiamlerChrysler AG, the European Aeronautic Defense and Space Company (EADS), the Swedish Corrosion Institute and Chalmers University of Technology. Funding was also provided by the Swedish Research Council and Volvo Car Corporation. Additional research partners were the Department of Experimental Physics and the Department of Materials and Manufacturing Technology, Chalmers University of Technology. The cooperation of the industrial and academic partners has proven to be very rewarding. It has resulted in a deeper understanding of the mechanisms underlying the initial atmospheric corrosion of Al and Mg-Al alloys.

List of Publications

Paper 1

D. B. Blücher, R. Lindström, J.-E. Svensson, and L.-G. Johansson, "The Effect of CO_2 on the NaCl-Induced Atmospheric Corrosion of Aluminum", *J. Electrochem. Soc.*, **148** (4), pp. B127–B131, (2001).

Paper 2

D. B. Blücher, J.-E. Svensson, and L.-G. Johansson, "Carbon Dioxide: The Unknown Factor in the Atmospheric Corrosion of Aluminum?", *Proceedings of the 15th International Corrosion Congress, Granada, Spain; September (2002).*

Paper 3

D. B. Blücher, J.-E. Svensson, and L.-G. Johansson, "The NaCl-Induced Atmospheric Corrosion of Aluminum: The Influence of Carbon Dioxide and Temperature", *J. Electrochem. Soc.,* **150** (3), pp. B93–B98, (2003).

Paper 4

D. B. Blücher, J.-E. Svensson, L.-G. Johansson, M. Rohwerder and M. Stratmann, "Scanning Kelvin Probe Force Microscopy, a Useful Tool for Studying Atmospheric Corrosion of Mg-Al Alloys *in situ*", *J. Electrochem. Soc.,***151** (12), pp. B621–B626, (2004).

Paper 5

D. B. Blücher, J.-E. Svensson and L.-G. Johansson, "Influence of ppb Levels of SO_2 on The Atmospheric Corrosion of Aluminum in the Presence of NaCl", accepted for publication in *J. Electrochem. Soc.*

Paper 6

D. B. Blücher, R. Lindström, J.-E. Svensson and L.-G. Johansson, "The Influence of SO_2 on The Atmospheric Corrosion of Mg and Mg-Al Alloys", submitted to *J. Electrochem. Soc.*

Paper 7

D. B. Blücher, J.-E. Svensson and L.-G. Johansson, "The influence of CO_2, $AlCl_3 \cdot 6H_2O$, $MgCl_2 \cdot 6H_2O$, Na_2SO_4 and NaCl on the atmospheric corrosion of aluminum", submitted to *Corr. Sci.*

TABLE OF CONTENTS

1 Introduction

The need for fuel efficiency and increased performance in transportation systems continually places new demands on materials. The design criteria are concerned primarily with density, strength, stiffness and corrosion resistance. In recent years, the automotive industry has directed much effort towards decreasing the weight of vehicles. A weight reduction of 100 kg leads to a reduction in fuel consumption of 3 to 5%, depending on whether or not the reduction is used to downsize the driveline. A decrease in fuel consumption also lowers emissions of greenhouse gases, for example CO_2. A way to reduce the weight of vehicles is by replacing steel with lighter materials, such as aluminum or magnesium alloys, that have low weight and high strength. In the implementation of aluminum and magnesium alloys by car manufacturers, the capacity of these materials to withstand atmospheric corrosion is critical. The lack of information on atmospheric corrosion behavior impedes the use of light metal alloys, in particular Mg alloys for exterior applications. Another problem is the discrepancy in results obtained from a variety of accelerated corrosion testing methods [1]. The laboratory work presented here deals with the initial stages of atmospheric corrosion of Al and Mg-Al alloys and aims to deepen the understanding of the mechanisms underlying the atmospheric corrosion of these alloys.

Aluminum of the purity obtained from the electrolytic reduction of alumina is a relatively soft material. Alloying aluminum with copper yields a high-strength material used in aircraft, while corrosion resistance is obtained by alloying it with Mg. When both corrosion resistance and high strength are needed, Al-Cu or Al-Zn-Mg alloys are coated with a high purity aluminum to protect the core alloy, i.e. the cladding [2]. The problem with alloys is the potential difference between the phases, which leads to an increased susceptibility to galvanic corrosion [3].

The aim of this work is to contribute towards a better understanding of the mechanisms of the atmospheric corrosion of Al and Mg-Al alloys in humid air. The influences of CO_2, temperature, NaCl, SO_2, NO_2 and O_3 are investigated. The effect of CO_2 is of interest because it may be absent in some places, for example in occluded areas such as crevices and beneath organic coatings [4-6]. Hygroscopic salts accumulate in these places, which generates a corrosive environment. This is a problem for the aircraft and

car industries, as material failure due to corrosion attack can be fatal. However, it is very expensive to take an aircraft out of service for inspection; it would be beneficial for these industries to have a model for prediction. The effect of SO_2 was studied because sulfur rich corrosion scales have been reported in field studies [7]. Although the trend is generally decreasing amounts of SO_2, industrialized areas with high SO_2 concentration still exist [8]. In this type of atmosphere, the concentration of O_3 and NO_2 is often high as well. The synergistic effects of SO_2 with O_3 or NO_2 or both are interesting to explore as they may shed light on the mechanisms of oxidation. To help interpret the complex phenomena of real Mg-Al alloys, a synthetic model system was devised using physical vapor deposition (PVD) techniques to form μm sized artificial cathodic areas of Al on Mg.

2 General aspects of the atmospheric corrosion of Al and Mg-Al alloys

2.1 Aluminum and its alloys

Aluminum is present in nature not as a metal but only in oxidized form, much due to its reactivity. To obtain aluminum, the raw material used is bauxite ore. The process demands much energy: it involves electrolytic refining of $Al(OH)_3$ extracted from the ore and dissolved in cryolite, $NaAlF_6$ (Bayer and Hall-Heroult processes) [9]. The overall reaction is (1).

(1) $$2Al_2O_3(s) + 3C(s) \rightarrow 4Al(s) + 3CO_2(g)$$

Metallic Al has a face centered cubic structure (a=0.405nm) and its density is $2.7 g/cm^3$. It is very ductile and has an electrical conductivity of about 60% of that of Cu. Strength is augmented by alloying it with Cu, Zn and Mg. Aluminum alloys are denoted in separate series according to the major alloying element. The 1000 series is commercially pure aluminum with < 1% other elements. If the second digit is zero, no alloying elements have been added, and the composition of impurities lies within specified limits. This group of alloys has very good corrosion resistance and low resistivity, but its mechanical strength is limited. These alloys are used in reflectors, heat exchangers and in architecture. They are also chosen when thermal and electrical conductivity is preferred over mechanical strength [9]. The 2000 series is alloyed with Cu (about 4 - 5%) for excellent mechanical strength and machinability. However, the corrosion resistance is limited. Aluminum alloyed with Cu is used for aircraft. The 3000 series is alloyed with Mn (about 1.2%) giving moderate strength but high workability. It is applied in highway signs, radiators and roofing. The 4000 series is silicon rich (≤ 12%) with a low melting point and low coefficient of expansion. It is suitable for anodizing, for castings (wheels) and as filler material for brazing and welding. The 5000 series is magnesium-rich (0.3 - 5%), which provides good corrosion resistance in a marine atmosphere. It is used in boats and in cryogenic vessels. The 6000 series is a group of magnesium and silicon alloys with good formability. It is used for panels in transportation equipment. The 7000 series is alloyed with Zn (3 - 8%) and Mg. It has very high strength when heat treated and aged.

It is also used, as for the 2000 series, for aircraft construction. The 8000 series is alloyed with Sn and Li and is used for a few specialized applications [9, 10].

2.2 Magnesium and its alloys

Magnesium occurs naturally in the minerals dolomite ($MgCO_3 \cdot CaCO_3$) and magnesite ($MgCO_3$). The density of the hexagonal close packing Mg (a=0.32nm, c=0.52nm) is only 1.7g/cm^3. The density of the Mg-Al alloy AZ91D is 1.81g/cm^3. Today, Mg is mainly produced electrolytically by reduction of magnesium chloride [11]. Commercial Mg-based alloys always contain appreciable amounts of Al for corrosion protection [12]. This is advantageous in two ways: first an Al-rich passive layer is formed, which provides an increased corrosion resistance; second, a strengthening effect is achieved. The corrosion scale on Mg-Al alloys becomes more compact and protective with rising Al content [13]. The Mg-Al alloys usually have two phases: an α phase (2% Al in Mg ss) and a β phase ($Mg_{17}Al_{12}$). The β phase precipitates in the α phase grain boundaries, forming a three-dimensional network [12, 14]. In addition, small amounts of sub-micron intermetallic precipitates, such as Al_8Mn_5, are present [13]. These have mainly been identified in grain boundaries (between α and β phases). Other advantages of alloying with Al are increased hardness and castability. An Al content of 6% yields an optimum combination of strength and ductility. Above 6% Al, the alloy becomes heat treatable [12]. The α phase grains are about 20 - 30µm in diameter, whereas the β phase grains are about 2 - 10µm long and about 2µm wide. The zinc is added (about 1%) for increased strength and corrosion resistance in chloride containing electrolytes [12]. Manganese is added to form less harmful intermetallic compounds with iron [15]. Work is in progress to develop Mg-Al alloys with a better distributed β phase network for a more continuous Al-rich passive layer and, hence, an increased corrosion resistance. This is partly done with the addition of rare earth elements [12]. Most manufacturing of Mg-Al alloys is done by die-casting or hot working at 200 - 350°C. The first two letters in the standard magnesium alloy nomenclature identify the two most important alloying elements in an alloy, as follows: A is Al; E is rare earth metals; H is Th; K is Zr; M is Mn; Q is Ag; S is Si and Z is Zn. The following two digits indicate the percentage (w/w) of the constituents; thus AZ91D is Mg-Al-Zn with 9 wt. % Al and 1 wt. % Zn. The letter D indicates that

the relative degree of purity is high. In the BSE (backscattered electrons) image below, a polished AZ91D surface is seen.

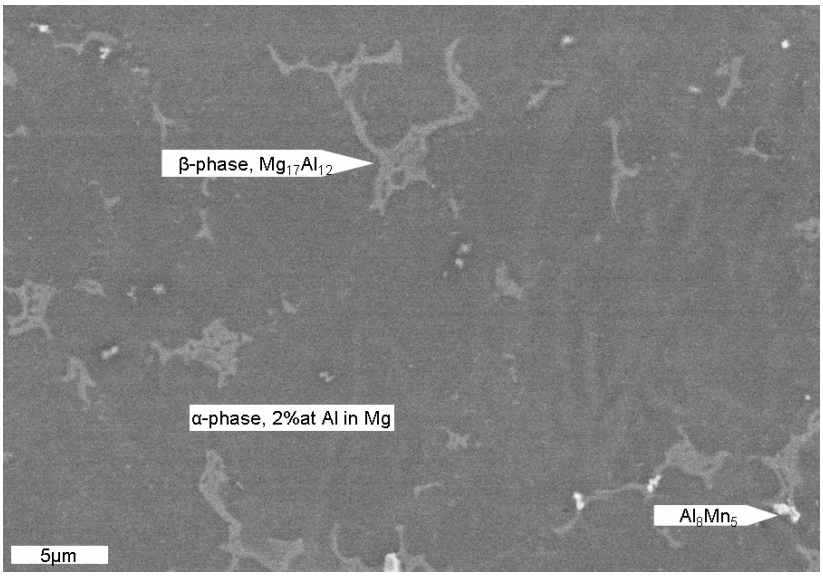

Figure 1. A polished AZ91D surface imaged with SEM (backscattered electrons).

2.3 Corrosion properties of Al and Al alloys

When exposed to dry air, most metals form oxides according to a Cabrera-Mott mechanism [16]. The corrosion resistance of aluminum alloys depends on the formation of a passive film consisting of an outer, porous aluminum oxide hydroxide layer and an inner, denser oxide that adheres well to the bulk [17]. It is a clear asset that the film is self-repairing, see reaction (2).

(2) $$4Al(s) + 3O_2(g) \rightarrow 2Al_2O_3(s)$$

The barrier layer prevents further oxidation and corrosion of the metal. Kaeshe [18] describes the passive barrier oxide on aluminum, grown under low temperature dry oxidation (tunneling of electrons being the rate limiting step [16]), as a 1 - 2nm thick amorphous layer. The insulating nature of this oxide layer protects against corrosion [19]. However, nonporous barrier-type oxides have flaws [20]. This is important to corrosion initiation [18]. All aluminum oxides and hydroxides are insoluble in water at neutral pH (log k_s = -30 to -34) [21]. The main corrosion products reported on Al are oxides and oxyhydroxides [7]. Several phases of aluminum (oxy)hydroxides exist according to the formula $Al(OH)_3$ (gibbsite, nordstrandite and bayerite) [22]. The

layered arrangement of bayerite, α-$Al(OH)_3$, has approximately hexagonal close packing structure [11].

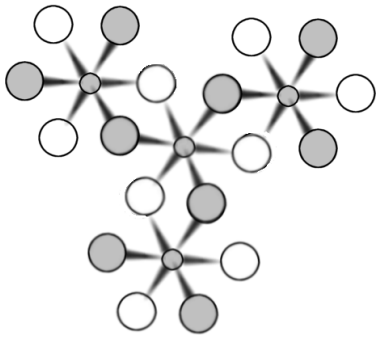

Figure 2. Part of a layer of α-$Al(OH)_3$ (idealized); the small circles are Al atoms and the open and filled circles are OH groups above and below the Al plane.

If a compound corresponds to the formula AlOOH, then the phases could be boehmite (orthorhombic γ-AlOOH) or diaspore [23]. Pseudoboehmite is a hydrated form of boehmite with slightly larger d-spacing [22]. Moreover, different kinds of aluminum hydroxy sulfates and chlorides have been reported [7].

In aqueous solution the stability region of $Al(OH)_3$ is about pH 4 - 10 when the Al^{3+} activity is in the milli-molar range. See the predominance diagram in Figure 3.

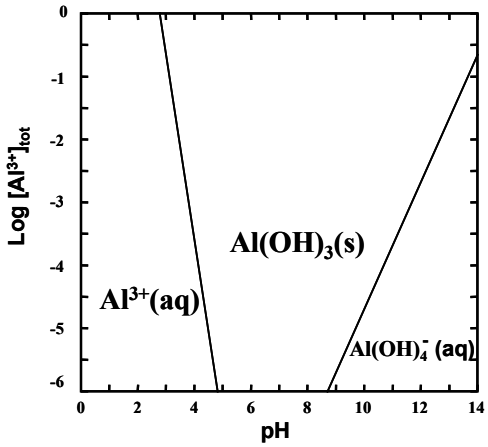

Figure 3. Predominance diagram for the aluminum-water system. The logarithm of the Al^{3+}(aq) activity is plotted against pH [24].

The passive film on aluminum can consequently be dissolved in alkaline and in acid solutions. These two types of corrosion mechanisms are seen throughout this work,

e.g. in Sections 2.3.1 and 2.3.2. Under neutral conditions, $Al(OH)_3(s)$ is stable. In acid environments $Al(OH)_3$ dissolves according to reaction (3).

(3) $Al(OH)_3(s) + 3H^+(aq) \rightarrow 3H_2O(l) + Al^{3+}(aq)$

In alkaline solutions, Kaesche [18] describes the anodic dissolution of Al as two coupled reactions (4 - 5) forming aluminate $Al(OH)_4^-(aq)$.

(4) $Al(s) + 3OH^-(aq) \rightarrow Al(OH)_3(s) + 3e^-$

(5) $Al(OH)_3(s) + OH^-(aq) \rightarrow Al(OH)_4^-(aq)$

This results in general corrosion. In weakly basic or neutral solution, the cathodic partial reaction (6) is suggested to be oxygen reduction [25]:

(6) $1/2O_2(g) + H_2O(l) + 2e^- \rightarrow 2OH^-(aq)$

In acid solution the cathodic reaction (7) is also oxygen reduction [25]:

(7) $1/2O_2(g) + 2H^+(aq) + 2e^- \rightarrow 2H_2O(l)$

In strongly alkaline and in strongly acidic solutions, hydrogen evolution, as in reactions (8 and 9), respectively, dominates [20].

(8) $H_2O(l) + e^- \rightarrow 1/2H_2(g) + OH^-(aq)$

(9) $2H^+(aq) + 2e^- \rightarrow H_2(g)$

2.3.1 Acidic dissolution (pitting corrosion)

In acid and neutral solutions, the hydroxylated alumina surface is positively charged [26]. According to Kaeshe, chloride ions can thus adsorb and change places with OH^- ions by an ion-exchange mechanism [18].

Three steps in localized corrosion attack are identified [27]: initiation, propagation and repassivation. The dissolution of the passive layer occurs as the formation of Al-Cl bonds weakens the Al-OH bonds (localized breakdown of the passive layer) [26, 28, 29]. The area around the pit is not affected by pitting corrosion because the cathodic reaction occurring here increases the pH and stabilizes the passive layer. The attack penetrates deeply (10 - 100µm) into the substrate. After initiation the attack is propagated as proposed by Wranglén [27], see Figure 4.

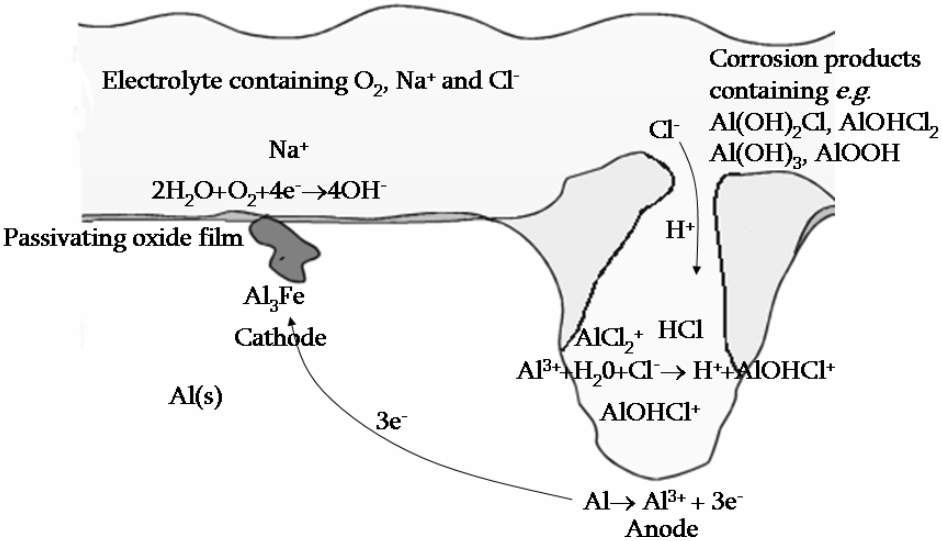

Figure 4. Electrochemical mechanism of pit propagation on aluminum. From Wranglén 1985 [27].

Chloride ions are enriched in the pit by migration along the potential gradient generated by the anodic and cathodic reactions [27]. Once the pit has been established, the Al^{3+} hydrolysis lowers the pH. Since aluminum chlorides are very soluble, the concentration of the chloride solution in the electrolyte is maintained [26, 30]. The conductivity in the pit increases with the salt concentration. The supply of O_2 is limited because of $Al(OH)_3$ precipitates at the pit mouth where the pH is higher. This counteracts the dilution of the pit electrolyte as it clogs the mouth [27], see Figure 4 above. Repassivation occurs when the conditions inside the pit allow a new protective layer to form. If the porous $Al(OH)_3$ diaphragm covering the pit mouth is ruptured, a dilution of the pit electrolyte can also promote repassivation [27]. This mode of corrosion attack exhibits quite low average corrosion rates. Aluminum constructions exposed to a chloride containing environment in the presence of CO_2 are subject to this type of corrosion attack, which is a problem and even cause sudden failure, especially

if the material is thin (radiators or air conditioning systems in vehicles). This is the dominant opinion in the literature [31].

The chloride ion is more aggressive towards Al than sulfate, in terms of pitting corrosion [31]. This can be explained by the fact that the sulfate ion competitively adsorbs onto the anodic areas, see Paper 5; basic aluminum hydroxy sulfates with low solubility then precipitate and impair further attack [7, 32].

2.3.2 Alkaline dissolution (general corrosion)

In alkaline solution the passive film dissolves in the form of aluminate $Al(OH)_4^-(aq)$, see reactions (4) and (5). This results in general corrosion. The cathodic reaction (6) is reported to occur on flaws in the passive layer, i.e. at grain, domain or both boundaries, or on intermetallic particles (precipitations or inclusions) [20, 33, 34]. The formation of high pH areas promotes the dissolution of Al as aluminate, which means anodic and cathodic reactions can occur at the same location. Anodic reaction also proceeds over the rest of the surface, although at a slower rate. In alkaline solution the surface of Al is negatively charged. This makes anion adsorption unfavorable and explains why chloride, for example, does not cause pitting corrosion [26].

The cathodic reaction proceeds over the entire surface, which explains why the alkaline type of corrosion attack is more general [18]. Hence, the total area of the cathodic reaction sites is crucial for the corrosion kinetics. In an unbuffered solution, the presence of sodium ions supports high pH in the cathodic areas, thereby promoting the anodic dissolution through reactions (4) and (5). Due to the presence of a pH gradient on the surface, $Al(OH)_3$ precipitates.

2.4 Corrosion properties of Mg and Mg-Al alloys

Upon exposure to dry air, magnesium is covered by an insulating layer of MgO of about 20 - 50nm (cubic halite structure) [35].

(10) $Mg(s) + 1/2O_2(g) \rightarrow MgO(s)$

In the presence of water vapor, MgO forms magnesium hydroxide:

(11) $MgO(s) + H_2O(g) \rightarrow Mg(OH)_2(s)$

At 25°C the hexagonal hydroxide has an equilibrium vapor pressure of less than $1 \cdot 10^{-6}$ atm of H_2O. Nordlien et al. report that the thickness of this layer is about 120 - 150nm but decreases with the amount of Al in the alloy [35]. The Mg is easily polarized anodically in bulk solution.

(12) $Mg(s) \rightarrow Mg^{2+}(aq) + 2e^-$

The cathodic reaction is generally believed to be hydrogen evolution as seen in reaction (8). In humid air, the dominant corrosion product forms according to reaction (13).

(13) $Mg^{2+}(aq) + 2OH^-(aq) \rightarrow Mg(OH)_2(s)$

Magnesium hydroxide is poorly protective (in contrast to the good protection of the passive layer on Al, see Section 2.3) due to its solubility in neutral and acidic aqueous solutions, see Pourbaix diagram in Figure 5 [36].

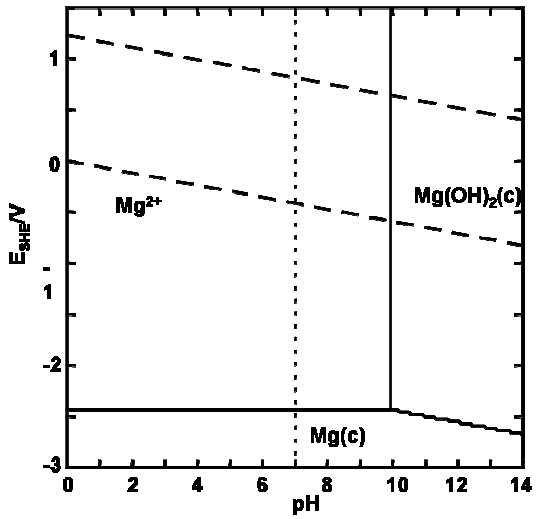

Figure 5. Pourbaix diagram for Mg where $[Mg^{2+}]$=0.1M. The thermodynamic stability diagram was constructed according to Puigdomench in 1983, which was based on the Solgaswater algorithm [37].

2.5 Galvanic corrosion in light metal constructions

Since the relative potential difference is quite large between the light metals and noble inclusions in alloys (*e.g.* containing Mn, Fe, Si or Cu), they are susceptible to galvanic corrosion attack, the matrix dissolving anodically and the cathodic reaction occurring on the intermetallic compounds. Another example of galvanic corrosion appears when some types of attachments and fasteners in nobler materials are used in engineering designs. This emphasizes the choice of a suitable type of surface treatment, type of alloy and design, if magnesium, for example, is to become a viable alternative in exterior vehicle applications.

2.6 Atmospheric corrosion: An overview of influences

The ability to withstand atmospheric corrosion is an important limiting factor for light metal alloys in outdoor applications, especially for Mg-based alloys and when light metal alloys are attached to other metals, for example in joints, see Section 2.5. The corrosion of light metal alloys in the atmosphere is governed by the interplay of water and corrosive substances on the surface. Atmospheric corrosion in the presence of an electrolyte such as NaCl(aq) is a special case of corrosion in an aqueous solution. This electrochemical process involves anodic dissolution, the cathodic reduction of oxygen or hydrogen evolution, and the transport of electrons, reactants and products between surfaces [38-40]. The diffusion of oxygen is generally not the rate limiting step in atmospheric corrosion [41]. Instead, the atmospheric corrosion of Al and Mg alloys is generally believed to be cathodically controlled [42]. In macroscopic electrochemical corrosion, laterally separated anodic and cathodic sites (enabled by the presence of a surface electrolyte with fair coverage) cause potential and pH gradients. This results in the migration of cations to the negatively charged cathodic areas and vice versa. The small monovalent ions (*e.g.* OH^-, H^+ and Cl^-) migrate readily [43]. In atmospheric corrosion the precipitation of corrosion products usually decreases the mobility of charge carriers in the surface electrolyte. This also leads to an increase in the resistivity of the system. As a result, the corrosion rate is reduced by blockage of the active sites [44]. As opposed to corrosion in bulk solutions, the corrosion products formed remain to a greater extent on the sample surface. In the field, water soluble corrosion products are often leached by precipitation [8].

The various phenomena in atmospheric corrosion have a wide range of characteristic length scales. On the nanometer scale, the materials exhibit noble precipitates and dislocations in the alloy as well as flaws in the passive film, which is of crucial importance for corrosion. On the micrometer scale we must consider alloy grain boundaries and, *e.g.*, the distribution of the β phase in Mg-Al alloys. The surface extent of the electrochemical cells involved in localized corrosion often reaches millimeters.

At the other end of the scale, corrosion rate in the field is often measured in mm/year, averaging over the whole surface. Typically, laboratory investigations of the atmospheric corrosion of metals use one or two selected techniques that can provide information only for some aspects of the corrosion reaction. In particular, the connection between surface chemistry, alloy microstructure and the rate of corrosion is seldom made. Atmospheric corrosion research is still dominated by field studies that compare the corrosion resistance of various materials and the corrosivity of different environments, with the aim to correlate corrosion rate and environmental parameters [7, 30, 45, 46]. Relatively few studies address the details of the series of processes that together generate the atmospheric corrosion reaction [7, 8, 30]. This explains the lack of information on the mechanism of corrosion of light metal alloys in the atmosphere.

The following average corrosion rates (μm/year) of Al, AZ91 and Zn exposed to outdoor conditions have been reported [42, 47], see Table I:

Table I. Corrosion rates (μm/year) for some materials exposed to outdoor conditions.

	Al	**AZ91**	**Zn**
Rural	0 – 0.1	2.8	0.2 – 3
Urban	< 1	14	2 – 16
Marine	0.4 – 0.6	6.4	0.5 – 8

The corrosion rates for Al are low and the rate for AZ91 is about the same compared to Zn. However, because light metal alloys suffer localized corrosion attack in the atmosphere, the average corrosion rate is not a good measure for them.

2.6.1 Relative Humidity

The relative humidity is a very important factor in the atmospheric corrosion of metals. Under atmospheric conditions, a thin film of adsorbed water molecules is present on all metal surfaces [48]. The initially formed oxide film is usually hydroxylated at the surface. The amount of adsorbed water at a given relative humidity has been shown to be about the same irrespective of the metal studied. The first reversibly adsorbed monolayer of water forms at about 25% RH, while a second layer forms at about 50% RH. The thickness of the adsorbed water layer increases quickly at higher humidity. At 70% RH about 3 - 4 monolayers are present. At 95% RH the amount of water corresponds to about 10 monolayers [49]. Volpe studied the adsorption of H_2O on aluminum oxide surface [48]. It is reported that the water is not, as in classical Langmuir adsorption, restricted to the surface, but represents the amount of water needed to fill the surface micro pores with adsorbate in a process resembling capillary condensation.

2.6.2 Sodium chloride

The corrosion rate of metals is greater in the presence of deliquescent salts. Soluble salts are hygroscopic and absorb water vapor from the atmosphere to form a solution. For NaCl this occurs at 75% relative humidity at room temperature [50]. At 95% RH, a NaCl solution is calculated to contain 11.66g of H_2O per gram of NaCl at equilibrium (given that the activity coefficient is equal to one). This corresponds to a 1.4M solution [51]. This liquid film dissolves atmospheric gases such as CO_2, SO_2 and NO_x. The mobility of the ions in the electrolyte enables charge balance to be maintained so that the anodic and cathodic reactions can proceed [39].

2.6.3 Carbon dioxide

The concentration of carbon dioxide in the atmosphere is currently about 350 parts per million (ppm); the largest seasonal variations of about 10 - 15 ppm are seen at high latitudes (north) [52]. Carbon dioxide dissolves in the water film present on a metal surface. The dissolved CO_2 is converted to carbonic acid. As a result, the pH in the surface water film decreases.

(14) $CO_2(g) \leftrightarrows CO_2(aq)$

(15) $CO_2(aq) + H_2O(l) \leftrightarrows HCO_3^-(aq) + H^+(aq)$ $pKa_1 = 6.35$ (over-all dissociation constant) [53]

(16) $HCO_3^-(aq) \leftrightarrows CO_3^{2-}(aq) + H^+(aq)$ $pKa_2 = 10.33$

It has been reported that CO_2 can be depleted in crevices on Zn [6] and beneath organic coatings [5]. A schematic diagram explaining this mechanism is presented in Figure 6.

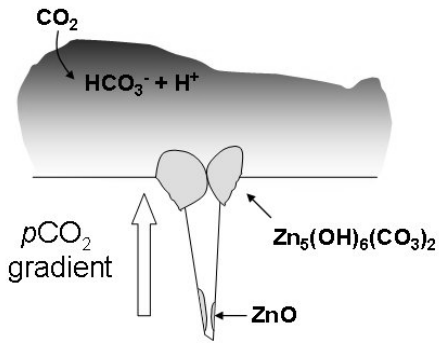

Figure 6. The presence of crystalline ZnO(s) on Zn is indirect evidence that there was low pCO_2 in the crevice [51].

2.6.4 Sulfur dioxide

Sulfur dioxide is an important corrosion accelerator for Al and Mg-Al alloys [7, 25, 42]. The main source of SO_2 is the combustion of fossil fuels and industrial processes [54]. Although the atmospheric levels of SO_2 are being reduced slightly in the western world, regions of very high SO_2 concentrations (industrial areas) still remain. According to the literature, the levels of SO_2 concentration in rural areas are < 1ppb but range up to 2000ppb in industrial areas [55]. The $SO_2(g)$ can dissolve in the surface electrolyte according to the following reactions [56].

(17) $SO_2(g) \leftrightarrows SO_2(aq)$ $K_H = 1.23 M/atm$

(18) $SO_2(aq) + H_2O(l) \leftrightarrows H^+(aq) + HSO_3^-(aq)$ $pK_a = 1.77$

(19) $HSO_3^-(aq) \leftrightarrows SO_3^{2-}(aq) + H^+(aq)$ $pK_a = 7.22$

The solubility of SO_2 in water is high, as seen in the Henry´s law constants of the reaction (17). For Al and Al alloys, the incorporation of sulfate into the corrosion

product is described by Mattsson [47]. Divalent cations such as Mg^{2+} (and Zn^{2+}) form insoluble sulfites, SO_3^{2-}. This does not apply for Al^{3+}. Friel detected metastable amorphous aluminum sulfate hydrate after exposure of Al to heavily polluted industrial atmospheres [57]. Aluminum exposed to 10 ppm SO_2 showed the presence of crystalline $Al_3(SO_4)_2(OH)_5 \cdot 9H_2O$ [58].

2.6.5 Atmospheric corrosion of Al and Al alloys

Besides the usual strong influence of humidity, most researchers agree that the corrosion rate of aluminum alloys in the atmosphere is determined mainly by the deposition of SO_2 and chloride and by the pH in rain [8]. If the oxide is thin enough, tunneling of electrons through the scale can proceed. The cathodic reaction typically occurs at the interface between the oxide and the electrolyte and the anodic reaction takes place at the metal-passive layer interface [34]. In the presence of flaws, grain boundaries and intermetallic compounds (*e.g.* $Al_{12}Fe_3Si$, α-AlFeMnSi, Al_2CuMg (S phase), Al_2Cu and Al_3Fe [59-61]), the electron transfer proceeds effortlessly [33, 34]. The occurrence of noble precipitates is therefore decisive in the susceptibility of Al alloys to atmospheric corrosion.

2.6.6 Atmospheric corrosion of Mg and Mg-Al alloys

Also for the Mg and Mg-Al alloys, the atmospheric corrosion is considered to be electrochemical in nature [42]. The anodic reaction is Mg dissolution, see reaction (12). The cathodic reaction may be oxygen reduction or hydrogen evolution, depending on pH, as described in reaction (7) or (8). The susceptibility of Mg-Al alloys to atmospheric corrosion is strongly related to the presence of noble precipitates. The cathodic reaction produces hydroxide ions, which raises surface pH in the cathodic areas. For 99.97% Mg in pure humid air, it was shown that corrosion is concentrated at a small distance from the submicrons of noble inclusions present, producing a characteristic circular pattern [62]. This feature can be understood in terms of a galvanic cell. Close to the cathode, pH is high, stabilizing the $Mg(OH)_2$ film, see Pourbaix diagram in Figure 5. The anodic dissolution of Mg thus appears at a distance from the noble inclusion, determined by the (radial) pH and potential gradients in the surface electrolyte. As a secondary effect, hydrogen evolution occurs at the anodic

sites by the direct reaction of the bare metal with the aqueous film. This *chemical* attack gives rise to deep pits in the metal.

The passive film on Mg-Al alloys is enriched with aluminum, which offers much better protective properties than pure Mg, see Section 2.2. In contrast to $Mg(OH)_2$, aluminum (oxy)hydroxide is insoluble at neutral pH, see Section 2.3. The passive film on the cathodic areas of Mg-Al alloys therefore tends to become aluminum-depleted, see Paper 4. On the other hand, the aluminum containing film is stable at a distance from the cathodic sites where pH is lower. As a result, the extremely rapid pitting characteristic of pure Mg is not seen on the Mg-Al alloys. As for Al (Section 2.3.1) pitting of Mg-Al alloys is usually connected to the presence of anions, *e.g.* chloride, see Paper 6. The relative potential difference between the α and β phases also influences the corrosion on Mg-Al alloys. Apart from some reports on the corrosion of Mg alloys in various electrolytes [14, 15], laboratory studies on the atmospheric corrosion of these materials barely exist in the literature [63].

3 Methods

3.1 Sample composition

The chemical composition in wt. % of the materials used in this study is shown in Table II. The reference material (Al 99.999%) showed impurity concentrations as Fe 0.7ppm, Mg 1.45ppm, S 0.9ppm and Si 0.99ppm. A 99.97% Mg (sand-cast ingot from Johnson & Matthey) was also used as a reference material for the investigations of the Mg-Al systems (3mm thick die cast plates from Dead Sea Magnesium or Norsk Hydro). The Al and Al alloys were cold rolled sheets supplied by Volvo Car Corporation, CSM Materialteknik AB or Goodfellow Ltd.

Table II. Composition (wt. %) of the materials used.

	Si	Fe	Cu	Mn	Mg	Ti	Zn	Al
AA5182	0.2	0.35	0.15	0.2	4.0	0.1	0.25	bal.
AA6016	1.0	0.5	0.2	0.2	0.25	0.15	0.2	bal.
AA2024-T3	0.50	0.50	3.8 - 4.9	0.3 - 0.9	1.2 - 1.8	0.05	0.25	bal.
AA1070	0.04	0.16	0.001	0.002	0.002	0.003	0.006	bal.
AZ91D	0.008	0.0022	0.0007	0.21	bal.	<0.001	0.74	8.9
Mg	0.003	0.0018	0.0003	0.0023	bal.	<0.001	0.005	0.003

The samples had a geometrical area of 20.0cm^2 (3.0 x 3.0 x 0.17)cm with a small hole for a nylon string. For the *in situ* AFM/SKPFM studies, (0.8 x 0.8)cm samples of about 0.7mm thickness were used.

3.2 Preparation of samples

Before exposure all of the samples were ground, with SiC paper (4000 mesh) in ethanol, and then polished with 1µm diamond paste from Struers. The samples were ultrasonically cleaned in ethanol (acetone for the Mg alloys), dried in air, and stored in a desiccator over silica gel for 24h. Sodium chloride and sodium sulfate were added by spraying the samples with a saturated solution of NaCl in 80:20 ethanol:water. The amount of NaCl and Na_2SO_4 added was determined gravimetrically. The $AlCl_3$ and $MgCl_2$ were applied to the samples by spreading a 3M solution on the surfaces with a latex plate. The amount of salt added was determined volumetrically. Care was taken

to avoid droplet formation on the samples during spraying. The distribution of salt on the surface after spraying was even, as verified with ESEM. The levels of particle chloride deposition reported from the field cover a very wide range, from 15µg $Cl^- \cdot cm^{-2} \cdot y^{-1}$ in rural areas far from the coast [64] to > 55000µg $Cl^- \cdot cm^{-2} \cdot y^{-1}$ in extreme marine environments [65]. The NaCl levels in this thesis, equivalent to 110 and 550µg $Cl^- \cdot cm^{-2} \cdot y^{-1}$ respectively, correspond to urban areas and to marine environments not in the immediate vicinity of the coastline.

3.3 Experimental setup

Two different experimental approaches are used in this study: corrosion studies (672h) to determine the corrosion rate and the formation of corrosion products and Time-Resolved trace gas Analysis of the Deposition (*TRAD*) to investigate the deposition rates of SO_2, NO_2 and O_3 on Al and Mg-Al during the first 20h of exposure. Both kinds of experiments were performed in a well-controlled synthetic environment. The exposure systems were made entirely of glass and Teflon. To avoid interactions between samples, only one sample at a time was exposed in each chamber (suspended on a thin nylon string in the middle of the chamber). The corrosion chambers were immersed in a water tank held at constant temperature (± 0.03°C). To avoid condensation in the parts of the system outside the water tank, the temperature in the room was kept at 25°C. The exposure gas was prepared from dried and purified air. Since the air purification system removes most of the CO_2 in the air, a carbon dioxide concentration of 350ppm was obtained by adding pure CO_2 from a cylinder and monitoring the concentration. Relative humidity, regulated by mixing dry air and air saturated with water vapor, was controlled with an accuracy of ± 0.3%. The SO_2(g) and NO_2(g) were added to the dry air stream via permeation tubes manufactured by the atmospheric corrosion group at Chalmers. The permeation rates of the SO_2 tubes corresponded to SO_2 concentrations of 46, 108, 546 and 1372ppb in the exposure gas. The permeation rates of the NO_2 tubes corresponded to a concentration of 200 and 560ppb. The O_3(g) was added (at a concentration of 200ppb) to the dry purified air flow by means of an ozone generator (UV radiation, $\lambda < 230$nm) to form atomic oxygen, which then reacted with dioxygen molecules to form O_3(g). The gas flow was $1dm^3$ / minute for most exposures.

3.3.1 Corrosion studies

To study the effect of prolonged exposures (672 hours) the setup in Figure 7 with eight parallel corrosion chambers were used. The whole gas flow (1dm^3 / minute) passes through each chamber in turn for 15 seconds. The chambers have an inner diameter of 55mm and a volume of 0.4dm^3. The net gas flow is 7mm·s^{-1}, corresponding to a Reynolds number (R_e) of about 25 in an empty chamber.

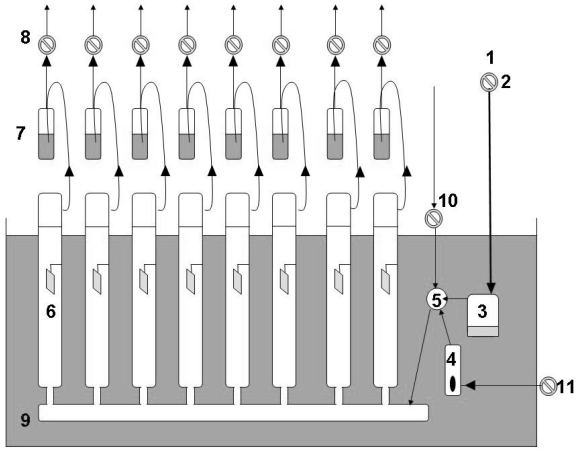

Figure 7. Experimental setup for exposures with 350ppm CO_2 and for some with ppb levels of SO_2 at 4 - 22.0°C. (1) pure air inlet; (2) mass flow regulators; (3) humidifier; (4) NO_2 and/or SO_2 permeation tubes; (5) mixing point; (6) exposure chambers with Al or Mg-Al samples; (7) gas trap; (8) solenoid valves; (9) thermostated water tank; (10) CO_2 or O_3 inlet; (11) carrier gas (purified air) for NO_2 and or SO_2.

For exposures above 22.0°C, an alternative setup was used, see Figure 8. This one is somewhat different from that shown in Figure 7 that the humidifier, the exposure chamber and the gas pipes are all immersed in a temperature-controlled water tank.

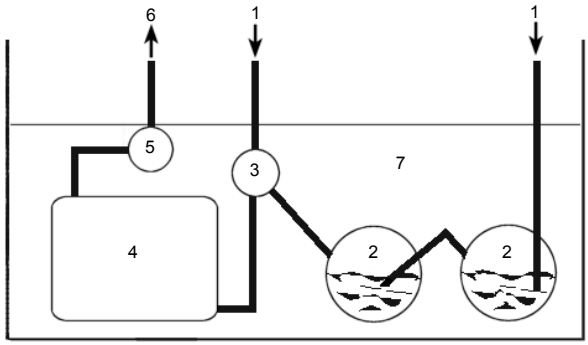

Figure 8 Experimental setup for exposures with 350ppm CO_2 at 38 - 60°C. (1) pure air inlet; (2) humidifier; (3) mixing point; (4) exposure chambers with Al samples; (5) humidity trap; (6) air outlet; (7) thermostated water tank.

Condensation problems are thus avoided. Part of the purified air stream passes two three-necked, round-bottom flasks containing water, while the other part functions as a carrier for 350ppm CO_2. The two air streams are mixed below the water surface to obtain correct relative humidity. Eight samples at a time were placed in the exposure chamber.

For exposures in the absence of CO_2, the samples were suspended inside a 3.5dm^3 desiccator filled with air. Beneath the samples there was 0.1dm^3 of 1.6M NaOH(aq) in equilibrium with 95% RH air. The NaOH solution takes up CO_2, verifying that the concentration of CO_2 during exposure is < 1ppm. The container temperature was controlled to within 0.2°C. It has already been shown that exposing samples in this apparatus produces results identical to those obtained when flowing CO_2-free air was used as in Figure 7 and Figure 8 [66]. This was also true for Al and Mg alloys. For exposures with sulfur dioxide, the SO_2 content in the gas leaving each chamber was determined by absorption in 1.0% H_2O_2(aq) and analysis as sulfate with ion chromatography. An empty corrosion chamber was used as a blank to determine the total amount of SO_2(g) in the exposure gas, which was 0% SO_2 deposition. This was about the same as using the ideal gas law on the net mass difference of the permeation tube before and after the exposure.

3.3.2 Time-Resolved Analysis of the Deposition (TRAD) of ppb levels of SO_2, NO_2 and O_3

The materials in the experimental setup and preparation of the gas mixture are the same as those used for the corrosion studies. The setup used in the SO_2 deposition studies is described in Figure 9.

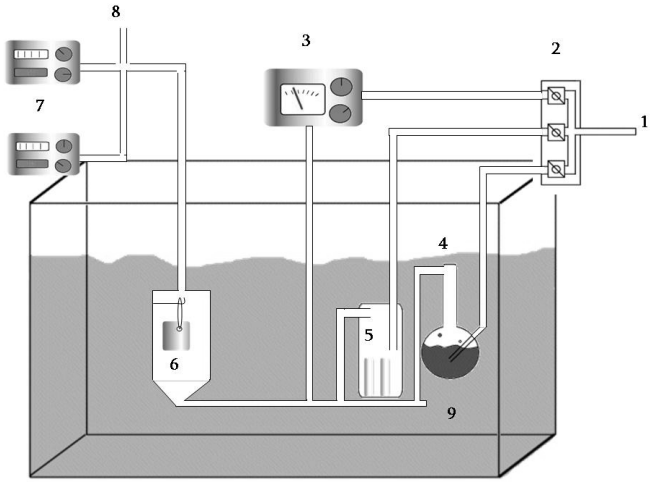

Figure 9. The experimental setup for TRAD at 22.0°C. (1) pure air inlet with pure CO_2(g) added from a cylinder; (2) mass flow regulators; (3) O_3 generator (UV light $\lambda < 230$nm); (4) humidifier; (5) NO_2 and/or SO_2 permeation tubes; (6) exposure chambers with Al or Mg-Al samples; (7) real-time gas analyzers for SO_2, O_3 and NO_x-NO_2; (8) air outlet; (9) thermostated water tank.

The gas flow (1.0dm^3 / minute.) results in a net gas velocity of 2.7cm·s^{-1} (laminar flow conditions, R_e = 50). Here, the setup consists of a single exposure chamber with continuous flow and real-time analysis of SO_2, NO_x and O_3 in the output gas. Analysis of SO_2 was made with a fluorescence instrument (Environnment AF21M), the sensitivity being 1ppb. The ozone concentration in the output gas was analyzed by means of an instrument based on UV photometry (Dasibi 1108). The NO and NO_x were analyzed with a chemiluminescence instrument (Environnment AC 30M). Before the start of each experiment the interaction of the pollutant with the reactor had reached a steady state so that the composition of the output gas from the corrosion chamber was constant. Each experiment was started when the sample was introduced into the chamber. The mass transfer-limited deposition of SO_2 was measured with an "ideal absorber" prepared by covering a standard sample or a dummy sample made from glass with a thin layer of NaOH(aq). The deposition rate (ng · cm^{-2} · s^{-1}) and the deposition velocity (cm · s^{-1}) on the samples were determined by measuring the difference between the input and output concentrations of the pollutants. The deposition velocity, V_d, is defined as the flux of an air pollutant to a surface, divided by the concentration in the gas: $V_d = F/c$ where F is the flux to the surface (g · cm^{-2} · s^{-1}) and c is the concentration of the pollutant in the gas (g · cm^{-3}) [67]. In this study, the concentration of the SO_2 is the mean of the input and output concentrations in the reaction chamber.

3.4 Quantitative analysis

3.4.1 Gravimetry

To monitor the corrosion process during exposure the samples were weighed once a week. To avoid disturbing the corrosion process, the samples were not dried before weighing. The weighing procedure lasted two minutes per sample. The mass gain recorded in this way is termed the wet mass gain. Following the completion of the 672 hours exposures, the dry mass gain of the samples was determined after they were stored over a desiccant at ambient pressure and temperature for 168 hours. The amount of corrosion products was determined by leaching followed by pickling the samples, with ultrasonic agitation. Water-soluble corrosion products and unreacted NaCl were first removed by leaching in milli-Q water (pH 7) at ambient temperature for one minute and then repeated for 30 minutes. The amount of sulfate and chloride removed by leaching was determined by IC and the sample mass was recorded.

The samples (only Al and Al alloys) were then pickled in a solution containing H_3PO_4 and CrO_3 (one liter of solution is prepared by mixing 50ml H_3PO_4 (85%) and 20.0g CrO_3 with milli-Q water) for 5 minutes at 80°C, after which they were washed in water and ethanol. This procedure was repeated three times. The sample mass was recorded after each step. Weighing the samples after the leaching and pickling process gives the metal loss. The metal loss caused by pickling (self corrosion) was determined by using an uncorroded sample and by measuring mass loss as a function of time. This effect was corrected for in the determination of the metal loss of the exposed samples. The ratio $\frac{(\text{mass gain} - \text{metal loss})}{\text{metal loss}}$ provides information on the stoichiometry of the corrosion product.

3.4.2 Desorption of CO_2 and SO_2

Carbonate on the samples was determined by decomposing the carbonate in acid and by thermal desorption. To decompose the carbonates, the samples were treated with 1M $HClO_4$(aq) in a three-necked flask. Immersing the samples in the acid converts

carbonate quantitatively to carbon dioxide according to the reactions (13) to (15), see Figure 10.

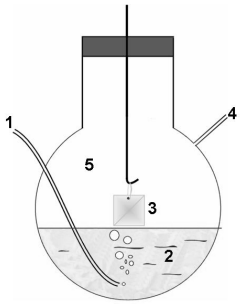

Figure 10. Setup for quantitative analysis of carbonate containing corrosion products on aluminum. (1) N_2(g) inlet; (2) 1.0M $HClO_4$(aq); (3) sample; (4) to CO_2(g) real-time analyzer; (5) closed reaction vessel.

A stream of 0.3dm^3 / minute of nitrogen was used to expel the carbon dioxide from the solution and carry it to the CO_2 analyzer (Binos 100). The sensitivity of this analysis corresponds to $10 \cdot 10^{-9}$mol CO_2 / sample. This is equivalent to less than a monolayer of carbonate [68]. By introducing weighed amounts of $BaCO_3$(s) into the system, the precision of the analysis was found to be ± 2%. The thermal desorption analysis for carbonate involved suspending the samples in a heated flow reactor that was purged by a stream of dry N_2(g). A thermocouple was placed in contact with the sample. The heating rate was 5°C / minute. The CO_2 analyzer used was the same as that in the acid decomposition analysis, and the sensitivity of the analysis was also the same.

To quantify the amount of IV-valent sulfur on the sample surface after exposure to SO_2(g) containing air, the same setup described above was used. Immediately after completion of the SO_2-deposition study, the sample was transferred to the setup given in Figure 10. The cell was purged with 11.67ml purified N_2(g) / second, and the output gas was analyzed with the setup shown in Figure 9. The removal of SO_2(g) from the exposed sample is based on the reverse of the reactions (17) to (19). The detection limit was about 0.1nmol of SO_2(g).

3.4.3 Ion chromatography (IC)

Ion chromatography was used for quantitative analysis of water-soluble anions (*e.g.* chloride and sulfate) on the samples after exposure (Dionex DX100 with an Ionpac AD9-SC column). This method was also used to determine the amount of SO_2(g) in

the output gas that oxidized to SO_4^{2-}(aq) by the H_2O_2 solution in the gas traps. The flow rate was 2 cm^3 / minute; 1.8mM Na_2CO_3 / 1.7mM $NaHCO_3$ was used for eluation.

3.5 Qualitative analysis

3.5.1 Optical microscopy

The microscope chosen for optical analysis of the corroded samples was a Zeiss JVC equipped with a charged couple detector camera. It is ideally used for measuring pit depths after the corrosion products have been removed, see Section 3.4.1

3.5.2 Scanning electron microscopy techniques: SEM and ESEM

The morphology of the corrosion products was analyzed with a Leo Ultra 55 SEM equipped with a field emission gun (FEG) and an Oxford Inca energy Dispersive X-ray (EDX) system. The FEG gives the increased resolution needed for analysis of small features. Since the corrosion scales on some of the exposed samples in this study were non-conductive, charge accumulations made it difficult to use a traditional SEM. One solution to this problem is to cover the surface with a conductive coating; another is to use an Environmental Scanning Electron Microscope (ESEM). In this work an ElectroScan 2020 equipped with a Link ISIS EDX system and an FEI Quanta 200 ESEM FEG with an Oxford Inca EDX system were used. In a SEM, an electron beam is emitted from the filament and hits the sample surface. In the interaction volume, which has the shape of a pear, a number of signals are generated, including secondary electrons (SEs), backscattered electrons (BSEs) and X-rays. The information volumes for the different signals are shown in Figure 11.

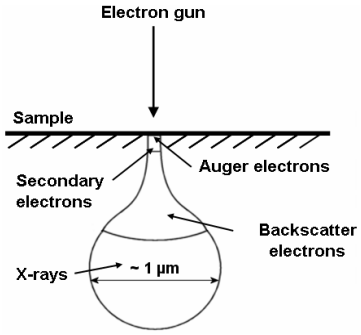

Figure 11. The diagram shows the excitation pear induced by the impact of a primary electron-beam on a sample surface.

The primary factor determining the size of this excitation pear is the acceleration voltage. An increase in voltage gives rise to a larger excitation pear. In this study, an acceleration voltage of 8 - 30kV was used for surface imaging (SE and BSE) and 10kV for EDX analysis. There are two key technologies that differentiate the ESEM from all other SEMs. The first is its gradient vacuum system with multiple pressure limiting apertures (PLAs). This system enables the electron beam to pass, but it is narrow enough to maintain a pressure gradient between the chamber (1 – 10 Torr) and the gun chamber (10^{-7} Torr), see Figure 12.

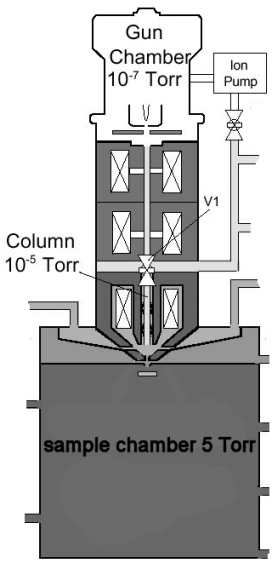

Figure 12. The ESEM vacuum system is divided into stages of increasing vacuum separated by pressure limiting apertures.

The second key technology of the ESEM is that water vapor present in the sample chamber is ionized by the secondary electrons emitted from the sample surface. This

generates an amplification of the secondary electron signal, a cascade effect. The negatively charged particles hit the secondary electron detector and the positively charged ones hit the sample surface and neutralize the build-up of negative charge on poorly conductive surfaces, see Figure 13.

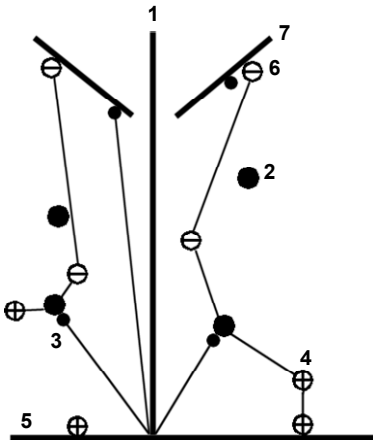

Figure 13. The ESEM uses gas ionization to amplify the secondary electron signal. In nonconductive materials, positive ions are attracted to a sample surface as charge accumulates from the beam. This tends to suppress charge artifacts. (1) Primary electron beam (2) $H_2O(g)$ (3) secondary electrons (4) positively charged ions (5) negatively charged sample surface (6) negatively charged ions (7) detector.

The electron beam is scanned across the sample surface, collecting data, as for a conventional SEM. The intensities of the secondary and sometimes backscattered electrons are used to produce an image of the sample surface.

3.5.3 The Focused Ion Beam (FIB) workstation

By standard techniques it is extremely difficult to obtain electron transparent samples from a corroded surface in a convenient way. With the introduction of the FIB (Focused Ion Beam) workstation, it is possible to cut out a thin layer from a position of interest on the surface of a sample. A FIB can very accurately position the ion beam on the surface and produce cross sections for a desired part of a specimen. The cross sections can either be inspected directly in the FIB or analyzed later, for example with SEM. In this study, a FEI 200 THP FIB was used. The system has a liquid gallium ion source with 30kV maximum acceleration voltage. For imaging, a 10pA ion beam current was used to minimize surface damage. For milling 500pA - 20000pA was used, depending on the desired milling precision.

3.5.4 Energy Dispersive X-ray (EDX) analysis

All the electron microscopes used in this study were equipped with EDX systems. When the primary electron beam interacts with a sample surface, as illustrated in Figure 11 above, characteristic X-rays are emitted. The incoming electron beam produces a secondary electron from an inner shell in one of the sample's atoms to jump to a higher energy level, leaving this atom in an excited state. An X-ray is emitted as the atom reorganizes. As the energy of this photon is characteristic for a specific type of atom, see Figure 14, this method can be used for mapping the sample surface for different elements, or for making quantitative measurements of the local composition.

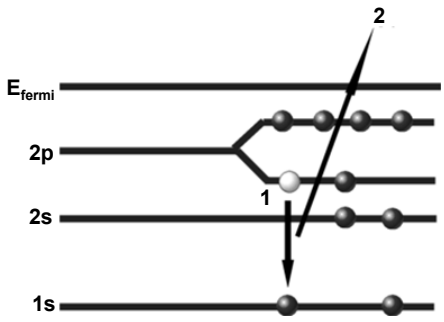

Figure 14. Energy diagram representing the emission of X-rays generated by the relaxation of excited atoms in the sample. An X-ray photon is emitted. (1) Electron jumping from a higher to a lower energy level; (2) characteristic X-ray.

3.5.5 Auger Electron Spectroscopy (AES)

Auger electron spectroscopy, AES, is accomplished by irradiating a sample with a focused electron beam in an ultra high vacuum. The interaction of the beam with the specimen is illustrated in Figure 11. The impact between the incoming electron beam and the sample surface cause vacancies in the electron shell of the atoms. After the excitation of core levels, the atom relaxes to its initial state by emitting either X-ray photons (see Section 3.5.4 above) or an Auger process. The emission of Auger electrons dominates for low atomic numbers, whereas emission of X-ray photons dominates for high atomic numbers. The mechanism of the Auger electron emission is that an electron from a higher energy level falls into a vacant lower energy level and transfers energy to a third electron, the Auger electron. This Auger electron is emitted

into the vacuum and detected. The energy of this type of electron depends on the difference between the energy levels involved [69], see Figure 15.

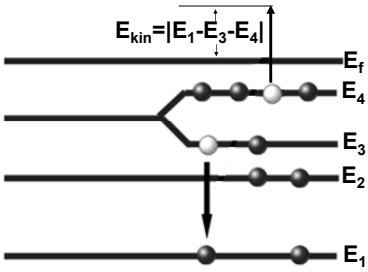

Figure 15. The Auger electron emission process.

A PHI 660 instrument was used. The primary accelerating voltage was 10kV and the beam current was 75nA. The depth profiles were obtained using a differentially pumped ion gun (Ar^+) with an acceleration voltage of 4.0kV. The sputter rates were calibrated on a flat sample of Ta_2O_5 with a known oxide thickness of 100nm. The collected raw data was refined with MultiPak v.6.0 software.

3.5.6 X-Ray Diffraction (XRD)

Grazing incidence X-ray diffraction (GI-XRD) was used for characterization of crystalline corrosion products (Siemens D-5000 equipped with a Göbel mirror, CuK_α radiation). The diffraction peaks of metallic Al and Mg were used as internal standards. The principle of X-ray diffraction, based on Bragg's law (20), is illustrated in Figure 16.

(20) $n\lambda = 2d \sin \Theta$

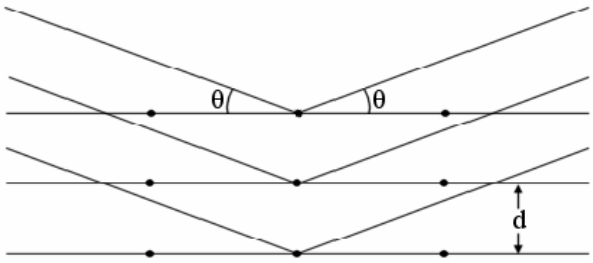

Figure 16. The parameters required to fulfill Bragg's law.

The wavelength is $\lambda = 1.54Å$ (CuK_α); d is the distance between the lattice planes; n is an integer number; and Θ is the incidence angle of the incoming X-rays. Since the Θ value is obtained from the experiment, the d value can be calculated. It is possible to use d values and the intensities of the peaks to determine what chemical compounds are present, as each crystal structure has a unique set of d values and intensities. For the identification of crystalline phases in the sample, the set of d values collected is compared with a computer based reference, *e.g.* the Powder Diffraction Files. The drawback of this technique is that reliable results are obtained only when the structure has been identified before. Amorphous compounds can not be identified. The principle of GI-XRD is that the position of the X-ray source is fixed with respect to that of the sample. A moving detector scans the angles of the diffracted beams for intensity measurement. In this way a diffractogram is obtained, which can be compared with the database. Since the corrosion product film is thin, the incident X-ray beam angle has to be very low, typically 0.3°, see Figure 17. The moving detector is equipped with Soller slits to select the diffraction angle, Θ_2 and a secondary flat monochromator to eliminate the rest of the K_β radiation.

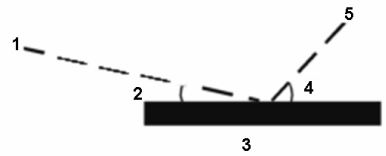

Figure 17. Schematic image of the instrumental setup for the grazing incidence X-ray diffraction. (1) X-Ray source with fixed position; (2) incident angle $\Theta_1 = 0.3°$; (3) sample; (4) Θ_2; (5) moving detector, $\Theta = (\Theta_1 + \Theta_2)/2$

3.5.7 Atomic Force Microscopy (AFM) with Scanning Kelvin Probe Force Microscopy (SKPFM)

Atomic Force Microscopy (AFM) with Scanning Kelvin Probe Force Microscopy (SKPFM) is a valuable tool for studying the initial stages of atmospheric corrosion on Al and Mg-Al systems. Two kinds of scanning probe microscopes were used in this study (*Nanoscope IIIa Multimode and Dimension 3000 by Digital Instruments*). Both were equipped with extender electronics modules, enabling surface potential measurements when engaged in tapping mode. In tapping mode, the topography and the Volta potential distribution were mapped simultaneously *in situ* with sub-micrometer resolution. The main advantage of this technique is its capacity to image

non-conducting surfaces. The atomic force microscope is equipped with a small cantilever (tip) to scan the surface (Olympus Micro Cantilevers, n^+ silicon conductor, with a resonant frequency of about 279kHz and a spring constant of about 27N/m). The van der Waal forces of the surface cause a measurable deflection of the oscillating tip, which allows the surface topography to be measured. The principle of SKPFM is to scan the surface in tapping mode to determine the topography on a line by line basis. The tip is then lifted to a fixed height, typically 50nm, and the surface is rescanned in "lift mode", see Figure 18.

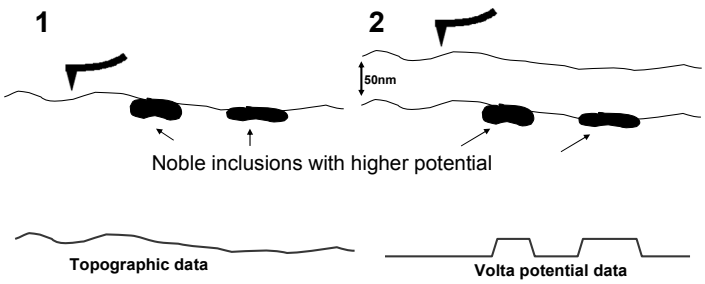

Figure 18. The principle of scanning Kelvin probe force microscopy: (1) measuring the topography by *in situ* tapping mode AFM; (2) increasing the tip-sample height to 50nm and measuring the surface potential.

When rescanning, the tapping piezo is turned off, but an AC voltage is applied to the tip, which stimulates oscillation of the cantilever in the presence of an electric field. The magnitude of the oscillations, monitored by the AFM, is eliminated on a point by point basis during the lift mode rescan by adding a DC voltage to the tip to balance it. This approach to potential measurement is not possible in aqueous solution, because the large voltages applied to the tip cause Faradaic reactions in the solution. Nevertheless, the application is well suited for studying the thin electrolytes present in atmospheric corrosion. The measurement of the variation in electrical potential has excellent lateral resolution. The instruments were equipped with customized *in situ* cells allowing the monitoring of corrosion under controlled conditions, see Figure 19.

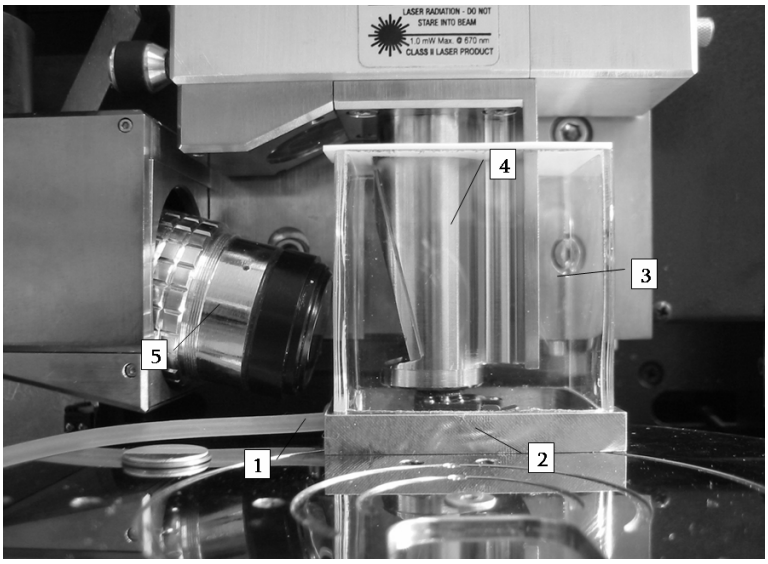

Figure 19. The in situ cell attached to Dimension 3000 used for investigations of the initial stages of atmospheric corrosion under well controlled exposure conditions. (1) Gas inlet; (2) sample; (3) corrosion cell of silica glass; (4) scanner; (5) CCD camera.

The CO_2 concentration was either < 1ppm or 350ppm. For exposures with < 1ppm CO_2, the carbon dioxide was removed from the air with Ascarite filters (silica gel overdrawn with NaOH). A concentration of < 1ppm CO_2 was achieved. The relative humidity was regulated with humidifiers.

In comparison with other techniques that can provide information on surface potentials such as the scanning Kelvin probe, scanning Kelvin probe force microscopy features superior lateral resolution (nm range) as well as the option to couple the measurement to surface topography. These unique features enable *in situ* measurements of the effects of microstructure in the initial stages of atmospheric corrosion of Al and Mg-Al systems.

3.5.8 The Scanning Kelvin Probe (SKP)

To enable comparison of the absolute potentials of materials studied *in situ*, and of phases before and after exposure, a scanning Kelvin probe was employed. The Kelvin probe consists of a metallic reference electrode, which is separated from the sample by a dielectric medium and connected to the sample by a metallic conductor. The technique is unique insofar as it allows a non-contact measurement of electrode potentials, and therefore also corrosion potentials. The Kelvin probe is a technique that has been used for decades by surface physicists to measure work functions [70]. The

scanning version of the classical capacitor setup was first introduced by Parker and Warren [71], who studied lateral variations in work functions using gold and graphite with a resolution of several mm. Since then, the scanning Kelvin probe technique has been steadily improved, and a resolution of some tens of µm is easily achieved [72, 73]. A detailed description of the method is available [70]. The SKP was calibrated before each exposure to the standard hydrogen electrode by a measurement of the Volta potential difference over a $Cu/CuSO_4$ reference electrode [5]. The setup used is shown in Figure 20.

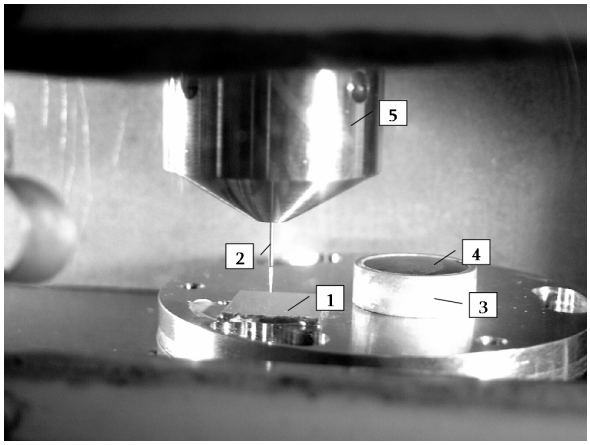

Figure 20. The *in situ* SKP chamber used for regular Kelvin probe measurements. (1) Sample; (2) needle; (3) container made of Cu; (4) $CuSO_4$(aq); (5) scanner.

During the SKP measurement, the temperature was 22.0°C and the relative humidity was held constant at about 85% RH. To measure the absolute potential of the β phase in AZ91D, an artificial batch of $Mg_{17}Al_{12}$ was die cast and SKP measurements were made on its polished surface.

4 Results and discussion of atmospheric corrosion

4.1 Al in CO_2-free humid air

Sodium chloride is a very efficient corrosion accelerator for Al, especially in the absence of CO_2, see Figure 21. The corrosion rate in the absence of CO_2 is about 20 times higher compared to exposures with 350ppm CO_2.

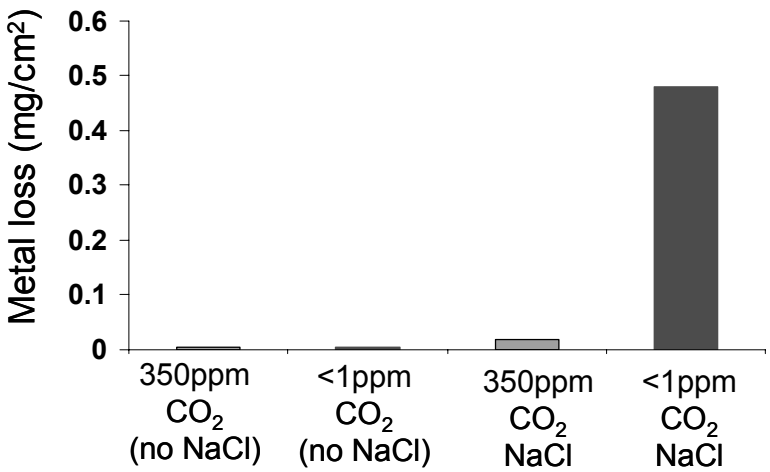

Figure 21. Corrosion rates for AA1070 in the absence and in the presence of 350ppm CO_2 after exposure to 95% RH for 672 hours at 22.0°C. Prior to exposure, either 70µg NaCl/cm^2 was added or no NaCl was added. The scatter in the metal loss was about ± 5%.

Without NaCl, the corrosion attack was negligible. The mode of the corrosion attack in the presence of NaCl was uniform after 672h of exposure. Scanning electron microscopy showed that circular features of about 100 - 300 µm in diameter were present on about 60% of the sample surface, see Figure 22.

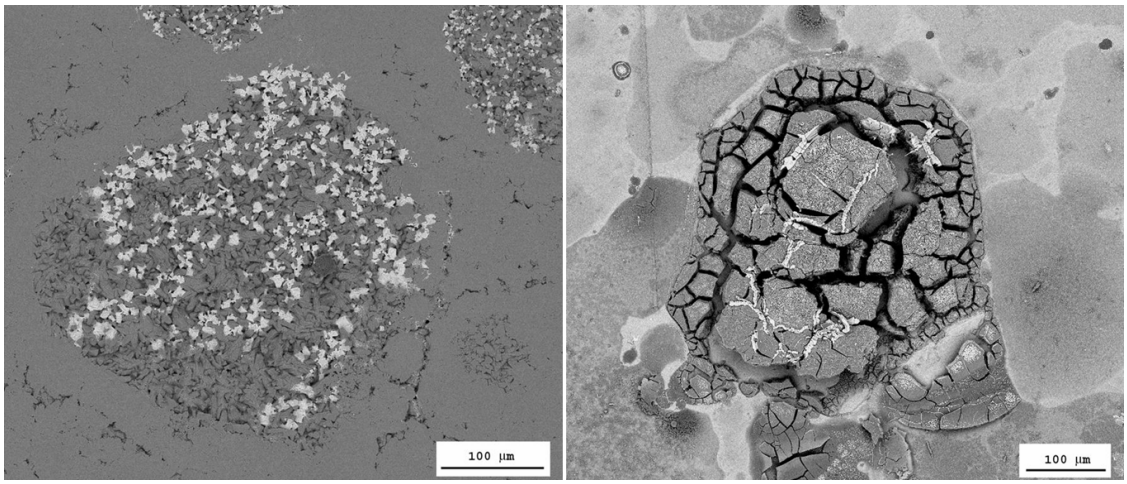

Figure 22. SEM (backscattered electrons) images of Al exposed to 95%RH for 672 hours in the absence (left) and in the presence of 350ppm CO_2 (right). The temperature was 22.0°C and 70µg NaCl/cm^2 was added prior to exposure. Images by L. Ingemarsson [74].

The corrosion scale contains areas of amorphous $Al(OH)_3(s)$ revealed by energy dispersive X-ray (25at. % Al and 75at. % O) and areas with crystalline α-$Al(OH)_3(s)$, bayerite (XRD). This is in accordance to the finding of crystallites of similar shape after immersing Al in a chloride containing solution with high pH [20]. In some places, chloride was enriched at the interface between the bulk metal and the hydroxide layer, see Figure 23.

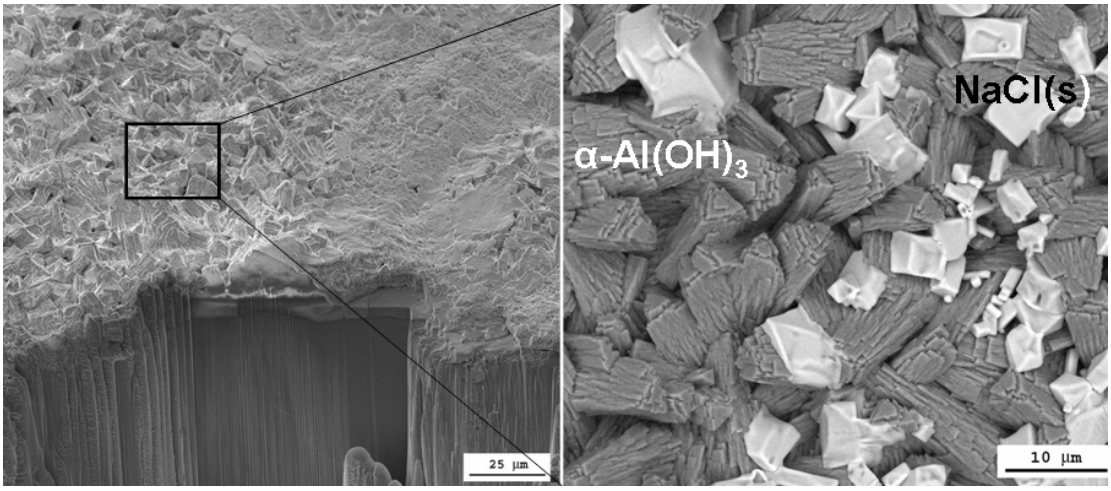

Figure 23. ESEM images of pure Al exposed to 95% RH without CO_2 for 672 hours. The temperature was 22.0°C and 70µg NaCl/cm^2 was added prior to exposure. The cross section to the left was made by the focused ion beam technique (SE image). The magnification of the area in the square (right) is imaged by BSE. L. Ingemarsson [74].

Almost all the chloride added (> 99%) could be leached in water, see Paper 1. After leaching and pickling the surface appeared to be undulated. The average surface

roughness was about 10μm. No pitting was evident. The rapid corrosion rate in the absence of CO_2 on Al and the other alloys investigated (Al-Mg-Si, Al-Mg and Al-Cu-Mg, see Paper 2) was believed to be due to the formation of high pH areas originating from the cathodic reaction (6). The high pH destabilizes the passive layer (see Figure 3), whereupon dissolution is caused by the two coupled anodic reactions (4 and 5). When no buffering capacity of CO_2(g) is available, the pH of the surface electrolyte becomes high, and rapid general corrosion proceeds, see Section 2.3.2. This is supported by the fact that bayerite was found by X-ray diffraction indicating that high pH was present in the surface electrolyte during exposure to CO_2-free air, see cover. Ginsberg (1962) affirmed that pH 9 or above is required for bayerite to form [75]. A proposed mechanism is illustrated in a schematic drawing, see Figure 24.

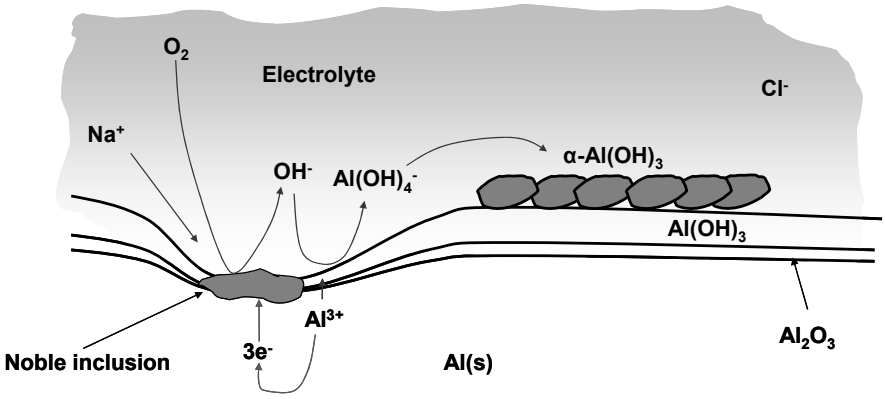

Figure 24. Schematic mechanism of the atmospheric corrosion of Al in humid air with NaCl(aq) in the absence of CO_2.

Sodium ions migrate to cathodic areas and contribute to the high pH formed, whereas chloride anions migrate through the electrolyte towards the anodic areas present on the rest of the surface. The same behavior is evident for the alloys studied here, see Paper 2. At a certain thickness of the corrosion scale (about 10μm), the mass transfer becomes limiting. The crucial thickness required for protection is reached by prolonging the exposure time, raising the temperature or increasing the amount of salt added.

4.2 Al in humid air with 350ppm CO_2

In atmospheric corrosion of Al in humid air with 350ppm CO_2, NaCl was observed to increase the atmospheric corrosion of Al. However, the corrosion rate is about 7 - 30

times faster in the absence of CO_2 in comparison with 350ppm CO_2, depending on what alloy is used, see Figure 25.

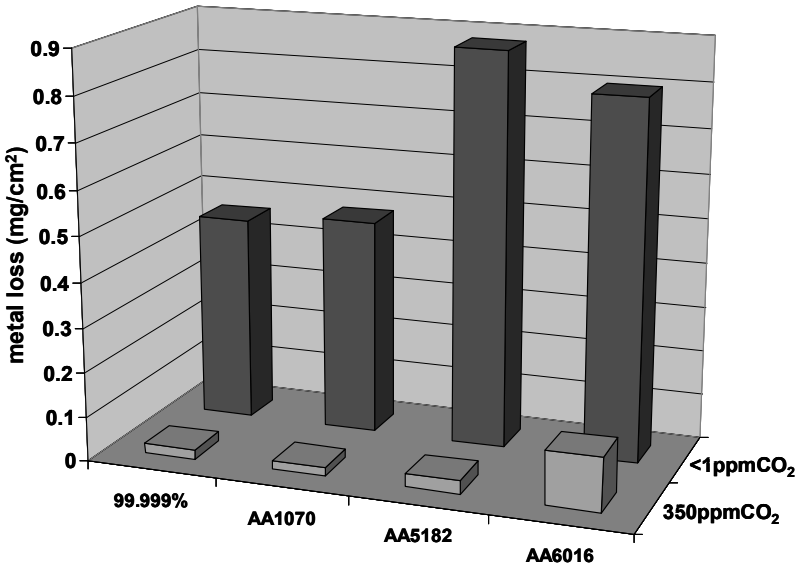

Figure 25. Corrosion rate in the absence (back row bars) and in the presence of 350ppm CO_2 (front row bars) after exposure to 95%RH for 672 hours at 22.0°C. Here, 70µg NaCl per cm^2 was added. The scatter in the metal loss was about ± 5%.

The mode of the corrosion attack was localized (pitting corrosion). The crusts covering the pits were rich in Cl (10at. %), but the sodium content was low. The enrichment of chlorine in anodic areas on Al (localized corrosion) is supported by laboratory studies [76]. X-ray diffraction showed the presence of unreacted NaCl and $NaAl(OH)_2CO_3$, dawsonite. This compound was reported as a corrosion product on an Al-Mg-Si alloy exposed to similar conditions [77]. The amount of carbonate in the corrosion products was very low, see Paper 3. This implies that the effect of CO_2 is not primarily caused by the formation of a protective aluminum carbonate film but due to the acidity of the gas, see Section 2.6.3. All chloride applied could be leached in water. After leaching and pickling, the surface appeared uncorroded to the naked eye. However, some small pits (about 5 - 10 on the entire surface) could be seen; the average pit depth was about 5-35µm. The pitting is however more enhanced for the Al-Mg-Si and Al-Cu-Mg alloys, due to the galvanic coupling between the Al matrix and the secondary phases and intermetallic compounds, see Paper 2. This is illustrated in a diagram of the schematic mechanism, see Figure 26.

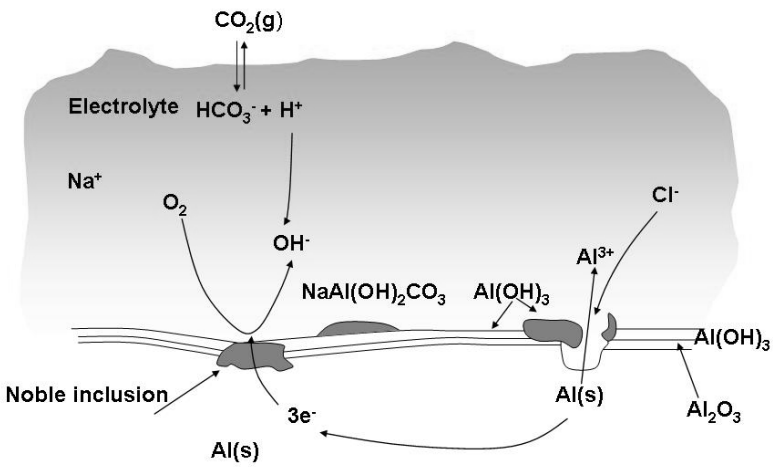

Figure 26. Schematic mechanism of the atmospheric corrosion of Al in humid air with NaCl(aq) in the presence of 350ppm CO_2.

Also in this environment, the cathodic reaction proceeds through the reduction of oxygen, forming OH^-. The slowing down of the corrosion of NaCl-coated Al in humid air by CO_2 occurs because CO_2 counteracts the development of high pH in the surface electrolyte, see 2.6.3. The chloride ions migrate to the positively charged anodic areas and destabilize the passive layer locally, see Section 2.3.1. This proceeds through the adsorption of negatively charged chloride ions, which causes weakening of bonds in the hydroxylated passive layer, which results in the formation of aluminum hydroxy chlorides that pass into solution, see Paper 1.

4.3 The effect of temperature on the atmospheric corrosion of Al

The temperature strongly influences the atmospheric corrosion on Al, see Figure 27.

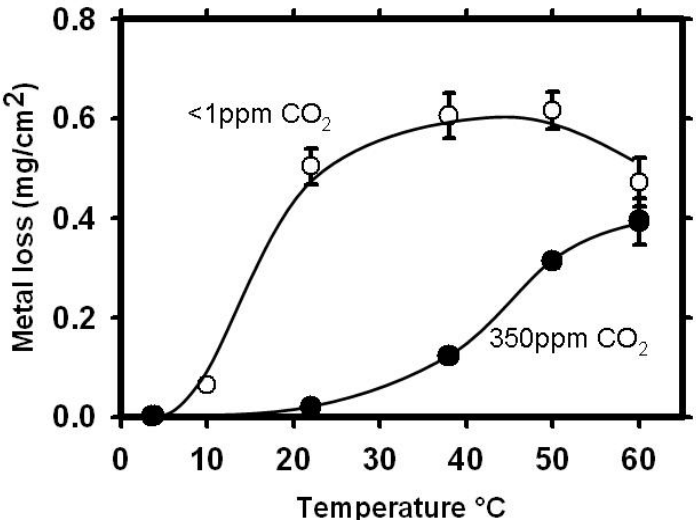

Figure 27. Corrosion rate on commercially pure Al, AA1070 as a function of temperature; 70µg NaCl/cm^2 was added prior to exposure. The relative humidity was 95% and the exposure time was 672 hours.

At 4°C the corrosion rate is very low, irrespective of whether NaCl is present or not. At 22.0°C, in the presence of NaCl, the corrosion rate is 20 times higher in the absence of CO_2 than for exposures with 350ppm CO_2. As the temperature is increased from 4 to 22.0°C, the corrosion rate increases by an order of magnitude in the absence of CO_2. In comparison, the same temperature increase from 4 to 22.0°C resulted in only a two-fold corrosion rate increase in the presence of 350ppm CO_2 (see Paper 3). The lack of increase in the corrosion rate between 22.0°C and 60.0°C is connected not only to the partial drying of the surface, which counteracts the expected faster kinetics at higher temperatures, but also to the thickness of the corrosion scale, compare Section 4.2. The strong temperature dependence is also reflected in the surface morphology, see Figure 28.

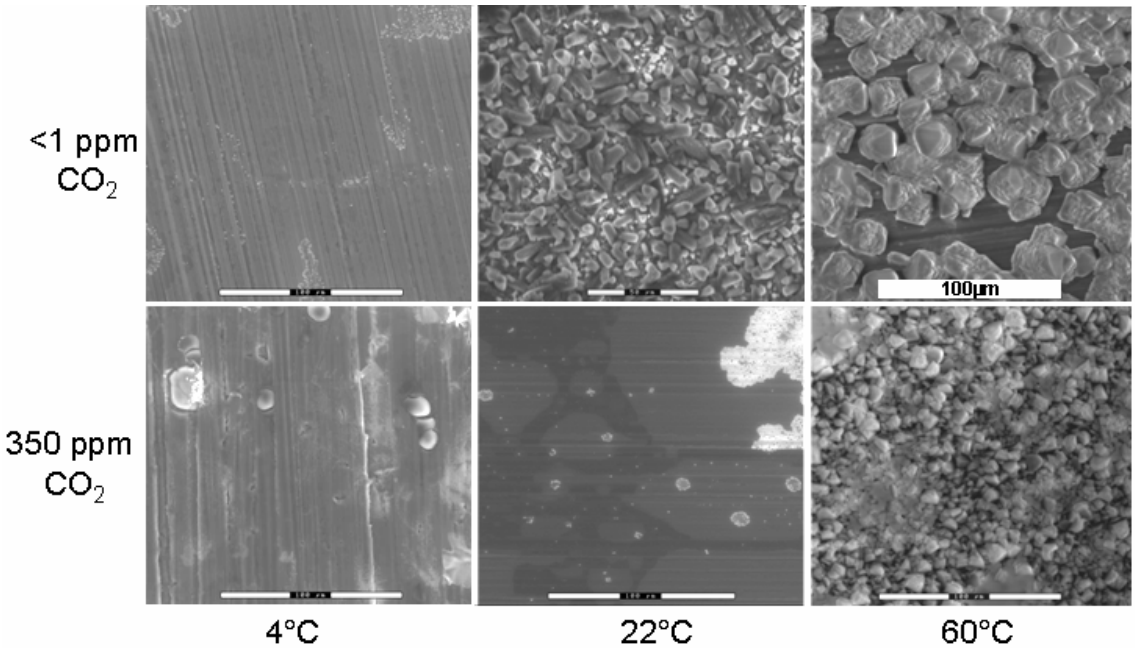

Figure 28. ESEM images of AA1070 exposed for 672 hours at 95%RH with 70µg NaCl/cm^2 added prior to exposure.

In the presence of CO_2, there is also a distinct increase in the corrosion rate with temperature, however this is shifted by 20°C towards higher temperatures. This effect is partly explained by the decrease in the solubility of CO_2 in water with increasing temperature, see Paper 3. The equilibrium pH of pure water in contact with 350ppm CO_2 is 5.6. According to Henry's law, the constant (K_H) is a measure of the solubility of a gas in a solution. For equilibrium reaction (15), this is expressed as $[CO_2(aq)] = K_H \cdot pCO_2$. The solubility of CO_2 in water is plotted against temperature in Figure 29.

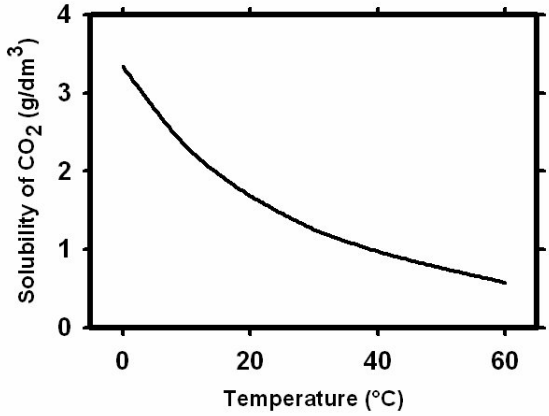

Figure 29. The solubility of CO_2 in water as a function of temperature [78].

Carbon dioxide can not neutralize the hydroxide formed at the cathodic areas rapidly enough to impede the anodic dissolution of Al as shown by reactions (4) and (5) at

"elevated" temperatures. Figure 30 shows the inhibition efficiency of CO_2 as a function of the CO_2 solubility in water.

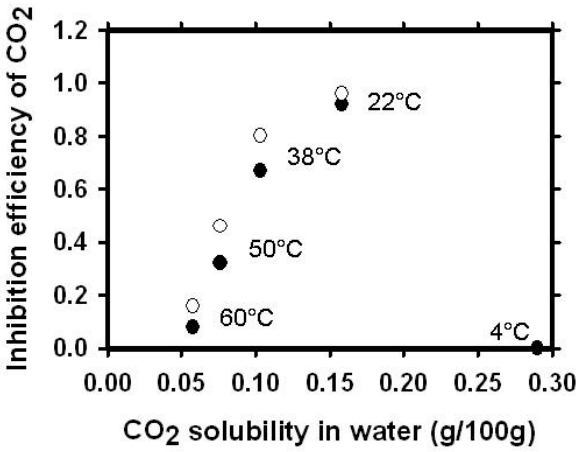

Figure 30. Inhibition efficiency of CO_2 as a function of the solubility of CO_2 in water for Al samples pre-treated with (o) 70µg NaCl/cm^2 and (•) 14µg NaCl/cm^2. The CO_2 solubility in water is according to [78].

The graph implies that the solubility of CO_2 is strongly correlated to its effectiveness as a corrosion inhibitor. The diminishing solubility of CO_2 with increasing temperature can explain why no carbonates were found in the corrosion products for exposures above 22.0°C. The transformation of poorly crystalline aluminum hydroxy carbonates to bayerite above 22°C has been reported in the literature [79].

4.4 The influence of $AlCl_3 \cdot 6H_2O$, $MgCl_2 \cdot 6H_2O$ and $NaSO_4$ on the atmospheric corrosion of Al

In the absence of CO_2, the corrosivity of the chloride salts studied increases in the order $MgCl_2 \bullet 6H_2O$ < $AlCl_3 \bullet 6H_2O$ < NaCl, see Fig. 31.

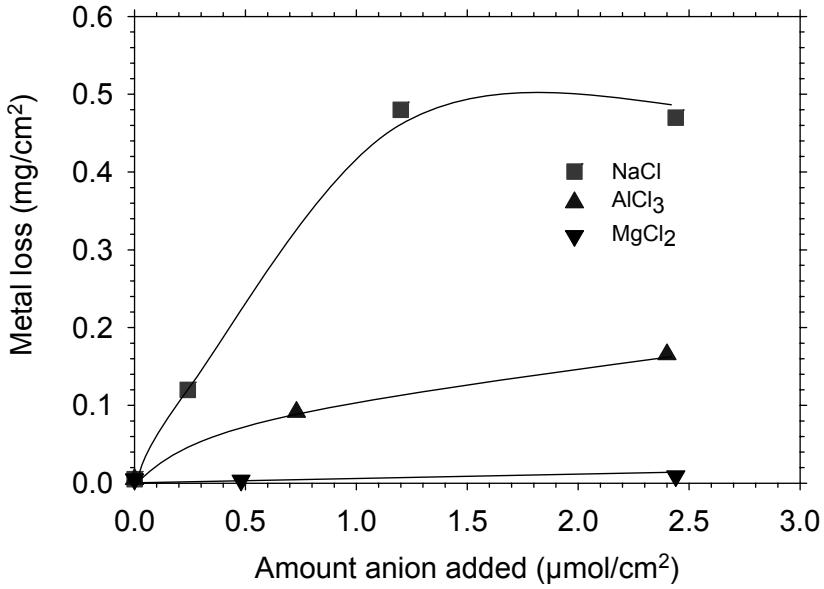

Fig. 31. Average corrosion rate of aluminium as a function of the amount of chloride added for NaCl, $AlCl_3 \cdot 6H_2O$ and $MgCl_2 \bullet 6H_2O$. The samples were exposed to air with <1ppm CO_2 at a relative humidity of 95%. The exposure time was 4 weeks and the temperature was 22.0°C. The scatter in metal loss was about ±5%.

Sodium chloride is very corrosive in this environment because the sodium ion supports the development of high pH in the cathodic areas, resulting in alkaline dissolution of the alumina passive film and rapid general corrosion. The low corrosivity of $MgCl_2 \bullet 6H_2O$ is explained by the inability of Mg^{2+} to support high pH values in the cathodic areas. The relatively high corrosivity of $AlCl_3 \bullet 6H_2O$ in the absence of CO_2 is explained by the formation of an acidic surface electrolyte and by the high solubility of aluminum hydroxy chlorides.

In the presence of carbon dioxide, the corrosion induced by the salts studied exhibit similar rates, see Paper 7. Carbon dioxide strongly inhibits aluminum corrosion in the presence of $AlCl_3 \bullet 6H_2O$ and especially, NaCl, while it is slightly corrosive in the presence of $MgCl_2 \bullet 6H_2O$. The inhibitive effect of CO_2 in the case of NaCl is attributed to its acidity. Carbon dioxide neutralizes the alkaline solution formed in the cathodic areas and forms solid carbonates. CO_2 decreases pH in the surface electrolyte resulting in a positively charged alumina film. Chloride adsorption on the passive film causes local depassivation, explaining the predominance of pitting corrosion in the presence of CO_2. The slowing down of aluminum chloride induced corrosion of aluminum by CO_2 may be connected to the formation of aluminum hydroxy carbonates. They form

amorphous precipitates that may interfere with the corrosion process. The magnesium chloride induced corrosion of aluminum is somewhat enhanced by CO_2. It is suggested that CO_2 accelerates the magnesium chloride induced corrosion of aluminum because it acidifies the electrolyte, keeping Mg^{2+} in solution.

In the absence of CO_2, Na_2SO_4 is less corrosive than NaCl, This is explained by the lower solubility of aluminum hydroxy sulfates in comparison to the chlorides. The average corrosion rate in the presence of CO_2 is the same for both salts. The main difference is that sulfate is less efficient than chloride in causing pitting of aluminum in neutral or acidic media.

4.5 The influence of SO_2 on the atmospheric corrosion of Al

Sulfur dioxide is a powerful corrosion accelerator for Al. The corrosion rate is about 10 times higher in the presence of SO_2 than in SO_2-free air, see Figure 32.

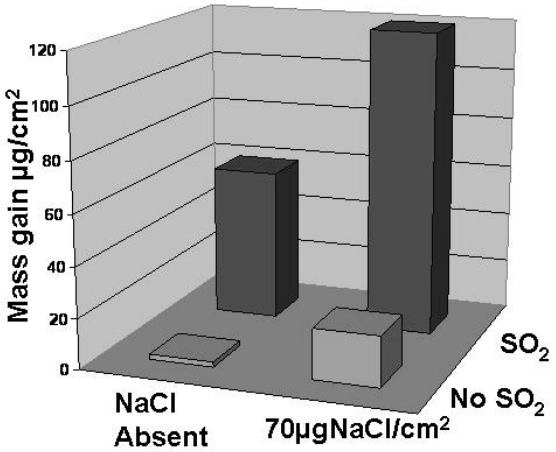

Figure 32. Corrosion rate (mass gain) in the presence of 96 ppb SO_2 (back row bars) and without SO_2 (front row bars) after exposure to 95% RH for 672 hours at 22.0°C. The scatter in the mass gain was about ± 5%.

In the graph below (Figure 33) it is evident from the slope of the curve that the corrosion process continues in the presence of SO_2.

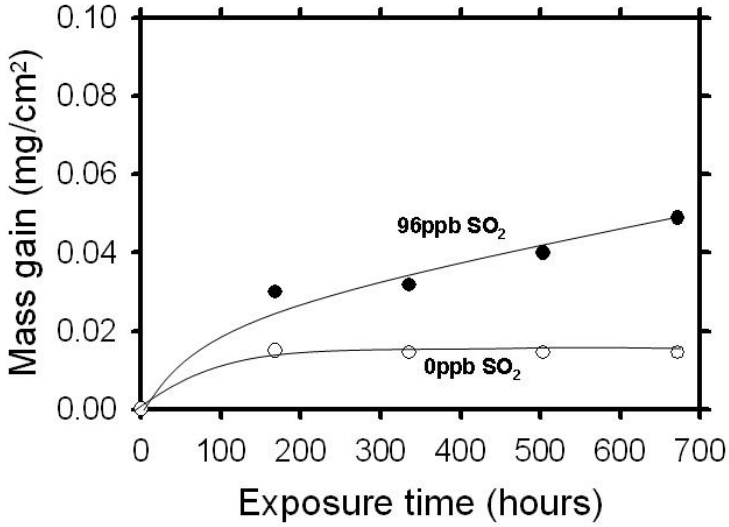

Figure 33. The mass gain as the function of exposure time for Al exposed to 96ppb SO_2 or in the absence of SO_2 at 95% RH. The scatter in the mass gain was about ± 5%.

After exposure, the samples were locally affected by corrosion, as about 50% of the surface was covered with white corrosion product islands (about 100µm), see Figure 34.

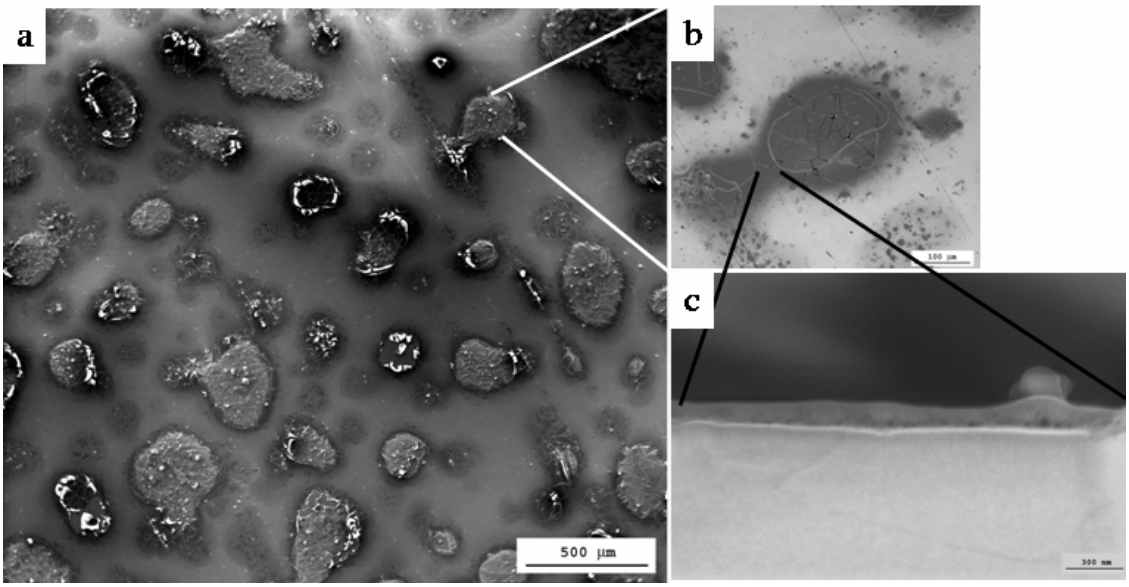

Figure 34. (a) SE and (b) BSE images of Al exposed to 96 ppb SO_2 at 95% RH for 672 hours. The temperature was 22.0°C. (c) FIB cross section of the corrosion island shown in (b). Images by L. Ingemarsson [74].

Auger depth profiling showed that the oxide film between the crusts had a thickness of about 7nm. No pitting was detected beneath the corrosion product crusts. The deposition rate of SO_2 on Al is almost independent on the SO_2 concentration, see Paper 5. Sulfur dioxide influences the atmospheric corrosion of Al, as it dissolves in the

surface electrolyte and generates an acidic environment; see reactions (17 to 19) in Section 2.6.4. The oxidation of (IV)-valent sulfur, on the surface, to sulfate produces more acid.

(21) $SO_2(ads) + H_2O(l) + 1/2O_2(g) \rightarrow 2H^+(ads) + SO_4^{2-}(ads)$

Since the sulfuric acid formed is strongly hygroscopic, it forms a surface electrolyte that reacts with the surface and converts the passive alumina film to a basic aluminum hydroxy sulfate, for example $Al_2SO_4(OH)_4 \cdot 7H_2O(s)$.

(22) $2Al(OH)_3(s) + 2H^+(aq) + SO_4^{2-}(aq) + 5H_2O(l) \rightarrow Al_2SO_4(OH)_4 \cdot 7H_2O(s)$

The local destabilization of Al is evidence of electrochemical cell activity proceeding on the sample surface. In the literature, reports on sulfate adsorbing on the passive layer of Al without causing pitting corrosion in bulk solutions can be found [80, 81]. In this work, the fraction of water-leachable sulfate decreased from 90%, after 168 hours of exposure, to 56% after 672 hours. The nature of the growth of the sulfate islands implies that repassivation of once active anodic areas proceeds by precipitation of aluminum hydroxy sulfates and the areas of anodic activity move outwards, see Paper 5. This produces circular clusters of sulfate islands and would explain the localized mode of corrosion attack.

4.6 The effect of SO_2 + NaCl on the atmospheric corrosion of Al

Sulfur dioxide is a very efficient corrosion accelerator towards Al in combination with NaCl, see graph in Figure 32. The SO_2 increases the NaCl induced atmospheric corrosion rate on Al by a factor 6. Even the smallest NaCl addition studied (14 $\mu g/cm^2$), after 20 hours, results in a deposition rate about 16 times higher than that of samples exposed without NaCl. The deposition of SO_2 on an ideal absorber (NaOH treated Al or glass) is presented for comparison, see Figure 35.

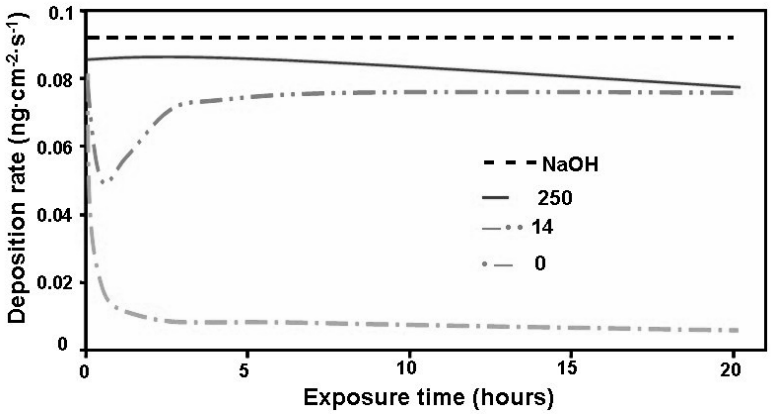

Figure 35. Deposition rate of SO_2 on aluminium for two amounts of NaCl (µg/cm^2) added prior to exposure as a function of time. The temperature was 22.0°C and the SO_2 concentration was 108ppb. The RH was 95%.

The results indicate that aluminum covered with NaCl(aq) shows behavior close to that of an ideal absorber (NaOH) for SO_2 at high relative humidity. After 672 hours exposure, the corrosion attack is localized in nature. White corrosion product islands (50 - 200µm) formed, covering 60% of the surface. However, no pitting could be detected beneath the corrosion crusts, see FIB cross section in Figure 36.

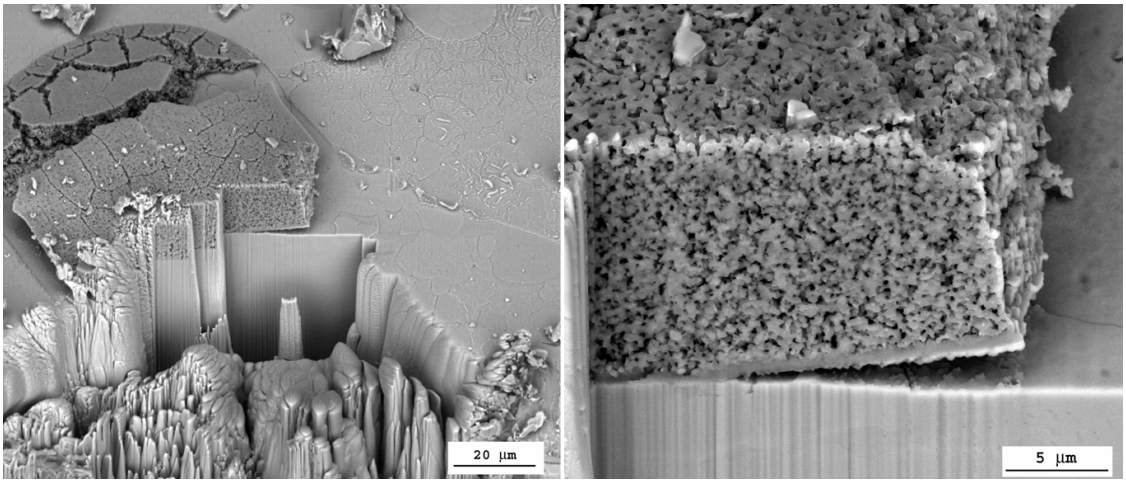

Figure 36. Cross section prepared with focused ion beam on Al exposed to 95% RH at 22.0°C for 672 hours. The SO_2 concentration was 96ppb and the amount of NaCl added prior to exposure was 70µg/cm^2. Delamination of the crust is evident. Images by L. Ingemarsson [74].

There was no substantial enrichment of S or Cl at the interface between the crusts and the Al substrate. Instead, energy dispersive X-ray analysis of the FIB milled cross section (Figure 36) indicated a uniform distribution of these species in the corrosion products. The thickness of the oxide film between the crusts was about 17nm (AES). The X-ray diffraction revealed aluminite, $Al_2SO_4(OH)_4 \cdot 7H_2O$.

A mechanism proposed to explain the atmospheric corrosion of Al in the presence of NaCl and SO_2 in humid air, see Figure 37.

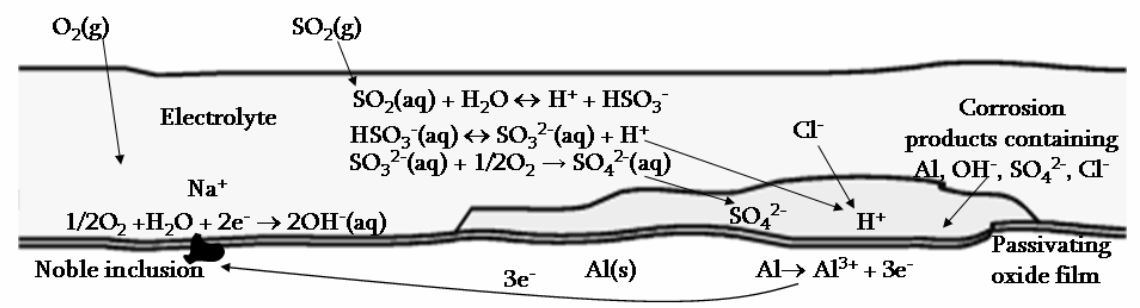

Figure 37. A suggested mechanism for the atmospheric corrosion of Al in the presence of NaCl and SO_2 in humid air.

Compared with chlorides, sulfates are less likely to cause pitting corrosion on Al, see Section 2.3.1 and 2.3.2. Part of the explanation for this is that aluminum hydroxy chlorides are more water soluble than basic aluminum hydroxy sulfates [36]. Water leaching and ion chromatography support this, see Paper 5.

4.7 Atmospheric corrosion of Mg-Al systems in CO_2-free humid air

Carbon dioxide strongly influences the NaCl induced atmospheric corrosion of Mg-Al alloys. The corrosion rate is about 3 times higher in the absence of CO_2 than in the presence of 350ppm CO_2, see Figure 38.

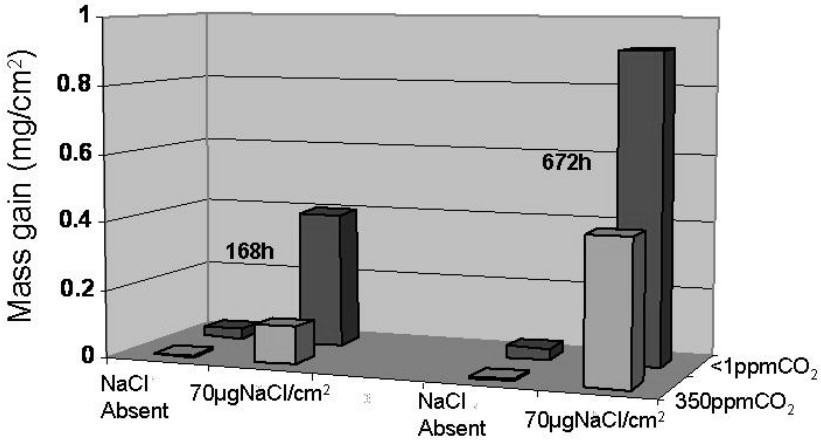

Figure 38. Corrosion rates with, and without, CO_2 for AZ91D exposed at 22.0°C for 168 and 672 hours. The relative humidity was 95%. Either 70µg NaCl/cm^2 or none was added prior to exposure. The scatter in the mass gain was about ± 5%.

In the absence of NaCl, the corrosion rate of AZ91D is quite slow. The strong dependence of carbon dioxide in the presence of NaCl is also reflected in the surface morphology, see Figure 39.

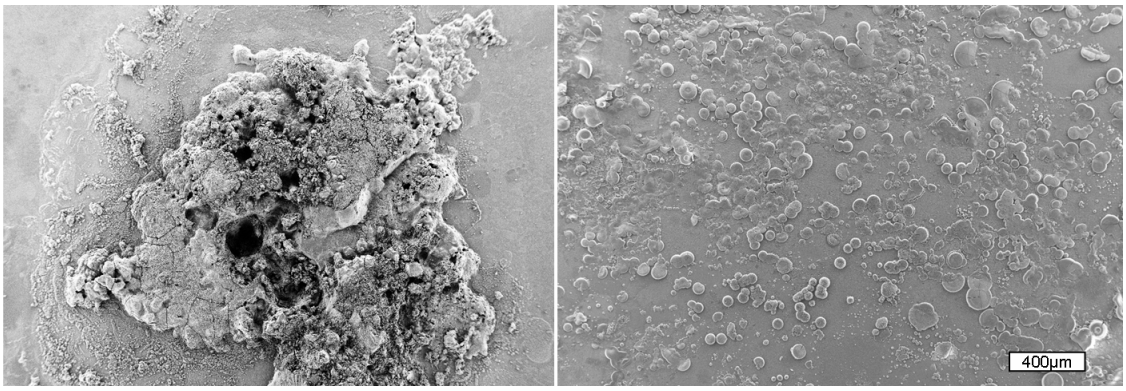

Figure 39. ESEM images (secondary electrons) of AZ91D samples exposed in the absence of CO_2 (left) and in the presence of 350ppm CO_2 (right) for 672 hours at 95% RH and 22.0°C; 70µg NaCl/cm^2 was added prior to exposure. Images by I. Maric.

Large corrosion product crusts (1 - 2mm) containing Mg/Al hydroxides and covering deep pits (10 - 100µm) developed discretely on the sample surfaces. Chloride was found to be enriched at the bottom of these pits. Between the crusts, circular areas (50 - 200µm) of about 200nm thickness were seen, see Figure 40.

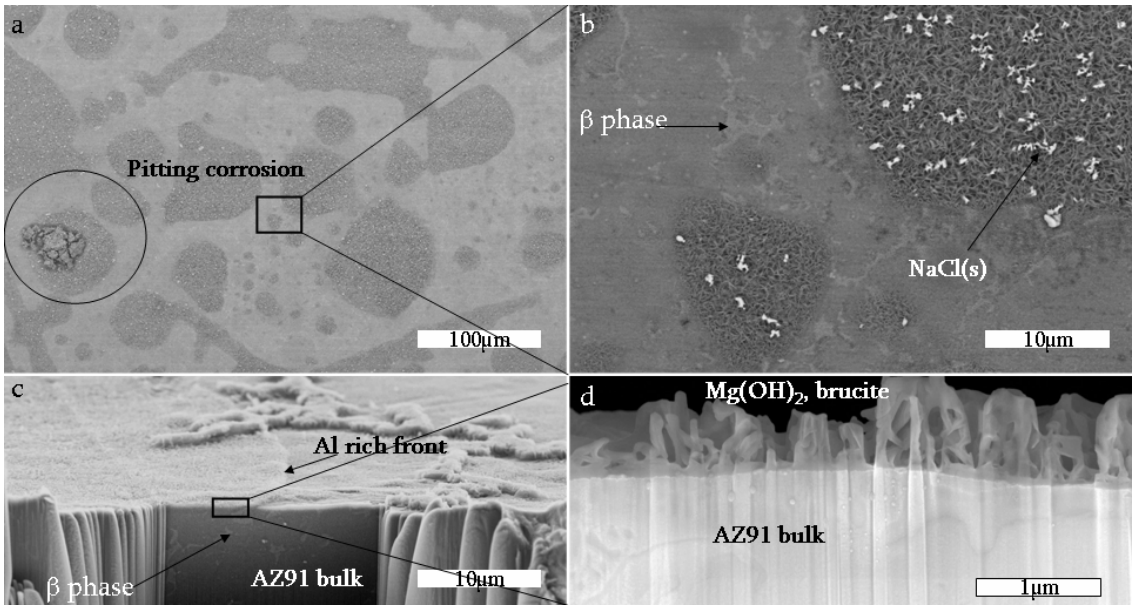

Figure 40. SEM images (BSE) of a corroded area on AZ91D in the absence of CO_2. The sample was coated with 70µg NaCl/cm^2 prior to exposure. The exposure time was 672 hours at 22.0°C and 95% RH. (a) Plane view showing localized corrosion attack; (b) the same area (squared) as in (a) but with higher resolution; (c) FIB cross section of an area with corrosion products reminiscent of those shown in (b); (d) the same area as squared in (c) but with higher magnification. Images by I. Maric

The circular areas between the crusts grow laterally with Al enriched at the front of the growth, see Paper 4. The formation of local electrochemical cells results in pH gradients over the surface, a high pH developing at the cathodic regions, while the pH at the anodic sites decreases. This affects the passive film because magnesium hydroxide is insoluble at high pH, whereas Al is not, see Sections 2.3 and 2.4. The local dissolution of the passive layer on AZ91D in the absence of CO_2 is illustrated in the EDX map in Figure 41. The circular area represents a cathodic region where aluminum has been dissolved from the passive film due to high pH, see Sections 2.3, 2.3.1 and 2.3.2. Corresponding aluminum enrichment can be seen at the periphery where pH is lower, see Figure 41.

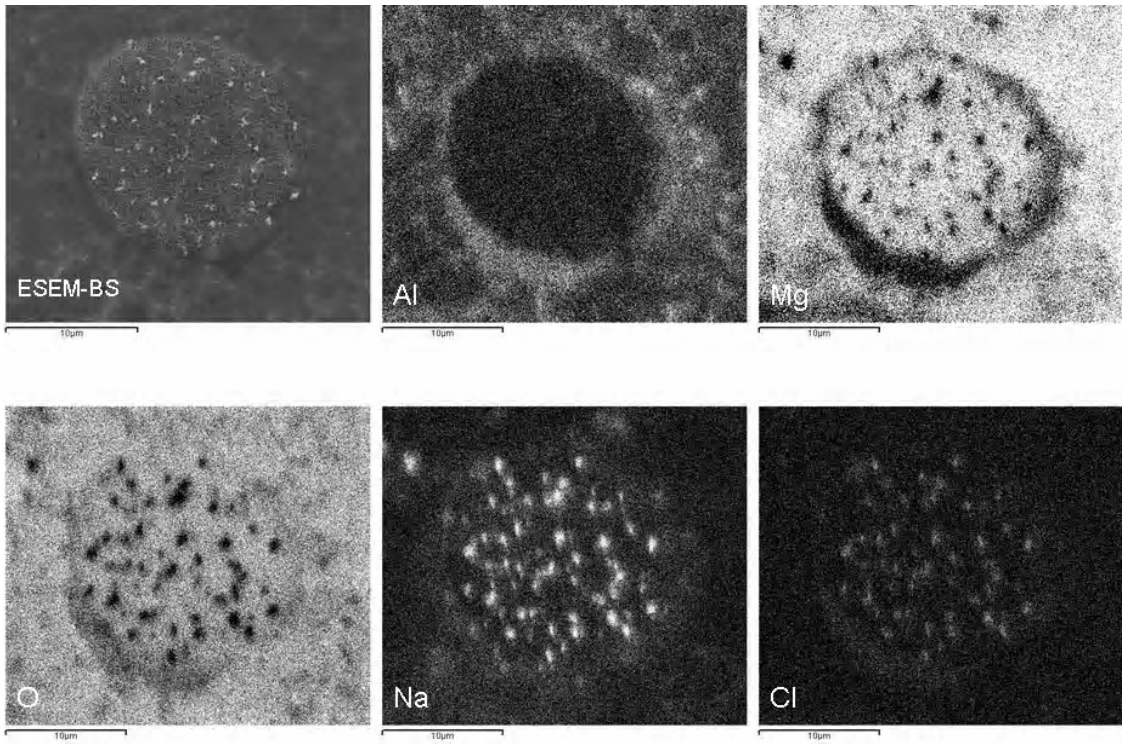

Figure 41. Energy dispersive X-ray maps (4kV) of a corroded area on AZ91D in the absence of CO_2. The sample was coated with 70µg NaCl/cm^2 prior to exposure. The exposure time was 672 hours at 22.0°C and 95%RH. The scale bar corresponds to 10µm. Images by I. Maric.

The depletion of Al on the cathodic areas was also observed with Auger electron spectroscopy, see Paper 4. Furthermore, crystalline $MgAl_2(OH)_8$ was also found with grazing incidence X-ray diffraction.

The initial effect of CO_2 on Mg-Al systems was addressed by investigating the electrochemistry of the corroding surface by *in situ* atomic force microscopy and scanning Kelvin probe force microscopy. A model system including physical vapor deposition of Al islands on Mg was devised to illustrate the complex behavior of the actual two phase alloy AZ91D. When exposed to CO_2-free air, the corrosion attack took place primarily between the Al dots on the Mg substrate, see Figure 42.

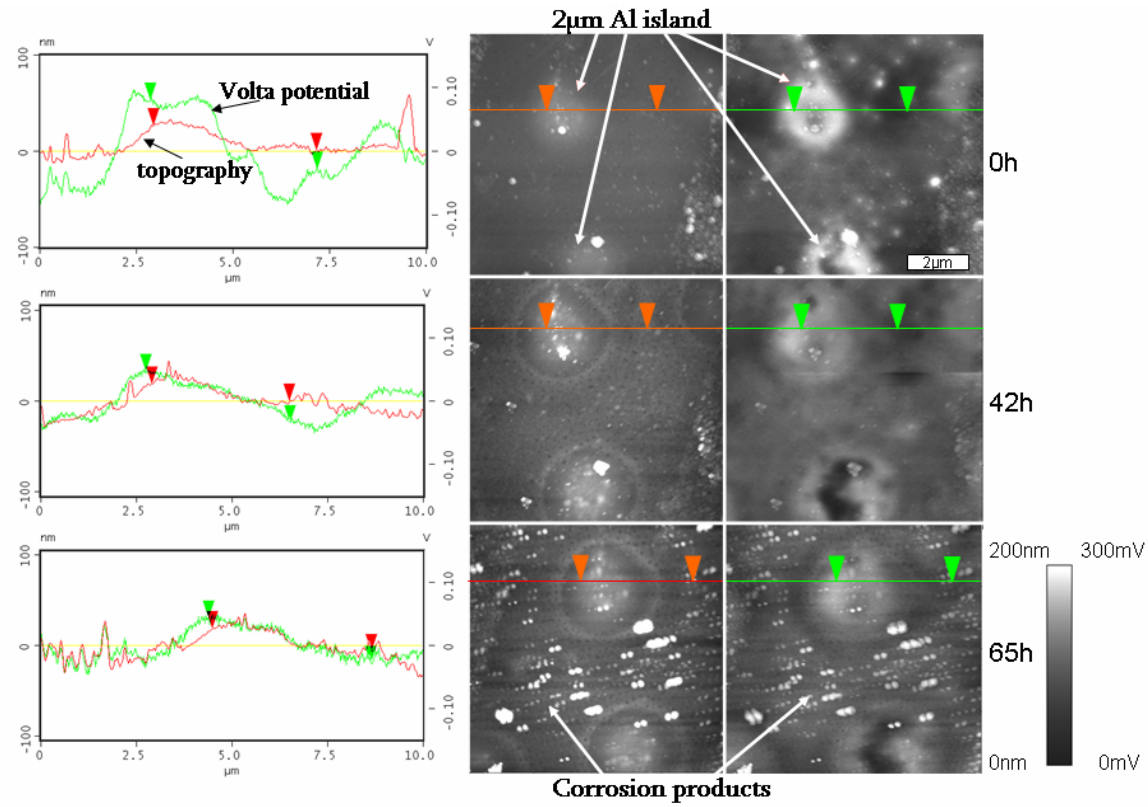

Figure 42. Time resolved *in situ* AFM and SKPFM images of PVD-deposited pure Al on pure Mg in the absence of CO_2. The relative humidity was 85% and the temperature was 22.0°C. The images in the left hand column show the topography by tapping mode AFM, while the right hand column shows Volta potential maps imaged using SKPFM. The brighter areas protrude from the surface in the topography images and have a higher relative potential in the Volta potential images. The height range is 200nm and the Volta potential range is 300mV.

The aluminum islands are cathodic and influence the corrosion on the magnesium substrate. Aluminum dissolves when the pH becomes high on the cathodic Al islands, see Section 2.3. The islands are surrounded by corrosion product halos. During the exposure a decrease in the thickness of the Al islands was evident, which indicates a continuous dissolution of Al because the cathodic reaction generates high pH areas, see Section 2.3.2. Between the halos and the Al islands, a narrow depression can be seen. The aluminum islands are surrounded by corrosion products that have precipitated on the Mg substrate. The AES line scan shows that these corrosion products are rich in Al, see Paper 4. Further away from the Al islands, the corrosion products are rich in Mg. When the same experiment was done using AZ91D, it was observed that the localized corrosion attack was initialized on the Al rich β phase, see Paper 4. The presence of intermetallic compounds or Al on Mg produces galvanic

couples on the surface, see Sections 2.2 and 2.4. The cathodic reaction takes place on the nobler, Al-rich areas (β phase, Al_8Mn_5 or the Al islands in the model system), whereas the anodic reaction takes place on the less noble α phase or Mg. The high pH formed at the cathodic areas leads to the dissolution of the Al-rich passive layer (reactions 4 and 5). The dissolved Al migrates as $Al(OH)_4^-$ towards the anodic substrate and precipitates as aluminum hydroxide or aluminum magnesium hydroxide. In the presence of NaCl, large electrochemical corrosion cells form. The pit distribution is sparse (about 1 pit per 4 cm^2). A corrosion mechanism is proposed in Figure 43 to explain the process described.

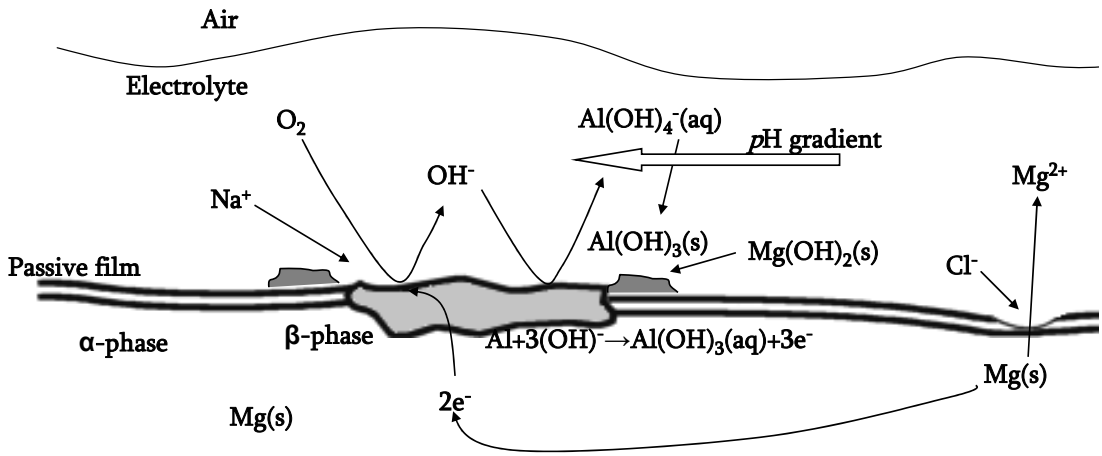

Figure 43. A mechanism proposed to explain the corrosion attack on Mg-Al systems in the absence of CO_2 in humid air when NaCl is present on the surface.

4.8 Atmospheric corrosion of Mg-Al systems in humid air with 350 ppm CO_2

The presence of 350ppm CO_2 slows the atmospheric corrosion on Mg-Al systems by a factor three compared with exposures in the absence of CO_2, see the bar chart in Figure 38. Furthermore, for these systems in humid air the corrosion rate is very low without NaCl as well.

The *in situ* AFM/SKPFM technique was employed to investigate the initial stages of the corrosion process on AZ91D in humid air. The difference in potential between α and β phases fundamentally influences early stages of corrosion attack. It is evident that, in the presence of 350ppm CO_2, the corrosion product distribution is more even than that of the corresponding experiment in the absence of CO_2, see Paper 4. Sub-

micron corrosion product agglomerations form all over the surface; on the α phase matrix as well as on the β phase areas (see Figure 39).

Also in this environment, the cathodic reaction occurs on nobler particles or on Al deposited on Mg. However, in this instance the CO_2 dissolved in the surface electrolyte provides a neutralization of the high pH formed, see Figure 44.

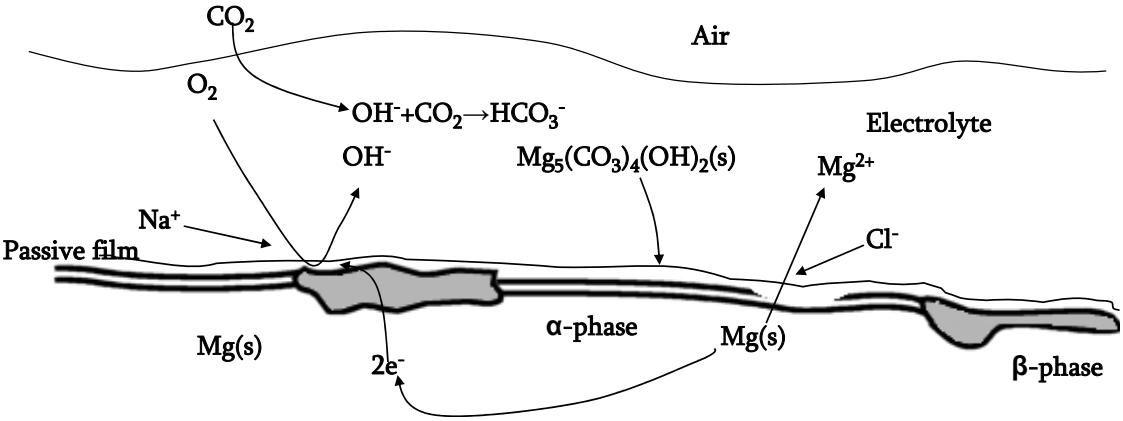

Figure 44. A mechanism proposed to explain the corrosion attack in the presence of 350ppm CO_2 in humid air when NaCl is present on the surface.

The kind of destabilization of the passive film seen in the absence of CO_2 does not occur in the presence of CO_2, see Sections 2.3, 2.3.1 and 2.3.2. Moreover, the precipitation of a protective layer of electronically insulating magnesium hydroxy carbonate retards the atmospheric corrosion rate. This is seen in reaction (23).

(23) $5Mg(OH)_2(s) + 4CO_2(g) \rightarrow Mg_5(CO_3)_4(OH)_2(s) + 4H_2O(l)$

This carbonate containing film is more protective than the $Mg(OH)_2$ formed in the absence of CO_2.

4.9 The effect of SO_2 on the atmospheric corrosion of Mg and Mg-Al alloys

Sulfur dioxide has a large impact on the atmospheric corrosion of Mg and Mg-Al alloys. The mass gain is about 15 times higher in the presence of SO_2 than for exposures without SO_2, see the bar chart in Figure 45.

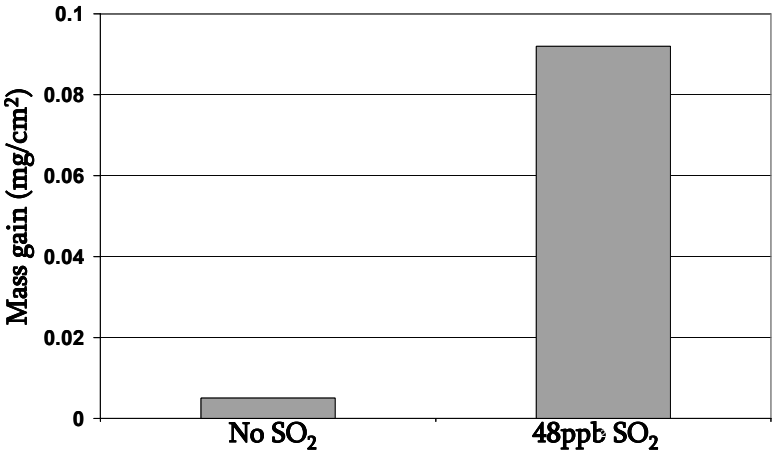

Figure 45. Mass gain without SO_2 and with 48ppb SO_2 for AZ91D exposed at 22.0°C 672 hours. The relative humidity was 95%. The scatter in the mass gain was about ± 5%.

The only corrosion product identified by XRD was magnesium sulfite, $MgSO_3 \cdot 6H_2O$. The SO_2 induced corrosion of magnesium and AZ91D is localized by nature, indicating the development of electrochemical cells, see Fig. 46.

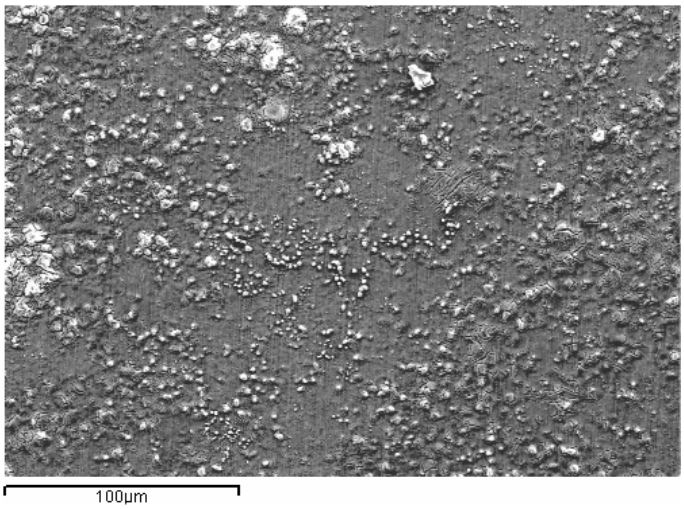

Fig. 46. SEM image (secondary electrons) of AZ91D exposed for 672h and 48ppb SO_2 at 22.0°C

At low relative humidity (≤ 50% RH) SO_2 deposition on Mg and AZ91D is a transient process that terminates when the surface of the oxide film is covered by S(IV) species. At high humidity (≥ 70% RH), the rate of SO_2 deposition on magnesium and alloy AZ91D is very high and limited by the mass transfer in the gas phase. It is proposed that the change from transient to steady-state SO_2 deposition is caused by the onset of electrochemical corrosion of magnesium, the cathodic current being supplied by oxygen reduction. At 60 % RH, the addition of O_3 or NO_2 strongly increases the SO_2

deposition rate on AZ91D. This effect is explained by O_3 and NO_2 acting as cathodic depolarizers, providing cathodic current for the corrosion of magnesium.

To investigate the initial corrosion attack on pure Mg in the presence of SO_2, the *in situ* AFM/SKPFM atmospheric corrosion cell was used, see Figure 19. The formation of discrete corrosion products that coalesce with time, forming larger agglomerates or corrosion product crusts (localized corrosion attack) is evidence of electrochemical corrosion, see Figure 47.

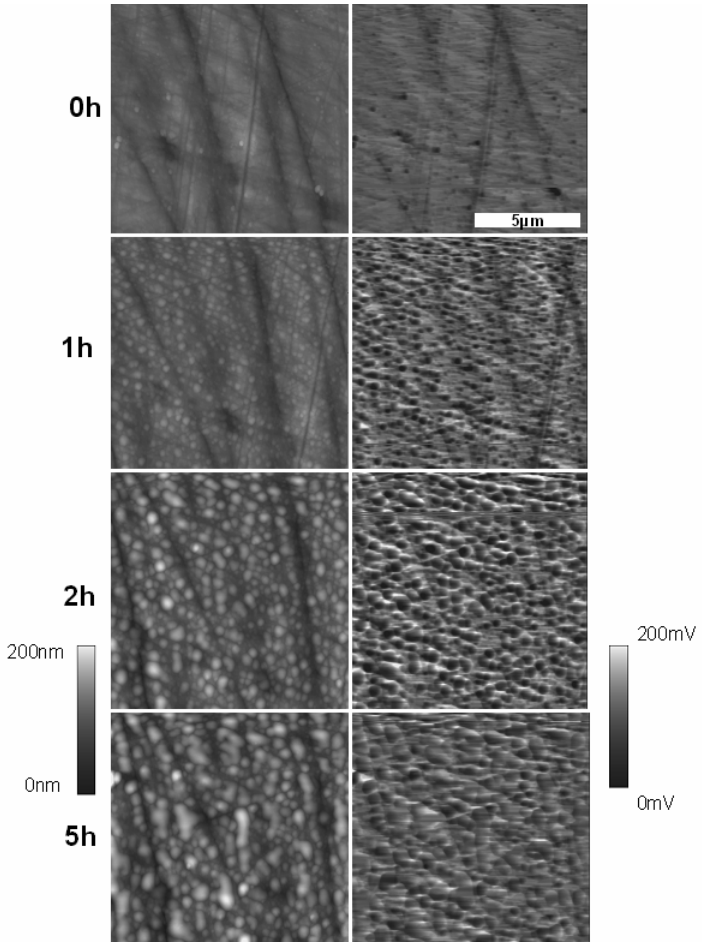

Figure 47. Time-resolved in situ AFM and SKPFM images of Mg in the absence of CO_2. Relative humidity was 60% and the temperature was 22°C. The SO_2(g) concentration was 48ppb. The images in the left hand column show the topography by tapping mode AFM while the right hand column shows Volta potential maps imaged by SKPFM. The brighter areas are protruding from the surface in the topography images and have a higher relative potential in the Volta potential images. The height range is 200nm and the Volta potential range is 200mV. The top row shows the Mg surface at the start of the experiment and the lower rows show the surface after 1, 2 and 5 hours.

4.10 The effect of SO_2 + NaCl on the atmospheric corrosion of Mg and Mg-Al alloys

Sulfur dioxide has a large impact on the atmospheric corrosion of Mg-Al alloys, also in the presence of NaCl. The mass gain is about 2 - 3 times higher in the presence of SO_2 than for exposures without SO_2, see the bar chart in Figure 48.

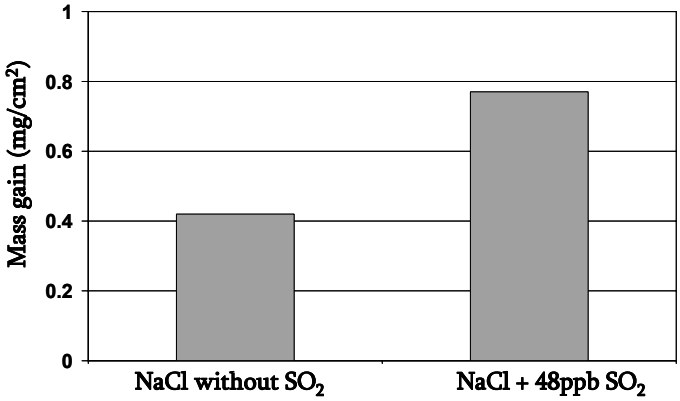

Figure 48. Mass gain without SO_2 and with 48ppb SO_2 for AZ91D exposed at 22.0°C for 672 hours. The relative humidity was 95%. 70µg NaCl/cm^2 was added prior to exposure. The scatter in the mass gain was about ± 5%.

The corrosion attack is localized in the combination of SO_2 and NaCl, corrosion product crusts (50 - 200µm in diameter) covering about 60% of the surface. The corrosion product crusts cover deep pits (about 10µm) in the alloy. The FIB cross section of one of these crusts (Figure 49) reveals preferential attack of the α phase. The energy dispersive X-ray analysis shows that chloride and sulfate are enriched at the interface of the corrosion crust and the alloy and in the areas previously occupied by the α phase. Crystalline magnesium sulfite was detected by GI-XRD after 672h.

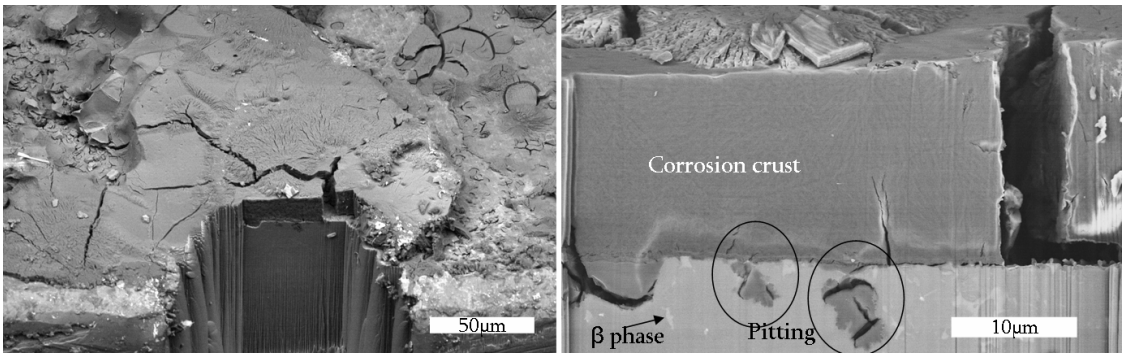

Figure 49. Atmospheric corrosion of AZ91D in the presence of NaCl and SO_2 (48 ppb SO_2, 672 hours exposure, 95% RH, 22.0°C, 70µg NaCl/cm^2). SEM (BSE) images. To the left, a cross section of a crust prepared by the FIB milling technique. To the right, the same crust at higher magnification.

5 Conclusions

Ambient concentrations of CO_2 (350ppm) strongly inhibit NaCl induced atmospheric corrosion of Al and Mg-Al alloys.

The NaCl induced corrosion of aluminum in humid air at room temperature is reduced by a factor of 20 by CO_2. Corrosion attack is uniform in the absence of CO_2, while it is localized in CO_2-containing air. The rapid corrosion of NaCl coated aluminum in humid CO_2-free air is attributed to the formation of areas with high pH caused by the cathodic reduction of oxygen. The sodium ion supports the change to high pH. At high pH, the passive film dissolves in the form of aluminate, $Al(OH)_4^-$, which explains the rapid general corrosion. The inhibitive effect of CO_2 is due to its acidity. Carbon dioxide neutralizes the hydroxide formed at the cathodic sites, which retards the dissolution of the passive film. In the presence of CO_2, NaCl promotes pitting corrosion, but the average corrosion rate is quite low. The strong inhibitive effect of CO_2 on NaCl induced atmospheric corrosion was also present for three commercial alloys (Al-Mg and Al-Mg-Si).

The temperature dependence of NaCl induced atmospheric corrosion of aluminum alloys is strongly non-linear. In the absence of CO_2, the corrosion rate increases by two orders of magnitude from 4°C to 22°C. The inhibitive effect of CO_2 declines above 22°C and disappears at 60°C. With increasing temperature, the inhibitive effect of CO_2 declines due to the decreasing solubility of CO_2 in water. Furthermore, at elevated temperatures, CO_2 is unable to hinder the corrosion attack because of the faster kinetics and the lower stability of aluminum carbonates. The temperature dependence is important for interpreting the results from accelerated corrosion tests and for explaining the atmospheric corrosion in different climates.

The inhibitive effect of CO_2 has important practical implications for the atmospheric corrosion behavior of aluminum and its alloys. The results imply that the susceptibility of aluminum alloys to crevice corrosion may be caused by a limited supply of CO_2. Similar effects may be involved in the occurrence of filiform corrosion of aluminum beneath organic coatings.

The corrosive effect of some soluble salts on aluminum is related to the acid-base properties of the cation and to the solubility of the corrosion products formed. In the absence of CO_2, the corrosivity increases in the order $MgCl_2 \cdot 6H_2O$ < $AlCl_3 \cdot 6H_2O$ < NaCl. In a CO_2 environment there is little difference in corrosion rates between the salts; NaCl is more corrosive than Na_2SO_4 in the absence of CO_2.

Moreover, on commercial die-cast Mg-Al alloys, the atmospheric corrosion rate is much faster in CO_2-free air than in air containing 350ppm CO_2. The corrosion attack is localized in the absence of CO_2, while general corrosion prevails in its presence. The inhibitive effect was attributed to the precipitation of insulating magnesium hydroxy carbonate on the surface, which interferes with the anodic and cathodic reactions and hampers the rate of atmospheric corrosion.

A useful technique for investigating the early stages of atmospheric corrosion attack is AFM/SKPFM. It allows for the simultaneous *in situ* investigation of the topography and the Volta potential during exposure; the resolution is in the sub-micrometer range. The AFM/SKPFM was used for studying the atmospheric corrosion of the two-phase Mg-Al alloy AZ91D and of a model system consisting of spots of pure Al deposited on Mg. The results show that CO_2 strongly influences the atmospheric corrosion of AZ91D and of the model system. In the absence of CO_2 the corrosion attack tends to be localized, while it is more evenly distributed in the presence of CO_2. It is suggested that the influence of CO_2 is connected to the formation of an insulating magnesium hydroxy carbonate film that interferes with the anodic and cathodic processes on the surface.

Sulfur dioxide is a powerful corrosion accelerator for aluminum in humid air. Sulfuric acid formation on the surface acidifies the surface electrolyte and destabilizes the alumina passive film. As a result, corrosion product “islands” form, containing aluminum hydroxy sulfate. The deposition rate of SO_2 on Al is slow, almost independent of the SO_2 concentration and is not limited by the oxidation of (IV) valent sulfur on the surface. The SO_2 deposition is enhanced by sodium chloride because of the corrosion reactions in the NaCl(aq) surface electrolyte. The rapid absorption of SO_2 explains the synergistic effect seen on the average corrosion rate when NaCl and SO_2 are combined. In contrast, the chloride-induced pitting of aluminum is greatly

reduced by SO_2. This is attributed to the formation of aluminum hydroxy sulfates that retard pit propagation because they are less soluble than the corresponding chlorides.

The presence of ppb levels of SO_2 strongly increases the corrosion of Mg and AZ91D. The only corrosion product identified was magnesium sulfite, $MgSO_3 \cdot 6H_2O$. The SO_2 induced corrosion of magnesium and AZ91D is electrochemical. At low relative humidity SO_2 deposition on Mg is a transient process that terminates when the surface of the oxide film is covered by S(IV) species. At high humidity, the rate of SO_2 deposition on magnesium and the alloy AZ91D is very high; it is limited by the mass transfer in the gas phase. At medium humidity (60% RH), SO_2 deposition on Mg exhibits a transition from an initial transient mode of SO_2 deposition to a steady-state mode of deposition where SO_2 is irreversibly bound to the surface. It is argued that this change is caused by the onset of electrochemical corrosion of magnesium, the cathodic current being supplied by oxygen reduction. At 60 % RH, the addition of O_3 or NO_2 strongly increases the SO_2 deposition rate on AZ91D. This effect is explained by O_3 and NO_2 acting as cathodic depolarizers. In the presence of SO_2, Mg-Al alloys suffer preferential attack on the α phase.

6 Future work

In the future, it would be interesting to investigate the temperature dependence of the atmospheric corrosion of Al and Mg-Al alloys in the presence of ppb levels of SO_2, $SO_2 + NO_2$ and $SO_2 + O_3$. In a preliminary study on the effect of CO_2 on the corrosion of Al, a number of specimens exposed for different periods of time were investigated [74]. It was found that the approach of time-resolved investigation provided valuable insights in the dynamics of the corrosion process. Therefore it is suggested that the same approach should be used also for investigating the effect of SO_2, NO_2 and O_3 on light metal alloys.

The custom made tapping mode AFM/SKPFM atmospheric corrosion cell enables investigation with nanometer resolution, of the local electrochemical processes taking place on the corroding metal surface *in situ*. The topography and the Volta potential can be measured simultaneously in well-controlled atmospheres on corroding AA2024-T3, AA7010, and model systems made by PVD consisting of combinations of Al, Cu, Zn, Fe, Si and Mg. The influence of relative humidity, ppb levels of SO_2, NO_2 and O_3, and the synergistic effects of these, on the initial mechanisms of the atmospheric corrosion of light metal alloys would be beneficial and fascinating to examine with this method in the future.

Also the ESEM can be directed to *in situ* investigation of the initial growth of corrosion scales on light metals in humid air. The advantage of this method is the possibility to study the formation of the corrosion products in real time.

Analysis of crystalline compounds in the corrosion scale formed on Al and Mg-Al alloys should also be carried out by electron backscattered diffraction (EBSD). The idea of using this method is that the detailed microstructural investigations require only SEM; the time consuming TEM sample preparation and analysis is not needed.

A cross-disciplinary approach to connect surface chemistry, alloy microstructure and the rate of corrosion of light metals would be valuable to apply in the future. The combination of instrumentation, such as *in situ* SKPFM, FIB, SEM, EDX and TEM

will then be used to carry the research further and to fill in gaps in the understanding of atmospheric corrosion. The aim is to link the corrosion mechanisms on the macroscopic and microscopic scale. This will facilitate a qualitative step forward in the science of atmospheric corrosion.

7 Acknowledgments

I would first like to thank my supervisors, Professor Lars-Gunnar Johansson and Associate Professor Jan-Erik Svensson for valuable discussions, guidance in experiments, and encouragement.

I am grateful to Professor Oliver Lindqvist for giving me the opportunity to work at the Department of Environmental Inorganic Chemistry at Chalmers University of Technology.

The EC project, “Mg-Chassis”, contract number G3RD-CT-2000-00287, the Swedish Research Council, and Volvo Car Corporation are gratefully acknowledged for their financial support of the project.

Furthermore, I want to thank the following persons:

Associate Professor Mats Halvarsson, Linda Ingemarsson, Ivica Maric, and Torbjörn Jonsson, for cooperation with microscopy and microanalysis;

Michael Rohwerder, Ph.D., Mariusz Wicinski, and Sascha Frezneck, Ph.D., at the Max Planck Institut für Eisenforschung (MPIE) for help with physical vapor deposition, scanning Kelvin probe, scanning Kelvin probe force microscopy and for the opportunity to do research at the MPIE;

Henrik Asteman, Ph.D., for help with scanning electron microscopy and Auger electron spectroscopy;

Associate Professor Vratislav Langer for assistance with X-ray diffraction;

Mats Norell, Ph.D., for help with Auger electron spectroscopy;

Mats Ström and Gunnar Ström, Ph.D., at Volvo Car Corporation for stimulating discussions; and

Esa Väänänen, Roger Sagdahl, Eva Lundqvist and Charlotte Bouveng for technical support.

I thank my former and present colleagues in the corrosion group, Anna Axelsson, Nicklas Folkeson, Kristina Hansson, Ph.D., Helena Josefsson, Anders Järdnäs, Rakel Lindström, Ph.D., Pierre Lindqvist, Annika Niklasson, Farschid Orwang, Ph.D., Carolina Pettersson, Jesper Pettersson, Bagas Pujilaksono and Karin Segerdahl, Ph.D., for their contribution to an inspiring working environment.

8 References

1. L. Bourdeau, A. Jussiaume, E. Perrot, G. Stroem, and D. Thierry, *Galvatech 2001, International Conference on Zinc and Zinc Alloy Coated Steel Sheet, 5th, Brussels, Belgium, June 26-28,* pp. 295 (2001).
2. G. Sowinski and D. O. Sprowls, *Atmos. Corros., [Pap. - Int. Symp. Atmos. Corros.],* pp. 297 (1982).
3. G. Wranglen, *An Introduction to Corrosion and Protection of Metals*, (1985).
4. K. S. Ferrer and R. G. Kelly, *Proceedings - Electrochemical Society,* pp. 176 (2003).
5. W. Furbeth and M. Stratmann, *Progress in Organic Coatings,* **39**, 23 (2000).
6. T. Falk, J. E. Svensson, and L. G. Johansson, *J. Electrochem. Soc.,* **145**, 39 (1998).
7. T. E. Graedel, *J. Electrochem. Soc.,* **136**, 204C (1989).
8. C. Leygraf and T. E. Graedel, *Atmospheric Corrosion*, Wiley, New York (2000).
9. F. King, ed., *Aluminum and its Alloys,* Ellis Horwood Series in Metals and Associated Materials, Ellis Horwood Limited, New York (1987).
10. J. R. Davis, ed., *Aluminum and Aluminum Alloys,* ASM Specialty Handbook, ASM International (1993).
11. N. N. Greenwood and A. Earnshaw, *Chemistry of the Elements, 2nd Edition*, (1997).
12. M. Avedesian, H. Baker, and Editors, eds., *ASM Specialty Handbook: Magnesium and Magnesium Alloys*, (1998).
13. J. H. Nordlien, K. Nisancioglu, S. Ono, and N. Masuko, *J. Electrochem. Soc.,* **144**, 461 (1997).
14. G. Song, A. Atrens, and M. Dargusch, *Corrosion Science,* **41**, 249 (1999).
15. G. L. Makar and J. Kruger, *International Materials Reviews,* **38**, 138 (1993).
16. N. Cabrera and N. F. Mott, *Repts. on Progress in Physics,* **12**, 163 (1949).
17. M. R. Tabrizi, S. B. Lyon, G. E. Thompson, and J. M. Ferguson, *Corrosion Science,* **32**, 733 (1991).
18. H. Kaesche, *Passivity Met., Proc. Int. Symp., 4th*, 935 (1978).
19. O. Kubaschewski and B. E. Hopkins, *Oxidation of Metals and Alloys*, (1962).
20. G. M. Brown, K. Shimizu, K. Kobayashi, G. E. Thompson, and G. C. Wood, *Corrosion Science,* **34**, 2099 (1993).
21. R. Grauer, *Werkst. Korros.,* **32**, 113 (1981).
22. W. N. Martens, R. L. Frost, J. Bartlett, and J. T. Kloprogge, *Journal of Materials Chemistry,* **11**, 1681 (2001).
23. W. A. Deer, R. A. Howie, and J. Zussman, *An Introduction to the Rock-Forming Minerals*, (1966).
24. M. J. N. Pourbaix, *Atlas of Electrochemical Equilibriums in Aqueous Solutions. 2nd ed*, (1974).
25. K. Barton, *Schutz gegen atmosphärische Korrosion*, Verlag Chemie GmbH, Weinhem (1973).
26. W. Stumm and Editor, eds., *Aquatic Surface Chemistry: Chemical Processes at the Particle-Water-Interface*, (1987).
27. G. Wranglen, *An Introduction to Corrosion and Protection of Metals*, (1972).
28. H. Kaesche, *The Corrosion of Metals; Physico-Chemical Principles and Actual Problems*, (1966).

29. S. Lee and H. S. White, *J. Electrochem. Soc.,* **151**, B479 (2004).
30. S. B. Lyon, G. E. Thompson, J. B. Johnson, G. C. Wood, and J. M. Ferguson, *Corrosion (Houston, TX, United States),* **43**, 719 (1987).
31. W. Zhang and G. S. Frankel, *J. Electrochem. Soc.,* **149**, B510 (2002).
32. H. Boehni and H. H. Uhlig, *J. Electrochem. Soc.,* **116**, 906 (1969).
33. J. A. Richardson and G. C. Wood, *Corros. Sci.,* **10**, 313 (1970).
34. W. Vedder and D. A. Vermilyea, *Trans. Faraday Soc.,* **65**, 561 (1969).
35. J. H. Nordlien, S. Ono, N. Masuko, and K. Nisancioglu, *J. Electrochem. Soc.,* **142**, 3320 (1995).
36. R. M. Smith and A. E. Martell, *Critical Stability Constants, Vol. 4: Inorganic Complexes*, (1976).
37. G. Eriksson, *Analytica Chimica Acta,* **112**, 375 (1979).
38. W. H. J. Vernon, *Trans. Faraday Soc.,* **27**, 582 (1931).
39. L. G. Johansson, *Marine Chemistry,* **30**, 113 (1990).
40. U. R. Evans, *The Corrosion and Oxidation of Metals: 1st Suppl. Vol*, (1968).
41. J. E. Svensson and L. G. Johansson, *J. Electrochem. Soc.,* **140**, 2210 (1993).
42. H. P. Godard, W. B. Jepson, M. R. Bothewell, and R. L. Kane, *The Corrosion of Light Metals*, (1967).
43. W. Stumm, *Chemistry of the Solid-Water Interface: Processes at the Mineral-Water and Particle-Water Interface in Natural Systems*, (1992).
44. P. Eriksson, *Effects of SO_2 and NO_2 on metal surfaces: Atmospheric corrosion of copper and suface reactions on gold*, Doctoral, Department of Inorganic Chemistry, Göteborg University, Sweden (1992).
45. V. Vu Dinh, A. A. Mikhailov, Y. N. Mikhailovskii, P. V. Strekalov, and B. Do Thanh, *Zashchita Metallov,* **30**, 578 (1994).
46. R. T. Vashi and H. G. Patel, *Bull. Electrochem.,* **13**, 343 (1997).
47. E. Mattsson, *Chemtech,* **15**, 234 (1985).
48. L. Volpe, *Proc. - Int. Congr. Met. Corros.*, 4091 (1987).
49. P. B. P. Phipps and D. W. Rice, *ACS Symp. Ser.,* **89**, 235 (1979).
50. D. R. Lide, *CRC Handbook of Chemistry and Physics, 83rd Edition*, CRC Press LLC, Boca Raton, Fla. (2002).
51. J. E. Svensson and L. G. Johansson, *Corros. Sci.,* **34**, 721 (1993).
52. S. S. Butcher, R. J. Charlson, G. H. Orians, G. V. Wolfe, and Editors, *Global Biogeochemical Cycles*, Academic Press Inc., London (1992).
53. G. Hägg, *Allmän och Oorganisk Kemi*, Almqvist and Wiksell, Stockholm (1969).
54. H. Hultberg and P. Grennfelt, *Environmental Pollution (Oxford, United Kingdom),* **75**, 215 (1991).
55. B. J. Finlayson-Pitts and J. N. Pitts, Jr., *Atmospheric Chemistry: Fundamentals and Experimental Techniques*, Wiley-Interscience, Chichester, UK (1986).
56. J. G. Calvert and Editor, *Acid Precipitation Series, Vol. 3: Sulfur Dioxide, Nitrogen Oxide (NO), and Nitrogen Oxide (NO2) Oxidation Mechanisms: Atmospheric Considerations*, (1984).
57. J. J. Friel, *Corrosion (Houston, TX, United States),* **42**, 422 (1986).
58. S. Oesch and M. Faller, *Corrosion Science,* **39**, 1505 (1997).
59. N. Birbilis and R. G. Buchheit, *J. Electrochem. Soc.,* **152**, B140 (2005).
60. O. Lunder, J. Walmsley, F. Lapique, Y. Yu, and K. Nisancioglu, *ATB Metallurgie,* **43**, 412 (2003).
61. K. Shimizu, G. M. Brown, H. Habazaki, K. Kobayashi, P. Skeldon, G. E. Thompson, and G. C. Wood, *Corrosion Science,* **41**, 1783 (1999).

62. R. Lindstrom, L.-G. Johansson, G. E. Thompson, P. Skeldon, and J.-E. Svensson, *Corrosion Science,* **46**, 1141 (2004).
63. R. Lindström, *On the chemistry of atmospheric corrosion*, Doctoral, Department of Inorganic Chemistry, Göteborg University, Sweden (2003).
64. P. V. Strekalov, *Zashch. Met.,* **29**, 819 (1993).
65. V. Kucera and E. Mattsson, Atmospheric corrosion, In: *Chem. Ind. (Dekker)*, F. Mansfield, ed., Marcel Dekker, New York (1987).
66. R. Lindstrom, J.-E. Svensson, and L.-G. Johansson, *J. Electrochem. Soc.,* **147**, 1751 (2000).
67. J. A. Garland, *Atmos. Environ.,* **12**, 349 (1978).
68. J.-E. Svensson, *The Influence of Different Air Pollutants on the Atmospheric Corrosion of Zinc*, Department of Inorganic Chemistry, Göteborg University, Sweden (1995).
69. L. E. Davis, N. C. McDonald, P. W. Palmberg, G. E. Riach, and R. E. Weber, *Handbook of Auger Electron Spectroscopy*, Perkin/Elmer Corp., Eden Prairie, Minnesota (1978).
70. M. Rohwerder, P. Leblanc, G. S. Frankel, and M. Stratmann, *Application of Scanning Kelvin Probe in corrosion science*, (In Press 2004).
71. J. H. Parker and R. W. Warren, *Review of Scientific Instruments,* **33**, 948 (1962).
72. H. Baumgärtner and H. D. Liess, *Review of Scientific Instruments,* **59**, 802 (1988).
73. A. Broniatowski, W. Nabhan, B. Equer, and G. De Rosny, *Materials Science Forum,* **207-209**, 149 (1996).
74. L. Ingemarsson, Master Thesis, Experimental Physics, Chalmers University of Technology, Sweden (2005).
75. H. Ginsberg, W. Hueltig, and H. Stiehl, *Z. Anorg. Allgem. Chem.,* **318**, 238 (1962).
76. J. Weissenrieder, C. Leygraf, M. Gothelid, and U. O. Karlsson, *Applied Surface Science,* **218**, 154 (2003).
77. N. Le Bozec, D. Persson, A. Nazarov, and D. Thierry, *J. Electrochem. Soc.,* **149**, B403 (2002).
78. R. H. Perry, D. W. Green, and J. O. Maloney, eds., *Perry's Chemical Engineers' Handbook. 6th ed.*, NACE, Houston, Tex., USA (1996).
79. K. E. Hancock, G. E. Peck, D. L. Perry, J. L. White, and S. L. Hem, *Journal of Colloid and Interface Science,* **183**, 431 (1996).
80. R. T. Foley, *J. Electrochem. Soc.,* **122**, 1493 (1975).
81. Z. A. Foroulis and M. J. Thubrikar, *Werkst. Korros.,* **26**, 350 (1975).

Paper 1

Journal of The Electrochemical Society, **148** (4) B127-B131 (2001)
0013-4651/2001/148(4)/B127/5/$7.00 © The Electrochemical Society, Inc.

The Effect of CO_2 on the NaCl-Induced Atmospheric Corrosion of Aluminum

D. Bengtsson Blücher,[a,z] R. Lindström,[b] J-E. Svensson,[a] and L-G. Johansson[b,*]

[a]*Department of Inorganic Chemistry, Göteborg University, Göteborg SE-412 96, Sweden*
[b]*Department of Environmental Inorganic Chemistry, Chalmers University of Technology, Göteborg SE-412 96, Sweden*

A laboratory study of the effect of CO_2 and NaCl on the atmospheric corrosion of aluminum is reported. The samples were exposed to pure air with 95% relative humidity and the concentration of CO_2 was <1 and 350 ppm, respectively. Sodium chloride was added before exposure (0, 14, and 70 $\mu g/cm^2$). The main result is that the NaCl-induced atmospheric corrosion of aluminum is about 10 to 20 times faster in CO_2-free humid air compared to air containing ambient levels of CO_2. It is suggested that the rapid corrosion of aluminum coated with NaCl in humid CO_2-free air is connected to high-pH areas in the surface electrolyte that develop due to the cathodic reduction of oxygen. The anodic dissolution of aluminum is known to be enhanced by high pH. The unexpected corrosion-inhibitive effect of CO_2 is explained by the neutralization of the surface electrolyte. In the absence of CO_2, bayerite, $Al(OH)_3$, forms. Only minute amounts of carbonate were found on the surface after exposure to CO_2-containing air.
 [DOI: 10.1149/1.1354614]

Manuscript submitted April 12, 2000; revised manuscript received November 22, 2000.

The corrosion of aluminum in the atmosphere has mainly been investigated through field studies.[1-4] Few laboratory investigations in controlled environments have been published. Besides a strong humidity dependence it is generally agreed that deposition of SO_2 and chlorides and the pH in rain are major factors that determine the corrosion rate of aluminum. In the presence of SO_2, oxidizing agents such as O_3 and H_2O_2 may also play a role in the atmospheric corrosion of aluminum.[1]

The atmospheric corrosion of aluminum in the presence of a surface electrolyte such as NaCl(aq) is considered to be a special case of corrosion in aqueous solution. In contrast to bulk aqueous solutions, convection in the solution is insignificant in atmospheric corrosion and the corrosion products tend to remain on the surfaces where they form unless they are leached by rain, etc. The diffusion paths for, *e.g.*, oxygen molecules are short so that oxygen supply is usually not rate limiting for the overall corrosion rate. It is argued that if the differences between corrosion in an aqueous film on the metal surface and corrosion in a bulk solution are kept in mind, the insights gained in investigations of the corrosion reactions of aluminum in aqueous solution are quite useful for understanding the atmospheric corrosion of aluminum.

The concentration of carbon dioxide in the atmosphere is about 350 ppm.[5] The effect of CO_2 on the atmospheric corrosion of zinc was investigated by Falk *et al.*[6] and Lindström *et al.*[7] They report that ambient concentrations of CO_2 inhibit the NaCl-induced corrosion of zinc. This effect is important for understanding zinc corrosion in cases where the supply of CO_2 is limited, *e.g.*, in crevices and under paint films. In the case of zinc and copper, carbonate-containing corrosion products are often reported from the field.[8,9] In contrast, aluminum carbonate has not been identified as a corrosion product in the atmosphere.[1] The aim of the present study is to investigate the effect of ambient levels of CO_2 on the atmospheric corrosion of aluminum. The presence of such an effect would have important implications for the corrosion protection and corrosion testing of aluminum.

Experimental

Sample preparation.—Aluminum, AA 1070 (99.769% Al), was used in all experiments. The samples had a geometrical area of 20.0 cm^2. Before exposure the samples were polished on SiC paper in ethanol to 1000 mesh. The samples were ultrasonically cleaned in ethanol, dried in air, and stored in a desiccator over silica gel. NaCl was added by spraying the samples with a saturated solution of NaCl in 80% ethanol. In each experiment eight samples were exposed. 14 $\mu g/cm^2$ of NaCl was added to three of the samples, while 70 $\mu g/cm^2$ was added to another three samples. In addition, two reference samples were included that were not coated with NaCl. The amount of NaCl added was determined gravimetrically. Care was taken to avoid droplet formation on the samples during spraying. The distribution of salt on the surface after spraying was even. The samples were stored dry for about 24 h before exposure. The levels of particulate chloride deposition reported in the literature cover a very wide range; 15 $\mu g\ Cl^- cm^{-2} yr^{-1}$ is reported in rural areas far from the coast,[10] 60 $\mu g\ Cl^- cm^{-2} yr^{-1}$ was reported for metropolitan New York,[8] while deposition rates of over 55,000 $\mu g\ Cl^- cm^{-2} yr^{-1}$ have been found in extreme marine environments.[10] In comparison with reported deposition rates in the environment, the NaCl levels in the present work (equivalent to 110 and 550 $\mu g\ Cl^- cm^{-2}\ yr^{-1}$, respectively) correspond to urban areas and to marine environments not in the immediate vicinity of the coastline.

Experimental setup.—The experimental setup is described in Fig. 1. The exposure system is made entirely of glass and Teflon. There are eight parallel chambers through which the gas is sequentially distributed. The whole gas flow is passing through each chamber in turn for 15 s. The gas flow was 1000 mL/min in all experiments, corresponding to a gas velocity of 7 mm/s. Each sample was suspended in a thin nylon string in the middle of the chamber. Only one sample was exposed in each chamber. The chambers have an inner diameter of 55 mm and a volume of 0.4 L. The corrosion chambers are immersed in a water tank held at constant temperature. To avoid condensation in the parts of the system outside the water tank the temperature in the room was kept at 25°C. Relative humidity (RH) was regulated by mixing dry air and air saturated with water vapor. RH was 95% and was controlled with an accuracy of ±0.3%.

In the experiments with 350 ppm CO_2, pure carbon dioxide was added from a gas bottle and a CO_2 analyzer was used to monitor the concentration in the exposure gas. To expose samples in the absence of CO_2, the synthetic air was purified from CO_2 by letting it pass through two filters containing Ascarite II before entering the system. A concentration of less than 1 ppm CO_2 was achieved.

Methods of analysis.—To monitor the corrosion process during the exposure the samples were weighed once a week. In order not to disturb the corrosion process, the samples were not dried before weighing. The weighing procedure lasted 2 min per sample. The mass gain recorded in this way is termed the wet mass gain. After

* Electrochemical Society Active Member.
z E-mail: jes@inoc.chalmers.se

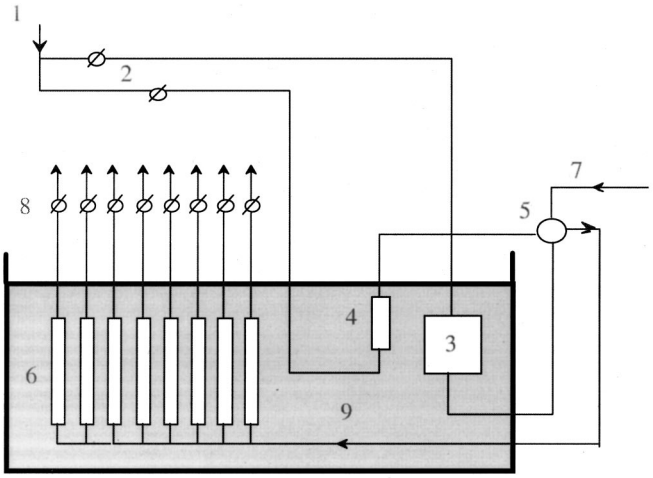

Figure 1. The experimental setup for the corrosion exposures: (1) dried purified air; (2) flow control; (3) humidifier; (4) vessels for permeation tubes; (5) mixer; (6) eight exposure chambers; (7) CO_2 inlet; (8) eight-channel solenoid valve; (9) water tank at constant temperature.

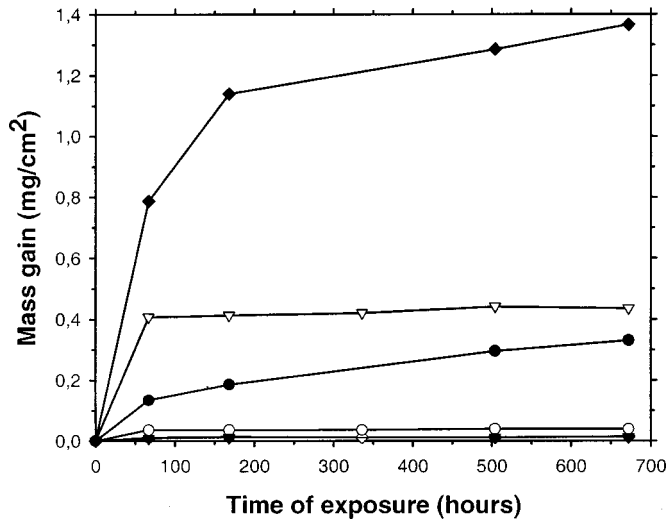

Figure 2. Mass gain as a function of exposure time for aluminum samples exposed to <1 ppm CO_2 and 350 ppm CO_2 at 22°C, with different amounts of NaCl, and RH 95%: (♦) <1 ppm CO_2 and 70 μg NaCl/cm^2; (▽) 350 ppm CO_2 and 70 μg NaCl /cm^2; (●) <1 ppm CO_2 and 14 μg NaCl/cm^2; (○) 350 ppm CO_2 and 14 μg NaCl/cm^2; (▼) <1 ppm CO_2 and no NaCl; and (◇) 350 ppm CO_2 and no NaCl.

the completion of the 4 week exposure the dry mass gain was determined after storing over a desiccant at ambient pressure and temperature for 1 week.

The amount of corrosion products was determined by leaching and pickling the samples using ultrasonic agitation. The water-soluble corrosion products and unreacted NaCl were first removed by leaching in pure water (pH 7) at ambient temperature for 2×1 min. Thereafter the samples were pickled in a solution of 50 mL H_3PO_4 (85%) and 20.0 g CrO_3/dm^3 in pure water for 3×5 min at 80°C and then washed in water and ethanol. Weighing the samples after the leaching and pickling procedure provided a measure of the metal loss. The self-corrosion loss during the corrosion product removal was measured and corrected for in the determination of the metal loss in the exposures.

The amount of water-soluble chloride leached from the samples was determined by ion chromatography (IC, Ionpac AD9-SC analytical column). The flow rate was 2 mL/min, and 1.8 mM Na_2CO_3/1.7 mM $NaHCO_3$ was used as eluent.

To determine the amount of carbonate in the corrosion products, the aluminum samples were transferred to an acid desorption cell consisting of a three-necked flask made of Pyrex glass containing 1 M $HClO_4$(aq). Immersing the samples in the acid quantitatively converted carbonate to carbon dioxide. A stream of 300 mL/min of nitrogen was used to expel the carbon dioxide from the solution and carry it to the CO_2 analyzer (Binos 100). The sensitivity of this analysis corresponded to 10×10^{-9} mol CO_2/sample. By introducing weighed amounts of $BaCO_3$(s) into the system, the precision of the analysis was found to be ±2%.

Crystalline corrosion products were analyzed by X-ray diffraction (XRD). A Siemens D5000 powder diffractometer (Cu Kα radiation) was used. The diffractometer was equipped with a grazing incidence beam attachment combined with a Göbel mirror. The diffraction peaks of metallic aluminum were used as an internal standard.

The corrosion products were also analyzed by environmental scanning electron microscopy (ESEM, Electroscan 2020). The samples were investigated using a magnification of 1000 and an acceleration voltage of 20 kV. An energy-dispersive X-ray detector (EDX, Link ISIS) was connected to the microscope.

Results

Mass gain and corrosion rate.—Figure 2 shows the wet mass gain as a function of exposure time at 22.00 ± 0.03°C. In the absence of NaCl, the wet mass gain is negligible in both atmospheres. The mass gain increases with the amount of NaCl added. The most striking result is that the mass gain is greatest in the absence of CO_2. It may be noted that the rapid initial mass increase of the NaCl-coated samples is partly due to the formation of NaCl(aq). Putting the activity coefficient of water equal to one, the NaCl(aq) solution on the surface is calculated to contain 11.66 g water per gram NaCl at equilibrium (95% RH), corresponding to a 1.4 M solution.[11] Accordingly, the samples coated with NaCl and exposed to CO_2-containing air appeared wet after the conclusion of the experiment, indicating the presence of NaCl(aq). In contrast, the samples exposed to CO_2-free air appeared dry within 1 week of exposure. This indicates that in the absence of CO_2, NaCl reacts to form other, less deliquescent, compounds on the surface.

In the presence of CO_2 there is no further mass gain after the first week (see Fig. 2). In contrast, the samples exposed to CO_2-free air gain mass throughout the exposure. The net mass gains in CO_2-free air are four and eight times greater compared to air with CO_2 for additions of 14 and 70 μg NaCl/cm^2, respectively.

The remarkable corrosion inhibitive effect of CO_2 on the NaCl-induced atmospheric corrosion of aluminum is even more evident in the mass gain of the samples after drying. Table I shows that the dry mass gain is about one order of magnitude greater in the absence of

Table I. Corrosion rate and corrosion product ratios at 22°C.[a]

CO_2 concentration (ppm)	NaCl (μg/cm^2)	Dry mass gain (mg/cm^2)	Metal loss (mg/cm^2)	Measured ratio
<1	0	0.0035	[b]	[b]
<1	14	0.24	0.12	3.0
<1	70	0.94	0.48	3.0
350	0	0.004	[b]	[b]
350	14	0.02	[b]	[b]
350	70	0.04	[b]	[b]

[a] The exposure time was 4 weeks and RH was 95%. The scatter in mass gain and metal loss results was about 7%. The corrosion product ratio corresponds to (dry mass gain + metal loss)/metal loss.
[b] The mass changes were too small for metal-loss determination.

Table II. Molar mass divided by metal mass for selected corrosion products of aluminum.

Product	Formula	Ratio
Aluminum oxide	γ-Al_2O_3	1.89
Akdalait	$Al_2O_3 \cdot \frac{1}{4} H_2O$	1.97
Boehmite	γ-AlOOH	2.22
Pseudoboehmite	$Al_2O_3 \cdot 2H_2O$	2.55
Bayerite	$Al(OH)_3$	2.89
Tucanite	$Al(OH)_3 \cdot \frac{1}{2} H_2O$	3.22
Aluminum chloride hydrate	$Al(H_2O)_6Cl_3$	5.00
Cadwaladerite	$AlCl(OH)_2 \cdot 6H_2O$	6.26

CO_2 compared to air containing 350 ppm CO_2. As the corrosion product composition is similar in the two environments, the dry mass gain results imply that the rate of corrosion is about 10 to 20 times more rapid when CO_2 is excluded. Unfortunately, the rate of corrosion in the presence of CO_2 was too small for reliable metal loss figures to be generated.

Table I shows the metal loss of samples exposed in air with <1 ppm CO_2 and coated with 14 and 70 μg NaCl/cm^2. The results show that metal loss is roughly proportional to the amount of NaCl added. The last column in Table I presents the ratio of the corrosion product mass (dry mass gain + metal loss) to the mass of the corroded metal (metal loss). The ratios found (3.0) are close to the corresponding value for bayerite, $Al(OH)_3$ (2.89). Table II presents the corresponding calculated ratios (corrosion product mass/aluminum mass) for selected aluminum corrosion products.

Corrosion product characterization.—The samples coated with NaCl and exposed in the absence of CO_2 were completely covered by evenly distributed white corrosion products. In all other cases, the metal was clearly visible after exposure.

ESEM images of samples coated with NaCl and exposed to CO_2-free environment show a corrosion product layer mainly consisting of 5-10 μm agglomerates covering the sample surface, see Fig. 3a. In contrast, the NaCl-coated surface appears relatively unaffected by corrosion after exposure to CO_2-containing air (see Fig. 3b). In this case occasional oxide islands (10 μm diam) are seen on a surface dominated by scratches originating from polishing. The aggregate of particles in the upper part of Fig. 3b contains NaCl.

Using XRD, bayerite [$Al(OH)_3$] was identified on the NaCl-coated samples exposed to CO_2-free air. No crystalline corrosion products formed in the presence of CO_2 or on the samples not coated with NaCl.

The IC analysis of the leaching water showed that almost all chloride was in water-soluble form after exposure. This is true for both environments. In accordance with this result, there are no reports in the literature of insoluble or even sparingly soluble aluminum hydroxy chlorides.[12] As noted above, the samples exposed in the absence of CO_2 appeared dry after exposure, while samples exposed to CO_2 were visibly wet. The presence of water on the samples exposed to CO_2-containing air is supported by the large difference between the wet and dry mass gain (compare Fig. 2 and Table I). This indicates that chloride is present on the surface as NaCl(aq). It is suggested that exposure in CO_2-free air converts the chloride added to the samples to amorphous, nondeliquescent, aluminum hydroxy chlorides.

An aluminum sample coated with 70 μg (1.2 μmol) of NaCl/cm^2 and exposed to CO_2-containing air for 72 h was analyzed for carbonate. The amount of carbonate found was quite small (0.01 μmol CO_3^{2-}/cm^2) compared to the amount of NaCl.

Discussion

The corrosion resistance of aluminum in the atmosphere is due to the presence of a thin oxide film on the metal surface. The air-formed passive film is hydroxylated on the surface. It is electrically insulating and relatively inert. The passive film grows by a mechanism involving field-assisted ion diffusion.[13,14] As the film increases in thickness the field diminishes and the film eventually ceases to grow. At ambient temperature the film only grows to about 2 nm thickness.[15]

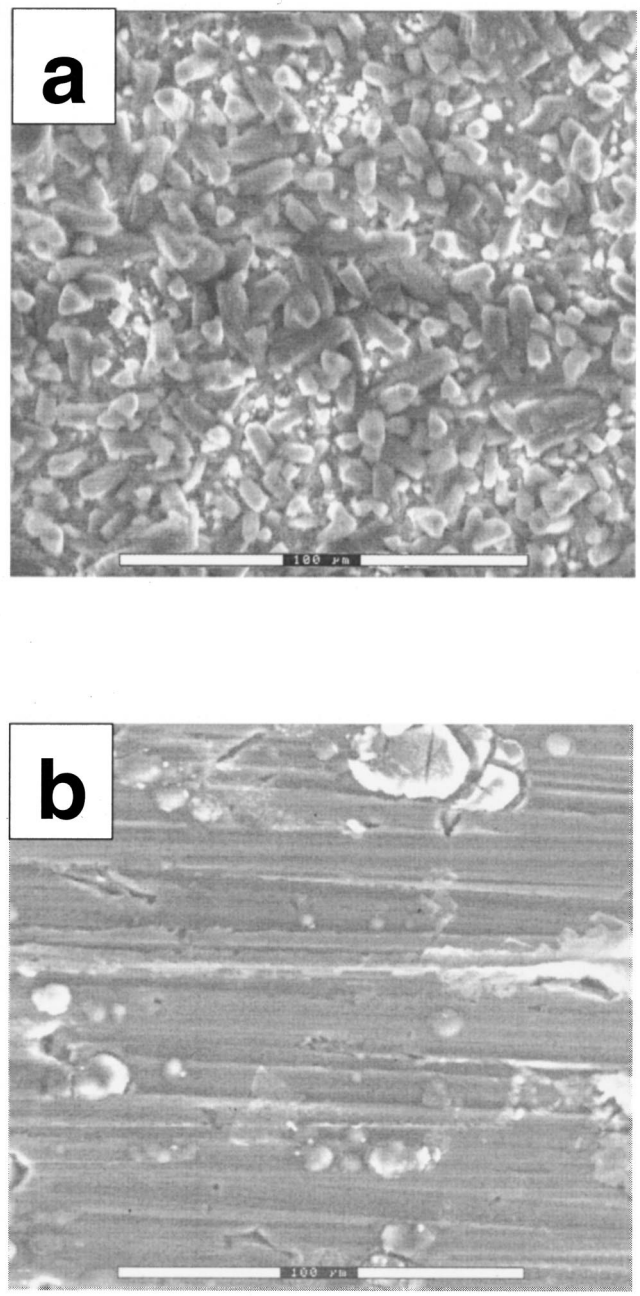

Figure 3. ESEM images of aluminum exposed to (a) <1 ppm CO_2 and (b) 350 ppm CO_2 for 4 weeks at 95% RH and 22°C. The amount of NaCl was 70 μg/cm^2.

In the present study the NaCl-coated samples absorb water from the gas phase, forming an aqueous electrolyte on the surface. In the presence of CO_2, the samples were visibly wet and NaCl(s) was identified on the surface after exposure. Also in the absence of CO_2, unreacted NaCl(aq) was present in the early stages of the experiment. Investigations regarding the corrosion reactions of aluminum in contact with bulk aqueous solutions containing NaCl are therefore

considered to be applicable to the NaCl-coated samples in the present study.

The corrosion of aluminum in aqueous solution has been extensively studied.[15-19] In pure water, aluminum is reported to corrode by an electrochemical mechanism. Due to the extremely rapid formation of aluminum oxide by the bare metal, aluminum is considered to be covered by an oxide film at all times.[15] The anodic reaction (the formation of Al^{3+} ions) therefore occurs at the metal/film interface. Once the passive film has formed, oxidation of Al to Al^{3+} can only proceed if the film is simultaneously thinned by dissolution at the film/water interface. In neutral and alkaline solution the anodic dissolution is therefore described by two coupled reactions[15]

$$Al + 3\ OH^- \rightarrow Al(OH)_3(s) + 3e^- \quad [1]$$

$$Al(OH)_3(s) + OH^-(aq) \rightarrow Al(OH)_4{}^-(aq) \quad [2]$$

The cathodic partial reaction may be hydrogen evolution or oxygen reduction

$$2H_2O + 2e^- \rightarrow H_2 + 2\ OH^- \quad [3]$$

$$\tfrac{1}{2}\ O_2 + H_2O + 2e^- \rightarrow 2\ OH^- \quad [4]$$

The cathodic reaction is reported to occur only on a small fraction of the film that is conducting due to doping by foreign elements. These ''flaws'' in the oxide may occur at grain boundaries or inclusions in the metal.[17,19] Because of the formation of hydroxide, the dissolution of the passive layer is enhanced at the cathodic sites. As pointed out by Vedder and Vermilyea,[17] this means that the anodic and cathodic reactions both occur at the same site, only the net reaction being cathodic. The anodic reaction also proceeds over the rest of the surface, although at a slower rate.[17] Since the thinning of the passive layer occurs through dissolution, this process implies that liquid water is necessary for corrosion to occur. This is supported by the observation that in the absence of contaminants, the formation of hydroxide on samples exposed to air with high humidity but avoiding condensation is negligible in comparison to the amount formed in contact with liquid water.[17]

It is well known that the presence of chloride ions in neutral aqueous solutions makes aluminum susceptible to pitting corrosion. The mechanism of attack has been the subject of much debate in scientific literature.[15,18,19] According to Kaeshe,[15] pitting is initiated through the adsorption of, *e.g.*, chloride on the alumina surface, causing the dissolution of the passive film. In accordance with this view, Stumm[20] reports that the dissolution of δ-alumina in aqueous solutions is promoted by the formation of surface complexes with various anionic ligands. They claim that the negative charge of the ligand causes the weakening of bonds in the hydroxylated surface, resulting in the formation of alumina species that pass into solution. In this view, the dissolution of alumina is a slow, nonequilibrium process strongly influenced by surface complexing with various ligands.

The adsorption of ions critically depends on surface charge. In acidic solution the alumina surface is positively charged while it is negatively charged in alkaline media.[20] For example, the pH of zero charge of γ-AlOOH in a noncomplexing aqueous solution is reported to occur at a pH of about 8.2.[21]

The importance of electric charge on chloride adsorption was realized by Foroulis and Thubrikar.[18] They suggested that the well-known potential dependence of pitting corrosion on aluminum in near-neutral, chloride-containing solutions is due to the field-assisted adsorption of Cl^- on the hydrated oxide film surface. As the aluminum surface is polarized anodically, the hydroxide surface becomes increasingly positively charged, resulting in chloride adsorption, dissolution of the passive film, and the initiation of pitting.

For aluminum at the open-circuit potential, in contact with a high-pH aqueous solution, chloride is not expected to be an efficient corrosion promoter. This is because at high pH the negative surface charge of alumina makes chloride adsorption unfavorable.

As already noted, high pH values enhance aluminum corrosion by promoting the anodic reaction through the formation of soluble aluminate species (see Reaction 2). Accordingly, aluminum immersed in an aqueous solution with high pH is affected by general corrosion rather than pitting.[15] The corrosivity of high-pH solutions toward aluminum can also be rationalized by thermodynamic arguments. Kaeshe reports that the thermodynamic solubility of the passivating alumina film increases as a function of pH above pH 7.[15]

Atmospheric corrosion of aluminum in the absence of CO_2.—By XRD it was shown that large amounts of bayerite [$Al(OH)_3$] form on aluminum coated with NaCl and exposed in the absence of CO_2. According to Ginsberg *et al.*,[22] pH values of 10 and higher are needed in order for bayerite to form. The authors report that at lower pH (8-9), alumina precipitates in the form of an X-ray amorphous gel or as the poorly crystalline pseudobohemite. From the presence of bayerite it is therefore concluded that high pH values occurred on the corroding aluminum surface during exposure.

Based on the reports in the literature on the corrosion of aluminum in aqueous solution,[15-19] it is proposed that the anodic dissolution reaction on the NaCl-coated samples is summarized by Reactions 1 and 2. As the supply of oxygen to the cathodes is expected to be good, the cathodic reaction on our samples is suggested to be represented by Reaction 4.

Oxygen reduction results in the formation of hydroxide ions, leading to an increase in pH at the cathodic sites. The negative charge of the hydroxide ions produced at the cathodes is compensated for by the migration of $Na^+(aq)$ in the surface electrolyte. It is proposed that this causes high pH values to occur on parts of the surface, explaining the formation of bayerite on the NaCl-coated samples. It is therefore suggested that the rapid corrosion experienced by aluminum coated with NaCl in humid CO_2-free air is explained by the evolution of high-pH areas. As discussed above, it is well known that the rate of corrosion of aluminum in aqueous solution increases above pH 7.

Influence of CO_2.—The most striking result in the present study is the discovery that CO_2-free humid air is far more corrosive toward NaCl-coated aluminum than air containing CO_2. This is surprising, especially as the amount of carbonate in the corrosion product is insignificant. The lack of carbonate in the corrosion product shows that the effect of CO_2 is not caused by the formation of a protective aluminum carbonate film. Previously, it has been shown that CO_2 slows down the NaCl-induced atmospheric corrosion of zinc.[6,7] It was argued that this effect is partly caused by insoluble zinc hydroxy chlorides that precipitate because of the decrease in pH caused by CO_2. As noted previously, there is no indication that insoluble aluminum hydroxy chlorides form in the present study. This shows that the formation of insoluble aluminum hydroxy chlorides is also not the cause for the corrosion inhibitive effect of CO_2. Instead it is proposed that the inhibitive effect of CO_2 is due to its acidity. CO_2 reacts with the hydroxide produced at the cathodic sites in the following way

$$CO_2(g) \rightleftarrows CO_2(aq) \quad [5]$$

$$CO_2(aq) + OH^-(aq) \rightarrow HCO_3{}^-(aq) \quad [6]$$

$$HCO_3{}^-(aq) + OH^-(aq) \rightarrow CO_3{}^{2-}(aq) + H_2O \quad [7]$$

It is suggested that the slowing down of the corrosion of NaCl-coated aluminum in humid air by CO_2 occurs because CO_2 counteracts the development of high pH in the surface electrolyte. As noted previously, aluminum is known to corrode rapidly at high pH. The observation that bayerite does not form in the presence of CO_2 indicates that high pH values do not occur in this environment, in accordance with our suggested mechanism.

It is well known that aluminum corrosion accelerates at low pH. However, the equilibrium pH in pure water in contact with 350 ppm

CO_2 in water is 5.6. This is well within the pH range where the passive film on aluminum is protective in noncomplexing solutions.[15]

It is argued that the CO_2 effect discovered in the present study has implications for the atmospheric corrosion of aluminum in general. It may be noted that aluminum is susceptible to crevice corrosion. This has been attributed to differential aereation cells.[23] The present results imply that the cause may instead be the limited supply of the corrosion-inhibiting CO_2. Similar effects may be involved in the occurrence of filiform corrosion of aluminum beneath organic coatings.

Conclusions

The most important result of this investigation is the discovery that CO_2 inhibits the NaCl-induced atmospheric corrosion of aluminum. In CO_2-free humid air the corrosion rate is 20 times greater compared to air containing ambient levels of CO_2.

It is suggested that the rapid corrosion of aluminum coated with NaCl in humid CO_2-free air is connected to high pH areas in the surface electrolyte that develop due to the cathodic reduction of oxygen. The anodic dissolution of aluminum is known to be enhanced by high pH. Accordingly, the inhibitive effect of CO_2 is suggested to be due to its acidity. CO_2 neutralizes the hydroxide formed at the cathodic sites with the result that the corrosion rate decreases. This explains the very limited corrosion rates in the presence of CO_2.

The inhibitive effect of ambient levels of CO_2 has important implications for the atmospheric corrosion of aluminum. The present results may contribute toward understanding crevice corrosion and corrosion beneath organic coatings and deposits where the supply of CO_2 is limited. Moreover, these findings may help in designing improved accelerated tests for the atmospheric corrosion of aluminum.

Acknowledgments

The authors thank Volvo Car Corporation for financial support and Norsk Hydro Aluminum for providing the material.

Charles University of Technology assisted in meeting the publication costs of this article.

References

1. T. E. Graedel, *J. Electrochem. Soc.*, **136**, 193 (1989).
2. R. T. Vashi and H. G. Patel, *Bull. Electrochem.*, **13**, 343 (1997).
3. E. Mattson, *CHEMTECH*, **15**, 234 (1985).
4. E. Johansson, KI report 1984:4, Swedish Corrosion Institute.
5. S. S. Butcher, R. J. Charlson, G. H. Orians, and G. V. Wolfe, *Global Biogeochemical Cycles*, Academic Press, Inc., London (1992).
6. T. Falk, J. E. Svensson, and L.-G. Johansson, *J. Electrochem. Soc.*, **145**, 39 (1998).
7. R. Lindström, J. E. Svensson, and L.-G. Johansson, *J. Electrochem. Soc.*, **147**, 1751 (2000).
8. T. E. Graedel, *J. Electrochem. Soc.*, **136**, 204 (1989).
9. T. E. Graedel, *J. Electrochem. Soc.*, **134**, 109 (1987).
10. P. V. Strekalov, *Prot. Met.*, **29**, 673 (1993).
11. J. E. Svensson and L.-G. Johansson, *Corros. Sci.*, **34**, 721 (1993).
12. *Ullmann's Encyclopedia of Chemical Technology*, Vol. A1 p. 538, VCH Verlagsgesellschaft, Weinheim (1985).
13. N. F. Mott, *Trans. Faraday Soc.*, **43**, 429 (1947).
14. N. F. Mott, *J. Chim. Phys.*, **44**, 172 (1947).
15. H. Kaeshe, in *Passivity of Metals*, R. P. Frankenthal and J. Kruger, Editors, p. 935, The Electrochemical Society, Inc., Princeton, NJ (1978).
16. M. Skeldon, K. Shimizu, P. Skeldon, G. E. Thompson, and G. C. Wood, *Corros. Sci.*, **37**, 1473 (1995).
17. W. Vedder and D. A. Vermilyea, *Trans. Faraday Soc.*, **65**, 561 (1969).
18. Z. A. Foroulis and M. J. Thubrikar, *Werkst. Korros.*, **5**, 350 (1975).
19. J. A. Richardson and C. G. Wood, *Corros. Sci.*, **10**, 313 (1970).
20. W. Stumm, *Aquatic Surface Chemistry, Chemical Processes at the Particle-Water Interface*, p. 197, John Wiley & Sons, New York (1987).
21. W. Stumm, *Chemistry of the Solid-Water Interface*, p. 20, John Wiley & Sons, New York (1992).
22. H. Ginsberg, W. Hüttig, and H. Stiehl, *Z. Anorg. Allg. Chem.*, **318**, 238 (1962).
23. U. R. Evans, in *The Corrosion and Oxidation of Metals*, p. 519, Edward Arnold Publishers, Ltd., London (1968).

Paper 2

Carbon Dioxide; The Unknown Factor in The Atmospheric Corrosion of Aluminum?

D. Bengtsson Blücher, J-E. Svensson
and L.- G. Johansson*

Department of Environmental Inorganic Chemistry, Chalmers University of Technology
S-412 96 Göteborg
*Department of Inorganic Chemistry, Göteborg University
e-mail: danielb@chalmers.se
phone: +46317722859
fax:+46317722853

Abstract

The atmospheric corrosion of two aluminum alloys, AA5182 and AA6016, was investigated in the laboratory. The alloys were exposed during four weeks under carefully controlled conditions. Two different concentration of CO_2, ambient (350ppm) and <1ppm, were studied. The relative humidity was 95% and the temperature was 22.0°C. Sodium chloride, (70µg/cm^2) was added to the samples prior to exposure. The corroded samples were analyzed by gravimetry, X-ray diffraction, ion chromatography, environmental scanning electron microscopy and energy dispersive X-ray analysis. The amount of carbonate was determined quantitatively.

The presence of ambient levels of CO_2 decreases the average corrosion rate by a factor of 30 and 7, for AA5182 and AA6016, respectively. However, AA6016 suffers pitting corrosion. In the absence of CO_2 both alloys suffer general corrosion, the corrosion-rate being about the same for AA5182 as for AA6016. The rate of corrosion of commercially pure aluminium (AA1070) is about half of that of the alloys. In the absence of NaCl the corrosion rate is negligible for all alloys investigated.

Keywords: atmospheric corrosion, laboratory study, AA5182, AA6016, NaCl

Introduction

Numerous field investigations indicate that the deposition of SO_2 and chloride and the pH of rain are important factors influencing the corrosion of aluminum in the atmosphere. However, field studies cannot provide detailed knowledge on the corrosion process. Moreover, the influence of other constituents of the atmosphere, such as CO_2, is largely unknown. A detailed knowledge of the atmospheric corrosion of aluminum can only be provided by performing laboratory investigations in controlled environments. Considering the present use and the potential applications of aluminum alloys, e.g., in the automotive industry, the lack of information on the atmospheric corrosion behavior presents a problem. Such information is essential in order to understand the corrosion behavior in the field.

A recent paper by Blücher et al. reports that ambient levels of CO_2 strongly inhibit the NaCl-induced atmospheric corrosion of commercially pure aluminum (AA1070) in humid air at 22°C [1]. The rapid NaCl induced corrosion of aluminum in humid CO_2-free air was attributed to an electrochemical corrosion process where the anodic dissolution of aluminum occurs in alkaline solution, forming soluble aluminate. It was argued that high pH regions

form in the surface (NaCl(aq)) electrolyte due to the cathodic reduction of oxygen. Accordingly, the inhibiting effect of CO_2 was explained by its acidity, neutralizing the hydroxide formed on the cathodes and thereby slowing down or preventing the formation of aluminate.

The aim of this paper is to investigate the effect of CO_2 on the NaCl-induced atmospheric corrosion on Al-Mg and Al-Mg-Si alloys.

Experimental

We report on the effect of ambient levels of CO_2 on the atmospheric corrosion of the cold rolled aluminum alloys AA5182 and AA6016. Commercially pure aluminum, AA 1070, is used as a reference and was studied in a previous paper [1]. Both alloys are used for automotive body panels. The chemical composition of these alloys is found in Table I.

Table I. Elemental composition in % w/w.

Alloy	Si	Fe	Cu	Mn	Mg	Ti	Zn
AA5182	0.2	0.35	0.15	0.2	4.0	0.1	0.25
AA6016	1.0	0.5	0.2	0.2	0.25	0.15	0.2
AA1070	0.04	0.16	0.001	0.002	0.002	0.003	0.006

The samples had a geometrical area of $20cm^2$ (dimensions 30x30x2 mm), polished on SiC paper in ethanol to 1000 mesh and sonicated in ethanol. Exposures were performed at 22.0°C. NaCl was added before exposure by spraying a solution of NaCl in 80/20 ethanol/water. In each experiment, a total of eight samples were exposed. To avoid interactions between samples, each sample is exposed in a chamber of its own. Four AA5182 and four AA6016 were pre-treated with 70µg $NaCl/cm^2$. The distribution of salt on the surface was even. The amount of sodium chloride added in this study (equivalent to 550 µg Cl^- cm^{-2} y^{-1}) correspond to chloride deposition rates in urban areas and to marine environments not in the immediate vicinity of the coastline [2-4].

The exposures in the presence of CO_2 were carried out in flowing purified air with a precise control of humidity and CO_2 concentrations. Pure CO_2 was added from a gas bottle and a CO_2-analyzer was used to monitor the concentration. The relative humidity was 95 % ± 0.3 %. Gas flow was 1000 ml/min, (gas velocity 7 mm/s). The exposures in the absence of CO_2 were performed using a hermetically closed glass container filled with air. The samples were suspended inside the 3.5 dm^3 container. Beneath the samples there was $0.1dm^3$ of 1.6M NaOH(aq) which is in equilibrium with 95% RH air. The NaOH solution getters CO_2, ascertaining that the concentration of CO_2 during exposure is <1ppm. The container temperature was controlled to within 0.1°C.The samples exposed to CO_2-containing were weighed once a week. The samples exposed in CO_2-free air were only weighed after exposure to avoid absorption of CO_2. The dry mass gain was determined after storing one week over a desiccant. Water-soluble corrosion products and NaCl were removed by leaching in pure water (pH 7) for 5+30 minutes at 25°C. The corrosion rate was determined from the metal loss after exposure. The metal loss was determined by pickling in a solution of 50 ml H_3PO_4 (85%) and 20.0 g CrO_3/dm^3 in 1000ml water for 2x8 minutes at 80°C. Ultrasonic agitation was used in leaching and pickling. The "self corrosion" during corrosion product removal was negligible. Carbonate in the corrosion product was determined by immersing the samples in 1M $HClO_4$(aq) in a three-necked flask. The treatment quantitatively converts carbonate to

carbon dioxide. A stream of 300 ml/min of nitrogen is used to expel the carbon dioxide from the solution and carry it to the CO_2 analyzer (Binos 100). The sensitivity of this analysis corresponds to $10x10^{-9}$mol CO_2/sample. By introducing weighed amounts of $BaCO_3$(s) into the system, the precision of the analysis was found to be ± 2%. Water-soluble chloride leached from the samples was determined by Ion Chromatography, IC, (Ionpac AD9-SC Analytical Column). Crystalline corrosion products were analyzed using a Siemens D5000 powder X-ray diffractometer (CuK_α radiation) with a grazing incidence beam attachment and a Göbel mirror. The samples were also studied by Environmental Scanning Electron Microscopy, ESEM (Electroscan 2020) equipped with an Energy Dispersive X-ray detector, EDX (Link ISIS). The macroscopic appearance of the exposed surfaces was studied using a Zeiss Optical Microscope with a CCD-camera.

Results

<1ppm CO_2

After exposure both alloys appeared dry. The sample surface was completely covered by grey corrosion products, see optical microscopy images in Fig 1a and 1b. In the case of alloy 5182, small white crusts were visible to the naked eye. Figure 2 shows ESEM images of AA 5182 and AA6016. The spool-formed 5-10 µm long crystals are typical of bayerite, α-$Al(OH)_3$ see Fig. 2 a and b. After removing the corrosion products investigation by optical microscopy showed that all of the metal surface was corroded. The maximum surface roughness of the corroded metal was about 10µm.

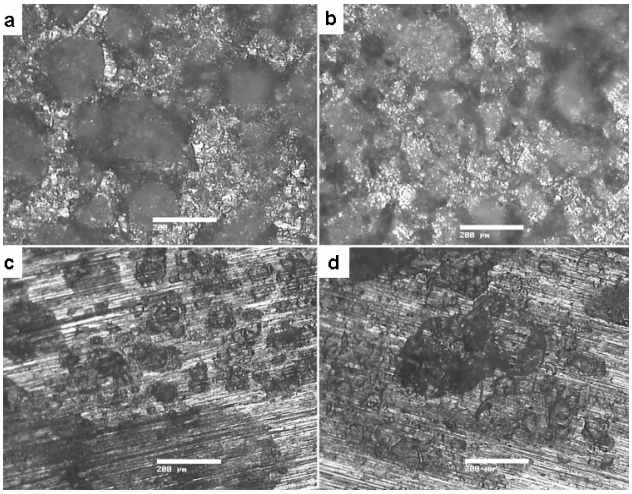

Fig. 1
Optical Microscopy images of aluminum exposed to <1 ppm CO_2 (top row) and 350 ppm CO_2 (bottom row) at 22°C for 4 weeks at 95% RH. AA5182 (a, c) and AA6016 (b, d). The amount of NaCl was 70µg/cm^2. The bars correspond to 400µm.

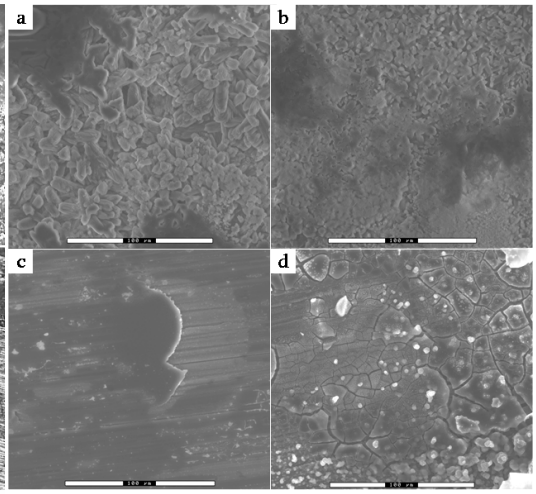

Fig. 2
ESEM images of aluminum exposed to <1 ppm CO_2 (top row) and 350 ppm CO_2 (bottom row) at 22°C for 4 weeks at 95% RH. AA5182 (a, c) and AA6016 (b, d). The amount of NaCl was 70µg/cm^2. The bars correspond to 100µm.

Table II presents the corrosion rate in the absence and in the presence of CO_2. The strong corrosion-inhibitive effect of CO_2 is evident. The corrosion rate in the absence of CO_2 is about the same for AA5182 as for AA6016. The rate of corrosion of commercially pure

aluminium (AA1070) is about half of that of the alloys. In the absence of NaCl the corrosion rate is negligible for all alloys investigated.

Table II. Corrosion rate and corrosion-product ratios at 22.00ºC.

Alloy	Concentration CO_2 (ppm)	NaCl (μg/cm^2)	Dry mass gain (mg/cm^2)	Corrosion product mass/metal loss	Metal loss (mg/cm^2)	Calculated average corrosion rate (μm•yr^{-1})
AA5182	<1	70	1.71	2.9	**0.88**	42
AA5182	350	70	0.06	3.2	**0.03**	1
AA6016	<1	70	1.56	2.9	**0.80**	39
AA6016	350	70	0.22	2.9	**0.12**	6
AA1070[#]	<1	70	0.96	3.0	**0.48**	23
AA1070[#]	350	70	0.04	n.a.	**0.02**[1]	1

The exposure time was four weeks and RH was 95%. The scatter in mass gain and metal loss results was about ±5%.
[1]) Calculated metal loss assuming that only $Al(OH)_3$ forms
[#]) Previous results [1]

The sum of the metal loss and mass gain represents the corrosion product mass. Dividing the corrosion product mass by the metal loss gives a ratio that is a measure of the corrosion product composition. Corresponding ratios for selected corrosion products are presented in Table III.

Table III. Molar mass divided by metal mass for selected corrosion products of aluminum.

Product	Formula	Ratio [a]
Aluminum oxide	γ-Al_2O_3	1.89
Akdalait	$Al_2O_3 \cdot 1/4H_2O$	1.97
Boehmite	γ-AlOOH	2.22
Pseudoboehmite	$Al_2O_3 \cdot 2H_2O$	2.55
Bayerite	α-$Al(OH)_3$	2.89
Gibbsite (Hydrargillite)	γ-$Al(OH)_3$	2.89
Tucanite	$Al(OH)_3 \cdot 1/2H_2O$	3.22
Aluminum chloride hydrate	$Al(H_2O)_6Cl_3$	5.00
Dawsonite	$NaAlCO_3(OH)_2$	4.48
Cadwaladerite	$AlCl(OH)_2 \cdot 6H_2O$	6.26
Brucite	$Mg(OH)_2$	2.40
Hydromagnesite	$Mg_5(CO_3)_4(OH)_2 \cdot 4H_2O$	3.85
Dypingite	$Mg_5(CO_3)_4(OH)_2 \cdot 8H_2O$	4.44
Korshunovskite	$Mg_2Cl(OH)_3 \cdot 4H_2O$	3.53

[a]In order to simplify a comparison with the corresponding values in Table II, the sodium and chloride masses were omitted when these ratios were calculated.

The corrosion product ratio found for the NaCl-treated alloy samples (AA5182 and AA6016) is close to that of $Al(OH)_3$, see Tables II and III. The only crystalline corrosion product detected by XRD was bayerite, α-$Al(OH)_3$ (compare Fig 2).

350ppm CO_2

Fig. 3 shows mass gain as a function of exposure time. The rapid initial mass gain reflects the formation of NaCl(aq). Putting the activity coefficients of Na^+(aq), Cl^-(aq) and H_2O(l) equal to one, the solution is calculated to contain 11.66 g water per gram of NaCl at equilibrium. The absorption of water vapor to form a NaCl(aq) solution on the sample surface occurred rapidly in all environments studied, the samples becoming visibly wet directly upon exposure.

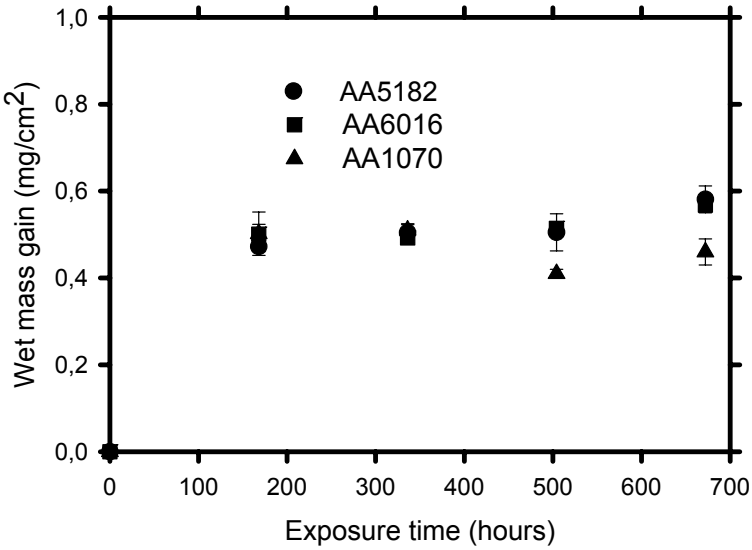

Figure 3. Mass gain as a function of exposure time for aluminum samples exposed to 350 ppm CO_2 at 22°C with 70µgNaCl/cm^2. The RH was 95%.

In comparison to the samples exposed in the absence of CO_2, the CO_2-exposed samples had much more electrolyte after completed exposure (0.05-0.1mg/cm^2 and 0.5mg/cm^2, respectively). To the naked eye, AA5182 appeared wet throughout the exposure. In contrast, AA6016 was not visibly wet after exposure. This difference is attributed to the different amounts of corrosion product present (see Table II).

After exposure to CO_2 containing air, about 50% of the sample surface was covered by corrosion product crusts. The rest of the sample surface appeared unaffected by corrosion, see Fig 1c, d and 2c, d. In the case of AA5182, the crusts were brownish and had a diameter of about 2mm (compare Fig 1c). On AA6016 the corrosion product crusts were white. After removing the corrosion products, pits could be seen underneath the crusts. The average pit depth was far greater on AA6016 (40µm) compared to AA5182 (3µm). This may be compared to AA1070 where the pit depth in a corresponding exposure was about 2µm [1]. The calculated average corrosion rate of AA6016 in our experiment corresponds to 6µm•yr^{-1}. See Table II. This is about six times the corrosion rate of commercially pure aluminum and about four times that of AA5182.

No bayerite formed in the presence of CO_2. The only crystalline corrosion product revealed by XRD was dawsonite ($NaAlCO_3(OH)_2$) which was identified on AA6016. Unreacted NaCl was found on all samples exposed to CO_2. The amount of carbonate in the corrosion products after exposure of AA5182 and AA6016, was 0.096 and 0.62 µmol/cm^2, respectively. This may be compared to the amount of NaCl added (1.2µmol/cm^2).

Discussion

Because NaCl forms an aqueous solution at high relative humidity, the NaCl-induced atmospheric corrosion of aluminum in humid air may be described as a form of aqueous

corrosion. Aluminum is known to corrode by an electrochemical mechanism in aqueous solution. The corrosion resistance of aluminum relies on the formation of an electrically insulating and relatively inert oxide film. In neutral and alkaline solution the anodic dissolution of aluminum is described by two coupled reactions while the cathodic reaction is considered to be oxygen reduction [5]:

$$Al + 3OH^- \rightarrow Al(OH)_3(s) + 3e^- \quad (1)$$

$$Al(OH)_3(s) + OH^-(aq) \rightarrow Al(OH)_4^-(aq) \quad (2)$$

$$1/2O_2 + H_2O + 2e^- \rightarrow 2OH^- \quad (3)$$

Several workers report that the cathodic reaction occurs on "flaws" in the oxide, i.e., at grain boundaries or noble inclusions in the alloy. The inclusions include intermetallic phases such as $Al_6(Mn,Fe)$, Al_8Mg_5, Mg_2Si or $Al_3(Fe,Mn)$ and only make up a small fraction of the surface [6-8]. In an unbuffered solution, the dissolution of the passive layer is enhanced at the cathodic sites because of the formation of hydroxide (3). This means that the anodic and cathodic reactions both occur at the same site. The anodic reaction also proceeds over the rest of the surface, although at a slower rate [8].

Chloride ions in neutral aqueous solutions are known to cause pitting corrosion of aluminum. According to Kaesche, pitting is initiated through the adsorption of, e.g., chloride ions on the alumina surface, resulting in the dissolution of the passive film [5]. However, chloride is not an efficient corrosion promoter for aluminum corrosion at high pH because the negative surface charge of alumina at high pH makes chloride adsorption unfavorable [9]. At high pH the anodic reaction is promoted by the formation of soluble aluminate (see reaction (2)), resulting in general corrosion rather than pitting [5].

It was recently reported that the NaCl-induced atmospheric corrosion of aluminum (AA1070) is very rapid in the absence of CO_2 at 22°C. The average rate of NaCl-induced atmospheric corrosion of aluminum at 22°C in CO_2-free humid air was about 20 times that in air containing ambient levels of CO_2 [1]. It was concluded that the corrosion attack involved alkaline dissolution of the passive film (see reaction (2)). It was argued that high pH regions develop in the surface electrolyte due to the cathodic reduction of oxygen. The slowing down of the corrosion of NaCl-coated aluminum in humid air by CO_2 was suggested to be due to its acidity, counteracting the development of high pH in the surface electrolyte by forming carbonate and hydrogen carbonate.

The present study shows that the inhibition of the general corrosion of aluminium in the presence of sodium chloride by CO_2, reported for commercially pure aluminium (AA1070), is also effective for Al-Mg and Al-Mg-Si alloys. The presence of ambient levels of CO_2 decreases the average corrosion rate by a factor of 30 and 7, for AA5182 and AA6016, respectively. In the absence of CO_2, the average corrosion rate of the two alloys is about twice as high compared to commercially pure aluminium. It is suggested that this is due to the higher concentration of intermetallic inclusions, increasing the cathodic area.

If the inhibitive effect of CO_2 on the general corrosion of aluminium in the presence of NaCl is due to its acidity, one may suspect that aluminium may become susceptible to chloride-induced pitting corrosion because of the lower pH values that prevail in the electrolyte in the presence of CO_2. The pitting corrosion of aluminium in an unbuffered chloride solution is

described by Wranglén [10]. According to Wranglén, cations (e.g. Na^+) accumulate at the cathodic sites (noble metallic inclusions at the surface) due to migration. By the same mechanism chloride ions accumulate at the anodic sites, resulting in the formation of an acidic aluminium chloride solution and pit formation [10]. The anodic dissolution of aluminium occurs in acidic solution:

$$Al(s) \rightarrow Al^{3+}(aq) + 3e^- \qquad (4)$$

A pH gradient is established between the cathodic sites and the bottom of the pits. At an intermediate pH range aluminium hydroxide precipitates, forming corrosion product crusts on top of the pits. The chloride in the pit solution is not consumed because there are no insoluble aluminium hydroxyl chlorides.

In the presence of CO_2, the NaCl-induced corrosion of the Al-Mg alloy AA5182 resembles that of commercially pure aluminium (AA1070). Pit formation occurs but pit depth is very small (2-3 μm). In contrast, the Al-Mg-Si alloy AA6016 exhibits much deeper pits (40μm). In the case of AA6016, ESEM/EDX showed that chloride is concentrated at the bottom of the pits while sodium is enriched on the uncorroded part of the surface. The development of deep pits and the elemental distribution suggest that Wranglén's mechanism is valid for the NaCl-induced atmospheric corrosion of AA6016 in the presence of CO_2. It may be noted that the average corrosion rate is much lower than in the absence of CO_2. However, as the former corrosion type results in pitting, NaCl-induced corrosion in the presence of CO_2 may still give rise to serious corrosion problems of this alloy. The identification of dawsonite on AA6016 after exposure to CO_2 in the presence of NaCl is in accordance with a recent paper by Le Bozec et al. [11].

Our results imply that Wranglén's pitting mechanism is effective on AA6016 in the presence of NaCl and CO_2, while it is not active on AA5182 and AA1070 [1]. The greater susceptibility of AA6016 to pitting corrosion in comparison to AA5182 is in accordance with the corrosion behaviour of the two alloy types (6XXX and 5XXX) in neutral chloride solution [12, 13]. In the presence of a stronger acid (e.g. H_2SO_4, formed by the deposition and oxidation of atmospheric SO_2) it is expected that AA5182 and AA1070 will also suffer this type of corrosion attack.

The present paper shows the importance of ambient concentrations of CO_2 for the atmospheric corrosion behaviour of aluminium alloys in the presence of soluble chlorides. In the absence of CO_2 the two alloys suffer rapid general corrosion. In the presence of CO_2, general corrosion is insignificant. However, chloride-induced pitting corrosion becomes an issue with AA6016. Alloy AA5182, is much less susceptible to this corrosion type.

Conclusions

This paper shows the strong corrosion-inhibitive effect of CO_2 towards the atmospheric corrosion of aluminium in the presence of NaCl. Ambient levels of CO_2 decreases the average corrosion rate by a factor of 30 and 7, for AA5182 and AA6016, respectively. In the absence of CO_2 the two alloys suffer rapid general corrosion. In the presence of CO_2, general corrosion is insignificant. Instead, AA6016 experience rapid pitting corrosion. In comparison, AA5182 appears much less susceptible to pitting in this environment. The inhibition by CO_2 of the general corrosion of Al alloys in the presence of NaCl is attributed to the neutralization of the hydroxide formed at the cathodes. The inhibitive effect of CO_2 may be relevant to, for

example, crevice corrosion and corrosion beneath organic coatings. In comparison to commercially pure aluminum, the corrosion rate of Al-Mg and Al-Mg-Si alloys is higher in all environments studied.

Acknowledgement

The authors would like to express their gratitude to Volvo Car Corporation and to the Swedish Research Council for financial support.

References

[1] D. B. Blucher, R. Lindstrom, J. E. Svensson, and L. G. Johansson, *J. Electrochem. Soc.*, **148**, B127, (2001).
[2] T. E. Graedel, *J. Electrochem. Soc.*, **136**, 193C, (1989).
[3] V. Kucera and E. Mattsson, in *Atmospheric corrosion*, ed. F. Mansfield, New York, (1987).
[4] P. V. Strekalov, *Zashch. Met.*, **29**, 819, (1993).
[5] H. Kaesche, *Passivity Met., Proc. Int. Symp., 4th*, 935, (1978).
[6] Y. W. Keuong, J. H. Nordlien, and K. Nisancioglu, *Journal of the Electrochemical Society*, **148**, B497, (2001).
[7] J. A. Richardson and G. C. Wood, *Corros. Sci.*, **10**, 313, (1970).
[8] W. Vedder and D. A. Vermilyea, *Trans. Faraday Soc.*, **65**, 561, (1969).
[9] W. Stumm and Editor, in Aquatic Surface Chemistry: Chemical Processes at the Particle-Water-Interface, 1987.
[10] G. Wranglen, *An Introduction to Corrosion and Protection of Metals* 1972).
[11] N. Le Bozec, D. Persson, A. Nazarov, and D. Thierry, in *Corrosion and Corrosion Protection*, J. D. Sinclair, M. W. Kendig, W. Plieth, W. H. Smyrls, Editors PV 200-22, p. 900, The Electrochemical Society Proceedings Series, Pennington, NJ (2001)
[12] R. B. Leggat and S. R. Taylor, *Corrosion (Houston)*, **55**, 984, (1999).
[13] B. A. Shaw, M. M. McCosby, A. M. Abdullah, and H. W. Pickering, *Jom*, **53**, 42, (2001).

Paper 3

Journal of The Electrochemical Society, **150** (3) B93-B98 (2003)
0013-4651/2003/150(3)/B93/6/$7.00 © The Electrochemical Society, Inc.

The NaCl-Induced Atmospheric Corrosion of Aluminum

The Influence of Carbon Dioxide and Temperature

D. Bengtsson Blücher,[a,*,z] J.-E. Svensson,[a,*] and L. G. Johansson[b,*,z]

[a]*Department of Environmental Inorganic Chemistry, Chalmers University of Technology, S-412 96 Göteborg, Sweden*
[b]*Department of Inorganic Chemistry, Göteborg University, S-412 96 Göteborg, Sweden*

Samples were exposed to purified air with 95% RH and <1 or 350 ppm CO_2 in the presence (70 or 14 $\mu g/cm^2$) or in the absence of NaCl. Temperature was 4, 10, 22, 38, 50, and 60°C. Samples were analyzed by gravimetry, X-ray diffraction, ion chromatography and environmental scanning electron microscopy/energy dispersive X-ray analysis. The two main results are the strong, nonlinear temperature dependence of corrosion and the inhibitive effect of CO_2 at ambient temperature. NaCl-treated aluminum corrodes rapidly in humid CO_2-free air because high pH areas develop due to the cathodic reduction of oxygen. This results in an enhanced anodic dissolution of aluminum. The inhibitive effect of CO_2 is attributed to its acidity. CO_2 neutralizes the hydroxide formed with the result that the corrosion rate decreases.
 [DOI: 10.1149/1.1545456]

Manuscript received January 31, 2002. This was Paper 525 presented at the Electrochemical Society Meeting, San Francisco, CA, Sept 2-7, 2001. Available electronically February 5, 2003.

The corrosion of aluminum in the atmosphere has mainly been investigated through field studies.[1-3] Few laboratory investigations in controlled environments have been published. Based on field investigations and using information from the corrosion behavior of aluminum in aqueous solution, it is generally agreed that, besides strong humidity dependence, the deposition of SO_2 and chloride are major factors that determine the corrosion rate of aluminum.

The levels of particulate chloride deposition reported in the literature cover a very wide range; 15 $\mu g\ Cl^-\ cm^{-2}\ y^{-1}$ is reported in rural areas far from the coast,[4] 60 $\mu g\ Cl^-\ cm^{-2}\ y^{-1}$ was reported for metropolitan New York,[5] while deposition rates of over 55,000 $\mu g\ Cl^-\ cm^{-2}\ y^{-1}$ have been found in extreme marine environments.[4,6]

The atmospheric corrosion of aluminum in the presence of an electrolyte such as NaCl(aq) is considered to be a special case of corrosion in aqueous solution. In contrast to bulk aqueous solutions, convection in the solution is insignificant in atmospheric corrosion, and the corrosion products tend to remain where formed unless they are leached by rain, etc. The diffusion paths for, *e.g.*, oxygen molecules are short so that the oxygen supply is usually not rate-limiting for the cathodic reaction.

Carbon dioxide occurs naturally in the atmosphere with a concentration of about 350 ppm.[7] However, the influence of CO_2 on atmospheric corrosion has not received much attention. In a recent paper by Blücher *et al.* it was reported that ambient levels of CO_2 strongly inhibits the NaCl-induced atmospheric corrosion of aluminum in humid air at 22°C.[8] Similar results have been reported for the atmospheric corrosion of zinc by Falk *et al.*[9] and Lindström *et al.*[10] The rapid NaCl-induced corrosion of aluminum in humid CO_2-free air was attributed to an electrochemical process with the anodic dissolution of aluminum occurring in alkaline solution, forming soluble aluminate. The inhibiting effect of CO_2 was attributed to its acidity, neutralizing the hydroxide formed at the cathodes thereby preventing the formation of aluminate.

The paper by Blücher *et al.*[8] is the starting point for the present study that investigates the effect of temperature on the NaCl-induced atmospheric corrosion of aluminum. The previously overlooked effect of CO_2 may help the understanding of the corrosion behavior of aluminum in cases where there is a limited supply of CO_2, for example in crevices and beneath coatings. Information on the influence of temperature is useful for interpreting accelerated corrosion tests and for predicting the atmospheric corrosion of aluminum in different climates.

Experimental

The samples were made from aluminum, AA 1070 (99.769% Al see Table I) (dimensions 30 × 30 × 2 mm), polished on SiC paper in ethanol to 1000 mesh and sonicated in ethanol. Exposures were performed at 4, 10, 22, 38, 50, and 60°C. NaCl was added before exposure by spraying a solution of NaCl in 80/20 ethanol/water. In each experiment, a total of eight samples were exposed. Two samples were not treated with NaCl and were used as references. 14 $\mu g/cm^2$ of NaCl was added to three of the samples, while 70 $\mu g/cm^2$ was added to another three samples. The distribution of salt on the surface was even. The amount of sodium chloride added in this study (equivalent to 110 and 550 $\mu g\ Cl^-\ cm^{-2}\ y^{-1}$, respectively) correspond to chloride deposition rates in urban areas and to marine environments not in the immediate vicinity of the coastline (see introduction).

The exposures in the presence of CO_2 were carried out in flowing purified air with a very precise control of humidity and CO_2 concentrations. Pure CO_2 was added from a gas bottle, and a CO_2 analyzer was used to monitor the concentration. For details of the apparatus used at 4 and 22°C, see a previous paper.[8] Relative humidity (RH) was 95 ± 0.3%. Gas flow was 1000 mL/min, (gas velocity, 7 mm/s). In the exposures in the presence of CO_2 at 38, 50, and 60°C an alternative setup was used in which the humidifier, the exposure chambers, and the gas pipes were immersed in a temperature-controlled water tank. The exposures in the absence of CO_2 were performed using a hermetically closed glass container filled with air. The samples were suspended inside the 3.5 dm^3 container. Beneath the samples there was 0.1 dm^3 of 1.6 M NaOH(aq) which is in equilibrium with 95% RH air. The NaOH solution getters CO_2, ascertaining that the concentration of CO_2 during exposure is <1 ppm. The container temperature was controlled to within 0.2°C. It was previously shown that exposures in this apparatus produced results identical to those obtained in flowing CO_2-free air using the setups described above.[10]

Table I. Elemental composition of AA1070 in % w/w.

Si	Fe	Cu	Mn	Mg	Ti	Zn	Al
0.04	0.16	0.001	0.002	0.002	0.003	0.006	99.769

* Electrochemical Society Active Member.
z E-mail: danielb@inoc.chalmers.se

Table II. Corrosion rate and corrosion-product ratios at 4°C.

Concentration CO_2 (ppm)	NaCl ($\mu g/cm^2$)	Dry mass gain (mg/cm^2)	Corrosion product mass/metal loss	Metal loss (mg/cm^2)
<1	0	0	[a]	[a]
<1	14	0.01	n.a.	0.005[b]
<1	70	0.01	n.a.	0.005[b]
350	0	0	[a]	[a]
350	14	0.01	n.a.	0.005[b]
350	70	0.02	n.a.	0.01[b]

The exposure time was four weeks and RH was 95%. The scatter in mass gain and metal loss results was about ±5%.
[a] The mass changes were too small for metal-loss determination.
[b] Calculated metal loss assuming that only $Al(OH)_3$ forms.

The samples exposed to CO_2-containing air at 4 and 22°C were weighed once a week. The samples exposed in CO_2-free air were only weighed after exposure to avoid absorption of CO_2. The dry mass gain was determined after storing one week over a desiccant. Water-soluble corrosion products and NaCl were removed by leaching in pure water (pH 7) for 1 + 2 + 30 + 30 min at 25°C. The samples were then pickled in a solution of 50 mL H_3PO_4 (85%) and 20.0 g CrO_3/dm^3 in 1000 mL water for 3 × 5 min at 80°C. Ultrasonic agitation was used in leaching and pickling. The self-corrosion during corrosion product removal was corrected for. Metal losses could be determined only when the dry mass gains exceeded 0.10 mg/cm^2.

Water-soluble chloride leached from the samples was determined by ion chromatography (IC, Ionpac, AD9-SC analytical column).

Carbonate on the samples was determined by decomposing the carbonate in acid and by thermal desorption. In the former case, the samples were treated with 1 M $HClO_4$(aq) in a three-necked flask. Immersing the samples in the acid quantitatively converts carbonate to carbon dioxide. A stream of 300 mL/min of nitrogen is used to expel the carbon dioxide from the solution and carry it to the CO_2 analyzer (Binos 100). The sensitivity of this analysis corresponds to 10×10^{-9} mol CO_2/sample. By introducing weighed amounts of $BaCO_3$(s) into the system, the precision of the analysis was found to be ±2%. The thermal desorption analysis for carbonate involved suspending the samples in a heated flow reactor which was purged by a stream of dry N_2(g). A thermocouple was put in contact with the sample. The heating rate was 5°C/min. The same CO_2 analyzer was used as in the acid decomposition analysis, and the sensitivity of the analysis was also the same.

Crystalline corrosion products were analyzed using a Siemens D5000 powder X-ray diffractometer (Cu Kα radiation) with a grazing incidence beam attachment and a Göbel mirror. The samples were also studied by environmental scanning electron microscopy, (ESEM, Electroscan 2020) with an energy dispersive X-ray detector (EDX, Link ISIS).

Table III. Corrosion rate and corrosion-product ratios at 10°C.

Concentration CO_2 (ppm)	NaCl ($\mu g/cm^2$)	Dry mass gain (mg/cm^2)	Corrosion product mass/metal loss	Metal loss (mg/cm^2)
<1	0	0	[a]	[a]
<1	14	n.a	n.a	n.a
<1	70	0.12	2.7	0.07

The exposure time was four weeks and RH was 95%. The scatter in mass gain and metal loss results was about ±5%.
[a] The mass changes were too small for metal-loss determination.

Table IV. Corrosion rate and corrosion-product ratios at 22°C.

Concentration CO_2 (ppm)	NaCl ($\mu g/cm^2$)	Dry mass gain (mg/cm^2)	Corrosion product mass/metal loss	Metal loss (mg/cm^2)
<1	0	0.01	n.a.	0.005[a]
<1	14	0.24	3.0	0.12
<1	70	0.96	3.0	0.48
350	0	0.01	n.a.	0.005[a]
350	14	0.02	n.a.	0.01[a]
350	70	0.04	n.a.	0.02[a]

The exposure time was four weeks and RH was 95%. The scatter in mass gain and metal loss results was about ±5%.
[a] Calculated metal loss assuming that only $Al(OH)_3$ forms.

Results

No NaCl additions.—In the absence of NaCl, aluminum corrosion was very slow at all temperatures (see Table II-VII). For samples exposed in CO_2-free air, the corrosion rate tends to increase with temperature. No crystalline corrosion products were found on the samples exposed in the absence of NaCl, and the metal losses were too small to be determined directly.

70 μg NaCl/cm² 4°C, <1 ppm and 350 ppm CO_2.—The corrosion of NaCl-treated samples at 4°C in CO_2-free air was very slight (see Table II). A rapid initial mass gain was registered, reflecting the formation of NaCl(aq). Putting the activity coefficients of Na^+(aq), Cl^-(aq), and H_2O(1) equal to one, the solution is calculated to contain 11.66 g water per gram of NaCl at equilibrium. The absorption of water vapor to form a NaCl(aq) solution on the sample surface occurred rapidly in all environments studied, the samples becoming visibly wet directly upon exposure. Examination with optical microscope, ESEM, and XRD after exposure showed the presence of NaCl(s) and no signs of corrosion (see Fig. 1a). In fact, NaCl(s) was detected after all exposures reported here, excepting the ones at 60°C. Within the accuracy of the IC analysis (±2%), almost all of the applied NaCl was removed by leaching in water after exposure.

10°C, <1 ppm CO_2.—The corrosion rate of the NaCl-treated samples at 10°C is about one order of magnitude greater than at 4°C (see Table II and III). In this case the metal loss could be determined directly. The sum of the metal loss and mass gain represents the corrosion product mass. Dividing the corrosion product mass by the metal loss gives a ratio that is a measure of the corrosion product composition. Corresponding ratios for selected corrosion products are presented in Table VIII. The corrosion product ratio found for the NaCl-treated samples is close to that of $Al(OH)_3$ (compare

Table V. Corrosion rate and corrosion-product ratios at 38°C.

Concentration CO_2 (ppm)	NaCl ($\mu g/cm^2$)	Dry mass gain (mg/cm^2)	Corrosion product mass/metal loss	Metal loss (mg/cm^2)
<1	0	0.01	n.a	0.005[a]
<1	14	0.33	2.8	0.18
<1	70	1.15	2.9	0.61
350	0	0.01	n.a	0.005[a]
350	14	0.11	2.8	0.06
350	70	0.23	2.9	0.12

The exposure time was four weeks and RH was 95%. The scatter in mass gain and metal loss results was about ±5%.
[a] Calculated metal loss assuming that only $Al(OH)_3$ forms.

Table VI. Corrosion rate and corrosion-product ratios at 50°C.

Concentration CO_2 (ppm)	NaCl ($\mu g/cm^2$)	Dry mass gain (mg/cm^2)	Corrosion product mass/metal loss	Metal loss (mg/cm^2)
<1	0	0.03	n.a	0.02[a]
<1	14	0.37	2.9	0.19
<1	70	1.17	3	0.59
350	0	0.02	n.a	0.01[a]
350	14	0.26	3	0.13
350	70	0.60	2.9	0.32

The exposure time was four weeks and RH was 95%. The scatter in mass gain and metal loss results was about ±5%.
[a] Calculated metal loss assuming that only $Al(OH)_3$ forms.

Table II and III). In accordance, bayerite [α-$Al(OH)_3$], was identified by XRD. In all exposures where the metal loss was large enough to be determined, (10-60°C, <1 ppm CO_2; 38-60°C, 350 ppm CO_2) (see Table III-VII) the corrosion product composition corresponded to $Al(OH)_3$ and bayerite was identified by XRD. Similarly to the exposures at 4°C, the NaCl-treated samples at 10°C appeared wet throughout exposure. Scratches from polishing that were visible in the optical microscope after exposure at 4°C were obscured by the formation of corrosion products at 10°C. The ESEM image in Fig. 1a shows corrosion products on the sample surface.

22°C, <1 ppm CO_2, and 350 ppm.—The atmospheric corrosion of NaCl-treated aluminum at 22°C was investigated in a previous paper.[8] In the present study the exposures at 22°C were repeated. The corrosion rates were the same as previously reported. Additional information (ESEM cross section analysis and new determinations of the carbonate content in the corrosion products) relating to 22°C is presented here. The presence of CO_2 had a tremendous effect on the NaCl-induced corrosion of aluminum at 22°C (compare Fig. 1a and Table IV). The corrosion rate in the absence of CO_2 was twenty times faster compared to when CO_2 was present. Figure 2 shows an ESEM cross section of a 10 μm thick corrosion product crust on a NaCl-treated sample exposed in the absence of CO_2. EDX analysis revealed that chloride is enriched at the hydroxide/metal interface while sodium is distributed throughout the hydroxide matrix. Spool-formed crystals, cut through during sectioning, can be seen on the sample surface. The morphology is typical of bayerite. Between crusts the corrosion product layer is about 5 μm thick while the elemental distribution of Na and Cl is similar to that in the crusts. In contrast, NaCl-treated samples exposed in the presence of CO_2 did not develop corrosion product crusts and the corrosion product layer was much thinner.

Table VII. Corrosion rate and corrosion-product ratios at 60°C.

Concentration CO_2 (ppm)	NaCl ($\mu g/cm^2$)	Dry mass gain (mg/cm^2)	Corrosion product mass/metal loss	Metal loss (mg/cm^2)
<1	0	0.06	n.a	0.03[b]
<1	14	0.46	2.9	0.24
<1	70	0.90	3	0.45
350	0	0	[a]	[a]
350	14	0.40	2.8	0.22
350	70	0.75	3	0.38

The exposure time was four weeks and RH was 95%. The scatter in mass gain and metal loss results was about ±5%.
[a] The mass changes were too small for metal-loss determination.
[b] Calculated metal loss assuming that only $Al(OH)_3$ forms.

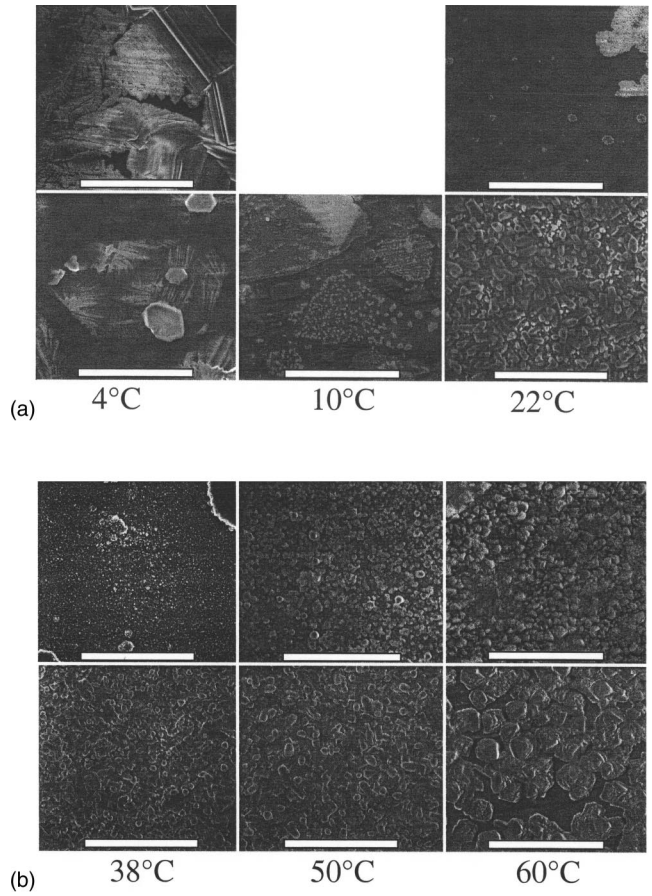

Figure 1. (a) ESEM images of aluminum exposed to 350 ppm CO_2 (top row) and to <1 ppm CO_2 (bottom row) at 4-22°C for 4 weeks at 95% RH. The amount of NaCl was 70 $\mu g/cm^2$. The bars correspond to 100 μm. (b) ESEM images of aluminum exposed to 350 ppm CO_2 (top row) and to <1 ppm CO_2 (bottom row) at 38-60°C for 4 weeks at 95% RH. The amount of NaCl was 70 $\mu g/cm^2$. The bars correspond to 100 μm.

In the presence of 350 ppm CO_2, the amount of carbonate found in the corrosion products using acid desorption after one and four weeks exposure was 0.08 and 0.23 $\mu mol/cm^2$, respectively. The amount of carbonate found may be compared to the amount of aluminum in the corrosion product (0.60 and 1.10 $\mu mol/cm^2$, respectively) and the amount of NaCl added (1.2 $\mu mol/cm^2$). No crystalline aluminum hydroxy carbonates were found. Heating the samples

Table VIII. Molar mass divided by metal mass for selected corrosion products of aluminum.

Product	Formula	Ratio[a]
Aluminum oxide	γ-Al_2O_3	1.89
Akdalait	$Al_2O_3 \cdot 1/4H_2O$	1.97
Boehmite	γ-AlOOH	2.22
Pseudoboehmite	$Al_2O_3 \cdot 2H_2O$	2.55
Bayerite	α-$Al(OH)_3$	2.89
Gibbsite (Hydrargillite)	γ-$Al(OH)_3$	2.89
Tucanite	$Al(OH)_3 \cdot 1/2H_2O$	3.22
Aluminum chloride hydrate	$Al(H_2O)_6Cl_3$	5.00
Dawsonite	$NaAlCO_3(OH)_2$	4.48
Cadwaladerite	$AlCl(OH)_2 \cdot 6H_2O$	6.26

[a] In order to simplify a comparison with the corresponding values in Table II-VII, the sodium and chloride masses was omitted when these ratios were calculated.

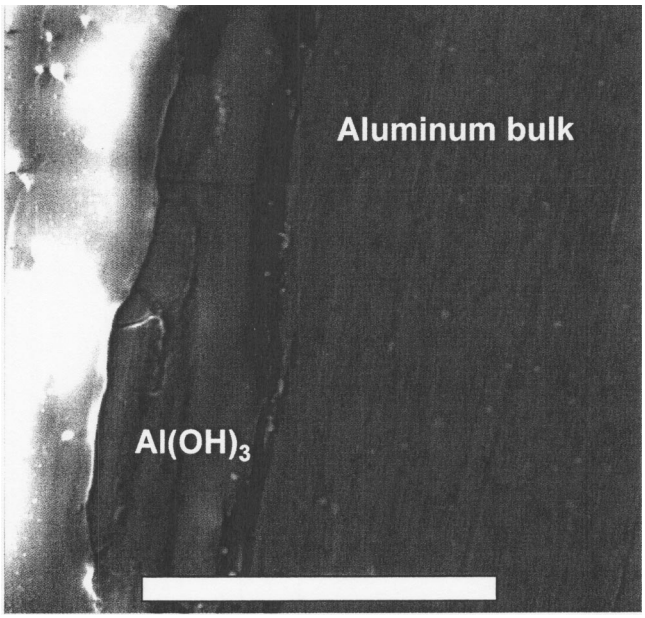

Figure 2. Cross-sectional ESEM of a corrosion product crust on a NaCl-treated sample exposed to 22°C with <1 ppm CO_2. The exposure time was 4 weeks at 95% RH. The amount of NaCl was 70 μg/cm^2. The bar corresponds to 20 μm.

in the thermal desorption cell resulted in a CO_2 peak at 130 ± 10°C, presumably corresponding to the decomposition of $NaHCO_3$. In addition, there was a broad continuum in the range 180-400°C with the maximum CO_2 desorption occurring at about 260°C. This feature may be due to CO_2 adsorbed on aluminum hydroxide or to amorphous aluminum hydroxy carbonates.

The NaCl(aq) electrolyte formed when the experiment started remained visible during the first week of exposure. During the later stages of the experiment the samples appeared dry to the naked eye. The drying up of the electrolyte is in accordance with the relatively small difference in the mass gain registered directly after the four-week exposure (wet mass gain) and the mass gain measured after storing one week over a desiccant (dry mass gain). Similar observations, indicating the gradual drying up of samples during exposure, were made in all cases where there was a rapid corrosion attack (with CO_2, 38-60°C, without CO_2, 22-60°C). The corrosion behavior was qualitatively the same.

38°C, <1 ppm CO_2, and 350 ppm.—The NaCl-treated samples exposed in the absence of CO_2 show slightly greater mass gains at 38°C compared to 22°C (compare Table IV and V). After exposure, the NaCl-treated samples were covered by a thick white layer of corrosion products, similar to those formed at 22°C. The spool-formed crystals on the sample surface correspond to bayerite (see Fig. 1b).

The dry mass gain of NaCl-treated samples exposed in the presence of CO_2 increased by a factor of six as temperature increased from 22 to 38°C (see Table IV and V). Table IV and V show that CO_2 inhibits aluminum corrosion at 38°C, although not to the extent seen at 22°C. The NaCl-treated samples appeared dry after exposure with an uneven distribution of thin white corrosion products. Corrosion product crusts of about 1 mm diam covered most of the surface. The ESEM image in Fig. 1b shows corrosion product crusts.

50°C, <1 ppm CO_2, and 350 ppm.—The corrosion rate of the NaCl-treated samples at 50°C in the absence of CO_2 is about the same as in the corresponding exposure at 38°C (see Table V and VI). At the end of the exposure the samples appeared dry. The surface was grayish with evenly distributed white spots. Figure 1b shows corrosion product morphology similar to that seen at 22 and 38°C. The ESEM image in Fig. 1b shows 10-20 μm long, spool-formed crystallites corresponding to bayerite.

In the presence of 350 ppm CO_2, comparison with the corresponding exposure at 38°C (see Table V and VI) shows a threefold increase in corrosion rate. The corrosion rate in the presence of CO_2 is between 50 and 70% of the rate in the absence of CO_2 (see Table VI). At the end of the exposure the samples appeared dry. The corrosion products formed an even layer with scattered millimeter size corrosion product crusts. The ESEM image in Fig. 1b shows that the corrosion product crystals have become coarser compared to the corresponding exposure at 38°. However, in comparison to the exposure to CO_2-free air at the same temperature, the crystallites are much smaller.

60°C, <1 ppm CO_2 and 350 ppm.—The corrosion rate of NaCl-treated samples at 60°C in the absence of CO_2 was about the same as in the corresponding environment at 38 and 50°C (see Table V-VII). The samples appeared dry after exposure and their appearance was similar to the corresponding 50°C exposure. At this temperature XRD also showed the presence of small amounts of gibbsite [γ-$Al(OH)_3$] besides bayerite. Figure 1b shows an ESEM image of the surface. The crystallites are considerably larger compared to the corresponding exposures at lower temperature. The corrosion product morphology is also different, the crystallites exhibiting columnar growth as opposed to the randomly orientated crystallites formed at lower temperature.

In the presence of 350 ppm CO_2, there is a 30 to 50% increase in corrosion rate (see Table VI through VII) comparing the corresponding exposure at 50°C. At 60°C the corrosion rates of NaCl-treated samples were about the same in the presence and in the absence of CO_2, see Table II. After exposure, grayish-white corrosion products had formed with millimeter size white crusts. Again, traces of gibbsite were identified together with bayerite. The ESEM image in Fig. 1b shows corrosion product morphology similar to that in the corresponding environment at 50°C. The crystallites are much smaller compared to the exposure to CO_2-free air at 60°C. No carbonate-containing corrosion products were found when immersing in 1 M $HClO_4$.

14 μg NaCl/cm^2.—The atmospheric corrosion behavior of aluminum treated with 14 μg NaCl/cm^2 was qualitatively the same as that observed for samples treated with 70 μg NaCl/cm^2, see Table II through VII. It may be noted that the corrosion product mass did not depend linearly on the amount of NaCl added. A fivefold increase in the amount of NaCl added resulted in an increase in the corrosion rate by a factor of two to four.

Discussion

The corrosion resistance of aluminum in the atmosphere is due to the presence of an electrically insulating and relatively inert oxide film. At 95% RH, NaCl forms an aqueous solution on the sample surface. Therefore, the NaCl-induced atmospheric corrosion of aluminum in humid air may be regarded as a special case of aqueous corrosion in a NaCl containing electrolyte. In neutral and alkaline solution aluminum is known to corrode by an electrochemical mechanism. The anodic dissolution is described by two coupled reactions[11] while the cathodic partial reaction is considered to be oxygen reduction

$$Al + 3OH^- \rightarrow Al(OH)_3(s) + 3e^- \quad [1]$$

$$Al(OH)_3(s) + OH^-(aq) \rightarrow Al(OH)_4^-(aq) \quad [2]$$

$$1/2O_2 + H_2O + 2e^- \rightarrow 2OH^- \quad [3]$$

The cathodic reaction is reported to occur only on flaws in the oxide at grain boundaries or inclusions in the metal that only make up a small fraction of the film.[12,13] In an unbuffered solution, the dissolution of the passive layer is enhanced at the cathodic sites by

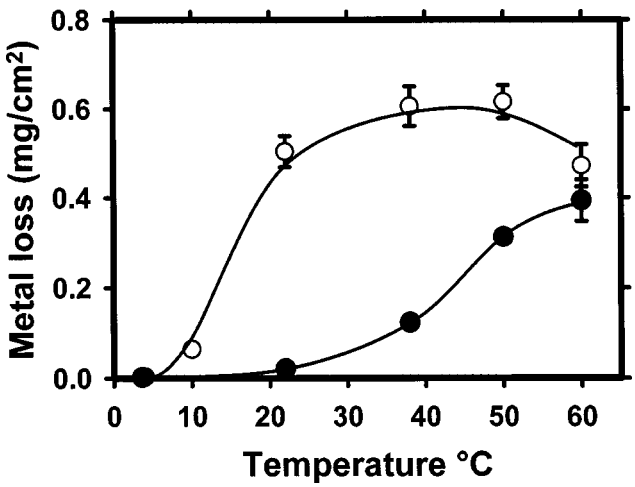

Figure 3. Metal loss as a function of exposure temperature for aluminum samples pretreated with 70 μg NaCl/cm^2 exposed to (○) <1 ppm CO_2 and (●) 350 ppm CO_2 for 4 weeks. The RH was 95%.

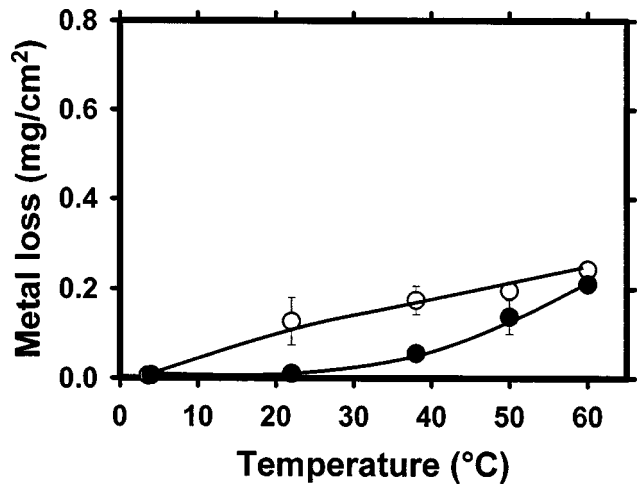

Figure 4. Metal loss as a function of exposure temperature for aluminum samples pretreated with 14 μg NaCl/cm^2 exposed to (○) <1 ppm CO_2 and (●) 350 ppm CO_2 for 4 weeks. The RH was 95%.

the formation of hydroxide (Reaction 3). This means that the anodic and cathodic reactions both occur at the same site. The anodic reaction also proceeds over the rest of the surface, although at a slower rate.[12] Chloride ions in neutral aqueous solutions are known to cause pitting corrosion of aluminum. According to Kaesche,[11] pitting is initiated through the adsorption of, *e.g.*, chloride ions on the alumina surface, resulting in the dissolution of the passive film. Chloride is not expected to be an efficient corrosion promoter for aluminum in contact with a high pH aqueous solution because the negative surface charge of alumina at high pH makes chloride adsorption unfavorable.[14] Instead, high pH promotes the anodic reaction through the formation of soluble aluminate (see Reaction 2). Therefore, aluminum is affected by the general corrosion rather than by pitting in high pH solutions.[11]

It was recently reported that the NaCl-induced atmospheric corrosion of aluminum is very rapid in the absence of CO_2 at 22°C.[8] It was concluded that the corrosion attack involved the alkaline dissolution of the passive film (see Reaction 2). It was argued that regions with high pH developed in the surface electrolyte due to the cathodic reduction of oxygen. The occurrence of high pH values on the corroding aluminum surface was supported by the identification of bayerite [α-$Al(OH)_3$] by X-ray diffraction (XRD) after exposure. According to reports in the literature, pH values of 9 and higher are needed in order for bayerite to form.[15] At neutral pH, where solubility of aluminum is small, it precipitates in the form of an X-ray amorphous gel or as the poorly crystalline pseudobohemite. The same investigation reported that the rate of the NaCl-induced atmospheric corrosion of aluminum at 22°C in CO_2-free humid air was 20 times that in air with ambient levels of CO_2.[8]

The limited amount of carbonate formed on NaCl-treated aluminum exposed to CO_2 in the present study implies that the effect of CO_2 is not primarily caused by the formation of a protective aluminum carbonate film. Instead, the slowing down of the corrosion of NaCl-coated aluminum in humid air by CO_2 is suggested to be due to its acidity, counteracting the development of high pH in the surface electrolyte by forming carbonate and hydrogen carbonate. This is supported by the observation that bayerite does not form in the presence of CO_2 at 22°C, indicating that high pH values does not occur in this environment. The present study shows the great importance of temperature for the NaCl-induced atmospheric corrosion of aluminum (see Fig. 3). At 4°C corrosion is very small and does not depend on whether CO_2 is present or not. In the absence of CO_2, an increase in temperature to 22°C results in an increase in corrosion rate by almost two orders of magnitude (see Table II and IV). In comparison, the same increase of temperature in the presence of CO_2 only resulted in a twofold increase of corrosion. As temperature is increased further, the rate of atmospheric corrosion in the presence of CO_2 accelerates while the rate of corrosion in the absence of CO_2 is more or less independent of temperature between 22 and 60°C. As a result, the rate of NaCl-induced atmospheric corrosion at 60°C is about the same in the presence and in the absence of CO_2. The strong dependence of corrosion rate on temperature between 4 and 22°C in the absence of CO_2 implies that the rate of corrosion is determined by one or more activated processes, for example, a charge-transfer or a dissolution reaction, *e.g.*, Reaction 1 or 2.

It was noted previously that the amount of electrolyte on the sample surface decreases during exposure. This implies that the NaCl(aq) solution formed initially, reacts on the corroding surface to form other water-soluble substances with less ability to attract water. These products are suggested to include compounds containing aluminum and chloride. One possible explanation for the lack of increase in corrosion with temperature between 22 and 60°C in the absence of CO_2 may be the partial drying up of the electrolyte. In this view, the decreasing amount of electrolyte counteracts the expected positive temperature dependence for the reactions involved in the corrosion process. In the presence of CO_2, there is also a drastic increase in corrosion with temperature, although it is shifted by 20-30°C towards higher temperature (see Fig. 3). The inhibiting effect of CO_2 on the NaCl-induced corrosion of aluminum at 22°C has already been described. The observation that the inhibitive effect of CO_2 is attenuated as temperature increases above 22°C and eventually disappears around 60°C may imply that the neutralization by CO_2 of the hydroxide formed in the cathodic reduction of oxygen is not rapid enough to inhibit the anodic dissolution of aluminum by Reactions 1 and 2 at higher temperatures. Figure 4 shows the inhibition efficiency of ambient levels of CO_2 towards the NaCl-induced atmospheric corrosion of aluminum as a function of the solubility of CO_2 in water.[16] The graph implies that the solubility of CO_2 is strongly correlated to its effectiveness as a corrosion inhibitor. (The solubility of CO_2 in the NaCl(aq) surface electrolyte,[17] is actually somewhat less than in pure water. However, the shape of the curve is essentially the same, it is only shifted slightly to the left.) The diminishing solubility of CO_2 with temperatures may explain why we find no carbonate in the corrosion products for samples exposed at 60°C. It may be noted that CO_2 is not inhibiting aluminum corrosion at all at 4°C, even though the solubility of CO_2 is at its greatest there. This apparent anomaly is related to the slow rate of electrochemical corrosion in the absence of CO_2 at this temperature. Ap-

parently, the cathodic reaction is not able to destabilize the passive film and, consequently, the acidic properties of CO_2 do not improve corrosion resistance.

Figure 4 shows metal loss as a function of temperature for samples treated with 14 μg NaCl/cm^2. In general, the results are similar to those already described for aluminum treated with 70 μg NaCl/cm^2, compare Fig. 3. Not unexpectedly, the results show that the atmospheric corrosion of aluminum is related to the amount of NaCl added. Samples treated with 14 μg NaCl/cm^2 exhibited corrosion rates corresponding to between 25 and 50% of the rates measured in the presence of 70 μg NaCl/cm^2, depending on temperature.

To summarize, the inhibitive effect of ambient levels of CO_2 in the temperature range 10-38°C has important implications for the atmospheric corrosion of aluminum. The present study contributes towards understanding the corrosion of aluminum in environments where the supply of CO_2 is limited. This includes crevice corrosion and corrosion beneath organic coatings and deposits. The propensity of aluminum to suffer crevice corrosion has previously been attributed to differential aeration cells.[18] The present work suggests that the cause may be CO_2 depletion. Similar effects may be involved in the occurrence of filiform corrosion of aluminum beneath organic coatings.

The very strong, nonlinear, dependence of aluminum corrosion on temperature is another important result of the present study. The discovery of this effect may help to interpret the results from field studies performed in different climates.

It is argued that the effect of temperature and CO_2 on the NaCl-induced atmospheric corrosion of aluminum reported in this study provides important input for the interpretation of accelerated tests for the atmospheric corrosion of aluminum. Indeed the results may be put to use in designing improved corrosion tests.

Conclusions

Our two main findings are the strong nonlinear temperature dependence of the atmospheric corrosion of aluminum and the inhibitive effect of CO_2 at ambient temperature. In the absence of CO_2, corrosion increases by two orders of magnitude from 4 to 22°C. CO_2 inhibits the NaCl-induced atmospheric corrosion of aluminum at 22°C by a factor of 10-20. The rapid corrosion of aluminum in the absence of CO_2 is connected to the formation of high pH regions in the surface electrolyte as a result of the cathodic reduction of oxygen. The anodic dissolution of aluminum is enhanced by high pH. Accordingly, the inhibitive effect of CO_2 is attributed to its acidity. CO_2 neutralizes the hydroxide formed at the cathodes, slowing down corrosion. The inhibitive effect of CO_2 is attenuated as temperature increases above 22°C and disappears at 60°C. The inhibitive effect of CO_2 is relevant to situations where the supply of CO_2 is limited, for example, crevice corrosion and corrosion beneath organic coatings. The nonlinear dependence of corrosion on temperature may be useful in interpreting results from accelerated corrosion tests and for explaining differences in the rate of aluminum corrosion in different climates.

Acknowledgments

The authors thank Volvo Car Corporation for financial support and Norsk Hydro Aluminum for providing the material.

Chalmers University of Technology assisted in meeting the publication costs of this article.

References

1. T. E. Graedel, *J. Electrochem. Soc.*, **136**, 204C (1989).
2. R. T. Vashi and H. G. Patel, *Bull. Electrochem.*, **13**, 343 (1997).
3. E. Mattsson, *CHEMTECH*, **15**, 234 (1985).
4. P. V. Strekalov, *Zashch. Met.*, **29**, 819 (1993).
5. T. E. Graedel, *J. Electrochem. Soc.*, **136**, 193C (1989).
6. V. Kucera and E. Mattsson, in *Atmospheric Corrosion*, F. Mansfield, Editor, Marcel Dekker, New York (1987).
7. S. S. Butcher, R. J. Charlson, G. H. Orians, and G. V. Wolfe, in *Global Biogeochemical Cycles*, Academic Press, Inc., London (1992).
8. D. B. Blucher, R. Lindstrom, J. E. Svensson, and L. G. Johansson, *J. Electrochem. Soc.*, **148**, B127 (2001).
9. T. Falk, J. E. Svensson, and L. G. Johansson, *J. Electrochem. Soc.*, **145**, 39 (1998).
10. R. Lindstrom, J.-E. Svensson, and L.-G. Johansson, *J. Electrochem. Soc.*, **147**, 1751 (2000).
11. H. Kaesche, in *Passivity of Metals*, R. P. Frankenthal and J. Kruger, Editors, p. 935. The Electrochemical Society Corrosion Monograph Series, Princeton, NJ (1978).
12. W. Vedder and D. A. Vermilyea, *Trans. Faraday Soc.*, **65**, 561 (1969).
13. J. A. Richardson and G. C. Wood, *Corros. Sci.*, **10**, 313 (1970).
14. W. Stumm and G. Furrer, in *Aquatic Surface Chemistry, Chemical Processes at the Particle-Water Interface*, W. Stumm, Editor, p. 197, John Wiley & Sons, New York (1987).
15. H. Ginsberg, W. Hueltig, and H. Stiehl, *Z. Anorg. Allg. Chem.*, **318**, 238 (1962).
16. *Perry's Chemical Engineers' Handbook*, 6th ed., R. H. Perry and D. W. Green, Editors, pp. 3-98, McGraw-Hill Book Company, New York (1984).
17. *Solubilities. Vol. I. (A-Ir) Inorganic and Metal-Organic Compounds*, 4th ed., W. F. Linke, Editor, p. 468, American Chemical Society, Washington, D.C. (1958).
18. U. R. Evans, in *The Corrosion and Oxidation of Metals: 1st Suppl.*, p. 519, Edward Arnold Publishers, Ltd., London (1968).

Paper 4

Journal of The Electrochemical Society, **151** (12) B621-B626 (2004)
0013-4651/2004/151(12)/B621/6/$7.00 © The Electrochemical Society, Inc.

Scanning Kelvin Probe Force Microscopy

A Useful Tool for Studying Atmospheric Corrosion of MgAl Alloys *In Situ*

D. Bengtsson Blücher,[a,z] J.-E. Svensson,[a] L.-G. Johansson,[b,*] M. Rohwerder,[c] and M. Stratmann[c,*]

[a]*Chalmers University of Technology,* [b]*Göteborg University, SE-41296 Göteborg, Sweden*
[c]*Max-Planck-Institut für Eisenforschung, D-40074 Düsseldorf, Germany*

Scanning Kelvin probe force microscopy (SKPFM) is used to study the initial stages of atmospheric corrosion of an AlMg alloy and of physical vapor deposition (PVD) deposited 2 μm Al dots on pure Mg. The latter system is used as a model of a two-phase AlMg alloy. The influence of CO_2 was studied *in situ* in humid air using SKPFM. This method allows for the *in situ* investigation of the evolution of the Volta potential during exposure, the resolution being in the submicrometer range. The temperature was 22.0°C, and the relative humidity was 85 or 95%. The concentration of CO_2 was <1 or 350 ppm. The corrosion products were analyzed by gravimetry, ion chromatography, X-ray diffraction, scanning electron microscopy, scanning Kelvin probe, and Auger electron spectroscopy. We found that the initial stages of atmospheric corrosion on magnesium are influenced by the presence of cathodic PVD-deposited aluminum. A similar effect was seen in the case of AZ91D, the aluminum-rich β-phase forming the cathodic areas. The β-phase is nobler compared to the substrate because of the higher Al content. In the absence of CO_2, the corrosion attack is localized in nature whereas the presence of ambient levels of CO_2 results in a more general corrosion attack. The inhibitive effect of CO_2 on the atmospheric corrosion of AZ91D is explained by the formation of a passivating layer of $Mg_5(CO_3)_4(OH)_2 \cdot 5H_2O$. In the absence of CO_2, the increase in pH originating from the cathodic reaction results in the dissolution of aluminum in the passive layer. A corrosion mechanism is proposed explaining the behavior in the two environments.
 [DOI: 10.1149/1.1809590]

Manuscript submitted January 27, 2004; revised manuscript received April 27, 2004. Available electronically October 28, 2004.

Because of their low weight/strength ratio, magnesium alloys are used in vehicles, the aerospace industry, and portable microelectronics. One of the more commonly used magnesium alloys is AZ91D (Al 8.9% and Zn 0.74%). The use of magnesium alloys is limited due to their susceptibility to corrosion, especially in the presence of soluble chlorides.[1]

The atmospheric corrosion of AZ91D has previously been studied in the laboratory on a longer time scale. It was reported that ambient levels of CO_2 slow down corrosion by a factor of three compared to when CO_2 is absent.[2] Carbon dioxide has also been shown to inhibit the atmospheric corrosion of Zn, Al, and Al alloys.[3] Different mechanisms for the inhibitive effect of CO_2 have been proposed.[4,5] This study aims at understanding the influence of Al-rich inclusions on the initial stages of the atmospheric corrosion of Mg and AZ91D in humid air in the presence and in the absence of CO_2.

Physical vapor deposition (PVD) offers a suitable method for depositing micrometer sized dots of pure aluminum on magnesium. By this method we can create a synthetic model system that is useful for interpreting the more complex phenomena occurring on real two-phase alloys. Stratmann *et al.* previously demonstrated the usefulness of the scanning Kelvin probe, SKP, in corrosion studies by mapping the Volta potential on corroding metal surfaces.[6,7] However, the influence of intermetallic precipitates on the corrosion process of light metal alloys requires a higher lateral resolution than is offered by this technique.

Previously, SKPFM was successfully used for investigating the corrosion on aluminum alloys,[8-11] pure Al,[12] and on pure Mg.[13] SKPFM has also been used *ex situ* to study the corrosion of duplex stainless steels.[14] However, the results from SKPFM can not be interpreted as being as straight forward as standard SKP. Although the physical principles of deriving the potentials are similar for SKPFM and SKP, the latter is more sensitive to convolution between the tip and surface features. The SKPFM tips used are pseudo-references since their Volta potential may vary from tip to tip due to slight differences in the oxide covering them. Further, contaminants deposited on the tip during scanning can give rise to deviations in the measured Volta potential.[15] SKPFM was first introduced for studying microelectronic applications.[16] The working principles of the Kelvin probe mode for atomic force microscopy (AFM) are discussed in more detail elsewhere.[17-19]

The main constituents of alloy AZ91D are α-phase [2% Al in Mg(ss)] and α-phase ($Mg_{17}Al_{12}$). In addition, small amounts of minor intermetallics, *e.g.*, Al_8Mn_5 are present. The β-phase is nobler than the α-matrix and precipitates in the grain boundaries of the α-phase, forming a three-dimensional network in the alloy. While the α-grains have dimensions of 5-10 μm, the β-phase precipitates have typical dimensions on the order of 2 μm. *In situ* AFM/SKPFM offers a valuable method for investigating the kinds of galvanic couplings present in AZ91D and in the model system in the submicrometer range. In the present study we investigate the atmospheric corrosion of alloy AZ91D *in situ*, focusing on the relation between corrosion and the difference in relative Volta potential between the two phases.

Experimental

A high purity die-cast aluminum-magnesium-zinc alloy, AZ91D, with nominal composition 90.1% Mg, 8.9% Al, 0.74% Zn, 0.21% Mn, 0.008% Si, 0.0022% Fe, 0.0007% Cu, 0.0004% Ni was used. For the physical vapor deposition (PVD) of pure Al (99.99%), pure Mg (Puratronic Mg ingot from Johnson Matthey) was used as a substrate.

The sample coupons had a geometrical area of 5.7 cm^2 (15 × 15 × 2) mm. In the *in situ* SKPFM exposures, only one side was exposed (2.25 cm^2). The samples were first mechanically ground to 1000 mesh in water and then polished with 1 μm diamond paste with a nonaqueous lubricating solution (Blue Lube from Struers). Thereafter the samples were polished with 0.2 μm OPS (a solution of 3% SiO_2 and 2% 1,3-butandiol in ethanol provided by Struers). The samples were then cleaned ultrasonically in acetone. The samples were stored in a dessicator for about 24 h before exposure.

In order to determine the influence of Al on Mg, PVD was deployed to create artificial cathodic areas of Al on Mg. The pure Mg sample was first polished to 0.2 μm as above. The sample surface was then partly covered by Quantifoil® to control the size and distribution of the Al islands. The aluminum islands had a circular shape and a diameter of 2 μm, the distance between the islands was

* Electrochemical Society Active Member.
z E-mail: danielb@chem.chalmers.se

about 4 μm. The thickness of the Al islands were 15 and 20 nm in the experiments carried out in the presence and in the absence of CO_2, respectively.

AFM and SKPFM in situ study of the initial stages of corrosion.—A Digital Instruments Nanoscope IIIa MultiMode AFM was used to image the surface topography and Volta potential distribution *in situ* with submicrometer resolution using an atmospheric corrosion cell. The instrument was equipped with an extender electronics module, enabling surface potential measurements when engaged in the tapping mode. The relative humidity (RH) was 85% and the temperature was 22°C. The CO_2 concentration was either <1 ppm or 350 ppm. The *in situ* measurement continued for 65 h. In exposures with no CO_2, the air was purified from CO_2 by using Ascarite filters (silica gel overdrawn with NaOH). A concentration of <1 ppm CO_2 was achieved.

The atmospheric corrosion chamber for this setup was made of glass and Teflon. Olympus Micro Cantilevers conducting n^+ silicon tips were used. The resonant frequency was about 279 kHz, and the spring constant was about 27 N/m.

The principle of SKPFM involves scanning the surface in the tapping mode to determine the topography on a line-by-line basis. The metal coated or doped silicon cantilever is then lifted a fixed distance, typically 20-50 nm, and the tip is rescanned across the surface in the lift mode. On the rescan, the tapping piezo is turned off, but an ac voltage is applied to the tip which stimulates oscillation of the cantilever in the presence of an electric field. The magnitude of the oscillations, monitored by the AFM, is zeroed out on a point by point basis during the lift mode rescan by adding a dc voltage to the tip to balance it. This approach to potential measurement is not possible in an aqueous solution, because the large voltages applied to the tip cause Faradaic reactions in the solution.[20] In contrast, the application is well suited for studying the thin electrolytes present in atmospheric corrosion.

A whole range of analytical techniques was used to characterize the corrosion products and study the corrosion mechanisms. For X-ray diffraction (XRD) measurements a Siemens D5000 powder diffractometer (Cu Kα radiation) using a grazing incidence beam attachment fitted with a Göbel mirror was used to determine crystalline corrosion products. The morphology of the corrosion products were analyzed by field emission (FE)-SEM, a LEO 1550 VP equipped with an Oxford Instruments INCA energy dispersive X-ray detector and a backscattered secondary electron detector.

To be able to compare the absolute potentials *in situ* of the studied materials and phases before and after exposure a SKP was used. The SKP was calibrated before each exposure to the standard hydrogen electrode by a measurement of the Volta potential difference over a Cu/Cu^{2+} reference electrode.[21] The principle of the Kelvin probe has been described previously.[7,22] During the SKP measurement, the temperature was 22°C and the relative humidity was held constant at about 85% RH. In order to measure the absolute potential on the β-phase in AZ91D, an artificial batch of $Mg_{17}Al_{12}$ was die cast and SKP measurements were performed on its polished surface.

Auger electron spectroscopy (AES) was used to determine the composition of the corrosion product layer by performing depth profiling. The AES analyses were performed with a scanning Auger microprobe (SAM) instrument (PHI 660). The primary accelerating voltage was 10 kV, and the beam current was 75 nA. The depth profiles were obtained using a differentially pumped ion gun (Ar^+) with acceleration voltage 4.0 kV. The etch rates were calibrated on a flat sample of Ta_2O_5 with a known oxide thickness of 100 nm. The collected raw data was refined using MultiPak v. 6.0 software. The spectra were recorded with a step size of 1 eV. The angle between the primary beam and the normal to the sample surface was 30°.

Results

CO_2-free air.—AFM/SKPFM.—Figure 1 shows AFM and SKPFM images of PVD deposited Al islands on Mg, measured *in situ* at 85% RH and 22°C in the absence of CO_2. The images in the left column show the topography by tapping mode AFM while the right column shows Volta potential maps imaged using SKPFM. The measurements show that the aluminum islands are cathodic and influence the corrosion of the magnesium substrate, see Fig. 1. The corrosion products accumulate primarily on the magnesium substrate between the aluminum islands. The aluminum islands are surrounded by corrosion product halos. The islands, originally about 20 nm thick, decreased to about 12 nm thickness after exposure. Between the halos and the Al islands a narrow trench can be seen. The aluminum islands are encircled by corrosion products that have precipitated on the Mg substrate. AES shows that these corrosion products are rich in aluminum. Further away from the Al islands the corrosion products are magnesium-rich. In addition, there are scattered Al-rich corrosion product accumulations that increase in number and size as the exposure continues.

The difference in Volta potential between the aluminum islands and the magnesium substrate at 85% RH is about 70 mV as measured with SKPFM. However, the Volta potential difference between pure Al and pure Mg at the same relative humidity as measured by SKP is about 600 mV (the SKP measurements are reported below). It is suggested that this discrepancy can be attributed to the small size of the islands; even though their shape is clearly resolved in the images, the correct measurement of the full potential difference requires larger patterns.[23-25] Other explanations of these observations could be the fact that Al is slightly polarized towards Mg and that the *in situ* SKPFM method does not allow for the measurement of the absolute potential differences as is the case for the regular Kelvin probe. According to reports in the literature,[23,24] SKPFM only measures a fraction of the full potential difference between adjacent surface features. The main reason for this is the effect of stray capacitance, derived from the entire cantilever area and not only from the tip. The passage of the cantilever over an undulated surface with intermetallic inclusions located far from the tip can significantly influence the Kelvin signal and hence lead to such deviations.[20] Hochwitz *et al.* report on deviations of a factor two or more.[24] These deviations are, however, not yet fully understood and are subject to further investigation.[15] The Volta potential difference between the magnesium substrate and the aluminum islands measured by SKPFM decreases with time. This is attributed to the formation of corrosion products on the Mg matrix.

In an analogous experiment, alloy AZ91D was exposed to the same environment. Figure 2 shows the corresponding time-resolved *in situ* AFM and SKPFM images, the left column showing the topography by tapping mode AFM and the right column showing Volta potential maps by SKPFM. Energy dispersive X-ray fluorescence on backscattered electron images revealed that the brighter (cathodic) areas in the Volta potential images correspond to β-phase ($Mg_{17}Al_{12}$) while the darker areas are α-phase (2% at solid solution Al in Mg). The β-phase is harder compared to the α-phase and protrudes from the surface after polishing. The formation of corrosion products occurs primarily on the anodic α-phase matrix (see encircled areas in Fig. 2). The corrosion products appear as dark spots in the Volta potential image. This implies that corrosion attack is influenced by the potential difference between the matrix and the β-phase. The size and number of corrosion product accumulations increases with time, indicating an ongoing corrosion process. A clear relative Volta potential difference between α and β-phase remains after 17 h exposure to humid air.

Figure 3 shows Auger electron spectroscopy depth profiles obtained on β-phase areas after one week of exposure at 22.0°C at 95% RH in the absence of CO_2. The environmental SEM image to the left shows where the AES profile was obtained. Aluminum is seen to be depleted in the corrosion product. This is in accordance with the rapid dissolution of the alumina film which was seen on pure Al in the model system. The slope of the Mg(me) and the Al(me) concentration curves suggests that there is an aluminum depletion in the β-phase, close the surface. The nominal composition of the β-phase is indicated to the right in the figure.

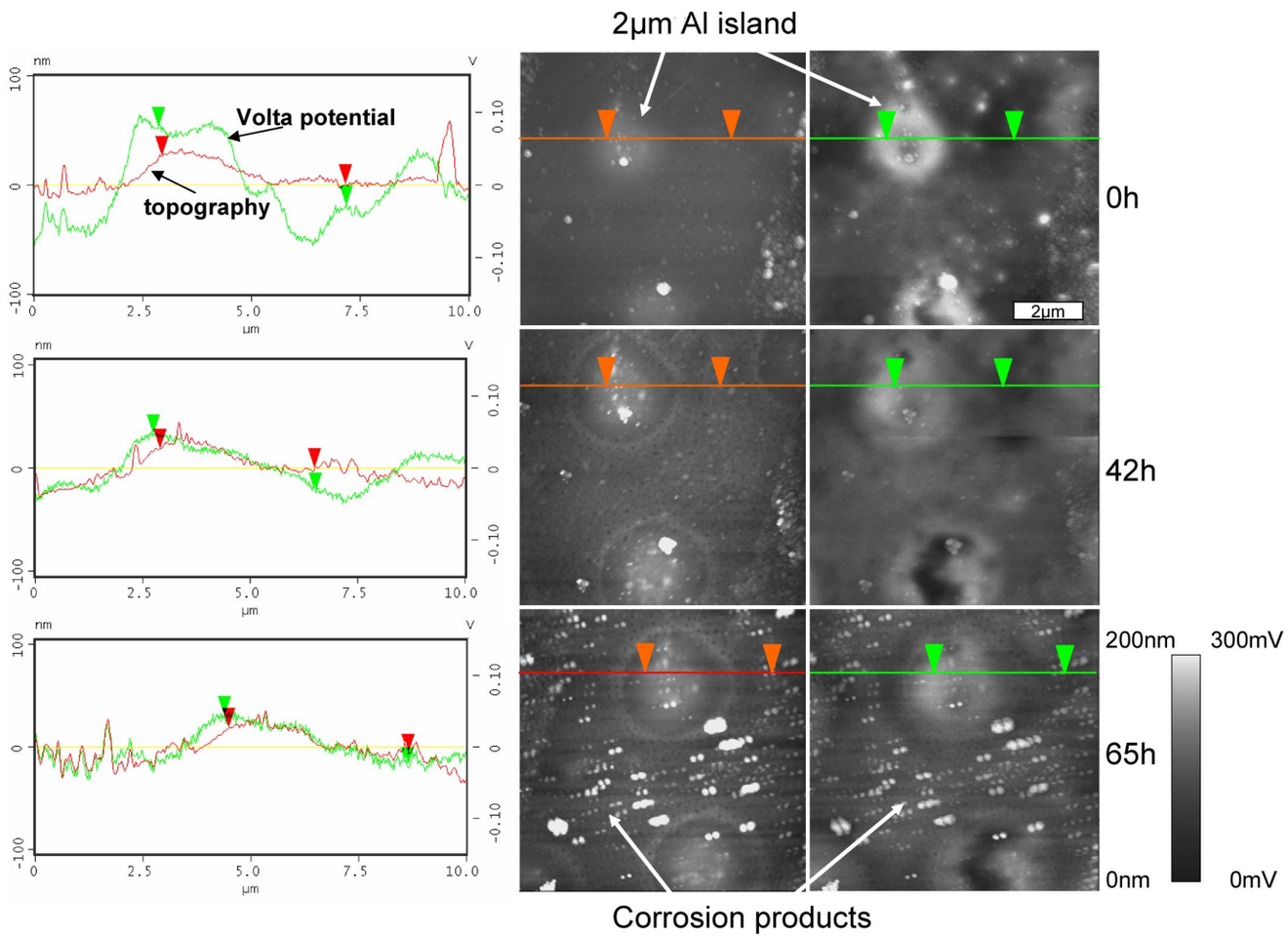

Figure 1. Time resolved *in situ* AFM and SKPFM images of PVD-deposited pure Al on pure Mg in the absence of CO_2. The RH was 85% and the temperature was 22°C. The images in the left column show the topography by tapping mode AFM while the right column show Volta potential maps imaged using SKPFM. The brighter areas are protruding from the surface in the topography images and have a higher relative potential in the Volta potential images. The height range is 200 nm and the Volta potential range is 300 mV.

Air with 350 ppm CO_2.— AFM/SKPFM.—The model system consisting of PVD-deposited Al islands on Mg was exposed *in situ* in the presence of ambient levels of CO_2 at 85% RH and 22°C for 67 h. In this environment corrosion was negligible, no change in the surface morphology being detected by AFM/SKPFM.

In contrast, alloy AZ91D suffered a measurable corrosion attack in this environment, (see *in situ* AFM and SKPFM images Fig. 4). The left column shows the topography by tapping mode AFM and the right column shows Volta potential maps obtained by SKPFM. As in Fig. 2, the brighter (cathodic) areas in the Volta potential images are β-phase while the darker areas are α-phase. In this case, submicronmeter corrosion product agglomerations form all over the surface, on the α-phase matrix as well as on the β-phase areas (see line scans in Fig. 4). The corrosion product distribution is more even in comparison to the corresponding experiment in the absence of CO_2. In the latter case, corrosion products form primarily on α-phase areas (compare Fig. 2).

Potential measurements by SKP.—Scanning Kelvin probe measurements were performed at 85% RH in CO_2-containing air at 22°C. The potentials of pure Mg, AZ91D, β-phase and pure Al were found to be −1350, −1300, −1050, and −700 mV, respectively. Measuring the potential of alloy AZ91D after 100 h exposure to the same environment showed a minor change in potential to −1250 mV. In a separate experiment, the potential of alloy AZ91 was measured after the 100th exposure at 85% RH in CO_2-free air. In this case the absolute potential was −1150 mV. The absolute potentials were calibrated against $Cu/CuSO_4$ having +318 mV against SHE. The higher absolute potential measured for the corroded samples is due to the formation of insulating corrosion products.

Discussion

Corrosion in the absence of CO_2.—The atmospheric corrosion of magnesium is reported to be electrochemical in nature,[26] magnesium dissolving anodically, Eq. 1

$$Mg(s) \rightarrow Mg^{2+}(aq) + 2e^- \quad [1]$$

The cathodic reaction may be hydrogen evolution or oxygen reduction[2,3]

$$2H_2O + 2e^- \rightarrow H_2(g) + 2OH^- \quad [2]$$

$$\tfrac{1}{2}O_2 + H_2O + 2e^- \rightarrow 2OH^-(aq) \quad [3]$$

In clean humid air the dominant corrosion product is reported to be $Mg(OH)_2(s)$.[26] The appreciable solubility of magnesium hydroxide in water ($Ks = 10^{-11.15}\ M^3$) implies that it dissolves to some extent in the adsorbed water layer present at 85% RH, creating a surface electrolyte.[27] Therefore it may be expected that the combi-

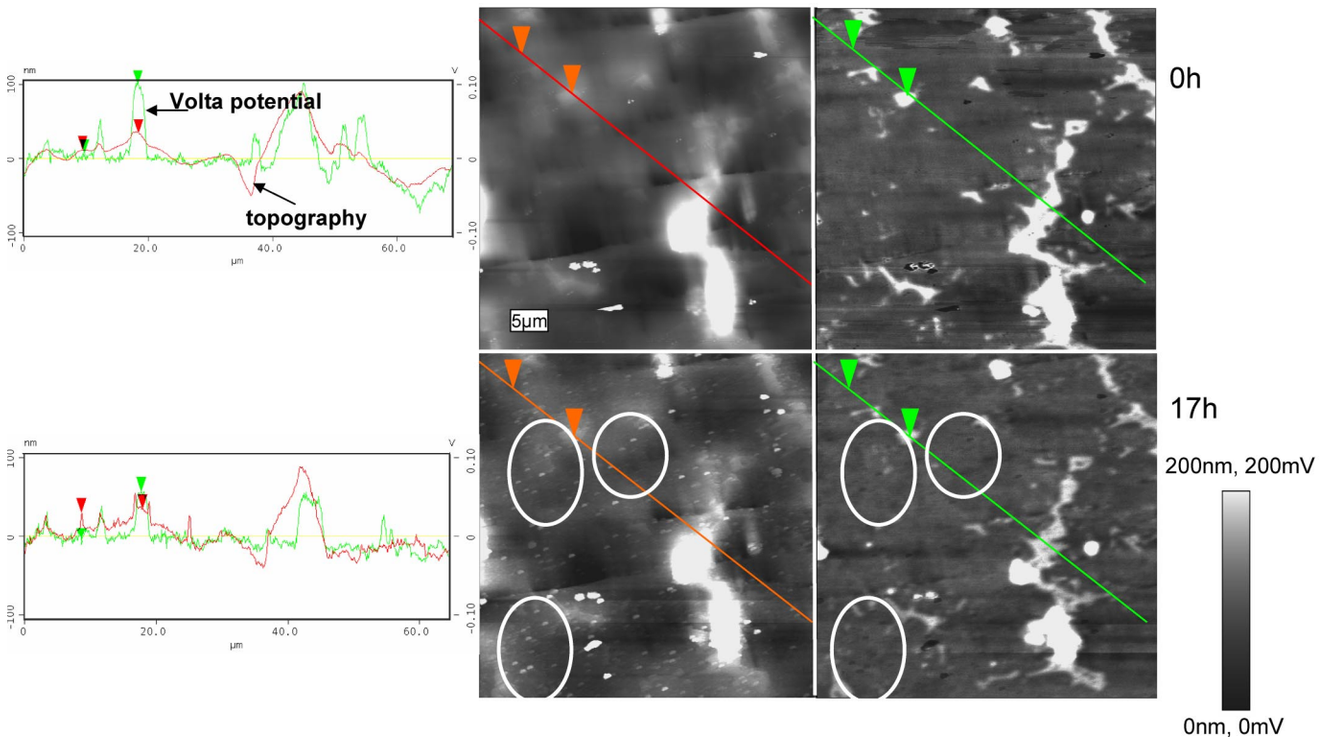

Figure 2. Time resolved *in situ* AFM and SKPFM images of AZ91D in the absence of CO_2. The RH was 85% and the temperature was 22°C. The images in the left column show the topography by tapping mode AFM while the right column show Volta potential maps imaged using SKPFM. Again, the brighter areas are protruding from the surface in the topography images and have a higher relative potential in the Volta potential images. The height range is 200 nm and the Volta potential range is 200 mV.

nation of Mg and Al will give rise to a galvanic couple on the surface. Accordingly, the SKPFM images of the corroding Al/Mg model system show that the atmospheric corrosion of Mg is influenced by the presence of the nobler Al. Further away from the Al islands, SAM shows that the corrosion products on the Mg substrate are rich in Mg, probably forming $Mg(OH)_2$. In contrast, the Al islands are surrounded by a halo consisting of Al-rich corrosion products (see Fig. 1).

The anodic dissolution of Al in neutral and alkaline solution is described by the following coupled reactions, 4,5:[28]

$$Al + 3OH^- \rightarrow Al(OH)_3(s) + 3e^- \quad [4]$$

$$Al(OH)_3(s) + OH^-(aq) \rightarrow Al(OH)_4^-(aq) \quad [5]$$

The localized corrosion seen in the absence of CO_2 is interpreted in terms of the formation of electrochemical corrosion cells on the sample surface. The cathodic reaction occurring on the Al islands gives rise to a local increase in pH. As a result, the passive film on aluminum is attacked and aluminum corrosion ensues. The dissolved

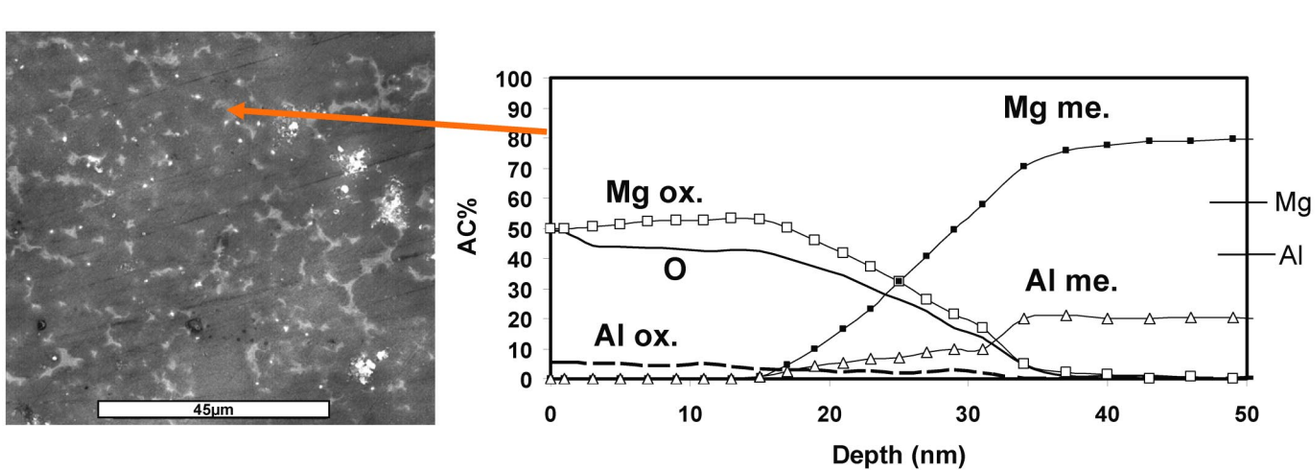

Figure 3. ESEM image and AES depth profiles of the corrosion product layer formed on the β-phase on AZ91D in the absence of CO_2 after 168 h exposure in 95% RH at 22.0°C.

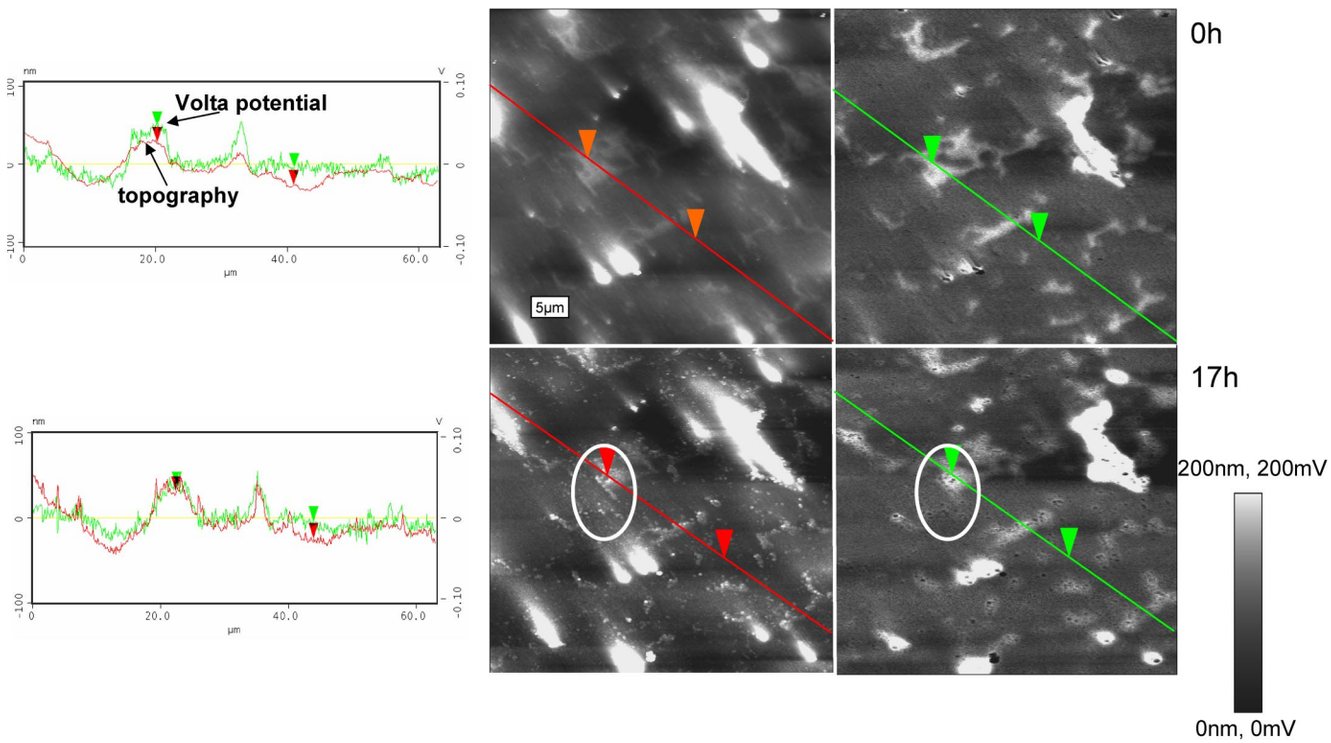

Figure 4. Time resolved *in situ* AFM and SKPFM images of AZ91D in the presence of CO_2. The RH was 85% and the temperature was 22°C. The images in the left column show the topography by tapping mode AFM while the right column show Volta potential maps imaged using SKPFM. The brighter areas are protruding from the surface in the topography images and have a higher relative potential in the Volta potential images. The height range is 200 nm and the Volta potential range is 200 mV.

aluminum species (aluminate) migrates towards the anodic substrate where it precipitates as aluminum hydroxide or aluminum magnesium hydroxide.

Similar to the model system, it is argued that the localized nature of the corrosion attack indicates that the atmospheric corrosion of alloy AZ91D in the absence of CO_2 is influenced by galvanic effects (see Fig. 2). The alloy features a β-phase which is cathodic relative to the α-phase matrix. It is suggested that initially, Mg dissolves anodically on the α matrix, (Reaction 1), while the cathodic Reaction 3 primarily occurs on the β-phase. The increase in surface pH due to the cathodic reaction results in the formation of soluble aluminate, Eq. 5. This is in accordance with the aluminum depletion of the passive film on the β-phase found by Auger profiling (Fig. 3).

A tentative corrosion mechanism in the absence of CO_2 in humid air is presented in Fig. 5.

Corrosion in the presence of CO_2.—Adding ambient concentrations of carbon dioxide to humid air results in slower corrosion and in a less localized mode of attack. It is argued that the inhibitive effect of CO_2 seen for Al/Mg and alloy AZ91D is partly explained by its acidic properties. Carbon dioxide tends to neutralize the surface electrolyte by reaction 6,7:[27]

$$CO_2(aq) + OH^- \rightarrow HCO_3^- \quad \log K = 7.35 \qquad [6]$$

$$HCO_3^- + OH^- \rightarrow CO_3^{2-} + H_2O \quad \log K = 3.67 \qquad [7]$$

The pH decrease in the surface electrolyte stabilizes the Al-rich passive layer, $Al(OH)_3$ being stable at an intermediate pH.

In the case of the model Al/Mg system it is argued that aluminum remains passive because high pH values do not develop on the cathodic aluminum areas in the presence of CO_2, explaining the lack of aluminum-containing corrosion products. Moreover, the lower pH on Al in the presence of CO_2 will hamper the development of galvanic couples on the surface because of the resulting lower conductivity in the surface electrolyte.

The atmospheric corrosion of pure Mg is reported to be inhibited by carbon dioxide.[29] This was attributed to the slightly protective nature of magnesium hydroxy carbonate that tends to accumulate on the surface. $Mg(OH)_2$ reacts with CO_2 to form magnesium hydroxy carbonate according to the following reaction

$$5Mg(OH)_2(s) + 4CO_2 \rightarrow Mg_5(CO_3)_4(OH)_2(s) + 4H_2O \quad [8]$$

It is suggested that this effect contributes to the slow corrosion of the Al/Mg model system.

A similar explanation for the slower corrosion and more even distribution of corrosion products found for alloy AZ91D in the presence of CO_2 is suggested. A tentative corrosion mechanism is presented in Fig. 6. Carbon dioxide neutralizes the surface electrolyte and forms hydroxy carbonate, *e.g.*, $Mg_5(CO_3)_4(OH)_2$. The ca-

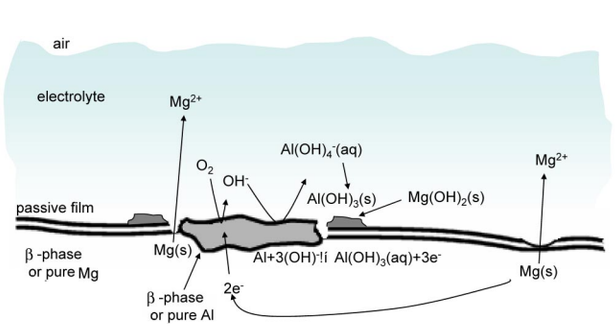

Figure 5. Suggested corrosion mechanism of the model system and AZ91D in humid air in the absence of CO_2.

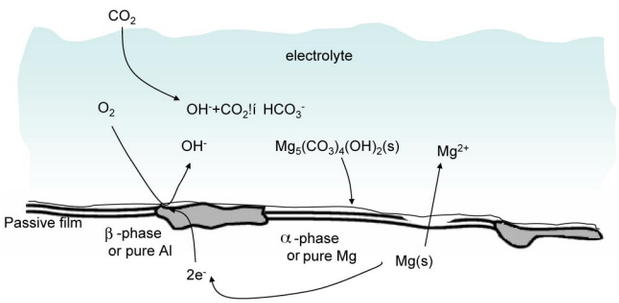

Figure 6. Suggested corrosion mechanism of the model system and AZ91D in humid air at ambient levels of CO_2.

thodic reaction on the β-phase is impaired by this insulating layer. In addition, the lower pH on the β-phase stabilizes the alumina-containing passive film. The decreased conductivity due to lower pH in the surface electrolyte will also tend to slow down electrochemical corrosion.

Conclusions

AFM/SKPFM was used for studying the initial stages of atmospheric corrosion of the two-phase MgAl alloy AZ91D and of a model system consisting of spots of pure Al deposited on Mg. AFM/SKPFM allows for the simultaneous *in situ* investigation of the topography and the Volta potential during exposure, the resolution being in the submicrometer range. The results show that CO_2 strongly influences the atmospheric corrosion of AZ91D and of the model system. In the absence of CO_2, the corrosion attack tends to be localized while it more evenly distributed in the presence of CO_2. It is suggested that the influence of CO_2 is connected to the formation of an insulating magnesium hydroxy carbonate film that interferes with the anodic and cathodic processes on the surface.

Acknowledgments

Max-Planck-Institut für Eisenforschung, the Swedish Research Council, the EC project Mg-Chassis, contract number G3RD-CT-2000-00287, and Volvo Car Corporation are gratefully acknowledged for their support to the project.

References

1. *ASM Specialty Handbook: Magnesium and Magnesium Alloys*, M. Avedesian and H. Baker, Editors, ASM, Materials Park, OH (1998).
2. R. Lindström, L. G. Johansson, and J.-E. Svensson, *Mater. Corros.*, **54**, 587 (2003).
3. K. S. Ferrer and R. G. Kelly, in *Critical Factors in Localized Corrosion-IV*, S. Virtanen, P. Schmuki, and G. S. Frankel, Editors, PV 2002-24, p. 176, The Electrochemical Society Proceedings Series, Pennington, NJ (2002).
4. T. Falk, J. E. Svensson, and L. G. Johansson, *J. Electrochem. Soc.*, **145**, 39 (1998).
5. D. B. Bluecher, J. E. Svensson, and L. G. Johansson, *J. Electrochem. Soc.*, **150**, B93 (2003).
6. S. Yee, R. A. Oriani, and M. Stratmann, *J. Electrochem. Soc.*, **138**, 55 (1991).
7. M. Stratmann and H. Streckel, *Corros. Sci.*, **30**, 681 (1990).
8. P. Leblanc and G. S. Frankel, *J. Electrochem. Soc.*, **149**, B239 (2002).
9. J. Zhao, G. Frankel, and R. L. McCreery, *J. Electrochem. Soc.*, **145**, 2258 (1998).
10. F. Andreatta, M. M. Lohrengel, H. Terryn, and J. H. W. de Wit, *Electrochim. Acta*, **48**, 3239 (2003).
11. V. Guillaumin, P. Schmutz, and G. S. Frankel, *J. Electrochem. Soc.*, **148**, B163 (2001).
12. P. Schmutz and G. S. Frankel, *J. Electrochem. Soc.*, **146**, 4461 (1999).
13. P. Schmutz, V. Guillaumin, R. S. Lillard, J. A. Lillard, and G. S. Frankel, *J. Electrochem. Soc.*, **150**, B99 (2003).
14. M. Femenia, C. Canalias, J. Pan, and C. Leygraf, *J. Electrochem. Soc.*, **150**, B274 (2003).
15. M. Rohwerder, E. Hornung, and M. Stratmann, *Electrochim. Acta*, **48**, 1235 (2003).
16. M. Nonnenmacher, J. Greschner, O. Wolter, and R. Kassing, *J. Vac. Sci. Technol. B*, **9**, 1358 (1991).
17. H. O. Jacobs, H. F. Knapp, and A. Stemmer, *Rev. Sci. Instrum.*, **70**, 1756 (1999).
18. H. O. Jacobs, P. Leuchtmann, O. J. Homan, and A. Stemmer, *J. Appl. Phys.*, **84**, 1168 (1998).
19. F. Robin, H. Jacobs, O. Homan, A. Stemmer, and W. Bachtold, *Appl. Phys. Lett.*, **76**, 2907 (2000).
20. M. Rohwerder, P. Leblanc, G. S. Frankel, and M. Stratmann, in *Methods for Corrosion Science and Engineering*, Marcel Dekker, Inc., New York (2004).
21. W. Furbeth and M. Stratmann, *Prog. Org. Coat.*, **39**, 23 (2000).
22. M. Stratmann, *Corros. Sci.*, **27**, 869 (1987).
23. A. K. Henning, T. Hochwitz, J. Slinkman, J. Never, S. Hoffmann, P. Kaszuba, and C. Daghlian, *J. Appl. Phys.*, **77**, 1888 (1995).
24. T. Hochwitz, A. K. Henning, C. Levey, and C. Daghlian, *J. Vac. Sci. Technol. B*, **14**, 457 (1996).
25. H. N. McMurray and G. Williams, *J. Appl. Phys.*, **91**, 1673 (2002).
26. H. P. Godard, W. B. Jepson, M. R. Bothewell, and R. L. Kane, in *The Corrosion of Light Metals*, p. 372, Wiley, New York (1967).
27. R. M. Smith and A. E. Martell, in *Critical Stability Constants*, Vol. 4: *Inorganic Complexes*, p. 257, Plenum, New York (1976).
28. H. Kaesche, in *Passivity of Metals*, R. P. Frankenthal and J. Kruger, Editors, p. 935, The Electrochemical Society Corrosion Monograph Series, Princeton, NJ (1978).
29. R. Lindstrom, J. E. Svensson, and L. G. Johansson, *J. Electrochem. Soc.*, **149**, B103 (2002).

Paper 5

Influence of ppb levels of SO_2 on the Atmospheric Corrosion of Aluminum in the Presence of NaCl

D. Bengtsson Blücher*, J-E. Svensson*, and L. G. Johansson*

Department of Chemical and Biological Engineering,

Chalmers University of Technology

SE-412 96 Göteborg, SWEDEN

danielb@chalmers.se

Abstract

The effect of ppb levels of SO_2 on the atmospheric corrosion on Al (99.999%) is investigated in the laboratory at 22°C. Exposure time is 20 and 672h. The effect of SO_2 concentration (46-1300ppb), relative humidity (70-99% RH) and the amount of NaCl applied prior to exposure (0-250µg/cm^2) was studied. In addition, the effect of O_3 and NO_2 on the SO_2 deposition rate is addressed. The samples are investigated by gravimetry, Gracing Incidence X-Ray powder diffraction (GI-XRD), ion chromatography (IC), optical microscopy (OM) and Environmental Scanning Electron Microscopy (E-SEM) equipped with Energy Dispersive X-Ray Fluorescence (EDX). SO_2 accelerates the atmospheric corrosion of Al, forming corrosion product "islands" containing aluminum hydroxy sulfate. Combining NaCl and SO_2 has a synergistic effect on the average corrosion rate. In contrast, the chloride-induced pitting of aluminum is significantly reduced by SO_2. The corrosivity of SO_2 is attributed to the acidification of the surface electrolyte that destabilizes the alumina passive film. The suppression of pitting corrosion by SO_2 is attributed to the formation of aluminum hydroxy sulfates that are less soluble than the corresponding chlorides and slows down pit propagation. At relative humidities above 70% RH, there is a measurable steady-state deposition of SO_2 that corresponds to the rate of formation of sulfate. The SO_2 deposition rate is not limited by the oxidation of (IV)-valent sulfur on the surface. SO_2 deposition is enhanced by sodium chloride because the corrosion reactions in the NaCl(aq) electrolyte result in high pH in the cathodic regions and the formation of aluminum hydroxide. Ozone in the ppb range has only transient effects on the SO_2 deposition rate whereas ppb-levels of NO_2 had no effect at all.

Introduction

The atmospheric corrosion of aluminum is basically electrochemical in nature[1], the corrosion process occurring in a thin layer of aqueous electrolyte. When aluminum is exposed to neutral and slightly acidic aqueous solutions containing chloride or other depassivating anions, the passive film tends to suffer local breakdown, giving rise to localized forms of corrosion[2]. Accordingly, pitting is the dominant type of aluminum corrosion in the atmosphere. Aluminum corrosion in the atmosphere has mainly been investigated by field studies[3-8]. Few laboratory investigations in controlled environments have been published[9-14]. Corrosion products formed on aluminum in the atmosphere usually contain appreciable amounts of sulfates and chlorides[4, 15]. Most authors agree that, besides the usual strong humidity dependence, SO_2 and chlorides are the most important corrosion accelerators for Al in the atmosphere. The corrosivity of chloride is expected because it is known to cause pitting of aluminum in aqueous solution[2]. The corrosivity of SO_2 may be related to its acidic nature as well as to the influence of soluble sulfates. It has been suggested that oxidizing agents such as O_3 and H_2O_2 can play a role in the atmospheric corrosion of aluminum in the presence of SO_2[4].

Sulfur dioxide is a major pollutant and the most important cause of acid rain[16]. The application of extensive air-pollution control technologies since the 1980s has lead to a decrease in SO_2 concentrations in many regions. The maximum concentration of SO_2 (24h average) in Göteborg, Sweden, in 2003 was 6 ppb[17]. The levels of particulate chloride deposition reported from the field cover a very wide range, from 15µg $Cl^-cm^{-2}y^{-1}$ in rural areas far from the coast[6] to >55000µg $Cl^-cm^{-2}y^{-1}$ in extreme marine environments[7]. The corrosivity of sulfur dioxide towards metals exposed in the atmosphere was first investigated by Vernon[13]. Few laboratory studies address the influence of low concentrations of SO_2 on the atmospheric corrosion of aluminum in the presence of NaCl[10, 18, 19].

Recently, we reported on the inhibiting effect of carbon dioxide towards the atmospheric corrosion of aluminum in the presence of NaCl[20]. The corrosion rate of Al was found to be 20 times higher in the absence of CO_2 compared to exposures in air with 350ppm CO_2. It was concluded that in the absence of carbon dioxide, the cathodic reaction gives rise to high pH regions in the surface electrolyte. In alkaline solution the passive film on aluminum tends to dissolve as aluminate ions, resulting in relatively rapid general corrosion. In the presence of CO_2 and NaCl, aluminum exhibits the usual pitting type corrosion. The inhibitive role of CO_2

was attributed to its acidic properties resulting in a buffering of the surface electrolyte. The results suggest that the corrosion accelerating effect of NaCl towards aluminum in neutral and slightly acidic conditions is mainly due to the depassivating effect of chloride ions. In contrast, when there is no acidic gases present, NaCl causes rapid general corrosion because high pH regions develop in the electrolyte. This mechanism of aluminum corrosion relies on the fact that sodium hydroxide is soluble. The latter type of behavior can occur in situations where the access of the ambient air is restricted, i.e. in crevices, lap joints and beneath coatings.

While SO_2 is expected to promote the atmospheric corrosion of aluminum because of its acidity, its effect on pitting is not known. The aim of this study is to investigate the effect of low SO_2 concentrations (ppb levels) on the atmospheric corrosion of pure aluminum in the presence and in the absence of. NaCl. In order to achieve this aim the deposition of SO_2 was also studied. The effect of oxidizing agents, *i.e.*, O_3 and NO_2, on SO_2 deposition rate on Al is also addressed.

Experimental

Sample preparation

High purity Al (99.999%) from Goodfellow was used in all experiments. The main impurities were Fe 0.7ppm, Mg 1.45ppm, S 0.9ppm and Si 0.99ppm. The samples had a geometrical area of 20.0cm^2 (3.0x3.0x0.17)cm. Before exposure the samples were ground on SiC paper in ethanol to 1000 mesh and then polished with 1µm diamond paste in blue lubricant from Struers. The samples were ultrasonically cleaned in ethanol, dried in air and stored in a desiccator over silica gel for 2h. Sodium chloride was added by spraying the samples with a saturated solution of NaCl in 80/20 ethanol/water. The amount of NaCl added (0-250µg/cm^2) was determined gravimetrically. Care was taken to avoid droplet formation on the samples during spraying. The distribution of salt on the surface after spraying was even as seen with E-SEM.

Experimental setup

Two different experimental approaches are used in this study: i) 672 h corrosion studies to determine the corrosion rate and the formation of corrosion products, see Fig. 1a and ii) Time-Resolved trace gas Analysis of the Deposition (TRAD) to investigating the deposition rate of SO_2, NO_2 and O_3 on Al during the first 20h of exposure, see Fig. 1b. Both kinds of experiments were performed in a well-controlled synthetic environment. The exposure systems are made entirely of glass and Teflon. The samples are suspended in a thin nylon string in the middle of the chamber. The corrosion chambers are immersed in a water tank held at constant temperature (22.0±.03 °C). To avoid condensation in the parts of the system outside the water tank the temperature in the room is kept at 25°C. The exposure gas is prepared from dried and purified air. Because the air purification system removes most of the CO_2 in the air we achieve a carbon dioxide concentration of 350ppm by adding pure CO_2 from a cylinder and monitoring the concentration. Relative humidity is regulated by mixing dry air and air saturated with water vapor. Relative humidity was 70, 90, 95 or 99 % and was controlled with an accuracy of ± 0.3 %. SO_2(g) and NO_2(g) were added to the dry air stream using permeation tubes manufactured by the authors. The permeation rate of the SO_2 tubes correspond to SO_2 concentrations of 46, 108, 546 and 1372 ppb in the exposure gas. The permeation rate of the NO_2 tube correspond to a concentration of 560ppb. O_3(g) was added to the dry purified air flow by means of an ozone generator (UV radiation, λ<230nm) to form atomic oxygen which then reacts with dioxygen molecules to form O_3(g). The gas flow was

1000mL/min in all exposures resulting in a net gas velocity of 2.7 cm/s in the cell (laminar flow conditions corresponding to a Reynolds number (R_e) of 50).

Corrosion studies (672h)

The equipment used in the corrosion exposures has been described previously[20]. There are eight parallel chambers, see Fig. 1a. The whole gas flow (1000mL/min) passes through each chamber in turn for 15 s. The chambers have an inner diameter of 55 mm and a volume of 0.4 l. The net gas flow is 7mm/sec (R_e=25) in an empty chamber. In order to avoid interactions between samples, only one sample is exposed in each chamber. The relative humidity was 95% and was controlled to an accuracy of about 0.3%. The SO_2 content in the gas leaving each chamber was determined by absorbing in 1% H_2O_2(aq) solution and analyzing as sulfate using ion chromatography. In order to determine the amount of SO_2 deposited on the samples, we compared this analysis to the results obtained using two empty corrosion chambers that were used as blanks. The deposition of SO_2 by the exposure apparatus was <1%.

To monitor the corrosion process during exposure the samples were weighed once a week. In order to avoid disturbing the corrosion process, the samples were not dried before weighing. The weighing procedure lasted two minutes per sample. The mass gain recorded in this way is termed the wet mass gain. After the completion of the 672 h exposures the dry mass gain of the samples was determined after storing over a desiccant at ambient pressure and temperature for one week.

The amount of corrosion products was determined by leaching and pickling the samples using ultrasonic agitation. The water-soluble corrosion products and unreacted NaCl were first removed by leaching in milli-Q water (pH 7) at ambient temperature for 1minute and then for 30 minutes. The amount of sulfate and chloride removed by leaching was determined by IC and the sample mass was recorded. Thereafter the samples were pickled in a solution containing H_3PO_4 and CrO_3 (1 l solution is prepared by mixing 50 ml H_3PO_4 (85%) and 20.0 g CrO_3 with milli-Q water) for 5 minutes at 80°C and then washed in water and ethanol. This procedure was repeated three times. The sample mass was recorded after each step. Weighing the samples after the leaching and pickling process provides a measure of the metal loss. The metal loss caused by pickling is measured using a blank and by measuring mass loss as a function of time on exposed samples. This effect was corrected for in the determination of the metal loss of the exposed samples. IC is used to analyze quantitatively for water-soluble anions (e.g. chloride and sulfate) on the samples after exposure (Dionex DX100 with an

Ionpac AD9-SC column). The flow rate was 2 ml/min and 1.8 mM Na_2CO_3 / 1.7 mM $NaHCO_3$ was used as eluent. GI-XRD is used for characterization of crystalline corrosion products (Siemens D-5000 CuK_α radiation equipped with a Göbel mirror). The diffraction peaks of metallic aluminum were used as an internal standard. The samples were also studied by E-SEM (Electroscan 2020) and EDX (Link ISIS).

Auger electron spectroscopy (AES) was used to determine the composition of the corrosion product layer by performing depth profiling. The AES analyses were performed with a Scanning Auger Microprobe (SAM) instrument (PHI 660). The primary accelerating voltage was 10kV and the beam current was 75nA. The depth profiles were obtained using a differentially pumped ion gun (Ar^+) with acceleration voltage 4.0kV. The etch rates were calibrated on a flat sample of Ta_2O_5 with a known oxide thickness of 100nm. The collected raw-data was refined using MultiPak v.6.0 software. The spectra were recorded with a step size of 1eV. The angle between the primary beam and the normal to the sample surface was 30°.

Time-resolved trace gas analysis (SO_2, NO_2 O_3)(20h)

The experimental setup used in the SO_2 deposition studies is described in Fig. 1b. A detailed description of the experimental technique has been presented elsewhere[21]. The set-up consists of a single exposure chamber with continuous flow and real-time analysis of SO_2, NO_x and O_3 in the output gas. SO_2, NO_2 and O_3 were added to the dry, purified air stream as described above. SO_2 was analyzed by a fluorescence instrument (Environnment AF21M), the sensitivity being 1 ppb. The ozone concentration in the output gas was analyzed by using an instrument based on UV photometry (Dasibi 1108). NO and NOx were analyzed by a chemiluminescence instrument (Environnment AC 30M). Before the start of each experiment the interaction of the pollutant with the reactor has reached a steady state so that the output gas from the corrosion chamber has a constant composition. An experiment is started when the sample is introduced into the chamber. The mass transfer-limited deposition of SO_2 is measured using an "ideal absorber". The latter is prepared by covering a standard sample or a dummy sample made from glass with a thin layer of NaOH(aq). The deposition rate ($ng/cm^2 \cdot s^{-1}$) and the deposition velocity ($cm \cdot s^{-1}$) on the samples are determined by measuring the difference between the input and output concentrations of the pollutants. The deposition velocity V_d is defined as the flux of an air pollutant to a surface, divided by the concentration in the gas: $V_d = F/c$ where F is the flux to the surface ($g \cdot cm^{-2} s^{-1}$) and c is the concentration of

the pollutant in the gas ($g \cdot cm^{-3}$) [22]. In our exposures, the concentration of the SO_2 is taken as the mean of the input and output concentrations in the cell. The same analytical techniques were used to analyze the samples after exposure as described above.

Results

Corrosion studies

The effect of SO_2 in the absence of NaCl

After 672 h in 96ppb SO_2 (95%RH, 22.0°C) the samples had lost much of their metallic lustre. White corrosion product "islands" formed early during exposure. The "islands" grew laterally with time, in some cases resulting in the coalescence of individual "islands". After 672 h about 50% of the sample surface was covered by evenly distributed 0.2mm diameter corrosion product islands (see ESEM image in Fig. 2). EDX indicated that the corrosion product crusts had a constant composition with about 66at%O, 27at%Al and 7at%S. Auger depth profiling showed that the oxide film between the crusts had a thickness of about 7nm. Table I presents dry mass gain and metal loss data for samples exposed with and without SO_2. Table I confirms that SO_2 is a powerful corrosion accelerator towards aluminum. These data may be used to determine the corrosion product ratio (total corrosion product mass/metal loss). Corresponding ratios for various aluminum corrosion products are presented in Table II. The slope of the mass gain curves in Fig. 3 indicates that there is an ongoing corrosion process in the presence of SO_2 while there is essentially no corrosion in the absence of SO_2. This is in accordance with the corrosion rate measurements in Table I. The corrosion rate after 672 h is <0.001mg/cm^2 in the absence of SO_2, whereas it is 0.016mg/cm^2 in the presence of SO_2. The deposition of SO_2 on aluminum in the absence of NaCl was approximately constant with time, 35±5% after one week to about 30±5% after 672 h. Based on the measured deposition rate of SO_2 and the corrosion product mass (672 hours, 96 ppb SO_2 see Table I) we can calculate the average sulfur content in the corrosion product. The amount of corrosion product in this case is 0.076mg/cm^2 (0.06 mass gain + 0 016 metal loss) corresponding to a total mass of 1.52 mg/sample. The amount of sulfate in the corrosion product is 6.0 μmoles/sample (determined indirectly by IC of the gas trap solution). By the electroneutrality condition, the amount of aluminum ions associated to sulfate is then 2/3 x 6.0 = 4.0 μmoles/sample. Assuming that the charge of the aluminum ions in the corrosion product is balanced by hydroxide and sulfate and that there is no water of hydration, the average corrosion product composition can be calculated. The calculation shows that the average sulfur content in the corrosion product (disregarding hydrogen) is 7.8 at%, in agreement with the 7 at% obtained by EDX (see above). The fraction of water leachable sulfate decreased from 90% after one week exposure to 56% after 672 h, indicating that insoluble sulfate forms on the surface with time. For the formation of crystalline corrosion products; see below.

The effect of NaCl in clean air (without SO_2)

The atmospheric corrosion of aluminum exposed to NaCl in clean, CO_2-containing air was described in a previous paper[20] and will not be described in detail here. Suffice it to say that the samples develop a small number of deep (10-20µm) pits covered by corrosion product crusts. Chloride is invariably found at the bottom of the pits. IR spectroscopy indicated the presence of amorphous sodium aluminum hydroxy carbonate ($NaAl(OH)_2CO_3$) on the sample surface. Recently, crystalline and amorphous dawsonite was also identified as a corrosion product on an AlSiMg alloy exposed to NaCl in humid air[23].

The effect of SO_2 in the presence of NaCl

The samples were visibly corroded after exposure to NaCl + SO_2. After 672 hours about 60% of the surface was covered by evenly distributed spheroidal white corrosion product islands with a diameter of a 100-250µm, see ESEM image in Fig 2. AES depth profiling showed that the oxide film between the crusts had a thickness of about 17nm. By EDX the composition of the crusts was found to be 15at%Al, 73at%O, 5at%Na, 4at%Cl and 4at%S. E-SEM/EDX analysis of a cross sections (prepared by Focussed Ion Beam, FIB) of the crusts showed no enrichment of Cl or S in the interface between the corrosion scale and the metal. The pits seen after pickling were much shallower (about 2µm). Fig. 4 shows wet mass gain as a function of time. A rapid initial wet mass gain was registered, mainly reflecting the formation of NaCl(aq). Accordingly, the samples became visibly wet directly upon exposure. The same behavior was exhibited in the absence of SO_2. The slope of the mass gain curve is greater in the presence of SO_2 compared to the clean air run indicating an ongoing corrosion process. Table I shows that after 672 hours corrosion is 3-4 times faster when SO_2 is present compared to samples exposed to NaCl in the absence of SO_2. The addition of NaCl in the presence of SO_2 can be seen to result in a doubling of the corrosion rate. The corrosion product ratio after 4 weeks (4.3) is significantly lower than for the case without NaCl (4.8). In the presence of NaCl, the deposition of SO_2 was (65%±5%) during the first week exposure. After 672 h exposure, the adsorption had decreased to about 55%±5%. The amount of leachable sulfate found after one and 672 h exposure were 50% and 40%, respectively. More than 99% of the added chloride could be removed by leaching in water.

Time-resolved trace gas analysis (SO_2, NO_2 O_3)(20h)

Influence of SO_2 concentration

Fig. 5 shows the deposition of SO_2 on Al as a function of time at different SO_2 concentrations (95% RH). During the first few minutes of exposure the deposition of SO_2 is very rapid in all environments studied. Thereafter, the deposition rate decreases rapidly and a steady state is reached after approximately 3 hours. It is notable that increasing the SO_2 concentration 30 times from 46ppb to 1372ppb only results in a threefold increase in the steady state deposition rate, see Table III. This means that the deposition velocity, V_d, is ten times lower at higher pSO_2.

Influence of NaCl

The deposition of SO_2 on aluminum pre-treated with different amounts of NaCl is illustrated in Fig. 6 as a function of exposure time (108ppb SO_2, 95%RH). Table IV shows the corresponding deposition rates and deposition velocities. The presence of NaCl strongly increases the steady-state deposition rate of SO_2 on aluminum. Even the smallest NaCl addition studied (14 $\mu g/cm^2$) results in about 16 times greater deposition rate after 20 hours compared to samples exposed without NaCl. The deposition of SO_2 on an ideal absorber (NaOH treated Al or glass) is presented for comparison. For smaller NaCl additions, an initial decrease in the deposition rate is evident. After a few hours, the SO_2 deposition rates are about the same irrespective of the amount of NaCl added prior to exposure. The results indicate that aluminum areas covered with NaCl(aq) approach the behavior of an ideal absorber for SO_2. In the case of a sample pretreated with 70µg $NaCl \cdot cm^{-2}$ and exposed for 96ppb SO_2 for 20h, about 60% of the deposited SO_2 could be removed as SO_4^{2-} by water leaching. This is twice the corresponding value found in the absence of NaCl. All the added chloride was retrieved by IC on water leaching solutions. A sample pretreated with 70µg $NaCl \cdot cm^{-2}$ exposed to 108ppb SO_2 for 20 days at 95%RH and 22.0°C was analyzed with GI-XRD using a cooled sample holder in order not to decompose possible crystalline hydrates in the corrosion products. By this technique evidence was found for small amounts of aluminite ($Al_2SO_4(OH)_4 \cdot 7H_2O$). This was the only crystalline corrosion product identified in this work.

Influence of SO_2 concentration on deposition rate in the presence of 70µg $NaCl \cdot cm^{-2}$

Fig. 7 shows the deposition of SO_2 as a function of time on aluminum with 70µg $NaCl \cdot cm^{-2}$ at different SO_2 concentrations (95%RH). Table V tabulates the corresponding deposition rates

and deposition velocities. Compared to exposures in the absence of NaCl, the steady state deposition rates are five times higher at 46 ppb SO_2, 20 times higher at 108ppb SO_2 and 15 times higher at 546ppb SO_2, see Table III and V. All the added chloride was removed by water leaching as evidenced by IC. Depending on the SO_2 concentration, steady state was reached after 20 to 10 hours. At steady state, a 12-fold increase in the SO_2 concentration from 46 to 546ppb results in a sevenfold increase of the deposition rate.

Influence of O_3 and NO_2 on SO_2 deposition

Fig. 8 shows the deposition of SO_2 on Al samples in the presence of O_3 or NO_2 as a function of time (108ppb SO_2, 95%RH). The deposition velocity and the deposition rate after 20 hours exposure can be seen in Table VI. The addition of 200ppb O_3 initially has a small effect on the SO_2 deposition rate, see Fig. 8 and Table VI. A 20% increase in the SO_2 deposition rate was observed directly after the addition of ozone. However, the effect was only transient and disappeared within one hour. The addition of 560ppb NO_2 to the gas stream had no detectable effect on the SO_2 deposition rate. The NO_2-added deposition results are therefore not presented.

Influence of relative humidity

As expected, relative humidity has a crucial importance for the deposition rate of SO_2 on aluminum (Fig. 9). At 90% RH and below, the SO_2 deposition rate is close to the limit of detection after about 10h. Increasing the relative humidity from 95 to 99% resulted in an increase in the SO_2 deposition rate by a factor of ten after 20 hours. The deposition velocities at steady state were about 25 times higher at 99% RH compared to exposures at 70% RH, see Table VII.

Desorption of SO_2

After exposing pure Al to 108ppb SO_2 at 22.0°C and 95%RH for 5h, the sample was transferred to a desorption cell flushed with N_2(g) (22.0°C, 95%RH). The output gas from the cell was studied by time-resolved SO_2 analysis. The amount of SO_2 desorbed from the sample corresponded to about 5% of the total amount of SO_2 deposited on the surface.

Deposition of NO_2 and O_3

At 95%RH and in the presence of 200ppb O_3 and 560ppb NO_2, respectively, there was no detectable deposition of either gas on aluminum. This was the case irrespective of whether NaCl was present on the surface or not.

Discussion

As noted in the introduction, the atmospheric corrosion of aluminum is an electrochemical process occuring in a surface electrolyte which is normally neutral or slightly acidic. Under those conditions the anodic dissolution of aluminum as $Al^{3+}(aq)$ is balanced by hydrogen evolution or oxygen reduction:

$$Al(s) \rightarrow Al^{3+}(aq) + 3e^- \quad [1]$$

$$1/2O_2(g) + H_2O + 2e^- \rightarrow 2OH^-(aq) \quad [2]$$

$$2H^+(aq) + 2e^- \rightarrow H_2(g) \quad [3]$$

$$Al^{3+}(aq) + 3OH^-(aq) \rightarrow Al(OH)_3(s) \quad [4]$$

According to Kaeshe[1], aluminum pitting is initiated through the adsorption of anions, *e.g.* chloride, on the alumina surface, causing local dissolution of the passive film. This is supported by Stumm and Furrer who report that the dissolution of γ-alumina in aqueous solutions is promoted by the formation of surface complexes with anionic ligands[24]. The adsorption of ions from a solution critically depends on surface charge, the alumina surface being positively charged in acidic conditions while it is negatively charged in alkaline media. The pH of zero charge of γ-alumina in chloride solution is about 7.5[25], other forms of alumina exhibiting similar values. The negative surface charge of alumina at high pH makes chloride adsorption unfavorable, explaining why chloride does not promote pitting corrosion in alkaline solution. In such a solution aluminum suffers general corrosion because of dissolution of the alumina film as aluminate[1]. As noted in the introduction, the strong inhibitive effect of CO_2 towards the NaCl induced corrosion of aluminum depends on its acidic character. When aluminum is exposed to humid air containing CO_2 in the presence of NaCl the surface electrolyte tends to be neutral or slightly acidic, stabilizing the passivating alumina film. As a result, the comparatively slow atmospheric corrosion of aluminum in the presence of NaCl and CO_2 takes the form of pitting corrosion. This is in accordance with pitting being the dominant mode of aluminum corrosion in the atmosphere[26]. The sensitivity of aluminum towards pitting corrosion varies greatly depending on the nature of the anion, chloride being a well-known pitting promoter. It is reported that while sulfate adsorbs on alumina and can be incorporated in the passive film, it does not promote aluminum pitting[1, 27, 28]. On the contrary, sulfate is reported to slightly inhibit the chloride-induced pitting of aluminum. It is suggested that these differences can be partly attributed to the influence of the

solubility of the corresponding hydroxy salts on pit propagation. While all aluminum hydroxy chlorides are very soluble in water, the solubility of the corresponding sulfates is much smaller (Compare the proportion of leachable sulfate and chloride in the results part). It is suggested that pit propagation is slow in the presence of sulfate because of the precipitation of aluminum hydroxy sulfates in the pit.

Sulfur dioxide is expected to influence aluminum corrosion in humid air because of its acidic character:

$$SO_2(g) \leftrightarrows SO_2(ads) \quad [5]$$

$$SO_2(ads)+H_2O \leftrightarrows H^+(ads)+HSO_3^-(ads) \quad [6]$$

$$HSO_3^-(ads) \leftrightarrows H^+(ads)+SO_3^{2-}(ads) \quad [7]$$

The oxidation of (IV)-valent sulfur on the surface to sulfate produces more acid:

$$SO_2(ads)+ H_2O+½O_2 \rightarrow 2H^+(ads)+SO_4^{2-}(ads) \quad [8]$$

The sulfuric acid formed is strongly hygroscopic and forms a surface electrolyte that reacts with the surface, converting the passivating alumina film to aluminum hydroxy sulfate, *e.g.*, $Al_2SO_4(OH)_4{\cdot}7H_2O$:

$$2Al(OH)_3(s) + 2H^+(aq) +SO_4^{2-}(aq) + 5H_2O \rightarrow Al_2SO_4(OH)_4{\cdot}7H_2O(s) \quad [9]$$

It is suggested that the resulting thinning of the oxide triggers electrochemical corrosion cells (reactions 1-3).

At low relative humidity, SO_2 deposition on alumina is a transient process. In this case, reactions [5-7] are the only processes running and no net deposition occurs once equilibrium is reached. Above 70% RH, the deposition of SO_2 does not stop after the initial transient reaction. This implies that the adsorbed SO_2 continues to react on the surface according to reactions [8] and [9]. The "steady state" SO_2 deposition would therefore correspond to the rate of formation of sulfate [8, 9]. The desorption of SO_2 from a sample exposed for 5 hours (108ppb SO_2 95%RH) supports this view, showing that part of the deposited SO_2 is present in the form of loosely bonded (IV)-valent sulfur. Most of the SO_2 deposition curves in Fig. 9

exhibit the expected monotonic decrease in the rate of SO_2 deposition. The 99% RH curve is an exception. The shape of that curve suggests that other reactions are active at very high water activities. It has been reported that, in the absence of contaminants, aluminum corrosion is relatively fast in contact with liquid water while it is very slow when liquid water is absent, even though relative humidity is high[29]. 99% RH represents a case when we are very close to condensation and it is suggested that the properties of the surface water approaches those of bulk water at this humidity, meaning that electrochemical corrosion reactions occur. The rapid uptake of SO_2 would then be a consequence of this corrosion reaction. The first (transient) part of the SO_2 deposition curves in Fig. 5 is fairly independent of SO_2 concentration. This is expected since deposition is dominated by SO_2 adsorption at this stage, the number of available surface sites being only weakly dependent on SO_2 concentration. At steady state, however, we do detect a relatively weak concentration dependence implying that the rate of sulfate formation [8, 9] depends on SO_2 concentration.

The influence of ozone on SO_2 deposition is informative. Being a potent oxidant, ozone readily oxidizes adsorbed (IV)-valent sulfur to sulfate[30]. When the oxidation of surface sulfite to sulfate is rate-limiting for SO_2 deposition, the addition of ozone therefore results in an increase in the SO_2 deposition rate[31]. In the present case, adding O_3 at a stage when the system has reached steady-state results in an increase in SO_2 deposition rate on Al by about 20%, (see Fig. 8). However, the effect disappears within 1 hour. The limited effect of ozone on SO_2 deposition implies that oxidation of (IV)-valent sulfur is not rate-limiting for SO_2 deposition. This is in accordance with the lack of influence of NO_2 additions on SO_2 deposition. It is suggested that the rate-limiting reactions in our case are the sulfatation of the passive film [9] or the formation of fresh $Al(OH)_3(s)$[4].

The exposure of aluminum to ppb levels of SO_2 results in the formation of corrosion product islands that cover about 50% of the surface after 672 h. There is no pitting and sulfate is evenly distributed in the islands. This is in accordance with the literature reports stating that, while sulfate adsorbs on alumina and can be incorporated in the passive film, it does not promote aluminum pitting[1, 28]. On the contrary, sulfate is reported to slightly inhibit the chloride-induced pitting of aluminum. In the present study, the average corrosion product composition (after 672 h exposure) corresponds to a mixture of aluminum hydroxide and aluminum hydroxy sulfate (compare the measured corrosion product ratio (4.8) in Table I with the corresponding values for the pure corrosion products in Table II). The fact that only

parts of the surface sulfate was leachable in water is in accordance with literature reports on the existence of sparingly soluble aluminum hydroxy sulfates[32].

The formation of sulfate-rich corrosion product islands shows that the alumina film is destabilized locally in the presence of SO_2 while it remains intact on other parts of the surface. This behavior is in accordance with an electrochemical corrosion mechanism. The absence of pitting implies that the anodes tend to repassivate, probably because of the formation of sparingly soluble hydroxy-sulfates. The lateral growth of the corrosion product islands would then imply a successive radial movement of the anodic areas as the "old" anodes become blocked by precipitates.

During the first few minutes of exposure the presence of NaCl has little effect on SO_2 deposition. This is expected because SO_2 deposition on Al is initially transport limited under the present conditions. The influence of NaCl becomes apparent after this initial stage. Instead of slowing down, as it does in the absence of NaCl, the rate of SO_2 deposition stabilizes at a high level (see Fig 6). One of the sinks for SO_2 in our system is the surface electrolyte:

$SO_2(g) \leftrightarrows SO_2(aq)$	[10]	K_H=1.23M/atm[30]
$SO_2(aq) + H_2O \leftrightarrows H^+(aq) + HSO_3^-(aq)$	[11]	$pK_a = 1.77$[30]
$HSO_3^-(aq) \leftrightarrows SO_3^{2-}(aq) + H^+(aq)$	[12]	$pK_a = 7.22$[30]

At 95% RH and 22 °C one g of NaCl absorbs 11.66g of water to form an aqueous solution. Calculations based on the relevant equilibrium reactions show that the reactive dissolution of SO_2 in the resulting aqueous solution can only account for an insignificant fraction of the deposited SO_2 (In the case of the greatest NaCl addition it corresponds to about two minutes of SO_2 absorption at the measured rate (see Fig 6)). This conclusion was verified by measuring SO_2 deposition on a dummy sample (made of glass) covered by the same amount of NaCl. Accordingly, SO_2 deposition rate is almost independent of the amount of NaCl applied to the aluminum samples. Another possible candidate reaction is ion exchange. Exchanging hydroxide in the alumina film for chloride from the solution releases hydroxide into solution, shifting the equilibria towards sulfite and increases SO_2 absorption. However, this process can also not explain the sustained rapid deposition of SO_2. Even a complete conversion of the passive film (assuming 2.2nm thick AlOOH film) to $Al(OH)_2Cl$ can only account for about 30 minutes worth of SO_2 deposition.

Instead it is proposed that the high SO_2 deposition rate on aluminum in the presence of NaCl is connected to the corrosion of the aluminum surface in the NaCl(aq) electrolyte. As noted above, the corrosion of aluminum in neutral or slightly acidic aqueous NaCl solution is an electrochemical process (reactions 1-3). The corrosion reaction gives rise to pH gradients over the surface, the anodic regions (at the bottom of the pits) being acidic due to hydrolysis of Al^{3+}(aq) while the cathodic regions (on the surface close to the pits) develop high pH due to the formation of hydroxide ions. The cathodic regions of the electrolyte-covered surface will therefore be efficient absorbers for SO_2 (see reactions 10-12). The continuing corrosion of aluminum in the presence of NaCl therefore explains the rapid and sustained uptake of SO_2 by the samples. In addition to this mechanism for SO_2 capture, the corrosion products formed by the hydrolysis of aluminum ions (reaction 4) also absorb SO_2.

In the present study, the combination of sulfur dioxide and sodium chloride results in a relatively rapid corrosion rate, the metal loss in SO_2 + NaCl environment being significantly greater than the sum of the metal loss recorded in the corresponding single factor exposures (see Table1). On the other hand, the chloride-induced pitting of aluminum is greatly reduced in the presence of SO_2. It is suggested that the increased rate of SO_2 deposition on aluminum in the presence of NaCl (see Fig 6) is responsible for the synergistic corrosion effect. Sulfur dioxide dissolution and sulfuric acid formation acidifies the surface electrolyte in comparison to the clean air case. This is because sulfate is stable at low pH in contrast to hydrogen carbonate, sulfuric acid being a far stronger acid than carbonic acid. The low pH destabilizes the alumina passive film, making aluminum more susceptible to corrosion. The low pH also leads to a positive surface charge of alumina, resulting in the adsorption of sulfate and chloride ions. The suppression of pitting corrosion by SO_2 is attributed to the formation of aluminum hydroxy sulfates. As noted above, our leaching results clearly show that aluminum hydroxy sulfates are much less soluble than the corresponding chlorides. It is suggested that the precipitation of aluminum hydroxy sulfates slow down pit propagation. This interpretation is supported by the fact that sulfur and chlorine occur together at the metal/corrosion product interface.

Conclusions

Sulfur dioxide is a powerful corrosion accelerator towards aluminum in humid air. The rate of SO_2 deposition on Al strongly depends on relative humidity. Sulfuric acid formation on the surface acidifies the surface electrolyte and destabilizes the alumina passive film, making aluminum more susceptible to corrosion. As a result, corrosion product "islands" form, containing aluminum hydroxy sulfate. The deposition rate of SO_2 on aluminum is not limited by the oxidation of (IV)-valent sulfur on the surface. SO_2 deposition is enhanced by sodium chloride because of the corrosion reactions in the NaCl(aq) surface electrolyte. Sodium ions support high pH in the cathodic regions resulting in reactive dissolution of SO_2. The rapid absorption of SO_2 explains the synergistic effect on the average corrosion rate seen when NaCl and SO_2 are combined. In contrast, the chloride-induced pitting of aluminum is greatly reduced in the presence of SO_2. The suppression of pitting corrosion by SO_2 is attributed to the formation of aluminum hydroxy sulfates that slow down pit propagation because they are less soluble than the corresponding chlorides. Ozone in the ppb range has only transient effects on the SO_2 deposition rate whereas NO_2 in the ppb range has no effect at all.

Acknowledgments

The Swedish Research Council and Volvo Car Corporation are gratefully acknowledged for their support to the project. Linda Ingemarsson is acknowledged for producing the E-SEM images.

References

1. H. Kaesche, *Passivity Met., Proc. Int. Symp., 4th*, 935 (1978).
2. G. Wranglen, in *An Introduction to Corrosion and Protection of Metals*, p. 288 pp., (1985).
3. G. Sowinski and D. O. Sprowls, *Atmos. Corros., [Pap. - Int. Symp. Atmos. Corros.]*, 297 (1982).
4. T. E. Graedel, *J. Electrochem. Soc.* **136**, 204C (1989).
5. R. T. Vashi and H. G. Patel, *Bull. Electrochem.* **13**, 343 (1997).
6. P. V. Strekalov, *Zashch. Met.* **29**, 819 (1993).
7. V. Kucera and E. Mattsson, in *Atmospheric corrosion*, F. Mansfield, ed., Marcel Dekker, New York (1987).
8. E. Johansson, *Rapp. - Korrosionsinst. (Stockholm)*, 53 pp. (1984).
9. B. Heimler, T. Sydberger, and N. G. Vannerberg, *Scand. Corros. Congr., Proc., 6th*, 27 (1971).
10. N. G. Vannerberg and T. Sydberger, *Corrosion Science* **10**, 43 (1970).
11. T. Sydberger and N. G. Vannerberg, *Corrosion Science* **12**, 775 (1972).
12. W. H. J. Vernon, *Transactions of the Faraday Society*, 113 (1927).
13. W. H. J. Vernon, *Trans. Faraday Soc.* **27**, 582 (1931).
14. W. H. J. Vernon, *Proceedings - Society of Chemical Industry, Chemical Engineering Group* **19**, 14 (1937).
15. M.E. Inmam, R.G. Kelly, S.A. Willard, and R. S. Piascik, in Proceedings of the FAA-NACE Symposium on Continued Airworthiness of Aircraft Structures, Atlanta,GA, USA, (1996).
16. C. Leygraf and T. E. Graedel, in *Atmospheric Corrosion*, p. 354, Wiley, New York (2000).
17. http://www.miljo.goteborg.se/, (2004).
18. K. Barton and E. Beranek, *Werkstoffe und Korrosion* **10**, 377 (1959).
19. G. Schikorr, *Werkstoffe und Korrosion* **15**, 457 (1964).
20. D. B. Blucher, R. Lindstrom, J. E. Svensson, and L. G. Johansson, *J. Electrochem. Soc.* **148**, B127 (2001).
21. J. E. Svensson and L. G. Johansson, *Corros. Sci.* **34**, 721 (1993).
22. J. A. Garland, *Atmos. Environ.* **12**, 349 (1978).
23. N. Le Bozec, D. Persson, A. Nazarov, and D. Thierry, *J. Electrochem. Soc.* **149**, B403 (2002).

24. W. Stumm and Editor, in *Aquatic Surface Chemistry: Chemical Processes at the Particle-Water-Interface*, (1987).
25. W. Stumm, in *Chemistry of the Solid-Water Interface: Processes at the Mineral-Water and Particle-Water Interface in Natural Systems*, p. 428 pp., (1992).
26. D. Bengtsson Blücher, J.-E. Svensson, and L. G. Johansson, *J. Electrochem. Soc.*, (2002).
27. W. Zhang and G. S. Frankel, *Journal of the Electrochemical Society* **149**, B510 (2002).
28. H. Boehni and H. H. Uhlig, *Journal of the Electrochemical Society* **116**, 906 (1969).
29. W. Vedder and D. A. Vermilyea, *Trans. Faraday Soc.* **65**, 561 (1969).
30. J. G. Calvert and Editor, in *Acid Precipitation Series, Vol. 3: Sulfur Dioxide, Nitrogen Oxide (NO), and Nitrogen Oxide (NO2) Oxidation Mechanisms: Atmospheric Considerations*, p. 254 pp, (1984).
31. J. E. Svensson and L. G. Johansson, *Journal of the Electrochemical Society* **140**, 2210 (1993).
32. J. L. Henry and G. B. King, *Journal of the American Chemical Society* **72**, 1282 (1950).

Tables

Table I. Corrosion rate and corrosion-product ratios at 22.0ºC.

Experimental conditions	NaCl ($\mu g \cdot cm^{-2}$)	Time of exposure (hours)	Dry mass gain ($mg \cdot cm^{-2}$)	Metal loss ($mg \cdot cm^{-2}$)	Corrosion product mass[#]/metal loss
No SO_2	0	672	<0.002	*	*
No SO_2	70	672	0.02	0.01[1]	-
96ppb SO_2	0	168	0.008	*	*
96ppb SO_2	70	168	0.036	0.011	4.3
96ppb SO_2	0	336	0.018	*	*
96ppb SO_2	70	336	0.091	0.027	4.4
96ppb SO_2	0	672	0.06	0.016	4.8
96ppb SO_2	70	672	0.12	0.036	4.3

The data shown are averages of duplicate and triplicate samples. The scatter in mass gain and metal loss results was about ±5% and the RH was 95%.
*) The mass changes were too small for metal-loss determination.
[#]) The corrosion product mass corresponds to the sum of the dry mass gain and the metal loss.
[1]) Calculated metal loss assuming that only $Al(OH)_3$ forms.

Table II. Ratios of corrosion product mass divided by aluminium mass for selected corrosion products of aluminium.

Product	Formula	Ratio[a]
Aluminum oxide	γ-Al_2O_3	1.89
Akdalait	$Al_2O_3 \cdot 1/4H_2O$	1.97
Boehmite	γ-AlOOH	2.22
Pseudoboehmite	$Al_2O_3 \cdot 2H_2O$	2.55
Bayerite	$Al(OH)_3$	2.89
Gibbsite (Hydrargillite)	γ-$Al(OH)_3$	2.89
Tucanite	$Al(OH)_3 \cdot 1/2H_2O$	3.22
Aluminum hydroxy sulfate	$Al_2SO_4(OH)_4 \cdot 4H_2O$	5.37
Aluminite	$Al_2SO_4(OH)_4 \cdot 7H_2O$	6.37
Aluminum sulfate hydrate	$Al_x(SO_4)_y \cdot z(H_2O)$	-
Aluminum chloride hydrate	$Al(H_2O)_6Cl_3$	5.00
Dawsonite	$NaAlCO_3(OH)_2$	4.48
Cadwaladerite	$AlCl(OH)_2 \cdot 6H_2O$	6.26

[a]In order to simplify a comparison with the corresponding values in Table I (corrosion rate), the sodium and chloride was omitted when these ratios were calculated.

Table III. Deposition velocity of SO_2 on aluminum after 20 hours exposure. The RH was 95% and the temperature was 22.0°C.

SO_2 Concentration (ppb)	Deposition rate ($ng \cdot cm^{-2} \cdot s^{-1}$)	Deposition velocity ($cm \cdot s^{-1}$)
46	0.004	0.037
108	0.004	0.016
546	0.01	0.008
1372	0.01	0.004

The scatter in the deposition velocities was below ± 0.001 $cm \cdot s^{-1}$ for the lower values and below ± 0.01 $cm \cdot s^{-1}$ for the higher values.

Table IV. Deposition velocity of SO_2 on aluminum after 20 hours exposure. The RH was 95% and the temperature was 22.0°C. The SO_2 concentration was 108 ppb.

Amount NaCl ($\mu g \cdot cm^{-2}$)	Deposition rate ($ng \cdot cm^{-2} \cdot s^{-1}$)	Deposition velocity ($cm \cdot s^{-1}$)
0	0.004	0.02
14	0.08	0.31
70	0.08	0.31
150	0.08	0.32
250	0.08	0.32
NaOH	0.09	0.40

The scatter in the deposition velocities was below ± 0.001 $cm \cdot s^{-1}$ for the lower values and below ± 0.01 $cm \cdot s^{-1}$ for the higher values.

Table V. Deposition velocity of SO_2 on aluminum after 20 hours exposure. The RH was 95% and the temperature was 22.0°C. The amount NaCl added was 70µg $NaCl \cdot cm^{-2}$.

SO_2 Concentration (ppb)	Deposition rate ($ng \cdot cm^{-2} \cdot s^{-1}$)	Deposition velocity ($cm \cdot s^{-1}$)
46	0.022	0.18
108	0.08	0.31
546	0.145	0.11

The scatter in the deposition velocities was below ± 0.001 $cm \cdot s^{-1}$ for the lower values and below ± 0.01 $cm \cdot s^{-1}$ for the higher values.

Table VI. Deposition velocity of SO_2 on aluminum after 20 hours exposure. The RH was 95% and the temperature was 22.0°C.

Environment	Deposition rate ($ng \cdot cm^{-2} \cdot s^{-1}$)	Deposition velocity ($cm \cdot s^{-1}$)
108ppb SO_2	0.004	0.016
108ppb SO_2 + 200ppb O_3	0.004	0.016
108ppb SO_2 + 560ppb NO_2	0.004	0.016

The scatter in the deposition velocities was below ± 0.001 $cm \cdot s^{-1}$ for the lower values and below ± 0.01 $cm \cdot s^{-1}$ for the higher values.

Table VII. Deposition velocity of SO_2 on aluminum after 20 hours exposure. The SO_2 concentration was 108 ppb and the temperature was 22.0°C.

% RH	Deposition rate ($ng \cdot cm^{-2} \cdot s^{-1}$)	Deposition velocity ($cm \cdot s^{-1}$)
99	0.048	0.19
95	0.004	0.016
90	0.002	0.008
70	0.002	0.008

The scatter in the deposition velocities was below ± 0.001 $cm \cdot s^{-1}$ for the lower values and below ± 0.01 $cm \cdot s^{-1}$ for the higher values.

FIGURE CAPTIONS

Figure 1a. Experimental set-up for exposures with 350ppm CO_2 and ppb-levels of SO_2 at 22°C and 95%RH. [1)] pure air inlet [2)]mass flow regulators [3)]humidifier [4)] NO_2 and/or SO_2 permeation tubes [5)]mixing point [6)]exposure chambers with Al samples [7)]gas trap (1% H_2O_2(aq)) [8)]solenoid valves [9)]thermostated water tank [10)]CO_2 and in some cases O_3 inlet.

Figure 1b. Experimental setup for the measurement of the SO_2 deposition rate on aluminum studied by Time-Resolved Analysis of the Deposition (TRAD) at 22°C and 95%RH [1)] pure air inlet [2)] mass flow regulators [3)] O_3 generator (UV light λ<230nm) [4)] humidifier [5)] NO_2 and/or SO_2 permeation tubes [6)] exposure chambers with Al samples [7)] real-time gas analyzers for SO_2, O_3 and NO_x-NO_2 [8)] air outlet [9)] thermostated water tank.

Figure 2. E-SEM images of aluminum exposed to [a]) 96 ppb SO_2 and no NaCl and [b)] 96 ppb SO_2 and 70µg NaCl·cm^{-2} added prior to exposure at 22.0°C for 672 h at 95% RH.

Figure 3. Wet mass gain as a function of exposure time for aluminium samples exposed to 96 ppb SO_2 (●) and to 0 ppb SO_2 (○) at 22.0°C. The RH was 95%. The samples were not coated with NaCl.

Figure 4. Wet mass gain as a function of exposure time for aluminium samples pre-treated with 70µg NaCl·cm^{-2} exposed to 96 ppb SO_2 (●) and to 0 ppb SO_2 (○) at 22.0°C. The RH was 95%.

Figure 5. Deposition rate of SO_2 on aluminium at different SO_2 concentrations as a function of time. The temperature was 22.0°C and the RH was 95%. The samples were not coated with NaCl.

Figure 6. Deposition rate of SO_2 on aluminium at different amounts of NaCl (µg·cm^{-2}) added prior to exposure as a function of time. The temperature was 22.0°C and the SO_2 concentration was 108 ppb. The RH was 95%.

Figure 7. Deposition rate of SO_2 on aluminium at different SO_2 concentrations as a function of time. The temperature was 22°C and the RH was 95%. The samples were coated with 70µg NaCl·cm^{-2} prior to exposure.

Figure 8. The influence of 200ppb O_3 on the deposition rate of SO_2 on aluminium as a function of time. The temperature was 22.0°C and the RH was 95%. The SO_2 concentration was 108ppb. The samples were not coated with NaCl.

Figure 9. Deposition rate of SO_2 on aluminium at different RH as a function of time. The temperature was 22.0°C and the SO_2 concentration was 108 ppb. The samples were not coated with NaCl.

Fig. 1

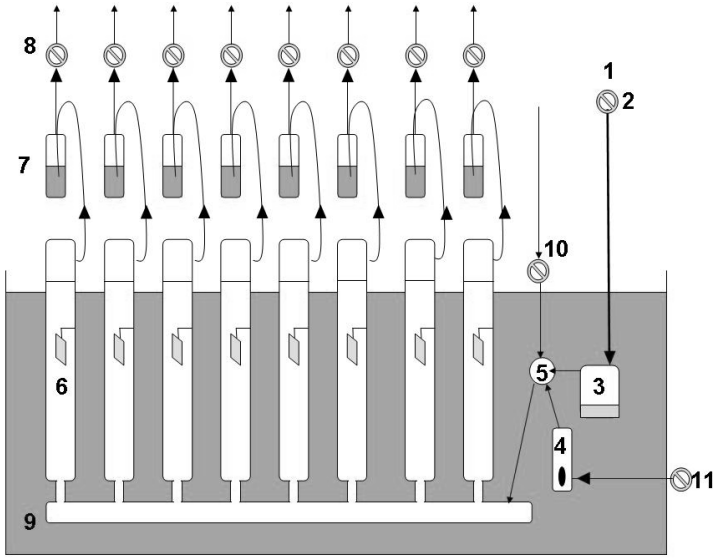

Fig. 1b

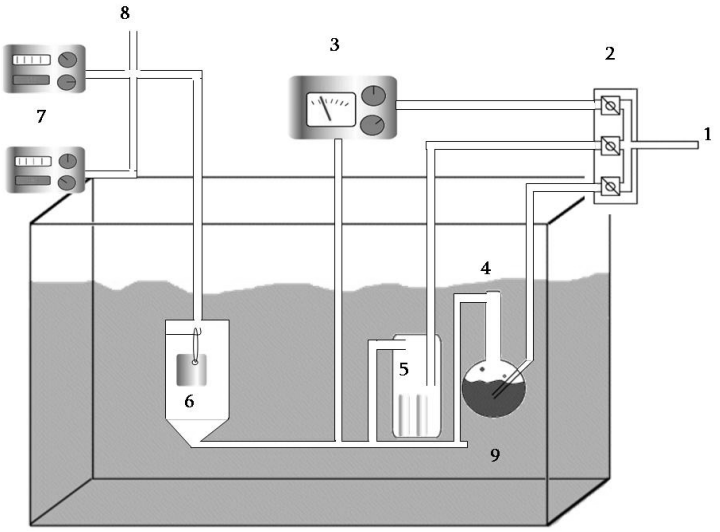

Fig. 2

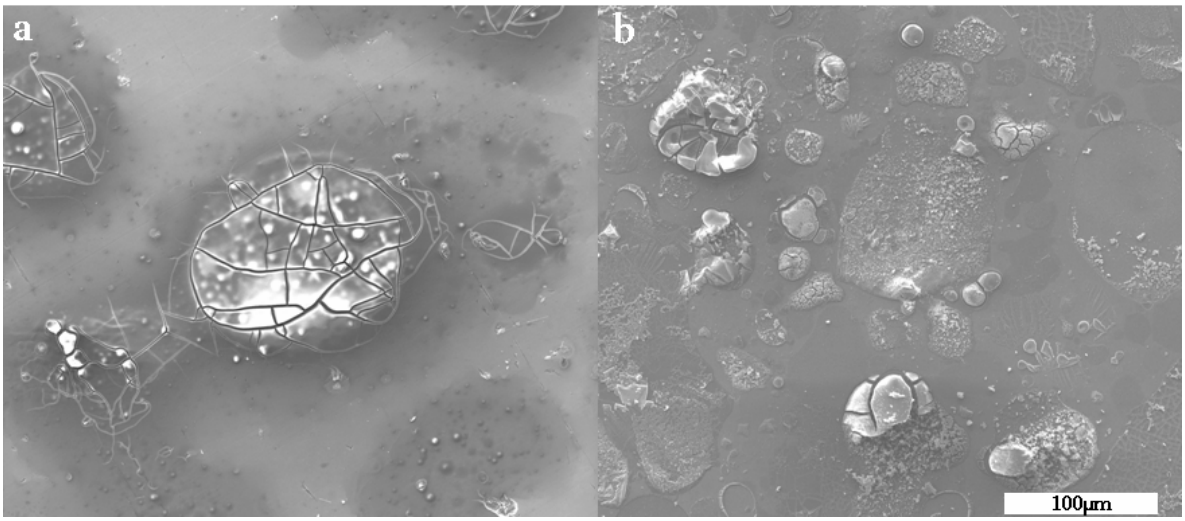

Fig. 3

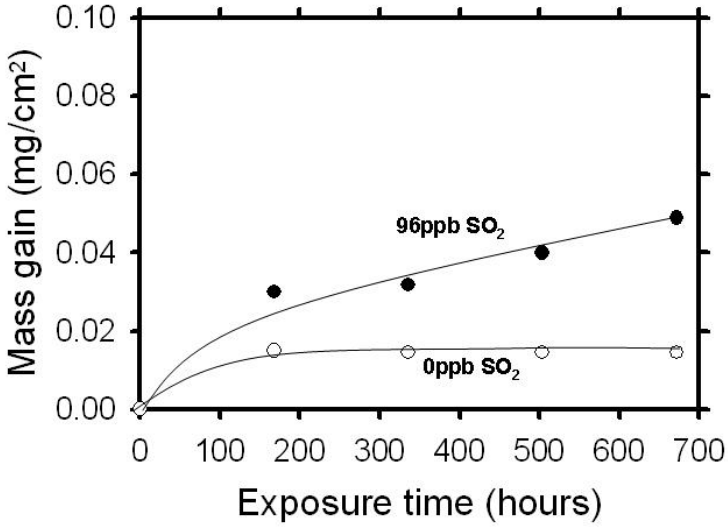

Fig. 4

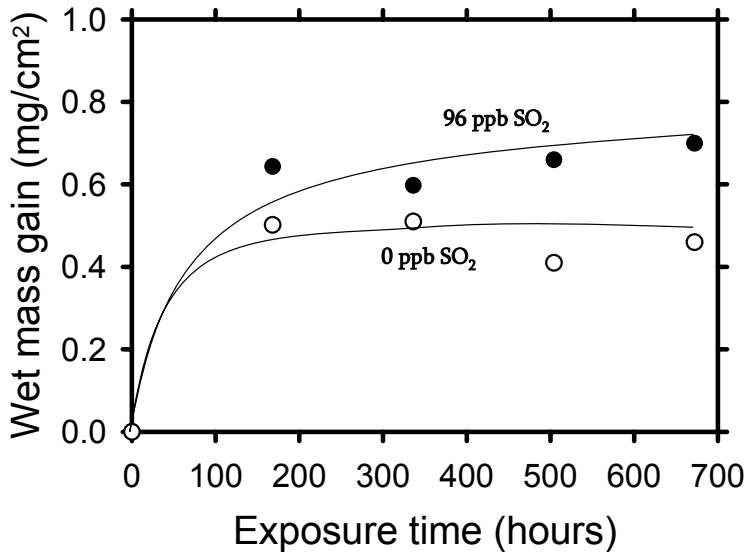

Fig. 5

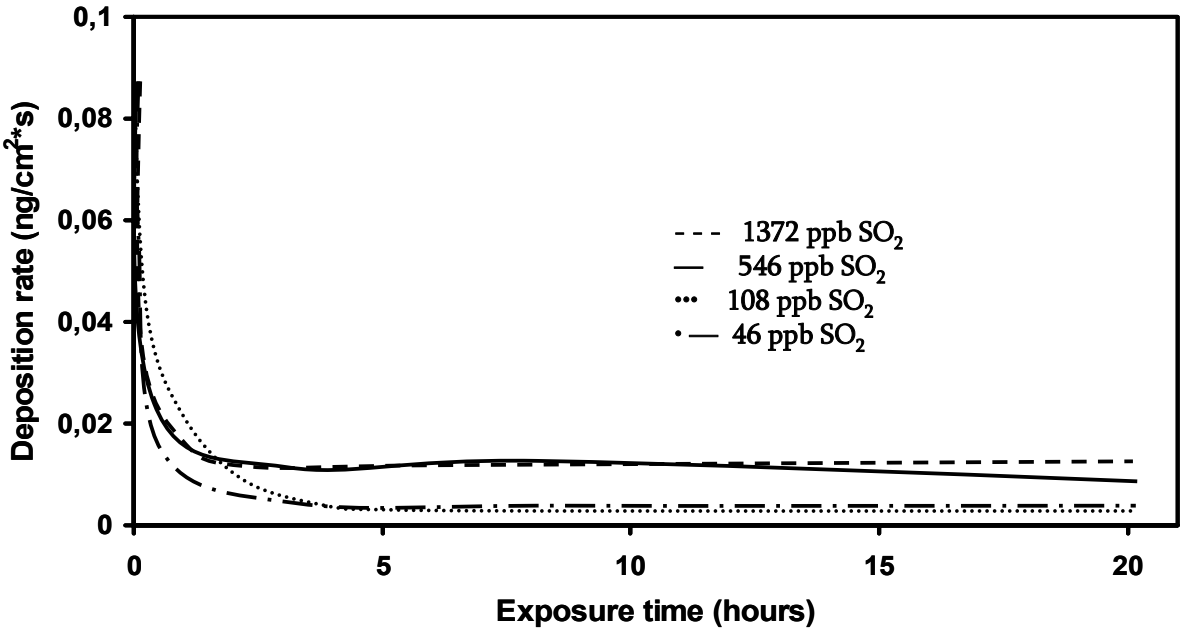
0,1
0,08
0,06
0,04
0,02
0
Deposition rate (ng/cm2*s)
1372 ppb SO2
546 ppb SO2
108 ppb SO2
46 ppb SO2
0
5
10
15
20
Exposure time (hours)

Fig. 6

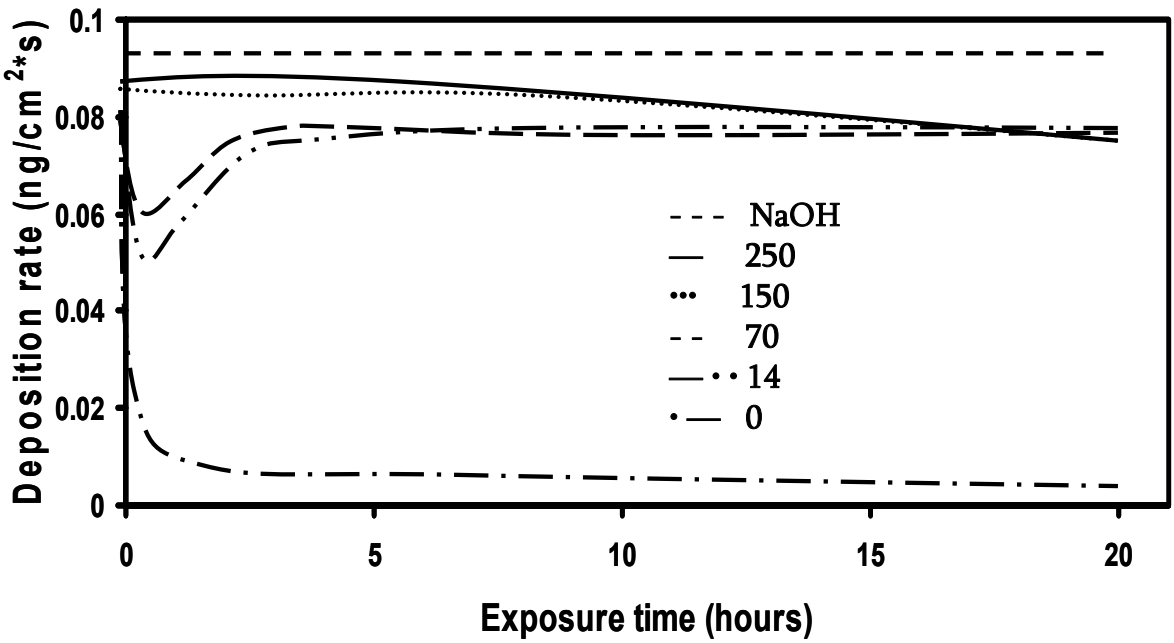
0.1
0.08
0.06
0.04
0.02
0
Deposition rate (ng/cm2*s)
NaOH
250
150
70
14
0
0
5
10
15
20
Exposure time (hours)

Fig. 7

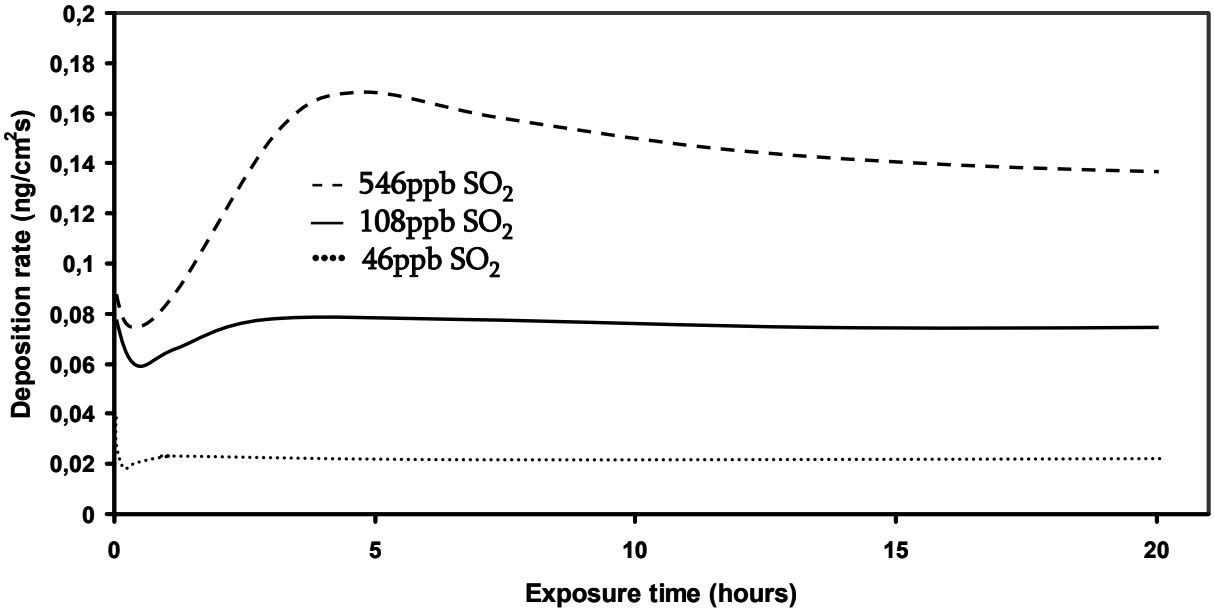
0,2
0,18
0,16
0,14
0,12
0,1
0,08
0,06
0,04
0,02
0
Deposition rate (ng/cm2s)
546ppb SO2
108ppb SO2
46ppb SO2
0
5
10
15
20
Exposure time (hours)

Fig. 8

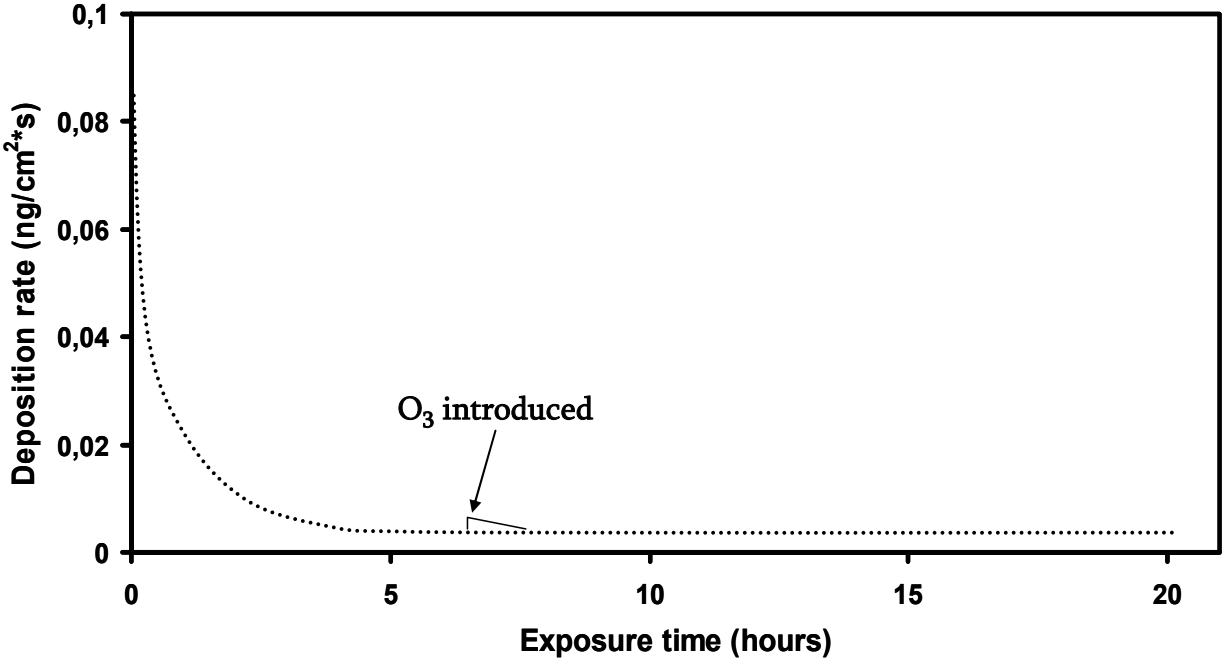
0,1
0,08
0,06
0,04
0,02
0
Deposition rate (ng/cm2*s)
O3 introduced
0
5
10
15
20
Exposure time (hours)

Fig. 9

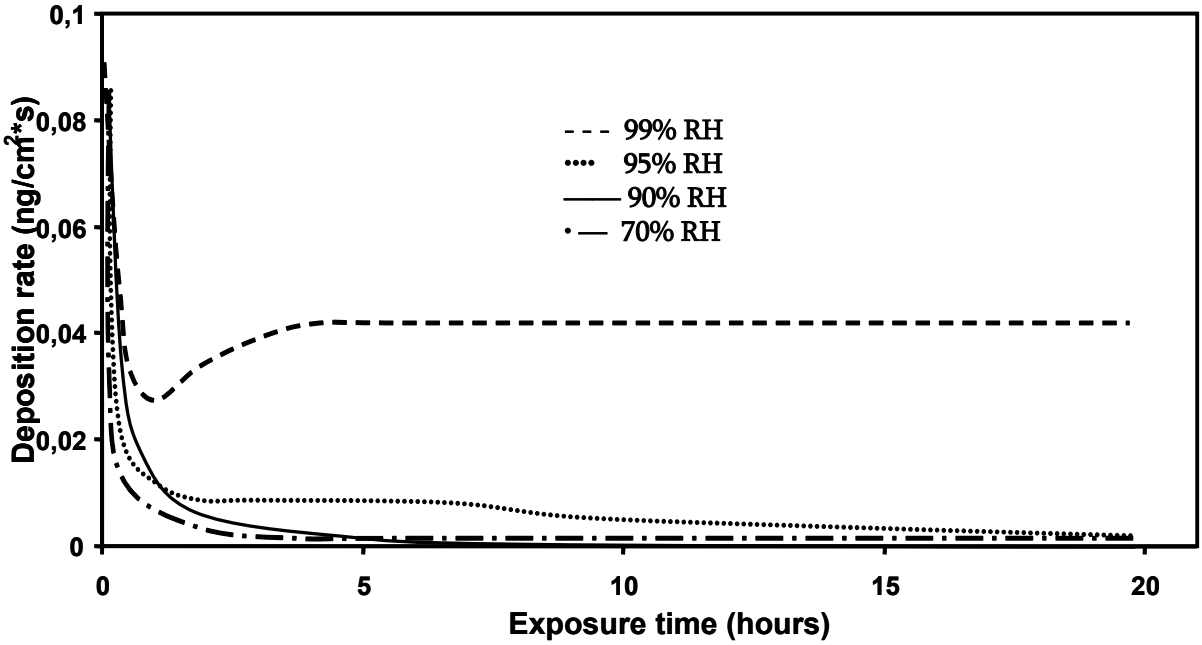
0,1
0,08
0,06
0,04
0,02
0
Deposition rate (ng/cm2*s)
99% RH
95% RH
90% RH
70% RH
0
5
10
15
20
Exposure time (hours)

Paper 6

The Influence of SO_2 on the Atmospheric Corrosion of Mg and Mg-Al alloys

Daniel Bengtsson Blücher*, Rakel Lindström# J.-E. Svensson, L. G. Johansson

Department of Chemical and Biological Engineering, Chalmers University of Technology, S-412 96 Göteborg, Sweden

*danielb@chalmers.se

#present adress: Laboratoire de Physico-Chimie des Surfaces, CNRS (UMR 7045), Ecole Nationale Supérieure de Chimie de Paris, 11 rue Pierre et Marie Curie, 75005 Paris, France

Abstract

This laboratory study addresses the effect of SO_2 on the atmospheric corrosion of an Mg-Al alloy, AZ91D, and pure Mg. The chemistry and kinetics of the SO_2 deposition to the surfaces and the SO_2 induced atmospheric corrosion are investigated. The influence of SO_2 concentration (50 - 500ppb) and humidity (50 – 100% RH) and addition of ppb levels of O_3 or NO_2 on the deposition rate of SO_2 was measured in real-time using a fluorescence instrument. The growth of corrosion products was followed by Fourier transform *in situ* infrared reflection absorption spectroscopy (FT-IRAS) and *in situ* scanning Kelvin probe force microscopy (SKPFM). The corrosion products were analyzed by gravimetry, ion chromatography (IC), grazing incidence X-ray diffraction (GI-XRD), ESEM, and focused ion beam (FIB) milling to make cross sections of corroded areas.

The presence of ppb levels of SO_2 strongly increases the corrosion of Mg and AZ91D compared to pure humid air. A linear mass gain is registered at 95 and 60% RH in the presence of 49 ppb SO_2. The only corrosion product detected by XRD was magnesium sulfite, $MgSO_3 \cdot 6H_2O$. The SO_2 induced corrosion of magnesium and AZ91D is localized by nature, indicating the development of electrochemical cells.At low relative humidity ($\leq$ 50% RH) SO_2 deposition on Mg is a transient process that terminates when the surface of the oxide film is covered by S(IV) species. At high humidity ($\geq$ 70% RH), the rate of SO_2 deposition on magnesium and alloy AZ91D is very high and limited by the mass transfer in the gas phase. It is proposed that the change from transient to steady-state SO_2 deposition is caused by the onset of electrochemical corrosion of magnesium, the cathodic current being supplied by oxygen reduction. At 60 % RH, the addition of O_3 or NO_2 strongly increases the SO_2 deposition rate on AZ91D. This effect is explained by O_3 and NO_2 acting as cathodic depolarizers, providing cathodic current for the corrosion of magnesium.

Keywords: atmospheric corrosion, laboratory study, magnesium, AZ91D, magnesium alloys, sulfur dioxide, nitrogen dioxide, ozone.

Introduction

The need for fuel efficiency and increased performance in transportation systems continually places new demands on materials. Due to their low weight/strength ratio, magnesium alloys have found widespread applications; from portable microelectronics to automobiles and aircraft [1]. However, the use of magnesium alloys is restricted by their susceptibility to corrosion, especially in the presence of NaCl. Previous work on the atmospheric corrosion of Mg alloys has shown that a somewhat protective carbonate-containing patina forms in ambient air [2]. Reports on the effect of SO_2 are scarce. An early study by Whitby on magnesium exposed to both indoor and outdoor environments, shows that carbonate and sulfate are found in large amounts on the exposed Mg surface [3]. Magnesium oxide is used in industrial processes as a sorbent for SO_2 [4]. In this study we aim to investigate the influence of SO_2 on the atmospheric corrosion of magnesium and some Mg-Al alloys by exposing them to carefully controlled laboratory air.

The corrosion of Mg-Al alloys in the atmosphere is governed by the interplay of water and corrosive substances on the surface. The process is electrochemical, involving anodic dissolution, the cathodic reduction of oxygen and/or evolution of hydrogen, and the transport of electrons, reactants and products between the active sites. Atmospheric corrosion research is still dominated by field studies, trying to correlate corrosion rate and environmental parameters [2, 5, 6]. Relatively few studies address the details of the series of reactions that together generate the corrosion processes. Thus, there is a lack of information on the corrosion mechanism of magnesium alloys in the atmosphere. Mg-Al alloys mainly suffer from localized forms of corrosion in the atmosphere [7, 8].

Reports on the effect of the influence of gaseous pollutants, such as SO_2, NO_2 and O_3, are scarce on the atmospheric corrosion of Mg and its alloys. Earlier we have shown that traces of SO_2 have a large impact on the atmospheric corrosion of magnesium alloys. Pure magnesium, AM50 and AZ91D are excellent getters for SO_2 at 95 % RH. At high humidity, the rate of deposition is constant with time and independent on the presence of NaCl [9].

The only sulfur containing corrosion product identified by XRD was magnesium sulfite ($MgSO_3 \cdot 6H_2O$). IC analyses revealed sulfite and sulfate on samples exposure to SO_2, whereas only sulfate was found on SO_2-exposed samples in the presence of NaCl.

The aim of this study is to investigate the influence of SO_2 on the atmospheric corrosion of pure Mg and Mg-Al alloys by exposing the samples in carefully controlled laboratory exposures. The deposition of SO_2 is studied as well as the influence of SO_2 on the mass gain. The effect of O_3 or NO_2 is also addressed.

Experimental

Sample preparation

AZ91D samples (30 x 30 x 3) mm were prepared from die-cast material. The pure Mg samples (30 x 30 x 4 mm) were cut from ingot. For the SO_2 deposition studies on AZ91D in the presence of NO_2 and O_3 and in the IRAS studies, smaller samples were used (15 x 15 x 3 mm). The compositions of the materials are shown in Table I.

Table I. Composition (wt. %) of the alloys investigated.

Material	%Mg	% Al	% Zn	% Mn	% Si	% Fe	% Cu	% Ni	%Pb
Pure Mg	99.97	0.003	0.005	0.0023	0.003	0.0018	0.0003	0.0002	0.001
AM20	97.4	2.1	0.04	0.4	0.01	0.0017	0.0016	0.0005	<0.0001
AM50	94.7	5.0	0.01	0.25	0.01	0.0016	0.0010	0.0007	<0.0001
AM60	93.7	6.0	0.01	0.25	0.01	0.0016	0.0010	0.0007	<0.0001
AZ91D	90.1	8.9	0.74	0.21	0.008	0.0022	0.0007	0.0004	<0.0001

Prior to exposure, the samples were ground on SiC paper (4000 mesh) in de-ionized water. Thereafter, the AZ91D samples were polished with 1µm diamond spray, whereas the Mg samples were polished with alumina slurry. The samples were ultrasonically cleaned in acetone, dried in air and stored over a desiccant for 2h before exposure. Sodium chloride was added by spraying the samples with a saturated solution of NaCl in 80:20 ethanol:water. The amount of NaCl added (70µg/cm^2) was determined gravimetrically. Care was taken to avoid droplet formation on the samples during spraying. The distribution of salt on the surface after spraying was even (E-SEM). To investigate the deposition rate of SO_2 on MgO, single crystals (10 x 10 x 1mm) were used.

Experimental setup

Two different experimental approaches were used in this study: prolonged corrosion studies (672 h) to determine the mass gain and the formation of corrosion products, and Time-Resolved trace gas Analysis of the Deposition (TRAD) to investigating the deposition rate of SO_2, NO_2 and O_3 on Mg and Mg-Al during the first 20h of exposure. Both kinds of experiments were performed in a well-controlled synthetic environment.

The exposure systems are made entirely of glass and Teflon. The samples are suspended in a thin nylon string in the middle of the chamber. In order to avoid interactions between samples, only one sample is exposed in each chamber. The corrosion chambers are immersed in a water tank held at constant temperature (22.0 ± .03 °C). To avoid condensation in the parts of the system outside the water tank the temperature in the room is kept at 25°C. The exposure gas is prepared from dried and purified air. Because the air purification system removes most of the CO_2 in the air we achieve a carbon dioxide concentration of 350 ppm by adding pure CO_2 from a cylinder and monitoring the concentration. Relative humidity is regulated by mixing dry air and air saturated with water vapor. Relative humidity was 50-100% and was controlled with an accuracy of ± 0.3 %. SO_2(g) and NO_2(g) were added to the dry air stream using permeation tubes manufactured by the authors. The permeation rates of the SO_2 tubes correspond to SO_2 concentrations of 48, 96 and 501 ppb in the exposure gas. The permeation rate of the NO_2 tube correspond to a concentration of 200 ppb. The ozone was added to the dry purified air flow by means of an ozone generator (UV radiation, $\lambda < 230$nm) to form atomic oxygen which then reacts with dioxygen molecules to form O_3(g).

Corrosion studies (672h)

There are eight parallel chambers, see Fig. 1. The whole gas flow (1 dm^3/min) passes through each chamber in turn for 15 s. The chambers have an inner diameter of 55 mm and a volume of 0.4 l. The net gas flow is 7mm/sec corresponding to a Reynolds number (R_e) of about 25 in an empty chamber. The SO_2 content in the gas leaving each chamber was determined by absorbing in 1% H_2O_2(aq) solution and analyzing as sulfate using ion chromatography. In order to determine the amount of SO_2 deposited on the samples, we compared this analysis to the results obtained using two empty corrosion chambers that were used as blanks. The deposition of SO_2 by the exposure apparatus was < 1%. To monitor the corrosion process during exposure the samples were weighed once a week. In order to avoid disturbing the corrosion process, the samples were not dried before weighing. The weighing procedure lasted two minutes per sample. The mass gain recorded in this way is termed the wet mass gain. After the completion of the 672 h exposures the dry mass gain of the samples was determined after storing over a desiccant at ambient pressure and temperature for one week. Water-soluble corrosion products were removed by leaching in milli-q water (pH 7) for 1 minute and then for 30 minutes at ambient temperature. The amount of water soluble anions removed by this process was determined by ion chromatography (Dionex DX100 with an

Ionpac AD9-SC column). The flow rate was 2 ml/min and 1.8 mM Na_2CO_3 / 1.7 mM $NaHCO_3$ was used for eluation. Grazing incidence X-ray diffraction (GI-XRD) was used for characterization of crystalline corrosion products (Siemens D-5000 CuK_α radiation equipped with a Göbel mirror, Cu K_α radiation). The diffraction peaks of metallic Mg were used as an internal standard. The samples were also studied by ESEM (Electroscan 2020) and EDX (Link ISIS).

Time-resolved trace gas analysis of the deposition (SO_2, NO_2 O_3)(20h)

The experimental setup used in the SO_2 deposition studies is described in Fig. 2. The gas flow (1.0 dm^3/min.) results in a net gas velocity of 2.7 cm/s (laminar flow conditions, $R_e = 50$). For the exposure of MgO, $Mg(OH)_2$ and $Mg_4(OH)_6CO_2 \cdot 4H_2O$, the gas flow was 0.7$dm^3$/min in order to increase the sensitivity of the analysis. The setup consists of a single exposure chamber with continuous flow and real-time analysis of SO_2, NO_x and O_3 in the output gas. SO_2, NO_2 and O_3 were added to the dry, purified air stream as described above. SO_2 was analyzed by a fluorescence instrument (Environnment AF21M), the sensitivity being 1 ppb. The ozone concentration in the output gas was analyzed by using an instrument based on UV photometry (Dasibi 1108). NO and NOx were analyzed by a chemiluminescence instrument (Environnment AC 30M). Before the start of each experiment the interaction of the pollutant with the reactor has reached a steady state so that the output gas from the corrosion chamber has a constant composition. An experiment is started when the sample is introduced into the chamber. The mass transfer-limited deposition of SO_2 is measured using an "ideal absorber", i.e. a glass plate (30 x 30 x 3 mm) with a thin layer of NaOH(aq). The deposition rate ($ng/cm^2 \cdot s^{-1}$) and the deposition velocity ($cm \cdot s^{-1}$) on the samples are determined by measuring the difference between the input and output concentrations of the pollutants. The deposition velocity V_d is defined as the flux of an air pollutant to a surface, divided by the concentration in the gas: $V_d = F/c$ where F is the flux to the surface ($g \cdot cm^{-2} s^{-1}$) and c is the concentration of the pollutant in the gas ($g \cdot cm^{-3}$) [10, 11]. In our exposures, the concentration of the SO_2 is taken as the mean of the input and output concentrations in the cell. The same analytical techniques were used to analyze the samples after exposure as described above.

AFM/SKPFM

Atomic Force Microscopy (AFM) with Scanning Kelvin Probe Force Microscopy (SKPFM) is a valuable tool for studying the initial stages of atmospheric corrosion on Al and Mg-Al systems. In this study, a Nanoscope IIIa Multimode was used (Olympus micro cantilevers, n^+ silicon conductor, with a resonant frequency of about 279 kHz and a spring constant of about 27N/m). In tapping mode, the topography and the Volta potential distribution were mapped simultaneously *in situ* with sub-micrometer resolution. The instrument was equipped with customized *in situ* cell to monitor the continuous corrosion process under well controlled exposure conditions. The setup is described elsewhere [7].

FT-IRAS

The formation of corrosion products was monitored by *in situ* FT-IRAS. The *in situ* FT-IRAS setup used consists of a chamber with a volume of 27 cm^3, in which the sample is exposed laterally to the weathering gas. A Fourier transform infrared spectrometer (BIORAD FTS 60A) was connected to the exposure cell. The exposure system is similar to that in the deposition study but the gas flow was approximately 1.33 dm^3/min. The temperature of the gas was 22°C and the SO_2 concentration was about 200 ppm. IRAS spectra were recorded in absorbance units (-log R/R0), where R is the reflectance of the exposed sample and R_0 the background reflectance obtained after 0.5 h of exposure to a dry atmosphere. Pure Mg and AZ91D were analyzed at high humidity (90% RH) and low humidity (50 and 60% RH). The corresponding spectra in the absence of SO_2 were also measured as a reference. The exposures lasted up to 2 hours.

Results

SO_2 deposition

The influence of humidity at 49 ppb SO_2 The deposition of SO_2 on pure magnesium and AZ91D at different humidities is shown as a function of exposure time in Fig. 3. The SO_2 concentration was 49 ppb. At high humidity (above 70% RH), SO_2 deposition is very rapid and constant with time on both materials. This SO_2 deposition rate is equal to that measured for an identical sample that had been covered by a thin layer of NaOH(aq) and represents the maximum SO_2 deposition rate that can be attained in our set-up, given the flow conditions, sample size and temperature. It represents the gas-transport limited value for deposition, meaning that all SO_2 molecules that impinge on the surface are deposited. At lower humidity, SO_2 deposition is initially in the gas-transport limited regime but decreases with time, signifying a saturation of the surface. AZ91D shows saturation at higher relative humidities than pure Mg, see Fig.2. At 50% RH, SO_2 deposition on AZ91D and pure magnesium drops to 1-2% of the maximum value after 12 hours.

The concentration dependence

In order to compare SO_2 deposition at different SO_2 concentrations it is useful to use the concept deposition velocity V_{dep}, rather than deposition rate. The deposition velocity is equal to the deposition rate of SO_2 on the sample surface (g/m^2s) divided by the concentration of SO_2 in the gas (g/m^3). The unit of the quotient is ms^{-1}. The SO_2 concentration in the calculation is the average of the input and output concentrations in the reaction chamber. At high humidity, SO_2 deposition is in the transport-limited regime in the SO_2 concentration range studied (49-501 ppb). Under the present conditions this corresponds to a deposition velocity of $0.26cms^{-1}$. At high humidity we are in the transport-limited regime for all SO_2 concentrations studied and the deposition rate is proportional to SO_2 concentration. The situation at lower humidity is different, as illustrated in Fig. 4, showing SO_2 deposition velocity on Mg and AZ91D as a function of exposure time at 60% RH for three different SO_2 concentrations. Initially, the deposition velocity equals the transport-limited value of $0.26cms^{-1}$ in all cases. With time, V_{dep} decreases, corresponding to a saturation of the surface with respect to SO_2 uptake. As expected, V_{dep} drops off more rapidly at higher SO_2 concentration. It may be noted that the SO_2 deposition velocity falls off much more rapidly with time for AZ91D than it does for pure magnesium. The two materials differ also in another respect. While V_{dep} drops monotonically with time for AZ91D, there is a change in curvature in the

case of pure magnesium. After the initial decrease, the deposition velocity increases again on Mg, indicating that the surface has become more reactive. The change of curvature (activation) is especially evident at 501ppb.

The influence of alloy composition

The different behaviour of pure Mg and AZ91D at 60% RH toward SO_2 deposition is attributed to the aluminium content in the alloy. In order to investigate the influence of aluminium content on SO_2 deposition, a number of Mg-Al alloys were exposed to 264 ppb SO_2 at 60% RH, see Fig 5. Initially, deposition is in the transport limited regime and therefore independent of alloy composition. After 20 h exposure, the deposition rates show a strong dependence on aluminium content. The two alloys with more than 6% aluminium exhibit very slow deposition rates. The activation step is more pronounced on the alloys low in aluminium.

In situ IRAS

In order to study the initial formation of surface species in the presence of SO_2, time-resolved IR spectra were obtained from pure Mg and AZ91D in the presence of 200 ppb SO_2 at different humidities. Fig. 6 shows spectra measured at 90 % RH in air.

Absorption bands appear at 3000-3500, 1650, 900-1150 and around 700cm^{-1}, the bands growing with exposure time. The band at about 2350cm^{-1} is due to CO_2(g). The broad band at 3000-3500 cm^{-1} is attributed to OH stretching vibrations in water. The corresponding H_2O bending vibration is seen at 1650 cm^{-1}. This water is either adsorbed on the surface or belongs to a solid salt hydrate. (Bulk water is considered to be absent because magnesium sulfite and magnesium sulfate do not form aqueous solutions at 90% RH.). In the absence of SO_2, the two water bands do not grow appreciably during exposure. This indicates that much of the water that is bound to the surface in the presence of SO_2 belongs to solid compounds that accumulate on the surface. The negative peak that appears around 3700cm^{-1} upon exposure to SO_2 is attributed to brucite ($Mg(OH)_2$). It is considered that brucite is present on the sample surface before exposure and is consumed by the reaction with SO_2. The region 850-1250 cm^{-1} corresponds to S-O stretching vibrations in sulfur-oxygen anions [12]. The strong peak centered around 980 cm^{-1} is attributed to sulfite. For $MgSO_3(H_2O)_6$(s), the corresponding peak appears at 936cm^{-1}. This is in accordance with the identification of $MgSO_3(H_2O)_6$(s) in the corrosion product by XRD after prolonged exposure to SO_2 in air (see below). The accumulation of water on the surface seen in the presence of SO_2 is attributed to the same

compound. No bands appeared that could be unambiguously attributed to sulfate. This is in contrast to the behavior of some other base metals such as zinc [13]. The lack of evidence for sulfate formation in air is supported by runs at the same SO_2 concentration and relative humidity but featuring N_2 instead of air as the carrier gas. The FT IRAS spectra obtained in N_2/SO_2 were essentially the same as in air. The absorption bands formed upon exposure to SO_2 at 60 and 50% RH were qualitatively the same as at 90% RH. However, the bands were weaker and did not grow as rapidly. At high relative humidity, the spectra obtained from AZ91D were qualitatively the same as for pure Mg. At lower humidity, the growth of the sulfite bands was slower than for pure Mg. To summarize, the FT IRAS results show that SO_2 forms sulfite on Mg and on AZ91D and that oxidation to sulfate is slow.

The effect of pre-exposure on SO_2 deposition

Metal corrosion processes often feature an induction period corresponding to the time needed to break down a passivating surface film [10]. Because of the lack of evidence for sulfate formation, it was assumed that the change in curvature seen in some SO_2 deposition curves (see Fig. 4 and Fig 5) on pure magnesium is caused by a depassivation or corrosion process that runs in parallel to SO_2 deposition. To test this hypothesis, we studied the effect of pre-exposure in clean humid air on the rate of SO_2 deposition on Mg at 60% RH. A Mg sample was pre-exposed for 13 hours at 95% RH in order to form a thick surface layer consisting of $Mg(OH)_2$. It was thought that the presence of a thick $Mg(OH)_2(s)$ layer would delay the change of curvature if it was due to depassivation or corrosion. As expected, the pre-exposed sample exhibited a much stronger decrease in SO_2 deposition rate with time than the reference sample, see Fig. 7. Moreover, the pre-exposed sample showed no upturn in the SO_2 deposition curve.

The effect of O_2 on SO_2 deposition

The SO_2 deposition curves measured at 60% RH (c.f. Fig. 3 and 4) show that the magnesium surface becomes depassivated subsequent to the initial reaction of SO_2 with the original surface film, resulting in an increased rate of deposition. Together with the outcome of the pre-exposure experiment (c.f. Fig 7), this implies that SO_2 deposition is not just due to reaction with surface $Mg(OH)_2(s)$ but that it depends on reactions involving the underlying metal, *i.e.*, that it relates to Mg corrosion. It is well-known is that magnesium corrodes by hydrogen evolution in aqueous solution [2]. Nevertheless, it was thought worthwhile to look at the effect of O_2 on SO_2 deposition at the same relative humidity (60%) (see Fig. 8). To our

surprise, the rate of deposition of SO_2 depends strongly on O_2, the rate of deposition in N_2 being only about one third of that in air. It may be noted that the exposure to N_2 included traces of O_2 (on the order of 10ppm). All deposition curves acquired in air or in 100% oxygen featured an activation step whereas the exposure in N_2 did not. The partial pressure of oxygen has a similar effect on the rate of deposition of SO_2 on alloy AZ91D but the effect is less marked. The sulfur dioxide deposition curve features an activation step on AZ91D in pure O_2.

SO_2 deposition on single crystal MgO

Because the deposition of SO_2 on magnesium appears to involve both a reaction with a solid surface film and the corrosion of the underlying metal it was decided to investigate SO_2 deposition on some solid compounds that may form part of the surface layer on magnesium. The deposition of SO_2 on a single crystal MgO specimen (10x10x1mm) was measured at different humidities at a SO_2 concentration of 50 ppb. The results showed that, at high relative humidity, the behavior of MgO towards SO_2 is very similar to that of magnesium metal. Likewise to the metal, SO_2 deposition on MgO is in the transport-limited regime at 95% RH. In contrast, the SO_2 deposition velocity on MgO at 60% relative humidity is very small and soon drops to zero. This was the case in air as well as in N_2. As noted above, magnesium metal exhibits relatively rapid SO_2 deposition at this humidity, especially in air.

The influence of NO_2 on the deposition rate of SO_2

Fig. 9 shows the influence of 200 ppb NO_2 in air on the SO_2 deposition rate on AZ91D. The SO_2 concentration is 48 ppb and relative humidity is 50, 60 and 70% RH. At 50% RH, the introduction of NO_2 only increases the SO_2 deposition initially and the effect prevails for less than an hour. At 60% RH, the introduction of NO_2 strongly increases SO_2 deposition so that it becomes mass-transfer limited. This is the case even when SO_2 has reached a fairly low level before NO_2 is introduced. It may be noted that the effect of NO_2 on SO_2 deposition remains when NO_2 is removed from the gas. The increased deposition rate prevails for as long as NO_2 is added. Because the SO_2 deposition reaction at 70% RH is in the transport limited regime already in the absence of NO_2 (compare Fig 2), adding NO_2 has no effect. The spikes seen in the curves when NO_2 is added is due to an instability in the gas flow.

The influence of O_3 on the SO_2 deposition rate

The effect of ozone on SO_2 deposition is similar to that of NO_2. However, the effect extends to lower humidity in the case of ozone (compare the 50% RH curves in Fig, 9 and 10). At

40% RH and below, the introduction of O_3 only resulted in a slight and temporary increase of the SO_2 deposition rate.

Desorption of SO_2

The desorption of SO_2 was investigated by transferring AZ91D and pure Mg samples exposed to SO_2-containing (264ppb) humid air to a reactor with flowing clean humid air and analyzing for SO_2. Samples exposed to SO_2 at 95% RH did not desorb measurable amounts (< 1ppb) while samples exposed at 60% RH exhibited small but measurable SO_2 desorption in clean air at 60 and 90% RH.

Four week exposures

The mass gains of Mg and AZ91D in different environments are shown in Table II. The concentration of SO_2 was 48 ppb and the concentration of NO_2 and O_3 was 200 ppb. The weighing performed every 168 hours showed increasing mass gains in all exposures involving SO_2. Sulfur dioxide is a powerful corrosion accelerator for magnesium, the accumulated mass gain after four weeks being 15 times higher after exposure to air with 48 ppb SO_2. The short-term deposition rate measurements described above imply that the deposition of SO_2 is in the mass transport-limited regime at 95% RH for both materials (see Fig 2). Accordingly, we find that the fraction of SO_2 deposited on AZ91D at 95% RH in the long term exposures is close to the maximum value. (When comparing the long-term and short-term exposures, it should be noted that the absolute values of the deposition rates are necessarily different because flow conditions are not the same.) As expected, SO_2 deposition is much slower at 60% RH. The increase in the SO_2 deposition rate registered when NO_2 and O_3 are present is also in accordance with the short-term results (compare Fig 6 and 7). However, in this case, SO_2 deposition lies below the maximum value in the long-term exposure. The mass gain at 60% RH in the presence of NO_2 or ozone is 4-5 times higher than in the absence of these gases. A comparison of the mass gains with the amount of deposited SO_2 implies that the magnesium sulfite formed corresponds to a large part the measured mass gain. However, the calculation is based on the assumption that all surface sulfite is present as magnesium sulfite hexahydrate. The presence of other sulfur-containing compounds would, of course change the situation somewhat. The remaining mass gain is due to hydroxides and carbonates or possibly to mixed hydroxy-sulfite. This still means that a large part of the magnesium ions in the corrosion product are associated with hydroxide and carbonate.

Table II. Mass gain of samples after 672 hours. The fraction of SO_2 deposited on the samples is also shown.

Material	Environment	% RH	fraction of SO_2 deposited (%)	Fraction of mass gain attributed to the deposition of SO_2 in the form of $MgSO_3 \cdot 6H_2O$	Dry mass gain (mg/cm^2)
Mg	Pure air	95	-	-	0.0055
AZ91D	Pure air	95	-	-	0.005
Mg	SO_2	95	n.a.	n.a.	0.092
AZ91D	SO_2	95	75	77	0.092
AZ91D	SO_2	60	15	88	0.016
AZ91D	$SO_2 + O_3$	60	61	88	0.065
AZ91D	$SO_2 + NO_2$	60	65	62	0.076

The SO_2 concentration was 48 ppb, the NO_2 and O_3 concentrations were 200 ppb and temperature was 22°C. The mass gain results represent average values for triplicate samples. The scatter in mass gain was about ±5%. The percentage of mass gain attributed to SO_2 deposition was calculated supposing that all deposited SO_2 forms $MgSO_3(H_2O)_6$ on the surface. The maximum fraction of SO_2 that can be deposited on the samples under the present experimental conditions corresponds to 75-80% of the SO_2 added to the exposure chambers.

The only sulfur containing corrosion product identified by XRD was magnesium sulfite hexahydrate ($MgSO_3 \cdot 6H_2O$). IC analyses revealed sulfite and sulfate on samples exposure to SO_2. However, it may be noted that at least a part of the sulfate found by IC was formed by oxidation of sulfite during analysis.

After 672 hours exposure the samples had lost their luster and had become dark. Optical microscopy revealed a transparent, glassy layer on the sample surface. In all cases the corrosion attack was localized in nature, see ESEM images in Fig. 11. The EDX analyses show that the corrosion products are enriched in oxygen and sulfur. Cross section analysis showed that sulfur is associated with oxygen in the oxide film.

Fig. 12. shows ESEM/EDX maps of AZ91D. The corrosion attack is localized. The β-phase is clearly seen in the secondary electron micrograph, indicating that the nature of corrosion attack is different on α- and β-phase in the presence of SO_2. The β-phase network is not

visible on an unexposed sample. The magnesium-rich α-phase regions exhibit higher oxygen yields compared to the β-phase. Sulfur is associated with oxygen in the corrosion product crusts. However, at the centre of the crusts, the relative sulfur content is lower.

Scanning Kelvin Probe Force Microscopy

In situ Scanning Kelvin Probe Force Microscopy (SKPFM) time-resolved measurements on Mg at 60% RH in air with 48ppb SO_2 is shown in Fig. 13. The top row shows the topography and the Volta potential maps at the start of the experiment. In the lower rows, the situation after 1, 2 and 5 hours is illustrated. The formation of discrete corrosion products that coalesce with time, forming larger agglomerates or corrosion product crusts (localized corrosion attack) is evidence of electrochemical corrosion.

Discussion

Interaction between SO_2 and Mg

Initially, the magnesium surface is covered by a thin oxide, the surface of which is hydroxylated in the presence of water vapor [8]. SO_2 reacts readily with this surface, forming surface sulfite:

$$Mg(OH)_2(surface) + SO_2(g) \rightarrow MgSO_3(ads) + H_2O \qquad (1)$$

At low humidity, SO_2 uptake is transient and not completely irreversible. The presence of loosely bonded S(IV) on the surface is in accordance with the tendency for the magnesium surface to "saturate" with SO_2. In contrast, there is no desorption of SO_2 from magnesium at high humidity, meaning that SO_2 is irreversibly deposited. This is in accordance with SO_2 deposition being in the gas transport limited regime at high humidity.

At medium humidity, (60% RH) SO_2 deposition on Mg exhibits a characteristic change in curvature after a few hours. The change in curvature denotes the transition from a transient mode of SO_2 deposition where some of the surface S(IV) is reversibly bound, to a steady-state mode of SO_2 deposition where SO_2 is irreversibly bound to the surface.

It is considered significant that the change of curvature is absent in N_2 environment and that it is also absent in the case of MgO in air. The fact that magnesium metal and oxygen are both necessary for the change in curvature in SO_2 deposition to occur implies that it is related to a reaction between magnesium metal and oxygen. The localized nature of corrosion attack of Mg in humid air with SO_2 (see ESEM image in Fig. 11) indicates that the corrosion of magnesium in humid air is electrochemical. This is also supported by SKPFM imaging from very early on (see Fig 13). It is therefore argued that the change from transient to steady-state SO_2 deposition is caused by the onset of electrochemical corrosion of magnesium, the cathodic current being supplied by oxygen reduction:

$$Mg(s) \rightarrow Mg^{2+}(aq) + 2e^-(aq) \qquad (2)$$

$$\tfrac{1}{2}O_2(g) + H_2O + 2e^- \rightarrow 2OH^-(aq) \qquad (3)$$

The induction period of a few hours before SO_2 deposition starts to increase after the initial decrease is considered to correspond to the depassivation of the metal, *i.e.*, the dissolution of the surface film:

$$SO_2(g) + H_2O \leftrightarrows H^+(ads) + HSO_3^-(ads) \quad (4)$$

$$MgO(s) + 2H^+(ads) \rightarrow Mg^{2+}(ads) + H_2O \quad (5)$$

It is argued that the limited amount of water present on the surface at 50% RH and below produces a low surface conductivity that reduces the importance of electrochemical processes on the surface and slows down depassivation.

The lack of evidence for significant oxidation of sulfite to sulfate in humid air suggests that this reaction is not involved in the change in curvature in the SO_2 deposition curves.

The formation of hydroxide ions and magnesium ions results in an increased deposition of SO_2 on the surface:

$$SO_2(g) \leftrightarrows SO_2(ads) \quad (6)$$

$$SO_2(ads) + 2OH^-(ads) \leftrightarrows SO_3^{2-}(ads) + H_2O(ads) \quad (7)$$

The sulfite formed will react with Mg^{2+}:

$$Mg^{2+}(ads) + SO_3^{2-}(ads) \rightarrow MgSO_3(ads) \quad (8)$$

After prolonged exposure magnesium sulfite hexahydrate forms:

$$MgSO_3(ads) + 6H_2O \rightarrow MgSO_3 \cdot 6H_2O(s) \quad (9)$$

At high humidity sulfite is unevenly distributed on the surface, no doubt because of migration to anodic areas. The high mobility of surface sulfite is not easy to reconcile with the limited solubility of crystalline magnesium sulfite (martell). One possible explanation is that metastable and probably amorphous sulfites form initially rather than the stable, crystalline variety.

Interaction between SO_2 and Mg-Al alloys

The localized nature of corrosion attack on AZ91D in air with 49 ppb SO_2 at 95% RH is illustrated in the SEM images in Fig 12. The Mg rich α-phase is seen to be preferentially attacked. This is in accordance with recent SKPFM measurements at this laboratory that show that the α-phase is anodic to the β-phase ($Mg_{17}Al_{12}$) [14].

At high relative humidity (95%), the SO_2 deposition rate is the same on pure Mg and on AZ91D (sees Fig 3). This is in accordance with the results from the four week exposures (see Table 2). This implies that the corrosion of Mg at high RH (95%) in SO_2 environment is not influenced by alloying with aluminum. However, at 60% RH the interaction between SO_2 and the metal depends strongly on alloy composition, the SO_2 deposition rate decreasing with increasing aluminum content (See Fig 5). Moreover, the change of curvature in the SO_2 deposition rate on pure Mg at 60% RH discussed above, becomes less marked with increasing aluminum content and is absent in the high Al alloys (AM60 and AZ91D). Nordlien has shown that the passive film on Mg-Al alloys is enriched in aluminum [15]. In comparison to magnesium oxide, alumina is much more stable in neutral and acidic environment [16]. It is therefore expected that the dissolution of the passive film by the acid formed by the hydrolysis of SO_2 (see reactions 4 and 5) will be become increasingly slow as the aluminum content in the alloy increases. This is suggested to explain the differences observed between Mg and Mg-Al alloys regarding SO_2 deposition at 60% RH. Apparently, the protective properties of the alumina-containing film are not sufficient to protect the material at high relative humidity.

The presence of ppb levels of ozone and NO_2 strongly increases the SO_2 deposition on AZ91D at 60% RH (see Fig. 9 and 10). The strong influence of O_3 and NO_2 at 60% RH can be seen also in the four-week exposures (see Table 2), the mass gains in the combined SO_2 + O_3 and SO_2 +NO_2 environments being 4-5 times higher than for exposures with SO_2 alone. It is argued that this effect has the same origin as the effect of oxygen on SO_2 deposition on pure Mg (see above). Thus, it is argued that the molecules themselves or some reaction product on the surface act as cathodic depolarizers, providing more cathodic current to the corrosion of magnesium:

$$O_3 + H_2O + 2e^- \rightarrow O_2(g) + 2OH^- \qquad (10)$$

$$NO_2(ads) + H_2O + 2e^- \rightarrow NO(g) + 2OH^- \quad (11)$$

The resulting increased formation of alkali would then explain the higher rate of SO_2 deposition in the presence of ozone and NO_2. It may be noted that the corrosion products were the same whether O_3 and NO_2 were present or not at 60% RH. In all cases, $MgSO_3 \cdot 6H_2O(s)$ was the only crystalline corrosion product detected.

Conclusions

The presence of ppb levels of SO_2 strongly increases the corrosion of Mg and AZ91D compared to pure humid air. A linear mass gain is registered at 95 and 60% RH in the presence of 49 ppb SO_2. The only corrosion product detected by XRD was magnesium sulfite, $MgSO_3 \cdot 6H_2O$. Sulfite also dominated the IRAS spectra. The SO_2 induced corrosion of magnesium and AZ91D is localized by nature, indicating the development of electrochemical cells. At low relative humidity SO_2 deposition on Mg is a transient process that terminates when the surface of the oxide film is covered by S(IV) species. At high humidity, the rate of SO_2 deposition on magnesium and alloy AZ91D is very high and limited by the mass transfer in the gas phase under the present conditions. At medium humidity, (60% RH) SO_2 deposition on Mg exhibits a characteristic change in curvature corresponding to the transition from a transient mode of SO_2 deposition to a steady-state mode of deposition where SO_2 is irreversibly bound to the surface. It is argued that the change from transient to steady-state SO_2 deposition is caused by the onset of electrochemical corrosion of magnesium, the cathodic current being supplied by oxygen reduction. At 60 % RH, the addition of O_3 or NO_2 strongly increases the SO_2 deposition rate on AZ91D. This effect is explained by O_3 and NO_2 acting as cathodic depolarizers, providing cathodic current for the corrosion of magnesium.

Acknowledgement

The Swedish Research Council, the EC project “Mg-Chassis”, contract number G3RD-CT-2000-00287 and Volvo Car Corporation are gratefully acknowledged for their support to the project.

References

1. M. Avedesian and H. Baker, eds., *ASM Specialty Handbook: Magnesium and Magnesium Alloys*, ASM International, Materials Park, OH, USA (1998).
2. R. Lindström, J.-E. Svensson, and L. G. Johansson, *J. Electrochem. Soc.,* **149**, B103 (2002).
3. L. Whitby, *Transactions of the Faraday Society,* **29**, 844 (1933).
4. J. A. Rodriguez, T. Jirsak, A. Freitag, J. Z. Larese, and A. Maiti, *Journal of Physical Chemistry B,* **104**, 7439 (2000).
5. H. P. Godard, W. B. Jepson, M. R. Bothewell, and R. L. Kane, *The Corrosion of Light Metals*, Wiley, New York (1967).
6. V. Vu Dinh, A. A. Mikhailov, Y. N. Mikhailovskii, P. V. Strekalov, and B. Do Thanh, *Zashchita Metallov,* **30**, 578 (1994).
7. D. B. Blueher, J. E. Svensson, L. G. Johansson, M. Rohwerder, and M. Stratmann, *Journal of the Electrochemical Society,* **151**, B621 (2004).
8. R. Lindström, L. G. Johansson, G. E. Thompson, P. Skeldon, and J.-E. Svensson, *Corrosion Science,* **46**, 1141 (2004).
9. R. Lindstrom, J.-E. Svensson, and L. G. Johansson, *15th ICC, Granada, Spain,* pp. (2002).
10. J.-E. Svensson and L. G. Johansson, *J. Electrochem. Soc.,* **140**, 2210 (1993).
11. J. A. Garland, *Atmos. Environ.,* **12**, 349 (1978).
12. H. D. Lutz, S. M. El-Suradi, and B. Engelen, *Zeitschrift fuer Naturforschung, Teil B: Anorganische Chemie, Organische Chemie,* **32B**, 1230 (1977).
13. J.-E. Svensson and L.-G. Johansson, *Proceedings of the 12th International Corrosion Congress, Houston, USA,* pp. 662 (1993).
14. D. B. Bluecher, J.-E. Svensson, L.-G. Johansson, M. Rohwerder, and M. Stratmann, *Journal of the Electrochemical Society,* **151**, B621 (2004).
15. J. H. Nordlien, K. Nisancioglu, S. Ono, and N. Masuko, *J. Electrochem. Soc.,* **144**, 461 (1997).
16. M. J. N. Pourbaix, *Atlas of Electrochemical Equilibriums in Aqueous Solutions. 2nd ed*, (1974).

Figure Captions

Fig. 1. Experimental setup for exposures with 350ppm CO_2 and for some with ppb levels of SO_2 at 4 - 22.0°C. (1) pure air inlet; (2) mass flow regulators; (3) humidifier; (4) NO_2 and/or SO_2 permeation tubes; (5) mixing point; (6) exposure chambers with Al or Mg-Al samples; (7) gas trap; (8) solenoid valves; (9) thermostated water tank; (10) CO_2 or O_3 inlet; (11) carrier gas (purified air) for NO_2 and or SO_2.

Fig. 2. The experimental setup for TRAD at 22.0°C. (1) pure air inlet with pure CO_2(g) added from a cylinder; (2) mass flow regulators; (3) O_3 generator (UV light $\lambda < 230$nm); (4) humidifier; (5) NO_2 and/or SO_2 permeation tubes; (6) exposure chambers with Al or Mg-Al samples; (7) real-time gas analyzers for SO_2, O_3 and NO_x-NO_2; (8) air outlet; (9) thermostated water tank.

Fig. 3. The SO_2 deposition as a function of exposure time in air with 49 ppb SO_2 at different relative humidities.

Fig. 4. Influence of SO_2 concentration and metal composition on the SO_2 deposition velocity on Mg and AZ91D. RH = 60%

Fig. 5. SO_2 deposition rate as a function of Al content in the Mg-Al alloys at 60% RH. The SO_2 concentration was 264ppb.

Fig. 6. Infrared absorption spectra at 200ppb SO_2 on Mg at 90%RH. The dry spectrum was recorded after pure air had passed through the reaction chamber for 30 minutes. The bottom spectrum was recorded after one hour in pure air at 90% RH.

Fig. 7. Influence of pre-exposure on the deposition of SO_2 on magnesium. RH was 60% and the SO_2 concentration was 264ppb

Fig. 8. Influence of O_2 on the deposition of SO_2 on magnesium. RH was 60% and the SO_2 concentration was 264ppb

Fig. 9. Influence of addition of 200 ppb NO_2 on SO_2 deposition on polished AZ91D samples at 50, 60 and 70% RH. The SO_2 concentration was 48 ppb.

Fig. 10. Influence of addition of 200 ppb O_3 on SO_2 deposition on polished AZ91D samples at 50, 60 and 70% RH. The SO_2 concentration was 48 ppb.

Fig. 11. ESEM image and EDX maps of Mg exposed to 49 ppb SO_2 at 95% RH for 672h. The temperature was 22.0°C. (a) secondary electron image; (b) magnesium; (c) oxygen; (d) sulfur.

Fig. 12. ESEM and EDX maps of AZ91D exposed to 49 ppb SO_2 at 95% RH. (a) secondary electron image; (b) Al; (c) Mg; (d) O; (e) S.

Fig. 13. Time-resolved *in situ* AFM and SKPFM images of Mg in the absence of CO_2. Relative humidity was 60% and the temperature was 22°C. The SO_2(g) concentration was 48ppb. The images in the left hand column show the topography by tapping mode AFM while the right hand column shows Volta potential maps imaged by SKPFM. The brighter areas are protruding from the surface in the topography images and have a higher relative potential in the Volta potential images. The height range is 200nm and the Volta potential range is 200mV. The top row shows the Mg surface at the start of the experiment and the lower rows show the surface after 1, 2 and 5 hours.

Figures

Fig 1

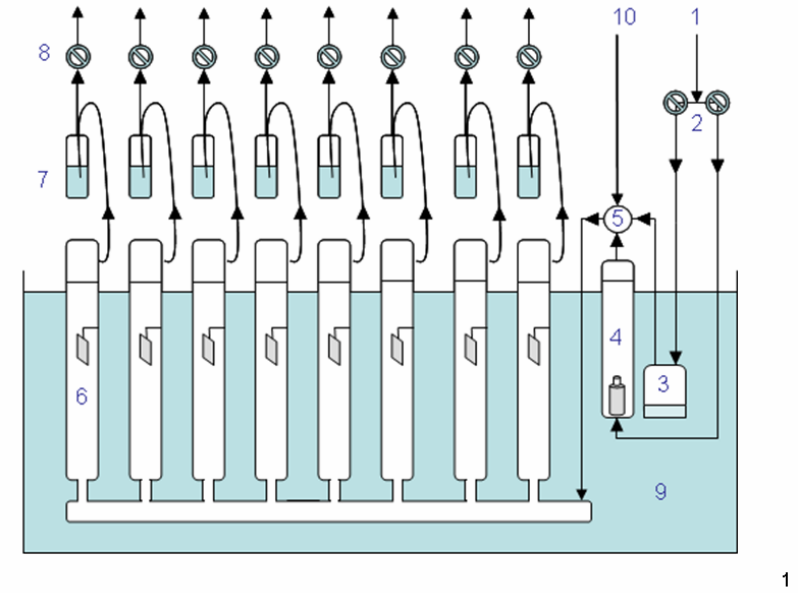

Fig 2

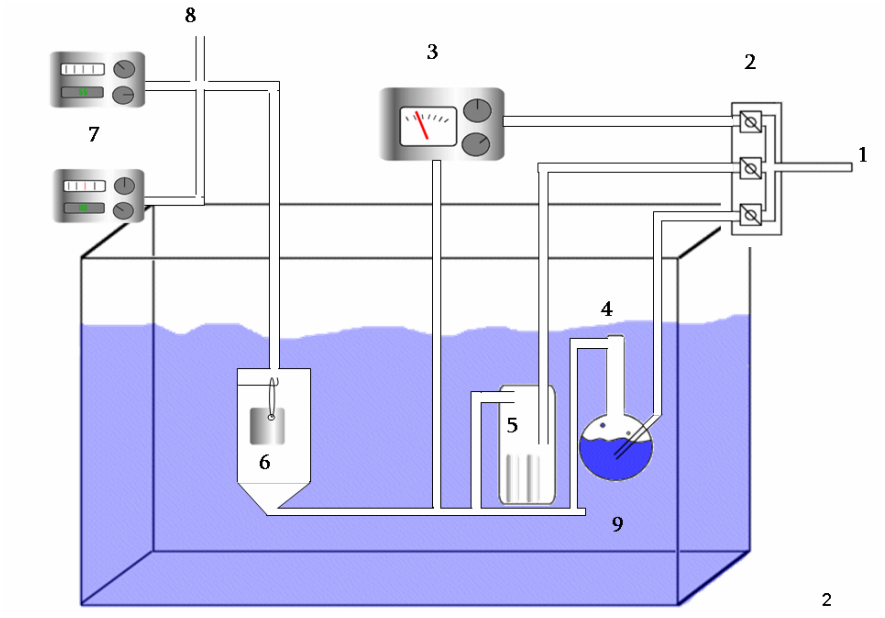

Fig 3

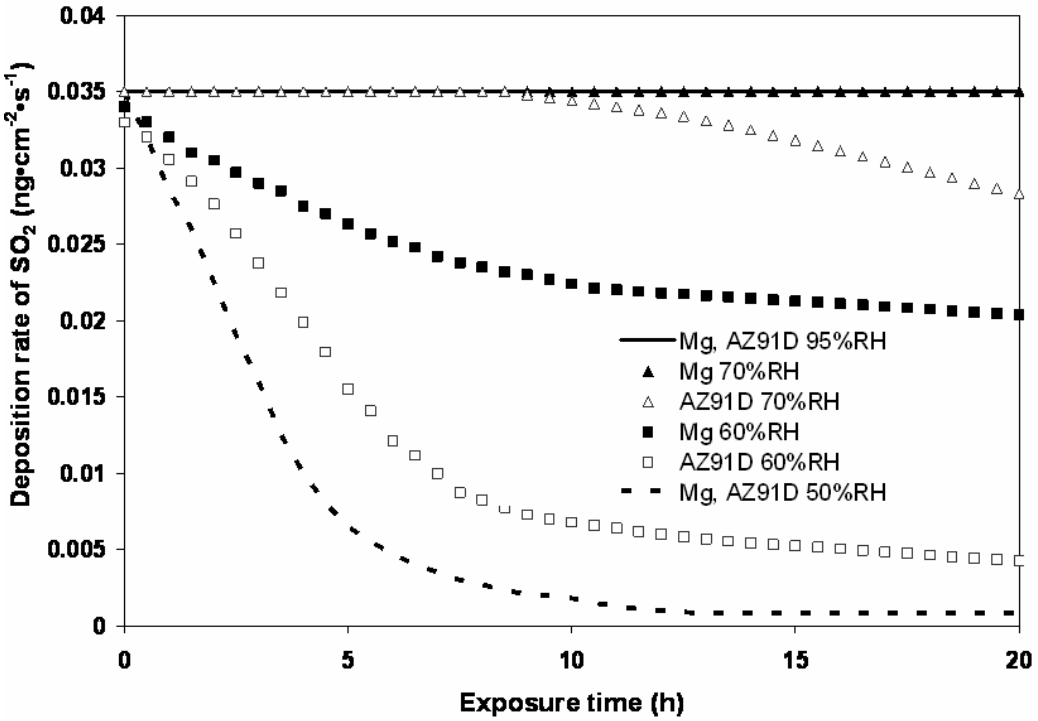
Deposition rate of SO_2 (ng•cm^{-2}•s^{-1})
0.04
0.035
0.03
0.025
0.02
0.015
0.01
0.005
0
0
5
10
15
20
Exposure time (h)
Mg, AZ91D 95%RH
Mg 70%RH
AZ91D 70%RH
Mg 60%RH
AZ91D 60%RH
Mg, AZ91D 50%RH

Fig 4

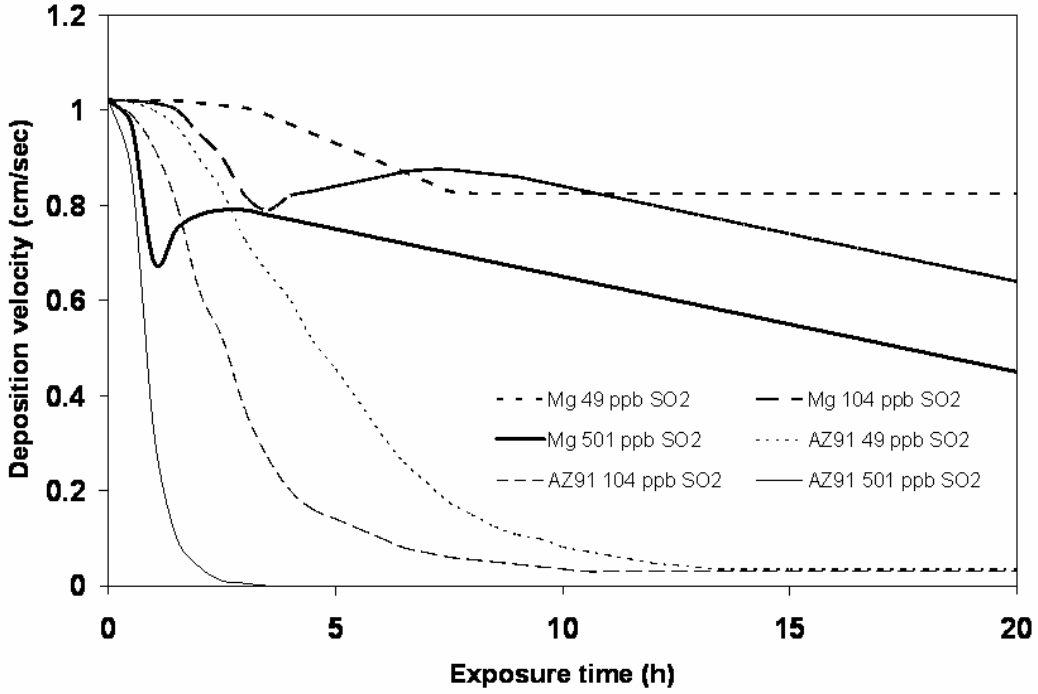
Deposition velocity (cm/sec)
1.2
1
0.8
0.6
0.4
0.2
0
0
5
10
15
20
Exposure time (h)
Mg 49 ppb SO2
Mg 104 ppb SO2
Mg 501 ppb SO2
AZ91 49 ppb SO2
AZ91 104 ppb SO2
AZ91 501 ppb SO2

Fig 5

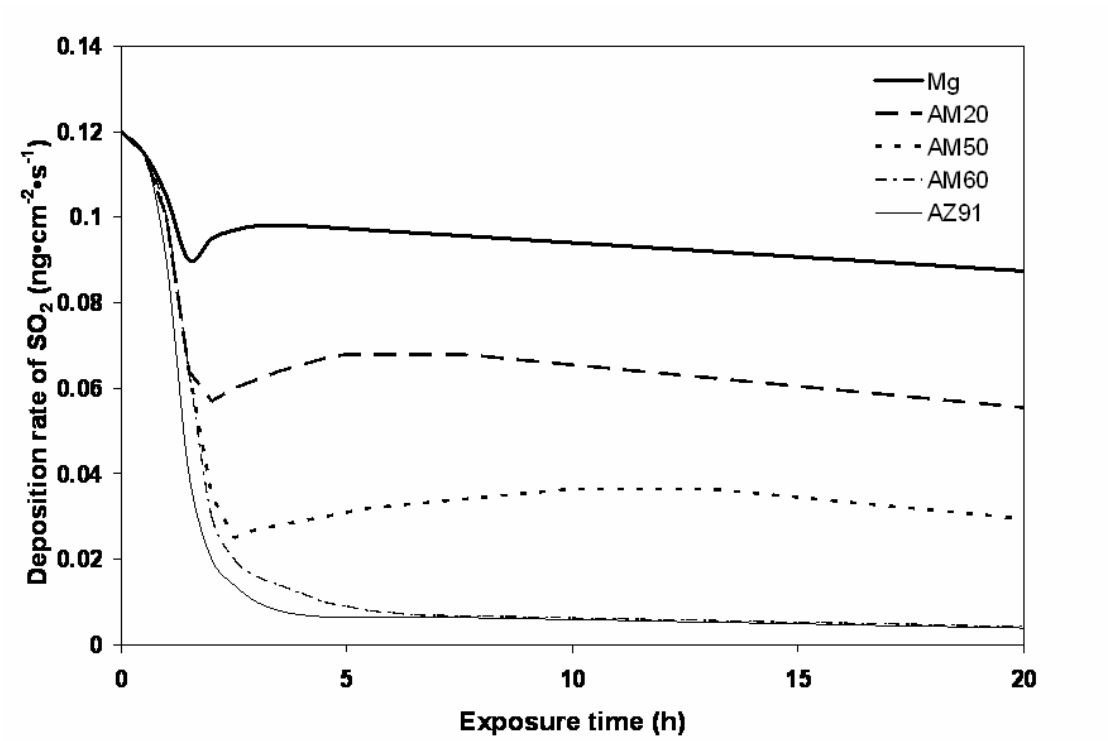
Mg
AM20
AM50
AM60
AZ91
Deposition rate of SO_2 (ng•cm^{-2}•s^{-1})
Exposure time (h)
0.14
0.12
0.1
0.08
0.06
0.04
0.02
0
0
5
10
15
20

Fig 6

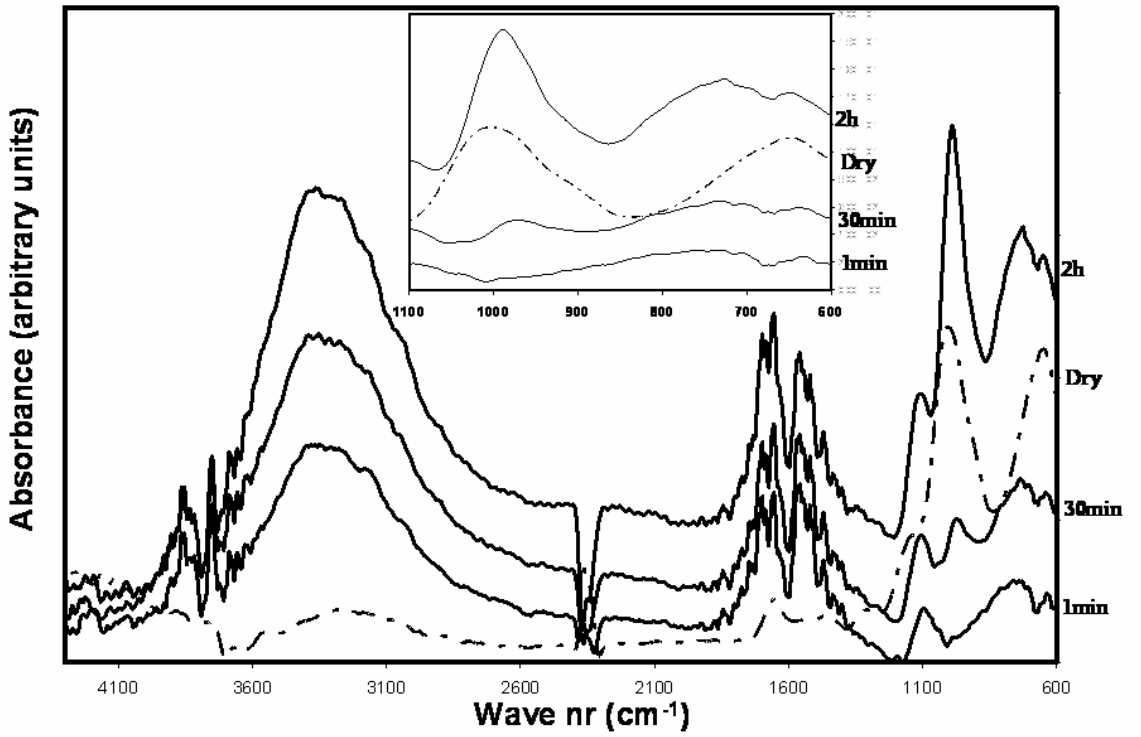
Absorbance (arbitrary units)
Wave nr (cm^{-1})
2h
Dry
30min
1min
4100
3600
3100
2600
2100
1600
1100
600
1100
1000
900
800
700
600

Fig 7

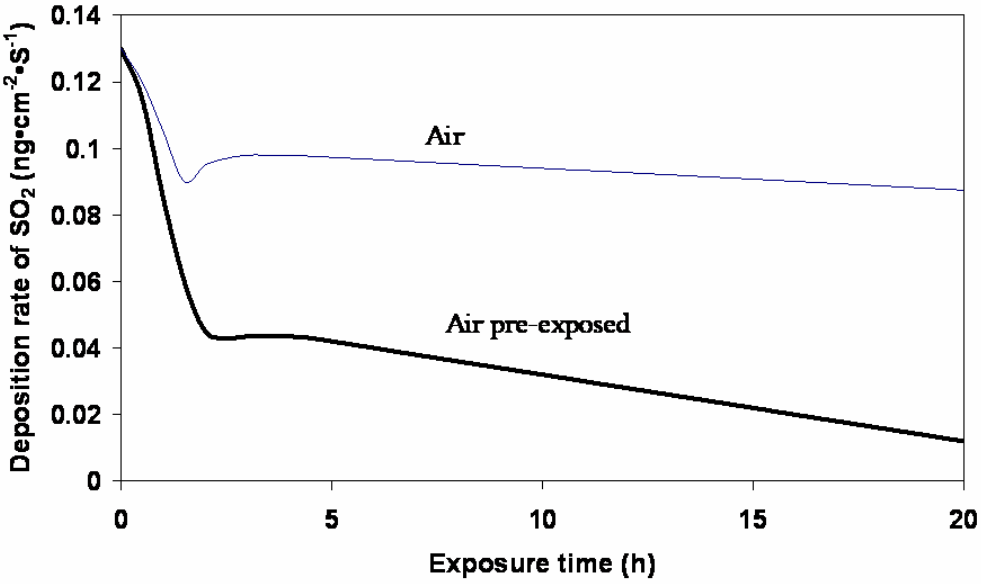
Deposition rate of SO_2 ($ng \cdot cm^{-2} \cdot s^{-1}$)
0.14
0.12
0.1
0.08
0.06
0.04
0.02
0
Air
Air pre-exposed
0
5
10
15
20
Exposure time (h)

7

Fig 8

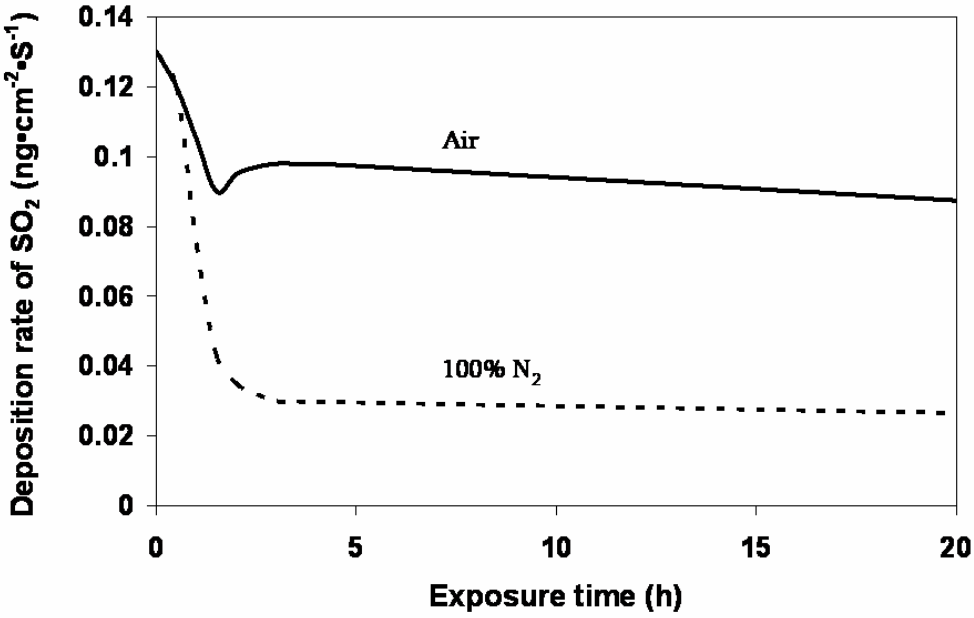
Deposition rate of SO_2 ($ng \cdot cm^{-2} \cdot s^{-1}$)
0.14
0.12
0.1
0.08
0.06
0.04
0.02
0
Air
100% N_2
0
5
10
15
20
Exposure time (h)

8

Fig 9

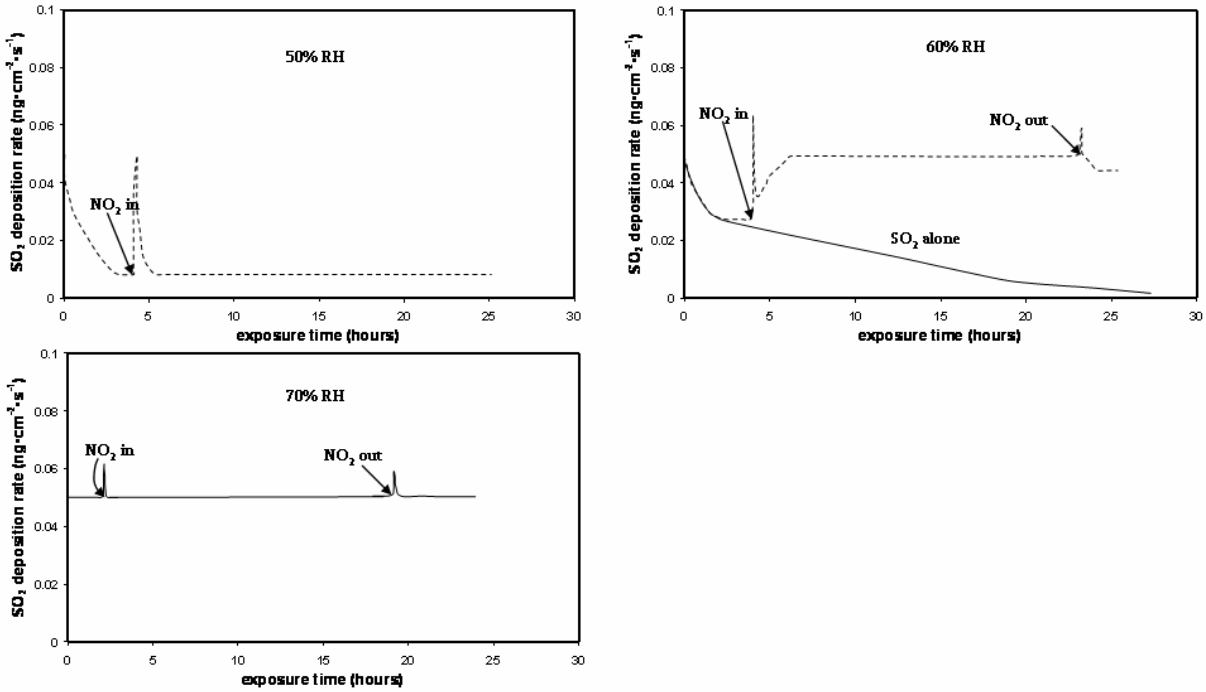
50% RH
60% RH
70% RH
NO2 in
NO2 out
SO2 alone
SO2 deposition rate (ng·cm-2·s-1)
exposure time (hours)

9

Fig 10

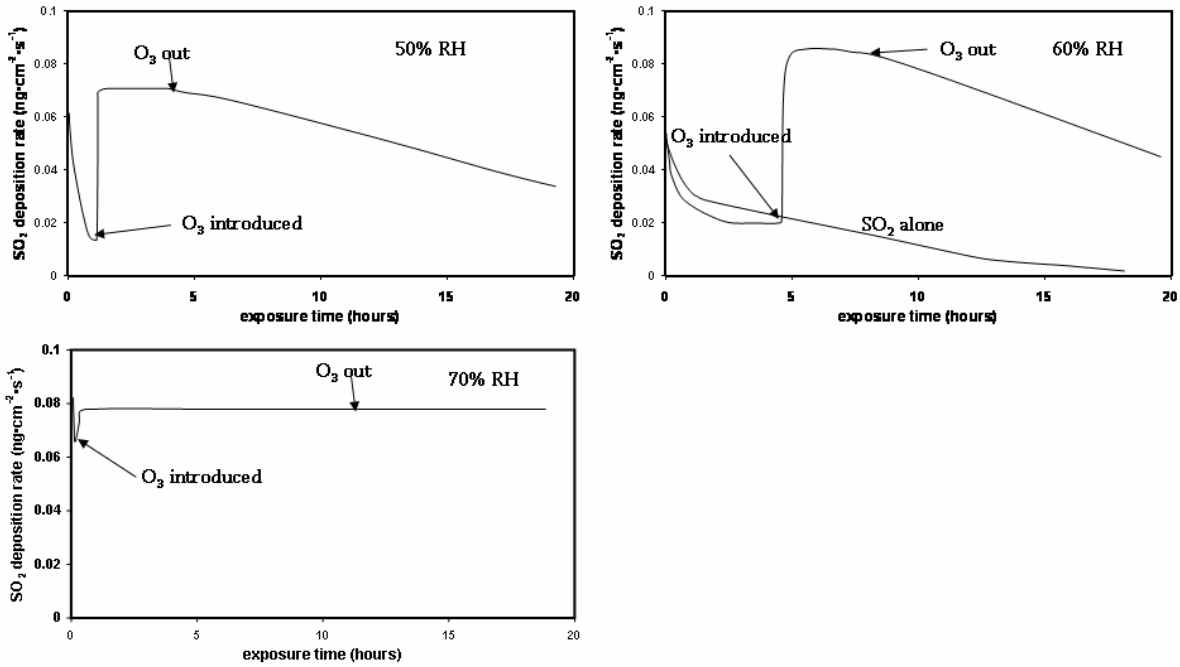
50% RH
60% RH
70% RH
O3 out
O3 introduced
SO2 alone
SO2 deposition rate (ng·cm-2·s-1)
exposure time (hours)

Fig 11

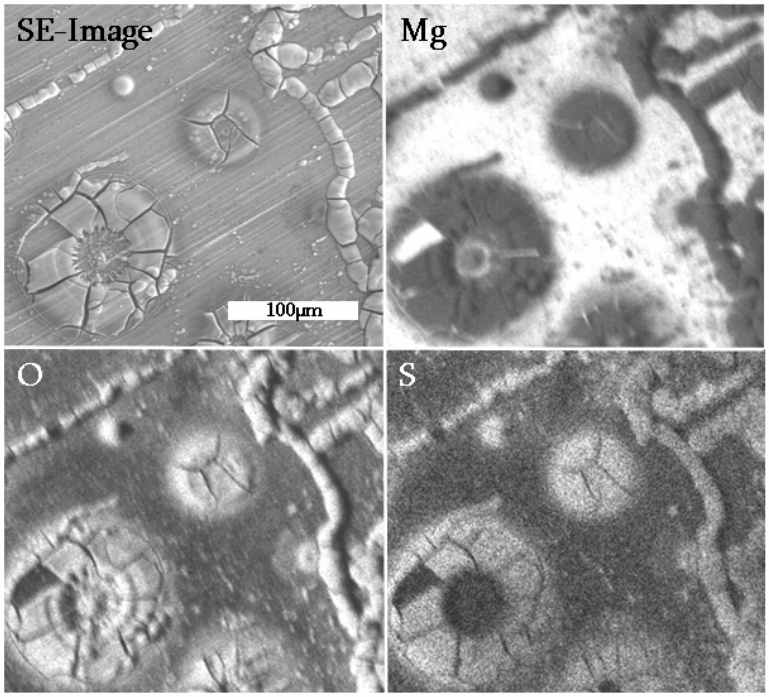

11

Fig 12

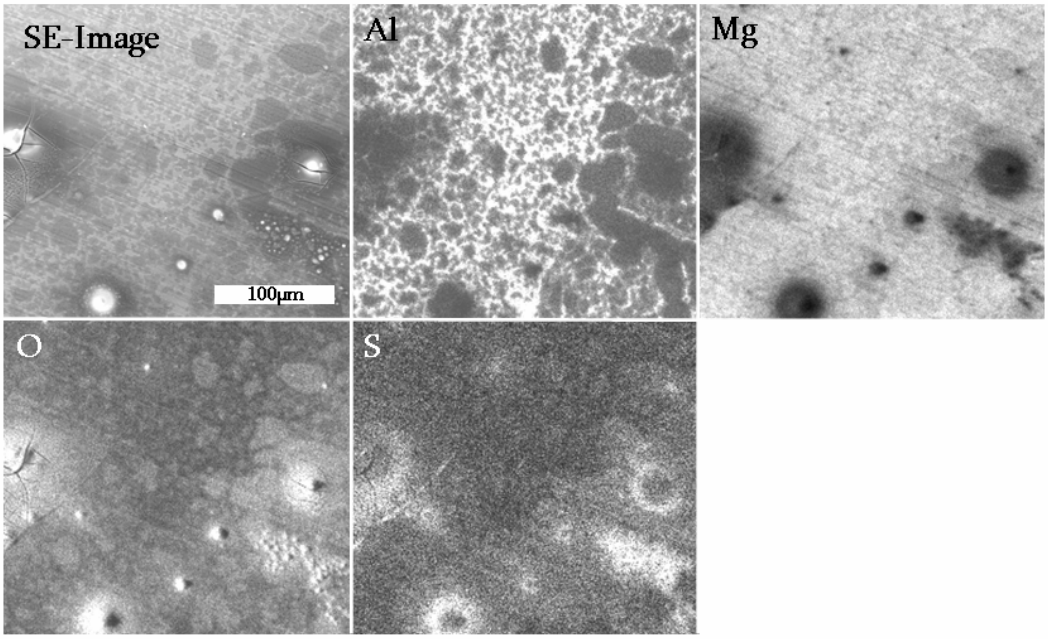

12

Fig 13

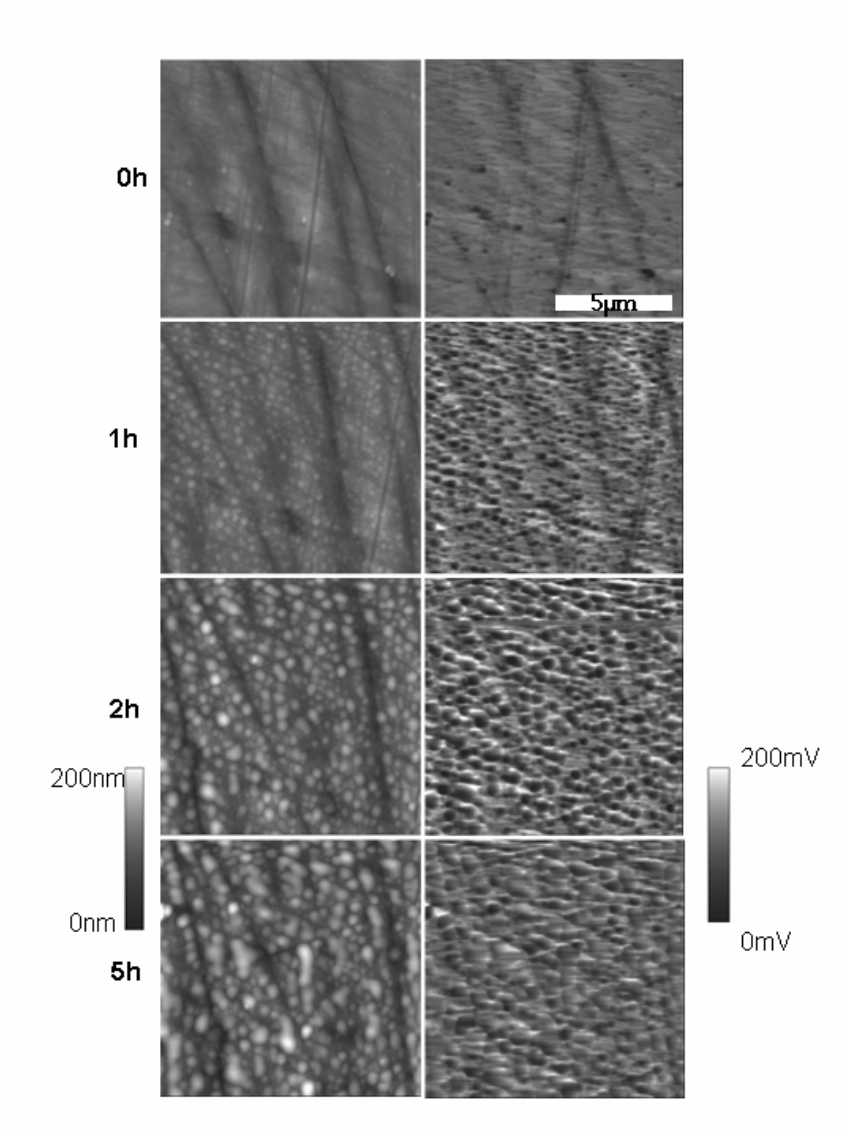

Paper 7

The influence of CO_2, $AlCl_3 \cdot 6H_2O$, $MgCl_2 \cdot 6H_2O$, Na_2SO_4 and NaCl on the atmospheric corrosion of aluminum

D. Bengtsson Blücher, J.-E. Svensson
and L.-G. Johansson

Department of Chemical and Biological Engineering, Chalmers University of Technology
S-41296 Göteborg, Sweden
e-mail: danielb@chalmers.se
Phone: +46 31 7722859
Fax: +46 31 7722853

Abstract

The influence of salt deposits on the atmospheric corrosion of high purity Al (99.999%) was studied in the laboratory. Four chloride and sulfate-containing salts, NaCl, Na_2SO_4, $AlCl_3 \bullet 6H_2O$ and $MgCl_2 \bullet 6H_2O$ were investigated. The samples were exposed to purified humid air with careful control of the relative humidity (95%), temperature (22.0°C), and air flow. The concentration of CO_2 was 350 ppm or < 1 ppm and the exposure time was four weeks. Under the experimental conditions all four salts formed aqueous solutions on the metal surface. Mass gain and metal loss results are reported. The corroded surfaces were studied by ESEM, OM, AES and FEG/SEM equipped with EDX. The corrosion products were analyzed by gravimetry, IC and grazing incidence XRD. In the absence of CO_2, the corrosivity of the chloride salts studied increases in the order $MgCl_2 \bullet 6H_2O$ < $AlCl_3 \bullet 6H_2O$ < NaCl. Sodium chloride is very corrosive in this environment because the sodium ion supports the development of high pH in the cathodic areas, resulting in alkaline dissolution of the alumina passive film and rapid general corrosion. The low corrosivity of $MgCl_2 \bullet 6H_2O$ is explained by the inability of Mg^{2+} to support high pH values in the cathodic areas. In the presence of carbon dioxide, the corrosion induced by the salts studied exhibit similar rates. Carbon dioxide strongly inhibits aluminum corrosion in the presence of $AlCl_3 \bullet 6H_2O$ and especially, NaCl, while it is slightly corrosive in the presence of $MgCl_2 \bullet 6H_2O$. The corrosion effects of CO_2 are explained in terms of its acidic properties and by the

precipitation of carbonates. In the absence of CO_2, Na_2SO_4 is less corrosive than NaCl, This is explained the lower solubility of aluminum hydroxy sulfates in comparision to the chlorides. The average corrosion rate in the presence of CO_2 is the same for both salts. The main difference is that sulfate is less efficient than chloride in causing pitting of aluminum in neutral or acidic media.

Introduction

The corrosion of aluminum in the atmosphere has mainly been investigated through field studies [1-5]. Few laboratory investigations in controlled environments have been published [2, 5, 6]. Except for studies on the effect of NaCl, investigations of the influence of atmospheric particulates on the corrosion rates of metals are scarce. Major components in aerosols include ionic substances such as chlorides and sulfates [2]. Dust particles have been reported to play a major role for corrosion indoors [5, 7]. Based on field investigations and using information from the corrosion behavior of aluminum in aqueous solution, it is generally agreed that, besides strong humidity dependence, the deposition of SO_2 and chloride are major factors that determine the corrosion rate of aluminum [5]. However, field studies cannot provide detailed knowledge on the corrosion process. A deepened understanding for the mechanisms of the atmospheric corrosion of aluminum can only be provided by performing laboratory investigations in controlled environments. One major problem is the discrepancy in the results from accelerated testing and laboratory exposures [8, 9]. This matter further emphasizes the importance of understanding the mechanisms behind atmospheric corrosion. Considering the present use and the potential applications of aluminum alloys, e.g., in the automotive industry, the lack of information on the atmospheric corrosion behavior in the presence of different salts presents a problem. Such information is essential in order to understand the corrosion behavior in the field. The aim of this paper is to investigate the effect of CO_2 on the salt-induced atmospheric corrosion on 99.999% Al. The previously overlooked effect of CO_2 may help to understand the corrosion behavior of aluminum in cases where there is a limited supply of CO_2 and enrichment of salt-deposits for example in crevices, occluded areas such as lap joints and beneath coatings [1, 10, 11].

Carbon dioxide occurs naturally in the atmosphere with a concentration of about 350 ppm [12].. In a recent paper by Blücher *et al*. it was reported that ambient levels of CO_2 strongly inhibits the NaCl-induced atmospheric corrosion of aluminum in humid air at 22°C [13]. Similar results have been reported for the atmospheric corrosion of zinc by Falk *et al*.[14] and Mg by Lindström *et al* [15]. The rapid NaCl-induced corrosion of aluminum in humid CO_2-free air was attributed to an electrochemical process with the anodic dissolution of aluminum occurring in alkaline

solution, forming soluble aluminate. The inhibiting effect of CO_2 was attributed to its acidity, neutralizing the hydroxide formed at the cathodes thereby preventing the formation of aluminate.

The accumulation of e.g. chloride, sulfate, sodium and magnesium on aluminium surfaces in different environments due to reaction with corrosive gases or particle deposition was reported by Sinclair 1982 [16]. Major components in aerosols include sea salt and other ionic substances such as sodium salts (sulfates and nitrates) and Al and Mg chlorides [17]. In lap joints, the limited supply of CO_2 as well as high amounts of chloride and sulfate was reported by Kelly [18]. The levels of particulate chloride deposition reported in the literature cover a very wide range; 15 µg Cl^- cm^{-2} y^{-1} is reported in rural areas far from the coast 60 µg Cl^- cm^{-2} y^{-1} was reported for metropolitan New York while deposition rates of over 55000 µg Cl^- cm^{-2} y^{-1} have been found in extreme marine environments [5, 19, 20]. Sea salt contains approximately 55% Cl^-, 30% Na^+, 8% SO_4^{2-}, 4% Mg^{2+}, 1% Ca^{2+} and K^+, and 0.2% Br^- by weight [21].

It was argued that the reason for the relatively slow corrosion induced by seawater is the presence of Mg^{2+} ions. It is well known that the atmospheric corrosion of metals is accelerated in the presence of soluble salts, e.g., chlorides and sulfates [5]. This effect is connected to the formation of a surface electrolyte at high relative humidity through the absorption of water vapor by the salt. The metal surface in contact with the aqueous solution corrodes by an electrochemical mechanism. In an analogy to the corrosion of metals in aqueous solution, several researchers say that the anions present in the electrolyte also influence the mechanism of atmospheric corrosion directly, i.e., by taking part in the anodic reaction [22, 23]. This is exemplified by the ability of chlorides to cause pitting corrosion of aluminum alloys and stainless steel in the atmosphere [4]. The tendency for the anion to form sparingly soluble corrosion products e.g., hydroxy salts has an important influence on the corrosivity of salts in the atmosphere. The influence of the cations on atmospheric corrosion has received less attention. The cation is not expected to interfere directly in the mechanism of the anodic or cathodic reaction. There is the obvious influence of the cation on the solubility of the salt and on its ability to attract water vapor to form a solution. However, the aqueous chemistry of the cation also has other important consequences for the chemistry of corrosion. This is especially true of its acid/base properties that determine the solubility as a function of pH. For example, the alkali ions do not form insoluble hydroxides whereas the

smaller divalent cations do. In addition, the divalent cations form sparingly soluble salts containing hydroxide together with other anions, notably carbonate, chloride, and sulfate. In the present paper the corrosivity of a few soluble chlorides and sulfates in humid air at 95% RH and 22.0°C is investigated in order to study the effect of the counter ion. Al is reported to form sparingly soluble aluminum hydroxy salts with sulfate [24]. The relative humidity 95% in our exposures was chosen in order that all salts NaCl, Na_2SO_4, $AlCl_3$, and $MgCl_2$ form aqueous solutions on the metal surface. The deliquescence points for the investigated salts are shown in Table I. In the case of the other salts investigated, the amounts added are very high compared to reported deposition rates in the ambient atmospheres [7]. The amounts of the cation added were equivalent, on a molar basis, to the amount of NaCl applied by blücher et al. 01 and 03 (14, 70 and in some cases 140μg/cm^2). This was done in order to make quantitative comparisons regarding the corrosivity of the salts.

Experimental

We report on the effect of four different salts, NaCl, Na_2SO_4, $AlCl_3$•$6H_2O$ and $MgCl_2$•$6H_2O$, on the atmospheric corrosion of 99.999% Al from Goodfellow. The main impurities were Fe 0,7ppm, Mg 1.45ppm, S 0.9ppm and Si 0.99ppm. *The effect of pCO_2 was studied*. The samples had a geometrical area of 20.0 cm^2 (3.0x3.0x0.17) cm. Before exposure the samples were ground on SiC paper in ethanol to 1000 mesh and then polished with 1µm diamond paste in blue lube from Struers. The samples were ultrasonically cleaned in ethanol, dried in air and stored in a desiccator over silica gel for 24h. Sodium chloride and sodium sulfate was added by spraying the samples with a saturated solution of NaCl in 80/20 ethanol/water. The amount of NaCl and Na_2SO_4 added was determined gravimetrically. Care was taken to avoid droplet formation on the samples during spraying. $AlCl_3$•$6H_2O$ and $MgCl_2$•$6H_2O$ were applied to the samples by spreading a 3M solution on to the surfaces using a latex plate. The amount of salt added was determined volumetrically. The distribution of salt on the surface after spraying was seen with E-SEM to be even. Duplicate samples of each salt were exposed.

Exposures were performed at 22.0°C. In each experiment, a total of eight samples were exposed. To avoid interactions between samples, each sample is exposed in a chamber of its own. The amount of sodium chloride added in this study (equivalent to 550 µg Cl^- cm^{-2} y^{-1}) correspond to chloride deposition rates in urban areas and to marine environments not in the immediate vicinity of the coastline [2-4].

The equipment used in the corrosion exposures *in the presence of CO_2* has been described previously[25]. There are eight parallel chambers, see Fig. 1a.

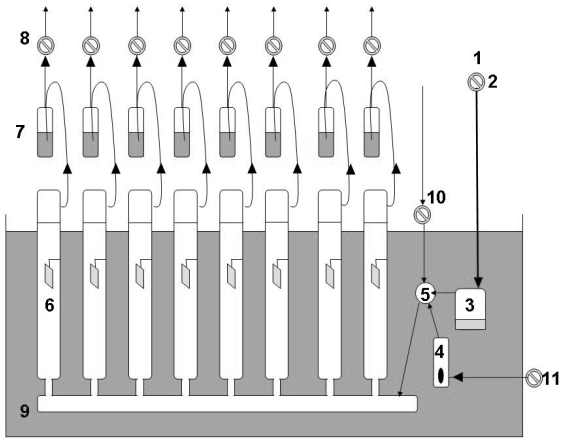

Figure 1a. Experimental setup for exposures with 350ppm CO_2 and for some with ppb levels of SO_2 at 4 - 22.0°C. (1) pure air inlet; (2) mass flow regulators; (3) humidifier; (4) NO_2 and/or SO_2 permeation tubes; (5) mixing point; (6) exposure chambers with Al or Mg-Al samples; (7) gas trap; (8) solenoid valves; (9) thermostated water tank; (10) CO_2 or O_3 inlet; (11) carrier gas (purified air) for NO_2 and or SO_2.

The whole gas flow (1000mL/min) passes through each chamber in turn for 15 s. The chambers have an inner diameter of 55 mm and a volume of 0.4 l. The net gas flow is 7mm/sec corresponding to a Reynolds number (R_e) of about 25 in an empty chamber. In order to avoid interactions between samples, only one sample is exposed in each chamber. The relative humidity was 95% and was controlled to an accuracy of about 0.3%.

To monitor the corrosion process during exposure the samples were weighed once a week. In order to avoid disturbing the corrosion process, the samples were not dried before weighing. The weighing procedure lasted two minutes per sample. The mass gain recorded in this way is termed the wet mass gain. After the completion of the 672 h exposures the dry mass gain of the samples was determined after storing over a desiccant at ambient pressure and temperature for one week.

The exposures in the *absence* of CO_2 were performed using a hermetically closed glass container filled with air. The samples were suspended inside the 3.5 dm^3 container. Beneath the samples there was 0.1dm^3 of 1.6M NaOH(aq) which is in equilibrium with 95% RH air. The NaOH solution getters CO_2, ascertaining that the concentration of CO_2 during exposure is < 1ppm. The container temperature was controlled to within 0.2°C. It was previously shown that exposures in this apparatus produced results identical to those obtained in flowing CO_2-free air using the set-

ups described above [26]. The samples exposed in CO_2-free air were only weighed after the exposure to avoid absorption of CO_2.

The amount of corrosion products was determined by leaching followed by pickling the samples, with ultrasonic agitation. Water-soluble corrosion products and unreacted NaCl were first removed by leaching in milli-Q water (pH 7) at ambient temperature for one minute and then repeated for 30 minutes. The amount of sulfate and chloride removed by leaching was determined by IC and the sample mass was recorded. The samples were then pickled in a solution containing H_3PO_4 and CrO_3 (one liter of solution is prepared by mixing 50ml H_3PO_4 (85%) and 20.0g CrO_3 with milli-Q water) for 5 minutes at 80°C, after which they were washed in water and ethanol. This procedure was repeated three times. The sample mass was recorded after each step. Weighing the samples after the leaching and pickling process gives the metal loss. The metal loss caused by pickling (self corrosion) was determined by using an uncorroded sample and by measuring mass loss as a function of time. This effect was corrected for in the determination of the metal loss of the exposed samples. The ratio $\frac{(\text{mass gain} - \text{metal loss})}{\text{metal loss}}$ provides information on the stoichiometry of the corrosion product. IC is used to analyze quantitatively for water-soluble anions (e.g. chloride and sulfate) on the samples after exposure (Dionex DX100 with an Ionpac AD9-SC column). The flow rate was 2 ml/min and 1.8 mM Na_2CO_3 / 1.7 mM $NaHCO_3$ was used as eluent. GI-XRD is used for characterization of crystalline corrosion products (Siemens D-5000 CuK_α radiation equipped with a Göbel mirror). The diffraction peaks of metallic Al were used as an internal standard. The samples were also studied by optical microscopy (Zeiss), E-SEM (Electroscan 2020 equipped with LINK ISIS EDX and a FEI 200 FEG/ESEM equipped with an Oxford INCA EDX).

Auger electron spectroscopy (AES) was used to determine the composition of the corrosion product layer by performing depth profiling. The AES analyses were performed with a Scanning Auger Microprobe (SAM) instrument (PHI 660). The primary accelerating voltage was 10kV and the beam current was 75nA. The depth profiles were obtained using a differentially pumped ion gun (Ar^+) with acceleration voltage 4.0kV. The etch rates were calibrated on a flat sample of

Ta_2O_5 with a known oxide thickness of 100nm. The collected raw-data was refined using MultiPak v.6.0 software.

Results

Chloride-induced atmospheric corrosion of aluminum in the absence of CO_2

Fig. 1b shows the average corrosion rate of aluminum in CO_2-free air at 95% RH as a function of the number of moles of chloride added for NaCl, $AlCl_3 \cdot 6H_2O$ and $MgCl_2 \cdot 6H_2O$. The corrosivity of the chloride salts studied increases in the order $MgCl_2 \cdot 6H_2O$ < $AlCl_3 \cdot 6H_2O$ < NaCl. In the absence of salt, the corrosion rate was very small (about 0.001mg/cm^2). At 95%RH all salts studied form an aqueous electrolyte on the sample surface. Accordingly, the samples became visibly wet shortly after the introduction into the exposure chamber. Table I shows the deliquescence point and the equilibrium concentration of the salt solutions formed.

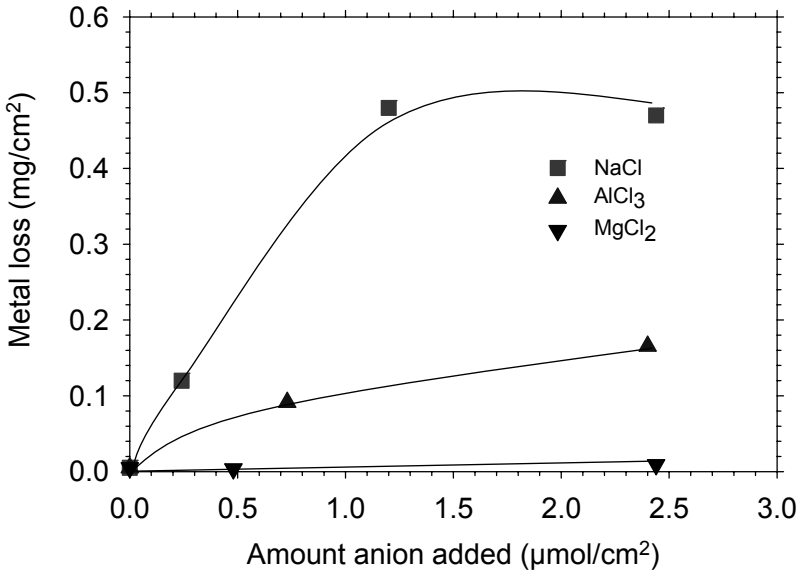

Figure 1b. Average corrosion rate of aluminium as a function of the amount of chloride added for NaCl, $AlCl_3 \cdot 6H_2O$ and $MgCl_2 \cdot 6H_2O$. The samples were exposed to air with <1ppm CO_2 at a relative humidity of 95%. The exposure time was 4 weeks and the temperature was 22.00°C.

NaCl

The corrosion rate depends linearly on the amount of NaCl added up to 1.2µmol NaCl/cm^2. A further increase in the amount of NaCl added does not result in higher corrosion rate. The NaCl(aq) electrolyte formed when the experiment started remained visible during the first week. During the later stages of the experiment the samples appeared dry. The rapid corrosion rate is evident when examining the morphology of the exposed samples. Samples pre-treated with

1.2µmol NaCl/cm^2 appeared white after exposure, the sample surface being completely covered by corrosion products. Optical microscopy images showed circular 0.2 mm diameter features covering about 60% of the sample surface, see Fig. 2.

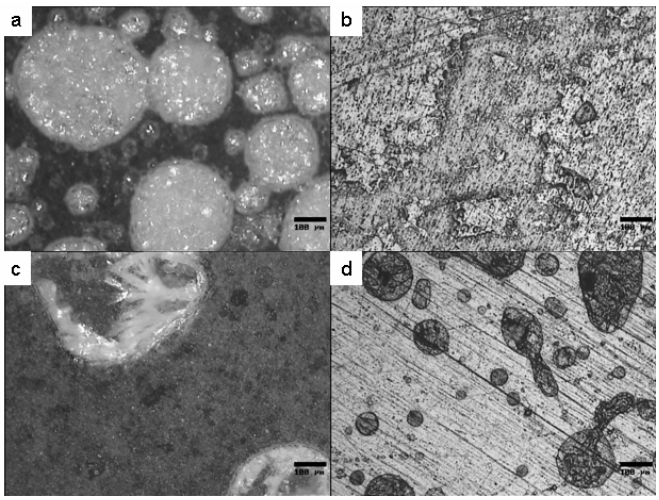

Figure 2. Optical microscopy images of aluminum exposed to air with <1 ppm CO_2 at 22.00°C for 4 weeks at 95% RH. a) 1.2µmol NaCl/cm^2, b) 1.2µmol $AlCl_3$•$6H_2O$/cm^2, c) 0.6µmol of Na_2SO_4/cm^2, d) 1.2µmol of $MgCl_2$•$6H_2O$ /cm^2. The black bars correspond to 100µm.

Analysis by E-SEM and EDX showed that the circular features were rich in Al, O, Na and Cl, see Fig. 2b.

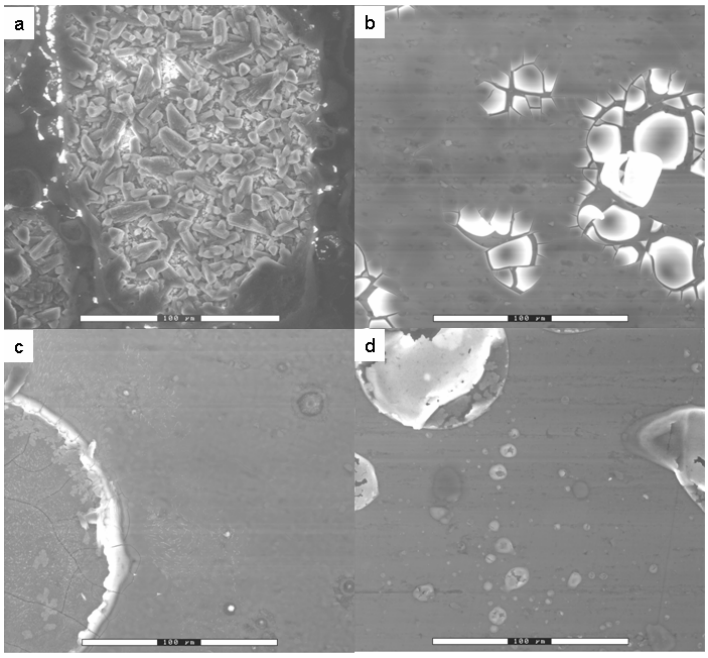

Figure 2b. Environmental SEM images of aluminum exposed to <1ppm CO_2 at 22°C for 4 weeks at 95% RH. The amount of salt added prior to exposure was: a) 1.2µmol NaCl/cm^2, b) 1.2µmol $AlCl_3$•$6H_2O$/cm^2, c) 0.6µmol Na_2SO_4/cm^2, d) 1.2µmol $MgCl_2$•$6H_2O$/cm^2. The bars correspond to 100µm.

The inner part of the circular features consist of Al - and O-rich crystallites of somatoidal shape of about 2 - 4µm in diameter and 10µm length. NaCl crystallites can be seen between the aluminum-containing crystals, see Fig. 3.

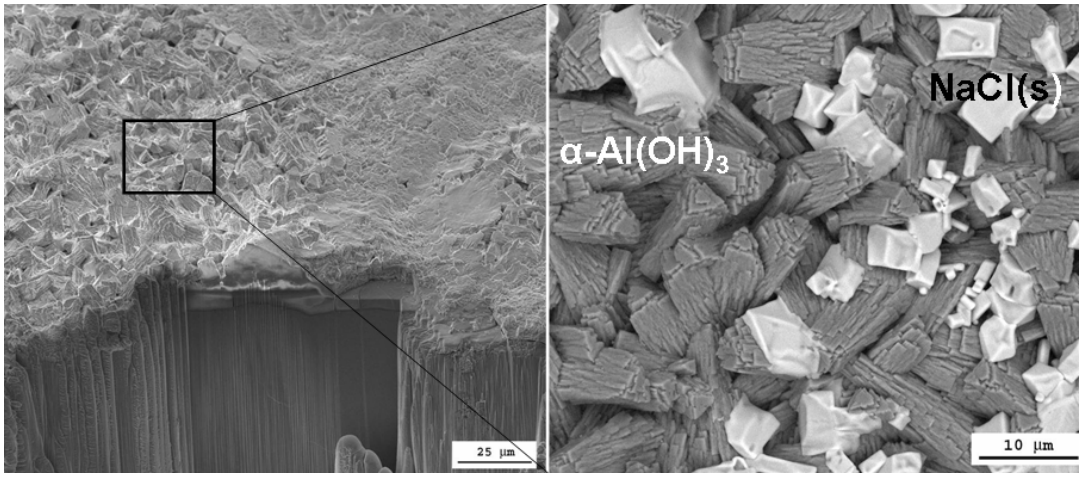

Fig. 3. ESEM images of Al exposed to 95% RH without CO_2 for 672 hours. The temperature was 22.0°C and 70µg NaCl/cm^2 was added prior to exposure. The cross section to the left was made by the focused ion beam technique (SE image). The magnification of the area in the square (right) is imaged by BSE. L. Ingemarsson[27].

The crystal agglomerations are about 10-15µm thick (see SEM of FIB cross section in Fig 3.) EDX analysis showed that the corrosion products contain 75at% O and 25at% Al. An amorphous 10 µm thick corrosion product scale covered the surface between the circular agglomerates (see Fig. 3). The scale featured occasional cracks that contained crystallites of the same type as found in the circular features. FIB cross sectioning and EDX showed that there was no Na and only a sporadic occurrence of Cl at the metal/corrosion product interface. X-Ray diffraction showed the presence of α-$Al(OH)_3$ (bayerite) and NaCl. Almost all the chloride applied (> 99%) was removed by leaching in water, see Table II. This is expected as no insoluble aluminum chlorides have been reported [5]. After leaching in water and pickling (see the experimental part) the metal surface appeared undulated with shallow craters and had an average surface roughness of about 7µm. No pitting was seen. Table II presents the corrosion product ratio (mass gain+metal loss)/(metal loss) for the samples. This ratio is related to the stoichiometry of the corrosion products and can be compared to the corresponding ratios (molar mass)/(mass of cation) of selected compounds in Table III. High values for the corrosion product ratio indicates that the fraction of Al in the corrosion products is low. For the samples that corroded in the presence of NaCl the ratio is about 3, corresponding to the formation of $Al(OH)_3$.

$AlCl_3$•$6H_2O$

In the presence of $AlCl_3 \cdot 6H_2O$ the aluminum corrosion rate is about one third compared to corrosion rate resulting from adding the same amount of chloride as NaCl, see Fig. 1b. The exposed samples appeared only partly corroded. In the experiment with the highest amount of $AlCl_3$•$6H_2O$, about 50% of the surface was covered by white agglomerates while the remaining surface retained its metallic lustre. The corrosion products showed a tendency to spall after exposure (during dry storage), especially in the cases when large amounts of $AlCl_3$•$6H_2O$ had been added. Optical microscopy revealed white corrosion products crusts, see Fig. 2. E-SEM and EDX showed that the crusts were rich in Al, O and Cl, see Fig. 2b. X-Ray diffraction showed the presence of $Al_2Cl(OH)_5$•$2H_2O$. For most samples, all of the applied chloride (>99%) was removed by leaching in water, see Table II. The lower values for found for leachable chloride in some cases is probably caused by losses by spallation. After leaching and pickling, the surface appeared dull grey. No pitting was observed.

$MgCl_2$•$6H_2O$

In comparison to $AlCl_3 \cdot 6H_2O$ and NaCl, the presence of $MgCl_2 \cdot 6H_2O$ causes very little corrosion on Al in the absence of CO_2 (see Fig. 1b.). For the largest chloride additions, the corrosion rate caused by NaCl is about 50 times higher than that recorded in the presence of $MgCl_2 \cdot 6H_2O$. Samples exposed in the presence of $MgCl_2 \cdot 6H_2O$ appeared uncorroded to the naked eye after exposure, optical microscopy showing unreacted salt, see Fig. 2. X-Ray diffraction showed the presence of unreacted $MgCl_2 \cdot 6H_2O$, bischofite. About 70% of the applied chloride could be leached in water, see Table II. This is probably due to the spalling of $MgCl_2$ after exposure. No pits were observed after leaching and pickling.

Chloride-induced atmospheric corrosion of aluminum in the presence of 350pppm CO_2

Four weeks exposure to this environment without added salt resulted in very slow corrosion (corresponding to a metal loss of about 0.001 mg/cm^2). Ambient concentrations (350ppm) of CO_2 decrease the aluminum corrosion rate considerably in the presence NaCl and $AlCl_3 \cdot 6H_2O$. In contrast, the rate of corrosion in the presence of $MgCl_2 \cdot 6H_2O$ is accelerated somewhat by CO_2 (see Fig. 4). After four weeks the average corrosion rate is about the same for all three salts studied. However, because the mode of corrosion attack in this environment tends to be localized, the average corrosion rate is not a good measure of corrosion. In the CO_2 exposures, all samples appeared wet throughout the exposure.

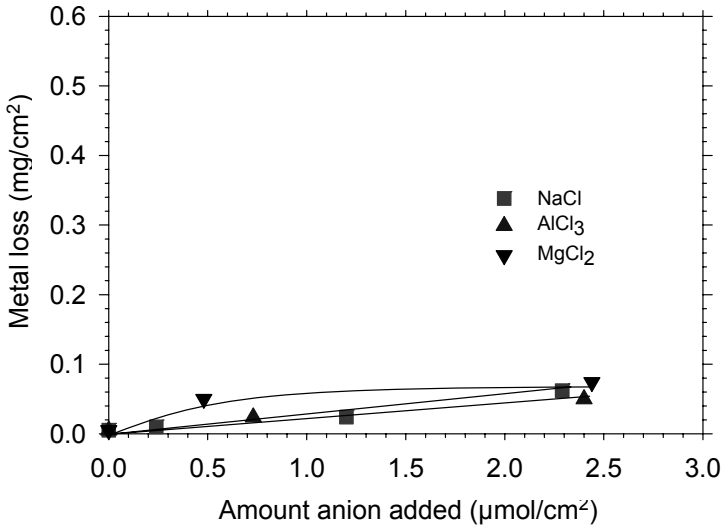

Figure 4. Average corrosion rate of aluminium as a function of added chloride. The samples were exposed to air with 350ppm CO_2 at a relative humidity of 95%. The exposure time was 4 weeks and the temperature was 22.00°C.

NaCl

Carbon dioxide decreases the NaCl-induced corrosion of aluminum by up to 20 times (compare Figs. 1b and 4.) In this environment the corrosion rate increases roughly linearly with the amount of NaCl added. After exposure, samples pre-treated with NaCl appeared locally affected by corrosion to the naked eye. Discrete white corrosion product crusts were present on the surface. Optical microscopy images showed unreacted NaCl together with corrosion product crusts, see Fig. 5.

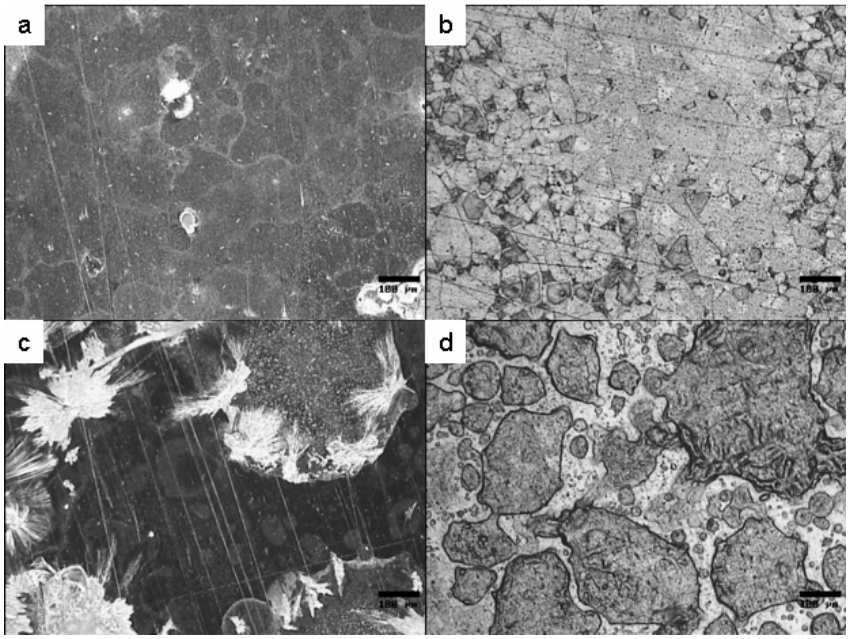

Figure 5. Optical microscopy images of aluminum exposed to air with 350ppm CO_2 at 22°C for 4 weeks at 95% RH. a) 1.2µmol NaCl/cm^2, b) 1.2µmol/cm^2 $AlCl_3$•$6H_2O$, c) 0.6 µmol Na_2SO_4/cm^2, d) 1.2µmol/cm^2 $MgCl_2$•$6H_2O$. The black bars correspond to 100µm.

Imaging and analysis by FEG/ESEM, and EDX showed that with 1.2µmol Na^+/cm^2 added, about 90% of the sample surface was covered by a very thin layer of corrosion products, see Fig. 5b. Tiny NaCl crystallites (0,1µm) were present on this part of the surface, see Fig 6.

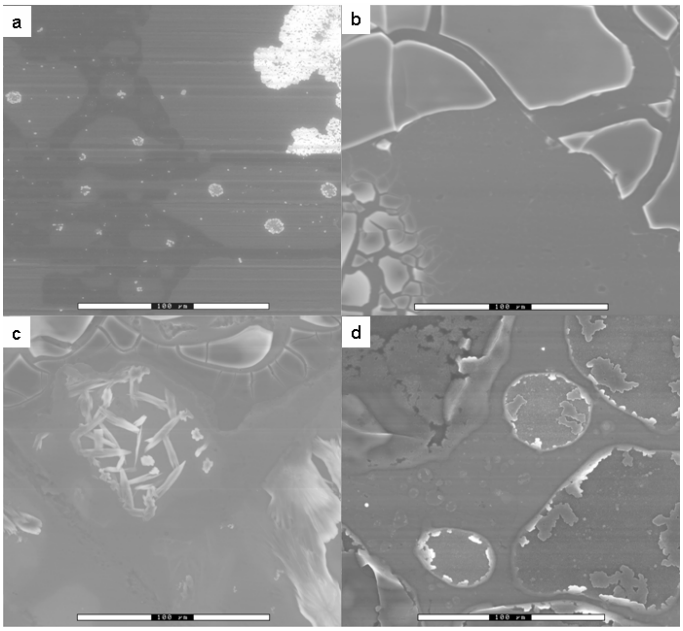

Figure 5b. Environmental SEM images of aluminum exposed to 350 ppm CO_2 at 22°C for 4 weeks at 95% RH. The amount of salt added prior to exposure was: a) 1.2µmol NaCl/cm^2, b) 1.2µmol $AlCl_3$•$6H_2O$ /cm^2, c) 0.6µmol Na_2SO_4/cm^2, d) 1.2µmol $MgCl_2$•$6H_2O$ /cm^2. The bars correspond to 100µm.

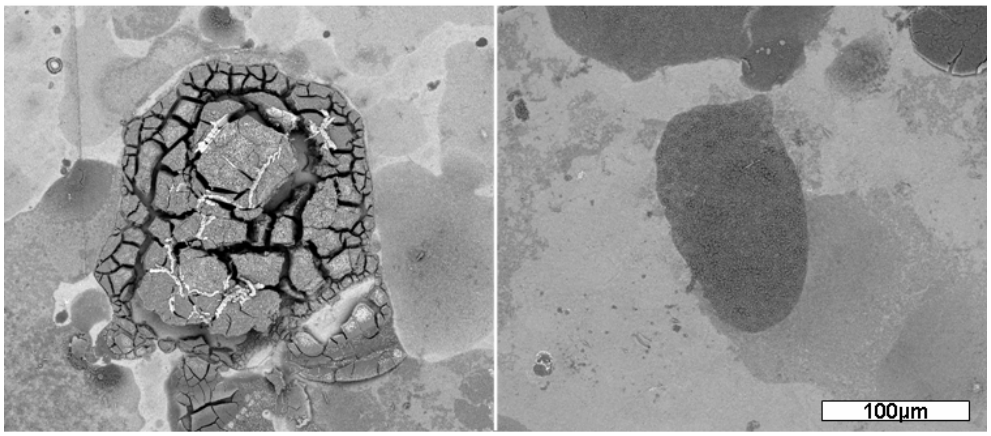

Figure 6. Environmental SEM backscattered electrons images of aluminum after four weeks in air with 350ppm CO_2 at 22°C at 95% RH. The image to the left shows a pit and the image to the right shows an area between the pits. 1.2µmol NaCl/cm^2 was added prior to exposure.

Auger electron spectroscopy (AES) depth profiling showed that the average corrosion scale thickness between the crusts was about 50nm. EDX showed that this thin layer contained about 12at% Na, 67at% Al, 13at%O and 8at% Cl. It may be noted that the elemental composition includes information from the aluminum bulk and from the small adjacent NaCl crystallites embedded in the oxide. The corrosion product crusts (200µm diameter) contained 20at% Al, 70at%O and 10at% Cl. Minor amount of sodium were also present. X-Ray diffraction showed the

presence of NaCl and $NaAl(OH)_2CO_3$ (dawsonite). All applied chloride could be leached by water, see Table IV. After leaching and pickling, the surface appeared uncorroded to the naked eye. However, some pits could be seen by optical microscopy, the average pit depth being about 35µm.

$AlCl_3$•$6H_2O$

For the addition of 0.7µmol Cl^-/cm^2 in the form of $AlCl_3 \cdot 6H_2O$, the corrosion rate in the presence of CO_2 is about one third of that in the absence of CO_2. The corrosivity of $AlCl_3$•$6H_2O$ is comparable to that of NaCl (see Fig. 4). The rate of corrosion depends roughly linearly on the amount of $AlCl_3$•$6H_2O$ added. After exposure, about 50% of the surface was covered by white areas while the remaining surface appeared not to be affected by corrosion. Spallation of corrosion products was observed for samples exposed with large amounts of added salt. E-SEM and EDX on a sample pre-treated with 1.2µmol Al^{3+} added showed and that the white corrosion products were rich in Al, O and Cl, see Fig. 5b. X-Ray diffraction gave evidence of $Al_2Cl(OH)_5$•$2H_2O$. All of the applied chloride could be leached in water, see Table IV.

$MgCl_2$•$6H_2O$

In contrast to the situation with $AlCl_3 \cdot 6H_2O$ and NaCl, ambient levels of CO_2 increases the magnesium chloride-induced corrosion of aluminum. To the naked eye, samples exposed in the presence of $MgCl_2$•$6H_2O$ appeared uncorroded after exposure. Optical microscopy images showed areas with dried salt, see Fig. 5. As expected, E-SEM and EDX showed that these areas were rich in Mg, Cl and O, see Fig. 5b. X-Ray diffraction verified the presence of unreacted $MgCl_2$•$6H_2O$, bischofite. After leaching and pickling, no pitting was observed using optical microscopy. About 70% of the applied chloride could be leached in water, see Table IV. Some chloride was lost by spallation when during storage in the desiccator.

<u>Comparison between the corrosive effects of NaCl and Na_2SO_4</u>

Air without CO_2

After a couple of days exposure, the samples with added NaCl and Na_2SO_4 appeared dry to the naked eye. Corrosion rate depends linearly on the amount of salt for small additions of sulfate

and chloride (see Fig. 7). With Na_2SO_4 the corrosive effect towards aluminum saturates at lower amounts of added salt than in the case of NaCl.

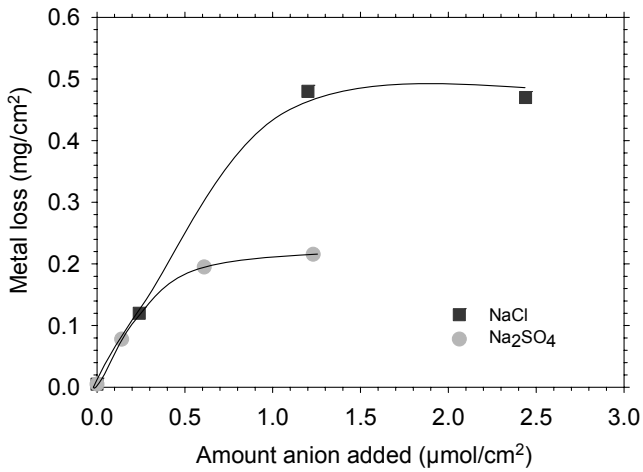

Figure 7. Corrosion rate of aluminium in the absence of CO_2 as a function of the amount of added Na_2SO_4 and NaCl. The exposure time was 4 weeks and the temperature was 22°C. The RH was 95%.

To the naked eye, samples pre-treated with 0.6µmol of Na_2SO_4 appeared white after exposure. Most of the sample surface was covered by circular crusts. An optical microscopy image of these features is shown in Fig. 2. E-SEM and EDX showed that they were rich in Na, S and O while the areas between these circles were rich in Al and O (see Fig. 2b). X-Ray diffraction showed the presence of unreacted Na_2SO_4, α-$Al(OH)_3$ (bayerite) and $NaAl(SO_4)_2 \cdot 11H_2O$ (mendozite). After the removal of the corrosion products, the surface appeared stained with grey areas. A small number of sites of localized corrosion attack were found after pickling sample. The pits were broad and shallow with an average depth of about 8µm. About 80% of the added sulfate could be leached in water, see Table V.

Air with 350ppm CO_2

Carbon dioxide inhibits the corrosion induced by both salts (compare Figs 7 and 8).

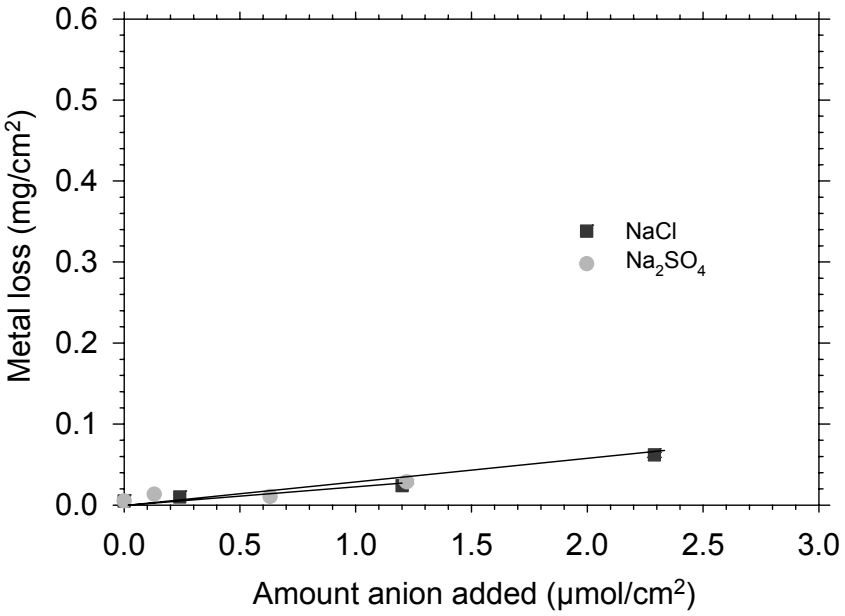

Figure 8. Corrosion rate of aluminium in air with 350 ppm CO_2 as a function of the amount of added Na_2SO_4 and NaCl. The exposure time was 4 weeks and the temperature was 22°C. The RH was 95%.

To the naked eye, aluminum with 0.6µmol/cm^2 of added Na_2SO_4 appeared uncorroded after exposure. The sample surface was partly covered by unreacted Na_2SO_4. Optical microscopy images showed circular features of about 400 µm in diameter, see Fig. 5. These crusts consisted of Na, S and O (E-SEM/EDX), see Fig. 5b. The areas between these salt crusts were rich in Al and O. X-Ray diffraction only showed evidence for unreacted Na_2SO_4. Almost all of the applied sulfate could be leached in water, see Table V. After removing the corrosion products, the sample surface was stained, featuring dull grey areas. Examining the surface further in optical microscopy revealed a slightly rough surface. No pitting could be observed. This is in contrast to the exposures with NaCl where pitting corrosion was evident.

Discussion

The results clearly illustrate the remarkable ability of CO_2 to inhibit the NaCl induced corrosion of aluminum (compare Figs 1b and 4). This effect has been reported previously [28]. The rapid NaCl induced corrosion of aluminum in the absence of CO_2 was attributed to the alkaline dissolution of the passive film:

$$Al(s) + 3OH^-(aq) \rightarrow Al(OH)_3(s) \quad (1)$$

$$Al(OH)_3(s) + OH^-(aq) \rightarrow Al(OH)_4^-(aq) \quad (2)$$

It was argued that regions with high pH develop in the surface electrolyte due to the cathodic reduction of oxygen:

$$\frac{1}{2}O_2(g) + H_2O + 2e^- \rightarrow 2OH^-(aq) \quad (3)$$

The sodium ion migrates to the cathodes and supports the high pH values in these areas. Chloride is not an efficient corrosion promoter for aluminum at high pH because the negative surface charge of alumina makes chloride adsorption unfavorable. (The isoelectric points of aluminum hydroxides and oxide hydroxides fall in the range 8-10) Therefore, NaCl gives rise to general corrosion of aluminum in the absence of CO_2 rather than pitting. The inhibitive effect of CO_2 was attributed to its acidity, neutralizing the alkaline solution formed in the cathodic areas by forming carbonate and hydrogen carbonate.

$$CO_2(g) \leftrightarrows CO_2(aq) \quad (4)$$

$$CO_2(aq) + OH^-(aq) \rightarrow HCO_3^-(aq) \quad (5)$$

$$HCO_3^-(aq) + OH^-(aq) \rightarrow CO_3^{2-}(aq) + H_2O \quad (6)$$

The predominance of pitting corrosion in the presence of CO_2 was explained in a similar way. Because of the lower pH values in the surface electrolyte in the presence of CO_2, chloride adsorbs on the positively charged alumina film, causing local depassivation.

The low corrosivity of $MgCl_2 \cdot 6H_2O$ is suggested to be explained by the limited solubility of magnesium hydroxide. In a concentrated aqueous solution of magnesium chloride, $Mg(OH)_2$ precipitates if pH exceeds 10. This means that the magnesium ions migrating towards the cathodic sites will tend to precipitate, resulting in a loss of electrolytic conductivity and in the deposition of an insulating $Mg(OH)_2$ layer on the electrode. The acidic pitting-type aluminum corrosion is not affected by this mechanism of inhibition. It is suggested that CO_2 accelerates the magnesium chloride induced corrosion of aluminum because it acidifies the electrolyte, creating more favourable conditions for pitting corrosion.

In the absence of CO_2, aluminum chloride is intermediate in corrosivity between NaCl and $MgCl_2$ (see Fig. 1b). Aluminum chloride forms an acidic surface electrolyte and precipitates as aluminum hydroxide if neutralized. This implies that aluminum chloride cannot support the type of alkaline corrosion described for NaCl and that corrosion belongs to the acidic pitting type. The acidic properties of the Al^{3+}(aq) cation and the high solubility of aluminum hydroxy chlorides are suggested to cause the relatively rapid corrosion in the absence of CO_2. The slowing down of aluminum chloride induced corrosion of aluminum by CO_2 may be connected to the formation of carbonate on the surface. Aluminum hydroxy carbonate form amorphous precipitates that may interfere with the corrosion process.

The comparison between NaCl and Na_2SO_4 shows that in the absence of CO_2, sodium chloride is more corrosive than the sulfate, especially when large amounts of salt are added (see Fig.7) Both salts are expected to support the formation of high pH areas on the surface and would be expected to cause similar corrosion effects. The lower corrosivity of sodium sulfate is suggested to be connected to the lower solubility of aluminum hydroxy sulfates in comparision to the chlorides. Carbon dioxide inhibits the atmospheric corrosion of aluminum in the presence of both NaCl and Na_2SO_4. The inhibitive effect of CO_2 on the Na_2SO_4 induced corrosion of aluminium is explained in the same way as for NaCl. The average corrosion rate in the presence of CO_2 is the same for both salts. The main difference is that sulfate is less efficient than chloride in causing pitting of aluminum in neutral or acidic media.

Conclusions

In the absence of CO_2, the corrosivity of the chloride salts studied increases in the order $MgCl_2 \cdot 6H_2O$ < $AlCl_3 \cdot 6H_2O$ < NaCl. Sodium chloride is very corrosive in this environment because the sodium ion supports the development of high pH in the cathodic areas, resulting in alkaline dissolution of the alumina passive film and rapid general corrosion. The low corrosivity of $MgCl_2 \cdot 6H_2O$ is explained by the inability of Mg^{2+} to support high pH values in the cathodic areas. The relatively high corrosivity of $AlCl_3 \cdot 6H_2O$ in the absence of CO_2 is explained by the formation of an acidic surface electrolyte and by the high solubility of aluminum hydroxy chlorides.

In the presence of carbon dioxide, the corrosion induced by the salts studied exhibit similar rates. Carbon dioxide strongly inhibits aluminum corrosion in the presence of $AlCl_3 \cdot 6H_2O$ and especially, NaCl, while it is slightly corrosive in the presence of $MgCl_2 \cdot 6H_2O$. The inhibitive effect of CO_2 in the case of NaCl is attributed to its acidity. Carbon dioxide neutralizes the alkaline solution formed in the cathodic areas and forms solid carbonates. CO_2 decreases pH in the surface electrolyte resulting in a positively charged alumina film. Chloride adsorption on the passive film causes local depassivation, explaining the predominance of pitting corrosion in the presence of CO_2. The slowing down of aluminum chloride induced corrosion of aluminum by CO_2 may be connected to the formation of aluminum hydroxy carbonates. They form amorphous precipitates that may interfere with the corrosion process. The magnesium chloride induced corrosion of aluminum is somewhat enhanced by CO_2. It is suggested that CO_2 accelerates the magnesium chloride induced corrosion of aluminum because it acidifies the electrolyte, keeping Mg^{2+} in solution.

In the absence of CO_2, Na_2SO_4 is less corrosive than NaCl, This is explained by the lower solubility of aluminum hydroxy sulfates in comparison to the chlorides. The average corrosion rate in the presence of CO_2 is the same for both salts. The main difference is that sulfate is less efficient than chloride in causing pitting of aluminum in neutral or acidic media.

The inhibitive effect of CO_2 on the NaCl and Na_2SO_4 is relevant to situations where the supply of CO_2 is limited, for example in crevices and beneath organic coatings.

Table I. The % relative humidity within a closed space when an excess of the substance indicated is in contact with a saturated aqueous solution of a given solid phase at 25°C.

Salt	Deliquescence point (%RH)	Electrolyte concentration at 95%RH (mol/kg H_2O)*
NaCl	75[29]	1.3
Na_2SO_4	93[29]	0.5
$AlCl_3$	30*	3.4
$MgCl_2$	33[30]	0.4

*Calculated according to Kusik and Meissner, 1978 [31].

Table II. Corrosion rate, corrosion product ratio and amount water soluble anions without CO_2 for different chloride-containing salts

salt	amount of salt applied ($\mu g \cdot cm^{-2}$)	amount of cation added ($\mu mol \cdot cm^{-2}$)	amount of anion added ($\mu mol \cdot cm^{-2}$)	mass gain ($mg \cdot cm^{-2}$)	corrosion product mass/metal loss	metal loss ($mg \cdot cm^{-2}$)	water soluble anion (%)
NaCl	142.5	2.44	2.44	0.84	2.8	0.47	99
NaCl	70	1.2	1.2	0.96	3.0	0.48	99
NaCl	14	0.24	0.24	0.24	3.0	0.12	99
NaCl	0	0	0	0.010	na	0.005	-
$AlCl_3$	162.5	1.22	3.66	0.079	1.5	0.17	Spallation
$AlCl_3$	32.5	0.24	0.73	0.16	2.7	0.092	99
$MgCl_2$	116	1.22	2.44	0.014	2.5	0.009	65
$MgCl_2$	23	0.24	0.48	0.005	2.5	0.004	-

The exposure time was 672h and the relative humidity was 95%. The scatter in mass gain and metal loss results was about 5%.

Table III. Ratios of corrosion product mass divided by aluminium mass for selected corrosion products of aluminium.

Product	Formula	Ratio[a]
Aluminum oxide	γ-Al_2O_3	1.89
Akdalait	$Al_2O_3 \cdot 1/4H_2O$	1.97
Boehmite	γ-AlOOH	2.22
Pseudoboehmite	$Al_2O_3 \cdot 2H_2O$	2.55
Bayerite	$Al(OH)_3$	2.89
Gibbsite (Hydrargillite)	γ-$Al(OH)_3$	2.89
Tucanite	$Al(OH)_3 \cdot 1/2H_2O$	3.22
Aluminum hydroxy sulfate	$Al_2SO_4(OH)_4 \cdot 4H_2O$	5.37
Aluminite	$Al_2SO_4(OH)_4 \cdot 7H_2O$	6.37
Mendozite	$NaAl(SO_4)_2 \bullet 11H_2O$	15.4
Aluminum sulphate hydrate	$Al_x(SO_4)_y \cdot z(H_2O)$	-
felsoebanyaite	$Al_4SO_4(OH)_{10} \bullet 5H_2O$	2.41
Aluminum chloride hydrate	$Al(H_2O)_6Cl_3$	5.00
Dawsonite	$NaAlCO_3(OH)_2$	4.48
Cadwaladerite	$AlCl(OH)_2 \cdot 6H_2O$	6.26
Bischofite	$MgCl_2 \bullet 6H_2O$	

[a]In order to simplify a comparison with the corresponding values in Table I (corrosion rate), the sodium and chloride was omitted when these ratios were calculated.

Table IV. Corrosion rate, corrosion product ratio and amount water soluble anions in the presence of 350ppm CO_2 for different chloride-containing salts

salt	environment	amount of salt applied ($\mu g \cdot cm^{-2}$)	amount of cation added ($\mu mol \cdot cm^{-2}$)	amount of anion added ($\mu mol \cdot cm^{-2}$)	mass gain ($mg \cdot cm^{-2}$)	corrosion product mass/metal loss	metal loss ($mg \cdot cm^{-2}$)	water soluble anion (%)
NaCl	350ppmCO_2	134	2.29	2.29	0.055	1.9	0.062	99
NaCl	350ppmCO_2	70	1.2	1.2	0.022	1.9	0.025	99
NaCl	350ppmCO_2	14	0.24	0.24	0.016	na	0.018[1]	99
NaCl	350ppmCO_2	0	0	0	0.010	na	0.005	-
$AlCl_3$	*350ppmCO_2*	*162.5*	*1.21*	*3.66*	*0.032*	*1.6*	*0.056*	*Spallation*
$AlCl_3$	*350ppmCO_2*	*32.5*	*0.24*	*0.73*	*0.070*	*3.9*	*0.024*	*Spallation*
$MgCl_2$	*350ppmCO_2*	*116*	*1.22*	*2.44*	*0.076*	*2.0*	*0.074*	*73*
$MgCl_2$	*350ppmCO_2*	*23*	*0.27*	*0.48*	*0.035*	*1.7*	*0.050*	*95*

The exposure time was 672h and the relative humidity was 95%. The scatter in mass gain and metal loss results was about 5%.
[1]) Calculated metal loss assuming that the corrosion product ratio is the same as for the case with 2.29µmol NaCl added, i.e. 1.9

Table V. Corrosion rate, corrosion product ratio and amount water soluble anions for NaCl and Na_2SO_4 in the absence and in the presence of CO_2

salt	environment	amount of salt applied ($\mu g \cdot cm^{-2}$)	amount of cation added ($\mu mol \cdot cm^{-2}$)	amount of anion added ($\mu mol \cdot cm^{-2}$)	mass gain ($mg \cdot cm^{-2}$)	corrosion product mass/metal loss	metal loss ($mg \cdot cm^{-2}$)	water soluble anion (%)
Na_2SO_4	<1ppmCO_2	174	2.45	1.23	0.25	2.2	0.22	80
Na_2SO_4	<1ppmCO_2	87	1.26	0.61	0.25	2.3	0.20	80
Na_2SO_4	<1ppmCO_2	20.5	0.29	0.14	0.036	1.5	0.078	76
Na_2SO_4	350ppmCO_2	173	2.44	1.22	0.073	3.6	0.029	89
Na_2SO_4	350ppmCO_2	89.5	1.26	0.63	0.038	4.6	0.011	86
Na_2SO_4	350ppmCO_2	18	0.25	0.13	0.027	3.0	0.014	66

The exposure time was 672h and the relative humidity was 95%. The scatter in mass gain and metal loss results was about 5%. [1]) Calculated metal loss assuming that the corrosion product ratio is the same as for the case with 2.29µmol NaCl added, i.e. 1.9

References

1. K. S. Ferrer and R. G. Kelly, *Proceedings - Electrochemical Society,* pp. 176 (2003).
2. C. Leygraf and T. E. Graedel, *Atmospheric Corrosion*, Wiley, New York (2000).
3. K. Shimizu, G. M. Brown, H. Habazaki, K. Kobayashi, P. Skeldon, G. E. Thompson, and G. C. Wood, *Corrosion Science,* **41**, 1783 (1999).
4. G. Wranglen, *An Introduction to Corrosion and Protection of Metals*, (1985).
5. T. E. Graedel, *J. Electrochem. Soc.,* **136**, 204C (1989).
6. R. E. Lobnig, D. J. Siconolfi, J. Maisano, G. Grundmeier, H. Streckel, R. P. Frankenthal, M. Stratmann, and J. D. Sinclair, *J. Electrochem. Soc.,* **143**, 1175 (1996).
7. J. D. Sinclair and L. A. Psota-Kelty, *Proc. - Int. Congr. Met. Corros.,* **2**, 296 (1984).
8. N. Le Bozec, D. Persson, A. Nazarov, and D. Thierry, *J. Electrochem. Soc.,* **149**, B403 (2002).
9. L. Bourdeau, A. Jussiaume, E. Perrot, G. Stroem, and D. Thierry, *Galvatech 2001, International Conference on Zinc and Zinc Alloy Coated Steel Sheet, 5th, Brussels, Belgium, June 26-28,* pp. 295 (2001).
10. W. Furbeth and M. Stratmann, *Progress in Organic Coatings,* **39**, 23 (2000).
11. J.-E. Svensson, *The Influence of Different Air Pollutants on the Atmospheric Corrosion of Zinc*, Department of Inorganic Chemistry, Göteborg University, Sweden (1995).
12. S. S. Butcher, R. J. Charlson, G. H. Orians, G. V. Wolfe, and Editors, *Global Biogeochemical Cycles*, Academic Press Inc., London (1992).
13. D. B. Bluecher, J. E. Svensson, and L. G. Johansson, *J. Electrochem. Soc.,* **150**, B93 (2003).
14. T. Falk, J. E. Svensson, and L. G. Johansson, *J. Electrochem. Soc.,* **145**, 2993 (1998).
15. R. Lindstrom, J. E. Svensson, and L. G. Johansson, *J. Electrochem. Soc.,* **149**, B103 (2002).
16. W. H. Ailor and Editor, *Atmospheric Corrosion*, (1982).
17. J. H. Seinfeld and S. N. P. J, *Atmospheric Chemistry and Physics: From Air Pollution to Climate Change*, ohn Wiley & Sons, Inc., New York (1998).
18. K. S. Ferrer and R. G. Kelly, *Proceedings - Electrochemical Society,* **2002-24**, 176 (2003).
19. V. Kucera and E. Mattsson, Atmospheric corrosion, In: *Chem. Ind. (Dekker)*, F. Mansfield, ed., Marcel Dekker, New York (1987).
20. P. V. Strekalov, *Zashch. Met.,* **29**, 819 (1993).
21. B. J. Finalyson-Pitts and J. N. Pitts, Jr., *Atmospheric Chemistry: Fundamentals and Experimental Techniques*, (1986).
22. K. Barton, *Schutz gegen atmosphärische Korrosion*, Verlag Chemie GmbH, Weinhem (1973).
23. L. G. Johansson, *Marine Chemistry,* **30**, 113 (1990).
24. H. Boehni and H. H. Uhlig, *J. Electrochem. Soc.,* **116**, 906 (1969).
25. D. B. Blucher, R. Lindstrom, J. E. Svensson, and L. G. Johansson, *J. Electrochem. Soc.,* **148**, B127 (2001).
26. R. Lindstrom, J.-E. Svensson, and L.-G. Johansson, *J. Electrochem. Soc.,* **147**, 1751 (2000).
27. L. Ingemarsson, Master Thesis, Experimental Physics, Chalmers University of Technology, Sweden (2005).
28. D. Bengtsson Blücher, J.-E. Svensson, and L. G. Johansson, *J. Electrochem. Soc.*, (2002).

29. D. R. Lide and H. P. R. Frederikse, *CRC Handbook of Chemistry and Physics, 78th Edition*, (1997).
30. J. F. Young, *Journal of Applied Chemistry,* **17**, 241 (1967).
31. C. L. Kusik and H. P. Meissner, *AIChE Symposium Series,* **74**, 14 (1978).